Responsive Theranostic Nanoparticles



Wen-Yen Huang

St Hilda's College
University of Oxford

Thesis submitted for the degree of

Doctor of Philosophy

Hilary 2013

Responsive Theranostic Nanoparticles

Wen-Yen Huang
St. Hilda's College, University of Oxford
Doctor of Philosophy in Inorganic Chemistry
Hilary 2013

Abstract

The development and use of nanotechnology towards theranostics (all-in-one disease diagnostics and therapeutic delivery) have been increasing in popularity in recent years, in particular the use of high capacity of nanomaterials to transport both imaging and therapeutic agents into pathological tissues or abnormal cells. In this work, biocompatible mesoporous silica nanoparticles (MSNs) that can be reliably endocytosed by cells are employed in the investigation of novel cancer treatment and magnetic resonance imaging (MRI). One of the principal aims is to develop T_1 contrast nanoparticles not only with extraordinarily high MRI contrast characteristics, but also tunability through surface chemistry and functional protein conjugation. In coupling paramagnetic Gd^{3+}-centres to MSNs, one can effectively marry the advantages afforded by increased molecular bulk with those engendered by confined water environment inside the porous network. Specifically, through exclusively biasing paramagnetic Gd^{3+}-centres in the internal spaces of nanoparticles, their mobility and interaction with water protons can be altered, significantly, with beneficial changes in molecular tumbling (τ_R), proton exchange (τ_M) and water diffusion (τ_D) within relaxation dynamics. These MRI nanoparticles with internalised Gd^{3+}-centres are additionally used in the development of tunable/responsive contrast agents through vectoring protein conjugation. The relaxivity of MSNs can be tailored depending on the separation distances between proteins and nanoparticles; significantly, the simultaneous retention of both high MRI contrast and protein vectoring is achieved by the insertion of long polyethylene glycol (PEG) chain. The image contrast can also be reversibly gated through the competitive displacement of surface proteins by their partner proteins. Specifically, these responsive nanoparticles possess a low contrast resulting from restricted water accessibility when protein moieties are conjugated on the particles, whereas the removal of proteins causes a transition of contrast from a low to high state. The MSNs synthesised in this work are used not only in diagnostic imaging but also in the delivery of therapeutic agents for cancer therapy. The agents can be either physically encapsulated inside the pores or chemically conjugated on the nanoparticles. For the former, their loading and release efficiencies are tunable by the electrostatic interactions with particle surface functional groups; while in the latter case, their retention on nanoparticles, as opposed to being released, plays an important role in the effectiveness of cancer treatment that is achieved by trigging programmed cell death (apoptosis) in this work. This nanoparticle conjugation secures the proteins' activity by facilitating their bypass of proteolytic degradation. Significantly, specially designed nanoparticles that demonstrate endo/lysosomal escape capability can reliably deliver therapeutic cytochrome *c* to cell cytosols for the initiation of a caspase cascade within apoptosis with high efficacy.

Acknowledgements

I would like to express my deepest appreciation to my supervisor, Dr Jason Davis, who provided me the opportunity to carry out such an interesting and multidisciplinary project. This thesis would not have been possible without his guidance throughout these years. I would also like to thank Dr Gemma-Louise Davies for all her help and support. Without her professional opinions, many practical obstacles would not have been easily overcome. The papers published during these years would not have existed without her collaboration. I am grateful to Dr Lowri Cochlin, Department of Physiology, University of Oxford for MRI assistance and advice and all other institutions (TEM in the Research Complex, Harwell, Rutherford Appleton Laboratory, Oxford; cell culture and surface analysis facilities in Department of Chemistry, University of Oxford) that provided equipment and technical help. I would also acknowledge financial support from the Wellcome Trust (WT094114MA).

I would like to thank all those present and former members of the Jason Davis group for their support and friendship over the years. Finally, a big thank to my parents for their endless love and support.

Contents

Chapter 1 Introduction 1-1

1.1 Mesoporous Silica 1-1

1.1.1 Synthesis and Formation Mechanism of Mesoporous Silica Materials 1-1

1.1.1.1 Particle Size and Morphology 1-3

1.1.1.2 Pore Structure and Size 1-4

1.1.2 Characterisation 1-8

1.1.3 Surface Modification and Application 1-10

1.1.3.1 Chemical Modification 1-10

1.1.3.2 Biomodification 1-12

1.2 Magnetic Resonance Imaging (MRI) 1-17

1.2.1 Inner-sphere Relaxivity 1-20

1.2.2 Outer-sphere Relaxivity 1-26

1.3 Drug Delivery with MSNs 1-29

1.4 Physiology of Nanomaterials with Cells 1-34

1.4.1 Endocytosis 1-34

1.4.1.1 Mechanism 1-34

1.4.1.2 Influence of Geometry (Shape and Size) on Endocytosis 1-37

1.4.1.3 Influence of Surface Chemistries on Endocytosis 1-40

1.4.2 Biodistribution, Clearance and Biocompatibility 1-43

1.4.2.1 General Behaviour 1-43

1.4.2.2 Biocompatibility of Silica 1-45

1.4.3 Apoptosis and Protein Therapeutics 1-47

1.5 Project Aims 1-52

1.6 References 1-55

Chapter 2 Experimental Section 2-1

2.1 Particle Preparation 2-1

2.1.1 Preparation of Plain MSNs 2-2

2.1.2 Preparation of Gd-DOTA MSNs by Post-grafting 2-3

2.1.3 Preparation of Gd-DOTA MSNs by Delayed Co-condensation 2-4

2.1.4 Preparation of Protein Conjugated Gd-DOTA Doped MSNs with Various Linkages 2-6

2.1.4.1 Direct Protein Conjugation to MSNs 2-6

2.1.4.2 Protein Conjugated MSNs *via* PEG Linker 2-7

2.1.4.3 Protein Conjugated MSNs *via* Disulfide Linker 2-10

2.1.4.4 Protein Conjugated MSNs *via* Biotin Linker 2-11

2.1.5 Preparation of Gd-DOTA Doped Non-porous Silica Nanoparticles 2-12

2.1.6 Preparation of Native FITC-MSNs, Primary amine Modified MSNs and Rhodamine-MSNs 2-13

2.1.7 Preparation of Imidazole Modified MSNs 2-13

2.1.8 Preparation of Cytochrome *c* Labelled MSNs & BSA Labelled MSNs 2-15

2.1.8.1 Protein Conjugated MSNs *via* Uncleavable Linker 2-15

2.1.8.2 Protein Conjugated MSNs *via* Cleavable Linker 2-16

2.1.9 Preparation of Rhodamine 6G Loaded MSNs and Capping with BSA through Disulfide Linker 2-17

2.2 Microarray Spotting 2-20

2.3 Cell Experiments 2-22

2.3.1 Fluorescent Labelling of Cellular Organelles 2-22

2.3.2 Cell Culture Procedure and Sample Preparation for Confocal Microscopy 2-23

2.3.3 Confocal Microscopy 2-24

2.4 Particle Characterisation 2-26

2.4.1 Physical Properties of Particles (Size, Morphology and Surface Charge) 2-26

2.4.2 Chemical Properties of Particles 2-27

2.4.3 Relaxivity Assessment 2-28

2.5 References 2-30

Chapter 3 Synthesis of Mesoporous Silica Nanoparticles and Location-tuned MRI Contrast 3-1

3.1 Introduction 3-1

3.2 Results and Discussion 3-7

3.2.1 Optimisation of Functionalised MSNs Preparation 3-7

3.2.2 Control of Amine and Gd^{3+}-chelate Location 3-9

3.2.3 Relaxivity Assessments 3-13

3.2.3.1 Gd Stability 3-13

3.2.3.2 Influence of Gd Location on Relaxivity 3-15

3.2.3.3 Influence of Gd Loading on Relaxivity 3-21

3.3 Conclusions 3-24

3.4 References 3-26

Chapter 4 Biological T_1 Contrast Gating 4-1

4.1 Introduction 4-1

4.2 Results and Discussion 4-5

4.2.1 Particle Preparation and Biomodification 4-5

4.2.2 Bio-vectoring Assessments 4-7

4.2.3 Relaxivity Assessments 4-9

4.2.3.1 PEG Tuned Relaxivity 4-12

4.2.3.2 Responsive and Switchable Relaxivity 4-17

4.3 Conclusions 4-24

4.4 References 4-25

Chapter 5 Engineering Cell-nanoparticle Interactions 5-1

5.1 Introduction 5-1

5.2 Results and Discussion 5-6

5.2.1 General Interactions of MSNs with Hela Cells 5-6

5.2.2 Confirmation of Endo/lysosomal Escapability 5-14

5.2.2.1 Co-incubation of Chloroquine and Luminescent MSNs with Hela Cells .. 5-15

5.2.2.2 MSNs Incubation Followed by Chloroquine Addition 5-16
5.2.3 Formulation of Novel Endo/lysosomal Escaping Nanoparticles 5-18
5.2.3.1 Surface Concentration Effect 5-19
5.2.3.2 Effect of Surface Functionalities 5-24
5.2.3.3 Time-dependent Endo/lysosomal Escape 5-31
5.3 Conclusions 5-34
5.4 References 5-37

Chapter 6 Nanoparticles for Therapeutic Delivery 6-1
6.1 Introduction 6-1
6.2 Results and Discussion 6-7
6.2.1 Drug Loading and Release Studies 6-7
6.2.2 Therapeutic Cytochrome *c* Delivery and Programmed Cell Death 6-18
6.3 Conclusions 6-31
6.4 References 6-33

Chapter 7 Conclusions and Future Work 7-1

Appendix A-1

Chapter 1 Introduction

1.1 Mesoporous Silica

1.1.1 Synthesis and Formation Mechanism of Mesoporous Silica Materials

Since the discovery of zeolite and its promising applications, the development of new porous materials has become a popular subject in scientific research for several decades. Zeolite, a porous aluminosilicate, has been intensively investigated and widely applied to the field of ion exchange[1], molecular sieve[2] and catalysis[3]. The porosity of this material allows guest molecules to freely diffuse in and out of the structure, and provides capability to accommodate them depending on their shape and size selectivity (the average pore size of this porous material ranges from 0.5 to 1 nm)[2, 4]. Its large surface area, on the other hand, has made zeolite an excellent platform for catalysis[3]. In addition, the adoption of zeolite to the fields of biomedicine[5-7], chemical sensing[8, 9] and hydrogen storage[10] amongst others has also been documented. However, more recently due to the requirement for carrying larger molecules such as enzymes or biomolecules, zeolite's apparent small pore size has limited its utility[4]. However, the Mobil Oil Corporation developed a novel M41S type of silica based molecular sieve which is characterised by a long range of ordered mesopores, a pore size between 3 to 5 nm and high surface area of >1000 cm^2g^{-1}.[11, 12] A number of studies investigating a variety of synthetic strategies to tailor the size, shape and pore

diameters of this M41S class of porous materials since their introduction has been reported.

M41S type molecular sieves are typically synthesised using stoichiometric amounts of a silica source (tetraethyl orthosilicate, TEOS, for example), a structure-directing agent (alkyltrimethylammonium halide surfactant is commonly used here), a basic catalyst (sodium hydroxide or triethanol amine, for instance) and water at various temperatures[11-13]. Subsequent removal of the templating surfactant using ion exchange or calcination results in a stable colloidal suspension. MCM-41, MCM-48 and MCM-50 (Mobil Composition of Matter No. 41, 48 and 50) are three main sub-divisions of M41S family that are categorised based on structural criteria[14]. MCM-41 possesses hexagonal mesospheres belonging to the *P6m* space group. MCM-48 structure shows cubic mesophase (*Ia3d*), which can be visualised as a two interlinked networks of spherical cages separated by continuous silicate frameworks. MCM-50, in uncalcined form, shows lamellar structure (*P2*), but after surfactant removal and post treatment, results into pillared layer material[14, 15]. SBA type (Santa Barbara Amorphous material) is another mesoporous silica family. SBA-15 is perhaps the most well-known type within this category[16]. It is synthesised using the triblock copolymer pluronic P123 $[HO(CH_2CH_2O)_{20}(CH_2CH(CH_3)O)_{70}(CH_2CH_2O)_{20}H]$ as a template and catalysised by hydrochloric acid. Notably here, the mesoporous materials fabricated under these acidic conditions result in thicker pore walls compared to ones synthesised with basic catalysis[17].

1.1.1.1 Particle Size and Morphology

The synthesis of mesoporous silica nanoparticles (MSNs) employs the so-called sol-gel technique. This is a wet-chemical process starting from a colloidal solution (sol) and followed by the formation of an integrated network (gel). Typically for the preparation of MSNs, silicon alkoxide precursors undergo a series of hydrolysis and condensation reactions under acidic or basic catalytic conditions. Hydrolysis occurs by the nucleophilic attack of the water oxygen on the silicon atom resulting in the replacement of alkoxy groups (OR) by hydroxyl (OH) (see the reaction equations below)[18, 19]. The subsequent condensation creates silica material and water/alcohol.

Hydrolysis: $Si\text{-}(OR)_4 + H_2O \rightarrow (RO)_3\text{-}Si\text{-}OH + ROH$

Alcohol condensation: $Si\text{-}(OR)_4 + HO\text{-}Si\text{-}(OR)_3 \rightarrow (RO)_3\text{-}Si\text{-}(OR)_3 + ROH$

Water condensation: $(RO)_3\text{-}Si\text{-}OH + HO\text{-}Si\text{-}(OR)_3 \rightarrow (RO)_3\text{-}Si\text{-}(OR)_3 + H_2O$

The rates of hydrolysis and condensation depend on the pH and markedly influence the size of resulting particles. The slowest hydrolysis rate occurs at pH 7 and other pH values lead to faster rates[24, 25]. In basic conditions, particles are highly ionised and therefore particle growth occurs *via* Ostwald ripening without aggregation or gelation, resulting in discrete uniform particles. Acidic conditions on the other hand cause the aggregation of the alkoxysilane networks and hence form bulk gels. Because a variety of variables, including silane source, reaction temperature, solvent (water) ratio etc., that affect particle growth are closely related to one another, the MSNs formation mechanism is highly complex and inconclusive. There, however, exist some general trends leading to particle size variation. In basic conditions, the particle size can be

increased by employing tetraalkoxysilanes with increasing carbon chain lengths[20, 21]. This difference in the particle size can be attributed to the variation in the reactivity of silica sources and the corresponding nucleation and grain growth rates. Notably here, the concentration of silane precursors is relatively insignificant in affecting particle size[22]. Conversely, at a fixed silane concentration, an increase in water content leads to an increase in hydrolysis/condensation rate and hence resulting particle size[20]. Reaction temperature has also been reported to vary the particle size. Increasing the temperature from 40°C to 80°C leads to a growth in particle size from 50 nm to 110 nm[23].

1.1.1.2 Pore Structure and Size

The porous features of all such porous silicate vary depending on the effective surfactant ion pair packing. This packing governs the assembled-micelle shape and thus the corresponding pore structure. Mathematically, this can be expressed as packing parameter '*g*'. For lyotropic liquid crystalline phase, $g = V/al$, where V is volume of surfactant tail, a is effective head group area and l is length of the extended surfactant tail[24, 25]. Due to the variation of different types of surfactant tails and head groups, g is tailorable. Typically, when $g < 1/3$, spherical micelles are produced; further increase in the concentration of surfactant to $g = 1/3$ results in cubic phase (*Pm3n*); hexagonal arrays (*P6m*) are formed when the value of $g = 1/2$; and when the g value lies in between 1/3 and 1/2, the formation of a cubic phase (*Ia3d*) occurs. A lamellar structure forms when g is equal to 1[26, 27].

It is clear that the surfactant chemistry is significantly important in the study of mesoporous material synthesis (where the arrangement and the subsequent removal of surfactant determines the porous structures) and also in the understanding of mesoporous structure formation mechanism. The nature of the surfactant governs the pore size, structure of pores, thickness of walls, phase and symmetry of materials. Surfactants consist of a hydrophilic polar head group and hydrophobic nonpolar hydrocarbon tail[28-30]. Due to this amphiphilic property, the surfactant molecules behave as active agents in aqueous solution showing high affinity to the water – organic interface. The nature of polar head group of surfactants (anionic, cationic, zwitterionic or non-ionic) and the pH conditions in which they are reacted determine their interaction with silica precursors[11, 12, 29].

The charges of silica precursors and surfactants (and their electrostatic interaction) vary depending on the pH of the solutions[11, 12, 18, 21]. Under basic conditions (whereby the silica species are present as anions), cationic surfactants are thus required to promote sufficient electrostatically attractive interactions [Fig. 1.1 (a); the conditions under which the M41S family is prepared][22, 23]. Conversely, negatively charged mediator ions [for cationic surfactants; Fig. 1.1 (b)] or anionic surfactants are used in acidic conditions [Fig. 1.1 (c); below the isoelectric point of the silica precursors, i.e. pH <2] where SBA type mesoporous materials are typically synthesised[22, 23]. In addition, the attractive interactions can also be mediated through hydrogen bonds [the case when non-ionic surfactants are used; Fig. 1.1 (d)][22, 23]. However, silica prepared

with non-ionic surfactants, possess thicker pore walls, due to a slower self-assembly of silica surfactant mesophase compared to ionic surfactants[31].

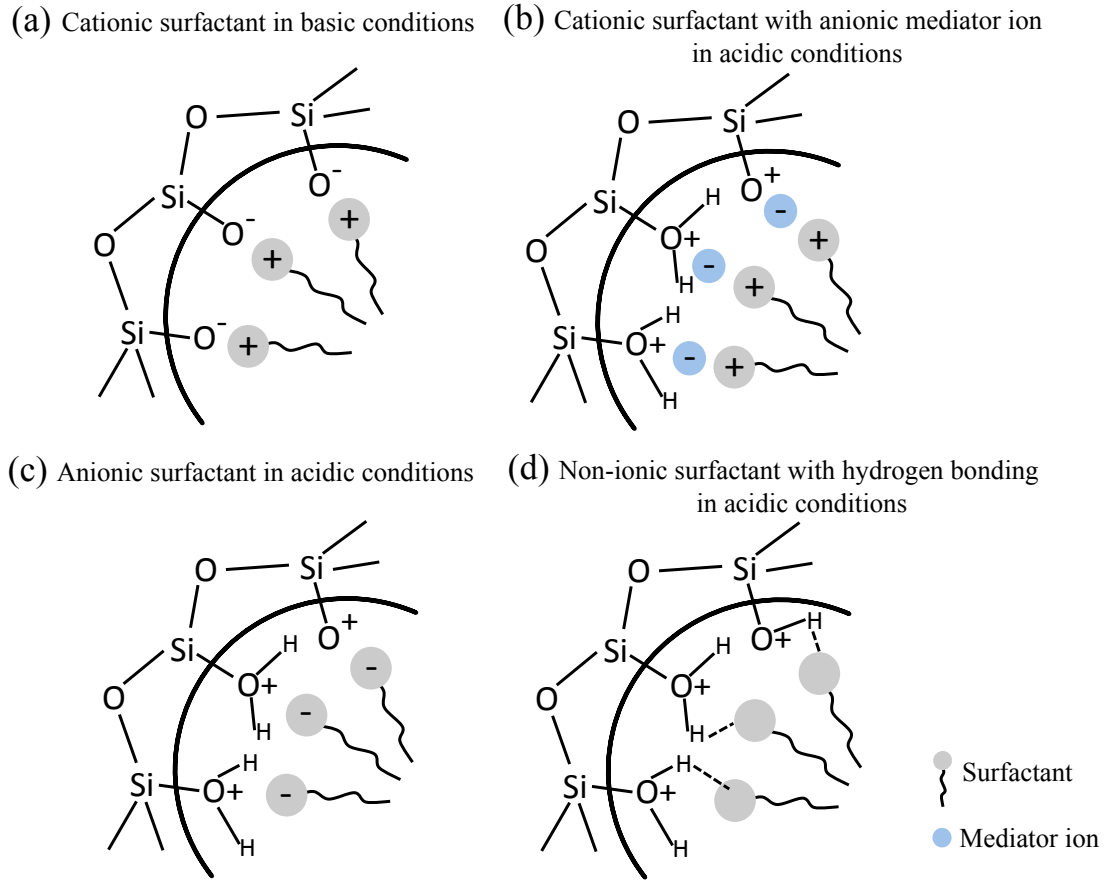


Fig. 1.1 Interactions between silicon alkoxides and head groups of surfactants in different pH conditions.

Surfactant molecules not only influence the behaviour of silica precursors through their interaction and associated reactivity, but also have great impact on the resulting pore sizes depending on their sizes. Prior works, for example, have indicated that the pore diameter of MCM-41 can be expanded from 1.8 nm to 3.7 nm by increasing the chain length of alkyltrimethylammonium halide surfactant from C8 to C18[12]. In

addition, there have been studies investigating pore size expansion by the addition of hydrophobic molecules during the reaction, such as aromatic hydrocarbons[32], long-chain alkanes[32], long-chain alkylamines[33] and auxiliary alkyl chemicals[34]. These additives are solubilised inside the hydrophobic regions of micelles formed by the surfactants leading to an increase in the micelle diameter and hence the pore size of the templated mesoporous products[35, 36]. In general, by increasing the amount of these additives, the pore size of mesoporous silica materials can be increased. For example, the pore diameter of MCM-41 can be expanded from 2.9 nm to 12 nm by increasing the ratio of silica source and 1,3,5-trimethylbenzene (a commonly used auxiliary chemicals)[35].

Although porous silica has been studied intensively for the past few decades, recently the rapid development of biochemical research has made them popular subjects again (especially MSNs), not only due to their superior physicochemical properties (large surface to volume ratio and highly tailorable surfaces) but also the biocompatibility and the lack of toxicity. This research, on the other hand, has urged the understanding of the formation mechanisms and the resulting morphologies/porous structures of these materials. The investigations are centralised on the control of various synthetic variables, including pH, temperature, water content, silica precursor and surfactant types etc. In general, sizes of particles prepared using the traditional Stöber technique are governed by the hydrolysis and condensation rates that are determined by pH, temperature, water content and silica source. The concentration of silica precursors, on

the contrary, is relatively insignificant in affecting particle size. Porous properties are mainly influenced by the nature of surfactants, their packing and pH conditions. Surfactant packing/concentration and pH greatly affect the structure of pores, whereas the size of surfactants and the presence/absence of hydrophobic additives control the pore sizes. Based on this knowledge, the synthesis of spherical MSNs in this thesis (that belongs to the M41S family) has employed the hydrolysis and condensation of TEOS with the templation of cetyltrimethylammonium bromide (CTAB) and the catalysis of basic triethanol amine at elevated temperature.

1.1.2 Characterisation

The most direct method to observe particle size and distributions of colloidal silica is electron microscopy [scanning electron microscopy (SEM) and transmission electron microscopy (TEM)[37]]. TEM holds several advantages over SEM in which the ability to visualise the inner structure of materials is perhaps the most significant (SEM generally can only provide morphological information from outer surface, whereas TEM is able to clearly image the internal porous structure[38, 39]). Particle size distributions can also be acquired by dynamic light scattering (DLS). This method measures Brownian motion of particle suspension and correlates it to particle size[40]. It should be noted that the diameter measured in DLS is a hydrodynamic diameter referring to a particle diffusing within a fluid. Therefore, any factors such as ionic concentration or solvent conductivity etc. in the fluid that would affect hydration of particle or its Brownian motion will result in different hydrodynamic size. Any change

to the surface of a particle that affects the diffusion speed will also correspondingly change the hydrodynamic size of the particle. Though the size measured by DLS is not the real physical size of particles, this is a commonly accepted method to determine particle dispersity using polydisperse index (PDI)[18, 37].

Another characterisation technique worth noting is ζ-potential surface charge measurement that determines the electrophoretic mobility of the particles in an electrical field and is closely related to the particle colloidal stability[18, 37]. The particle charge is one of the indicators for the physical stability of emulsions and suspensions. A high number of equally charged particles in a colloidal suspension leads to strong electrostatic repulsion between the particles resulting in high physical stability. The development of a net charge at the particle surface affects the distribution of ions in the surrounding interfacial region, resulting in a layer with an increased concentration of counter ions. The potential at the boundary between this layer and bulk dispersant is ζ-potential (Fig. 1.2).

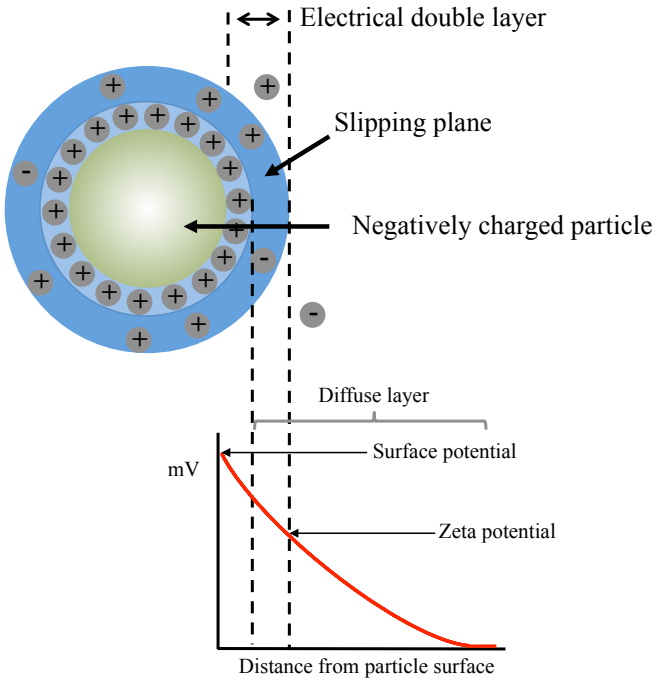


Fig. 1.2 Schematic representation of ζ-potential.

1.1.3 Surface Modification and Application

1.1.3.1 Chemical Modification

There are two major approaches generally involved in the functionlisation of MSNs; post-grafting and co-condensation. The former introduces functional groups by reacting with silanised chemicals after particle formation[41-43]. This method preferably produces particles with external modification. One way to guarantee that functional groups are exclusively conjugated on the outer surface of particles is to perform modification prior to the removal of template surfactant[43, 44]. The ability to selectively modify external surfaces is of importance from a great deal of applicative perspectives including, for example, those focussed on selective triggered drug delivery[45, 46]. The

initial development of MSNs-based drug delivery systems relies only on physical entrapment of small synthetic drug in the porous networks by electrostatic attraction[47] or weak hydrogen bonding[48, 49]. This approach, however, is incapable of preventing 'premature release' of drug molecules prior to the MSNs' approach of the target site, leading to a loss in therapeutic efficiency and side effects. In combination with cleavable linkage that is responsive to external stimulation, selectively modifying the exterior of MSNs with large materials, for example, to encapsulate drug has provided a solution to this premature releasing problem and a means to deliver drugs in a triggered fashion[45, 46]. Co-condensation allows functionalisation during the synthesis of nanoparticles. Although this method has the advantage of being a simple one-pot reaction, the introduced functional groups, due to different reactivity (compared to TEOS) and the subsequent hydrolysis/condensation rate, may influence the particle morphology and aggregation state[50, 51]. Lin *et al.*, for example, have investigated the morphological change by co-condensation of TEOS with various organosilanes such as silanised amine, urea, isocyanate, vinyl and nitrile[50]. Their results indicated significant impact of these functional groups on particle shape. An advantage of the co-condensation method is its ability to provide another control over the location of functional groups depending on the concentration and the addition time of these groups[41, 42, 52]. Specifically, the location of functional groups has significant impact on final properties and applications of nanoparticles. For example, in this thesis, the different locations of paramagnetic species within the porous structures have been shown to have impact on magnetic resonance signals (as described in Chapter 3). In

addition, the location bias engendered by the co-condensation technique can result in modification exclusively in the internal surfaces of MSNs allowing their external surface to be subsequently conjugated with different functional moieties[41, 42, 52], such as therapeutic proteins (biomodification); an area investigated in Chapter 6 of this thesis.

1.1.3.2 Biomodification

Recently, there have been increasing studies on the biomodification of silica nanoparticles. Most generated from a proposed requirement to vector therapeutics and or image contrast (theranostics)[53, 54]. Silica is amongst the most useful materials for such applications, with its versatility towards different surface modification protocols. The silica surface can be modified to contain amine, carboxyl groups, sulfide or avidin etc[55]. A common protocol for the immobilisation of biomolecules is the use of amino-group derivatisation. Nanoparticles can be modified with silanised amines which can then be conjugated with crosslinkers such as 1-ethyl-3-(-3-dimethylaminopropyl) carbodiimide hydrochloride (EDC) or water-insoluble N'-N'-dicyclohexyl carbodiimide (DCC) followed by the integration of carboxyl groups of biomolecules[55, 56] resulting in amide bonds (a half-life of about 600 years in neutral solution at 25°C[57] made them highly attractive for bioconjugation). EDC and DCC are the most readily available and commonly used carboiimide crosslinkers. EDC reacts with the carboxylic acid groups of biomolecules to form an active O-acylisourea intermediate that is easily displaced by nucleophilic attack from primary amino groups on the

nanoparticles in the reaction mixture. The O-acylisourea intermediate is unstable in aqueous solutions; failure to react with an amine results in hydrolysis of the intermediate and regeneration of the carboxyls. N-hydroxysuccinimide (NHS) or its water-soluble analogue (Sulfo-NHS) is often included in EDC coupling reactions to improve efficiency or create dry-stable (amine-reactive) intermediates (NHS esters) (Fig. 1.3). This crosslinking procedure can be carried out in a reverse order starting with the carboxylation of silica nanoparticles followed by reaction with amino groups of proteins.

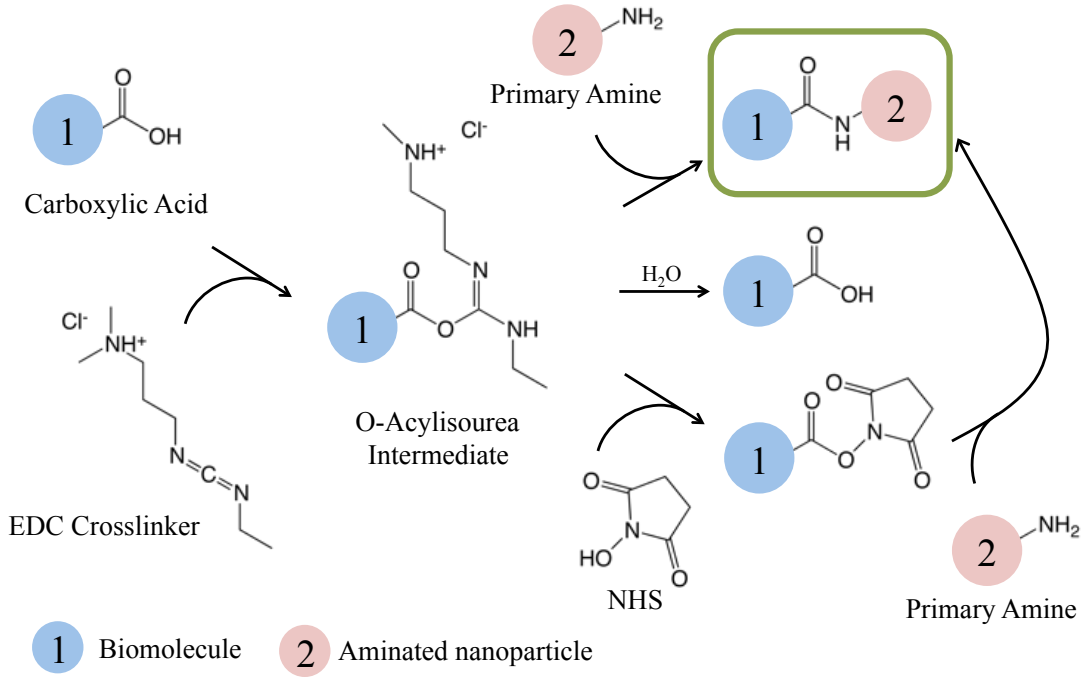


Fig. 1.3 Representation of carbodiimide reaction mechanism. Reaction of a carboxylic acid with a primary amine through a EDC linker with or without NHS to stabilise the O-acylisourea intermediate which is liable to hydrolysis leading to regeneration of a carboxylic acid. Highlighted structure is the desired final conjugate.

In addition to amine and carboxylate, as cysteine is the second least common amino acid in natural proteins[58], a more site-specific conjugation can often be performed at a unique cysteine residue (containing a thiolate) with thiol-reactive groups (maleimides or disulfides) modified silica nanoparticles. The maleimide groups react specifically with thiol groups when the pH of the reaction mixture is between pH 6.5 and 7.5 resulting in stable thioether linkages (Fig. 1.4). Disulfide-coupling chemistry has also been used for the immobilisation of oligonucleotides and proteins onto silica nanoparticles[59, 60]. 3-Mercaptopropyl trimethoxysilane, for example, has been grafted onto silica nanoparticles which can subsequently react with disulfide-modified oligonucleotides or proteins using a thiol/disulfide exchange reaction[59]. Silica surface modification is not limited to chemically mediated procedures. Avidin, for instance, can be coated onto the silica surface using various crosslinking chemistries as described above. The resulting avidin-coated nanoparticles can then be conjugated with biotinylated molecules based on the strong avidin-biotin affinity[61]. This non-covalent conjugation technique can be adapted to the immobilisation of antibodies to nanoparticles using their specific antigens[55].

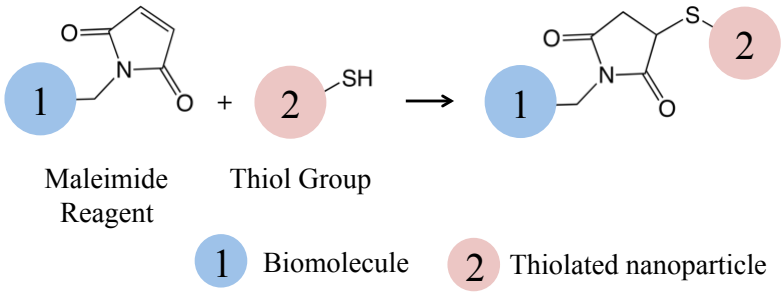


Fig. 1.4 Bioconjugation of a thiolate with a maleimide reagent.

The consequences of immobilisation of biomolecules on nanoparticles are worth noting prior to the practical applications. Studies have intended to summarise the properties of biomolecules after conjugation to nanoparticles; however, there is no consistent observation, presumably due to the variation in particle sizes, the nature of biomolecules, modification density or immobilisation techniques. Some have reported that nanoparticles' large surface area makes the conjugation of multiple antibodies on a single particle possible and leads to a multivalent effect, i.e. the stronger binding of nanoparticle conjugated antibodies towards antigens/receptors than in their free states[62-65]. For example, the binding affinity of nanoparticle-conjugated Herceptin (an antibody that is used to treat breast cancer) toward ErbB2 receptor (a receptor overexpressed in breast cancer) increases proportionally to the size of a nanoparticle owing to a higher antibody density on the nanoparticle surface[65]. Others, however, have reported keeping modification density consistent across different sizes of silica nanoparticles causes affinity decreases with increasing particle size when using biotin modified nanoparticles and streptavidin[66-69]. In these studies, the reduction in affinity is assigned to steric hindrance for 'active' biotin resulting from surface immobilisation. In more general terms, the multivalent effect is the result of high local concentration leading to high affinity, whereas particle surfaces can sterically prevent biomolecules from effectively binding onto their partners on the nanoparticles. The attractiveness of proteins as therapeutics results from their high specificity; however, therapeutic proteins are not only susceptible to proteolytic degradation but also are potentially immunogenic in patients and occasionally can induce anti-drug antibody responses

leading to adverse effects[70]. There is some prior work which have hinted that nanoparticles are capable of protecting proteins from degradation by either covalent conjugation or physical encapsulation in the porous structures[66, 84]. In combination with targeting moieties, these proteins can perform their activities at the specific sites without inducing any side effects. This nanoparticle stabilisation effect may be one of the most exciting advantages for protein immobilisation, which is particularly important in protein therapeutics[54, 71].

1.2 Magnetic Resonance Imaging (MRI)

Significant advances continue to be made in medical imaging through developments in the chemistry of imaging probes and the engineering of imaging devices. For example, an ability to visualise tissue morphology and cell function in real time would facilitate disease diagnosis. Several imaging modalities can be applied. Optical imaging has associated high sensitivity and spatial resolution that is down to sub-micro metre scale. However, the absorption and scattering characteristics of tissue components determine the penetration depth of light in tissues[72, 73]. Positron emission tomography (PET) is a highly sensitive radionuclide based imaging technique but is limited by relatively low spatial resolution (1 – 2 mm)[86, 87]. Magnetic resonance imaging (MRI) and computed tomography (CT) are both less sensitive, but they demonstrate a very high resolution, less than 200 μm[86, 87]. Among those, MRI is perhaps the most popular technique in molecular imaging and clinical radiology.

In ^{1}H MRI, the image contrast is generated from the variation of the nuclear magnetic resonance characteristics of water protons[74]. When water molecules are exposed to an external magnetic field (B_0), their nuclear spins will reach an equilibrium state with a (Larmor precession $\omega = -\gamma B$, where γ is gyromagnetic ratio and B is the magnitude of the magnetic field) frequency that is dependent on the strength of external magnetic field. On the application of an appropriate radiofrequency pulse (RF pulse) the net magnetisation vector associated with these spins will flip from a position parallel to the external field to the an anti-parallel position. After turning off the RF pulse, the

protons will relax back to their equilibrium states (Fig. 1.5).

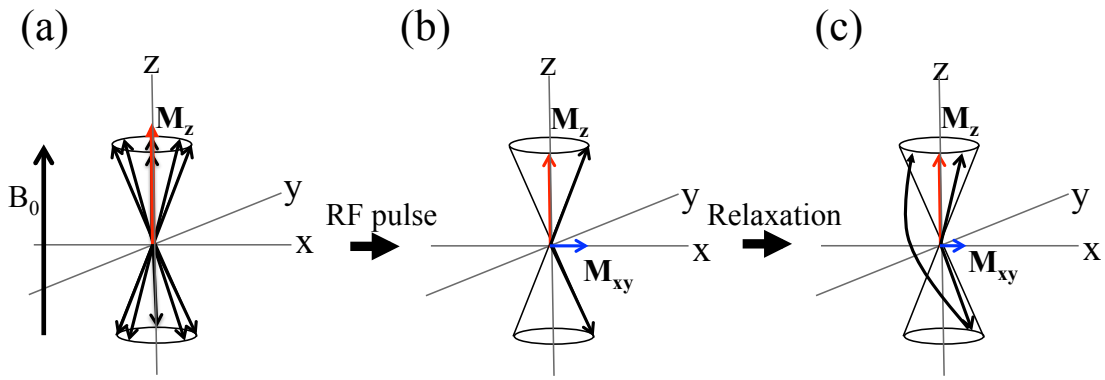


Fig. 1.5 Relaxation of the net magnetisation vector of the nuclear spins, precessing at Larmor frequency. (a) When placing water molecules in an external field (B_0), the net nuclear spin (M_Z) aligns with the field, z direction in the figure. (b) Application of a RF pulse results in a magnetisation vector in an anti-parallel position to the external field and accordingly, yields magnetisation components in both z axis (M_Z) and xy plane (M_{xy}). (c) After turning off the RF pulse, the magnetisation relaxes back to the equilibrium state.

This recovery in both the longitudinal and transverse magnetisation is termed 'relaxation'. The time it takes after an RF pulse for the proton (still precessing at Larmor frequency) to recover to its original longitudinal magnetic field is termed T_1 (or spin-lattice relaxation). The time it takes after an RF pulse for the relaxation of the transverse magnetisation to dissipate is termed T_2 (or spin-spin relaxation). Under most conditions, tissue proton density and the relaxation are usually high enough to provide sufficient contrast for quality MR images; however, some pathological conditions do not display specific enough changes in relaxation times to differentiate them from surrounding healthy tissue. In these cases, the use of MRI contrast agents that alter the local relaxation times of tissue is required[72, 74, 75]. Although approximately 35% of clinical MR scans utilise contrast media, a primary limitation of MR imaging is the

low sensitivity of detection of contrast agents and thus highly concentrated agents are required for enhanced signal intensity (0.1 - 0.6 mM)[76].

The effectiveness of a contrast agent can be quantified considering the change of relaxation rate per unit concentration of the agent and is defined as relaxivity[74, 75]. It can be classified into two categories depending on its influence on longitudinal (spin-lattice, T_1) or transverse (spin-spin, T_2) relaxation. Those that predominantly reduce T_1 are said to be "positive", whereas those that largely affect T_2 are "negative". With most pulse sequences, the positive contrast agent (T_1 agent) gives rise to increases in signal intensity and the negative agent (T_2 agent) causes a reduction in signal intensity. Iron oxide nanoparticles are the typical T_2 agent, whereas for proton T_1-weighted MR images, Gd^{3+}-based agents are the most common due to their high paramagnetic moment and long electron spin relaxation time (9 – 10 s)[75, 77]. Clinically, positive contrast (i.e. signal increase, using T_1 agents) is generally preferable to negative contrast (i.e. signal loss, using T_2 agents) due to the existence of other signal draining sources in tissues which can lead to false signal readings[78, 79]. It should be noted the free Gd^{3+} ion is toxic (as it disrupts physiological Ca^{2+} signaling[80]); chelations of Gd^{3+} are thus commonly employed in commercial Gd agents. These stable chelators, for example, include cyclic DOTA (1,4,7,10-tetraazacyclododecane-1,4,7,10-tetraacetic acid) and linear DTPA (diethylenetriaminepentaacetic acid) and are commercially available as Dotarem (Gd-DOTA) and Magnavist (Gd-DTPA), respectively (Fig. 1.6). The primary advantage of DOTA over DTPA is that it produces a more stable chelate

(as cyclic chelates have a higher activation energy barrier for both the complexation and dissociation than the linear chelates)[75, 81]. The former thus is employed in the preparation of silica nanoparticle based T_1 MR contrast agents throughout this thesis.

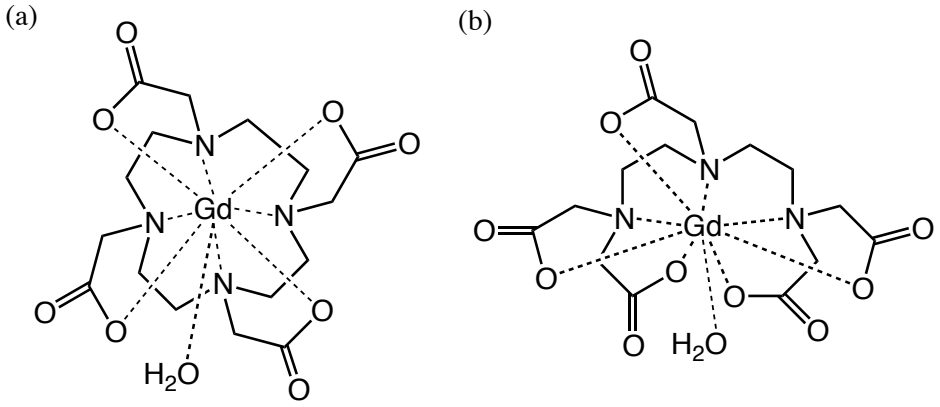


Fig. 1.6 Chemical structures of (a) cyclic Gd-DOTA and (b) linear Gd-DTPA.

1.2.1 Inner-sphere Relaxivity

As stated previously, a high concentration of Gd agents (clinically used molecular agents) is often required to result in sufficient signal intensity change for MR imaging. However, these molecular imaging agents are rapidly cleared i.e. have a very short blood circulation time (<30min)[82, 83], due to their small sizes. Their application is also limited by a default non-specific biodistribution (lack of target specificity). A variety of strategies have thus been proposed to overcome these limitations in which the theory described by Solomon, Bloembergen and Morgan (S.B.M. theory) is the most widely employed guide[84-86].

Relaxation of solvent water (bulk water) by a Gd^{3+}-complex is generally divided into

two components, inner-sphere and outer-sphere (Fig. 1.7). Both relaxations are composed of the contributions from longitudinal (T_1) and transverse (T_2) relaxation. The emphasis in this thesis will be on the longitudinal relaxation enhancement since this is the major effect of Gd^{3+}-based contrast agents. Inner-sphere relaxation refers to relaxation enhancement of water oxygen directly coordinated to the Gd^{3+} ion (Fig. 1.7); and outer-sphere relaxation describes relaxation enhancement of water molecules in the second coordination sphere (where the water molecule hydrates the complex through hydrogen bonding) and beyond (i.e. bulk water whose translational diffusion time governs the relaxation) (Fig. 1.7). Notably here, since it is difficult to quantify the numbers of second-sphere water and their lifetime, the overall relaxivity contributed from the second-sphere is often ignored[75].

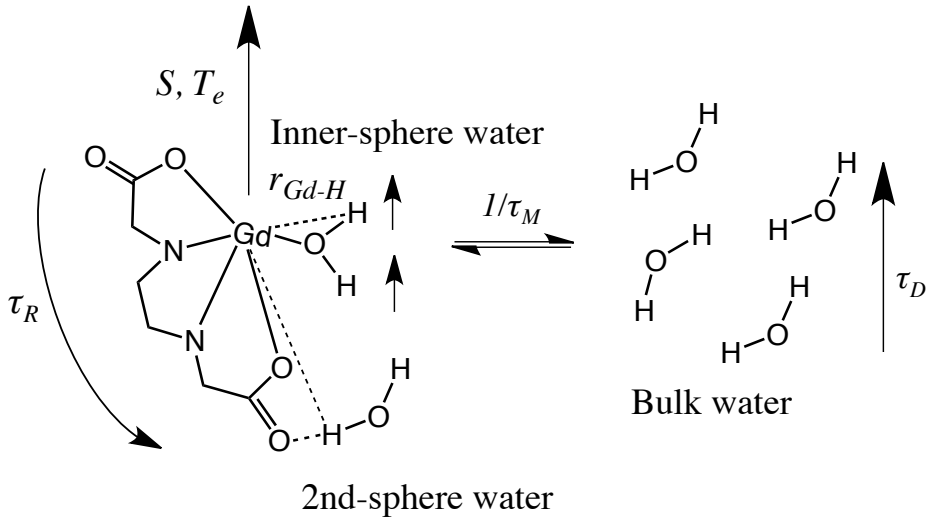


Fig. 1.7 Molecular parameters that influence inner- and outer-sphere relaxivity. τ_R is rotational correlation time related to the reorientation of the Gd^{3+} ion and water vector; τ_M is the residence time of the bound water; T_e is the electronic longitudinal relaxation time; S is spin quantum number; r_{Gd-H} is the electron spin-solvent nuclear spin distance; τ_D is diffusional correlation time.

The longitudinal relaxation contribution from the inner-sphere mechanism results from a chemical exchange of water molecules between the Gd^{3+}-centre and the bulk water as expressed in Eq. 1.

$$\left(\frac{1}{T_1}\right) = qPm\left[\frac{1}{T_{1M} + \tau_M}\right] \quad (1)$$

Here $1/T_1$ is longitudinal relaxation rate (directly related to the magnitude of relaxivity), τ_M is the residence time of the bound water, T_{1M} is the relaxation time of the bound water protons, q is the number of bound water molecules, and Pm is the mole fraction of water coordinated to the metal centre (Fig. 1.7)[75, 86]. The value of T_{1M}, within a dipole-dipole (DD) relaxation mechanism scheme, is given by the S.B.M. equations as outlined in Eq. 2. (γ is the nuclear gyromagnetic ratio, g is the electronic g factor, μ_B is the Bohr magneton, r is the electron spin-solvent nuclear spin distance, ω_s and ω_H are the electron and nuclear Larmor precession frequencies, respectively). τ_c in Eq. 2 is the correlation time and defined as Eq. 3 where τ_R is rotational correlation time related to the reorientation of the Gd^{3+} ion and water vector and T_e is the electronic longitudinal relaxation time. Importantly, the second term in the square brackets of Eq. 2 and T_e in Eq. 3 referring to electronic relaxation do not contribute appreciably at higher fields (greater than 1.5 T which are the common clinically used fields) and hence are often omitted[87].

$$\frac{1}{T_{1M}^{DD}} = \frac{2}{5}\frac{\gamma^2 g^2 S(S+1)\mu_B^2}{r_{Gd-H}^6}\left[\frac{3\tau_C}{1+\omega_H^2\tau_C^2} + \frac{7\tau_C}{1+\omega_S^2\tau_C^2}\right] \quad (2)$$

$$\frac{1}{\tau_C} = \frac{1}{\tau_R} + \frac{1}{T_e} + \frac{1}{\tau_M} \quad (3)$$

These equations highlight the critical role that each parameter has in obtaining high relaxation rate (and thus relaxivity). In general terms, greater numbers of bound water molecules (q, although this can pose a challenge in maintaining thermodynamic stability/kinetic inertness of the complex[75]), a faster water exchange rate (short water residence time τ_M) and a slower molecular tumbling speed (longer rotational correlation time τ_R) all serve to enhance relaxation/relaxivity.

Current contrast agent designs focus mainly on tuning inner-sphere parameters to obtain higher longitudinal relaxivity from the protons within the first coordination sphere[86]. Much effort has been invested in utilising the beneficial effects of increased rotational correlation time (τ_R), as afforded through conjugation of paramagnetic complexes to macromolecules or nanoparticles. Interestingly, the linkage structure, in the sense of linker flexibility, plays a notable role (Fig. 1.8). Linking paramagnetic complexes in a linear fashion, for example, generates an oligomer with anisotropic rotation where rotation about the short axis of the molecule is fast and limits enhancement[88] (Fig. 1.8 (a)). Multiple branched dendrimers have also been used to link gadolinium complexes (Fig. 1.8 (b)), where the contrasting effects of slow isotropic rotation (beneficial) and internal structural flexibility (disadvantageous) have been specifically noted[89]. Another approach to optimising the effects of motion on relaxivity has been to place the gadolinium at the centre of a large molecule (Fig. 1.8 (c)), where the lack of internal motion can result in remarkably high relaxivity[90]. These examples clearly indicate that rigidity of Gd^{3+}-centres truly plays a role in optimising

τ_R and the associated relaxivity. Therefore a number of studies have, accordingly, placed Gd^{3+}-complex on a more robust nanoparticle based platform.

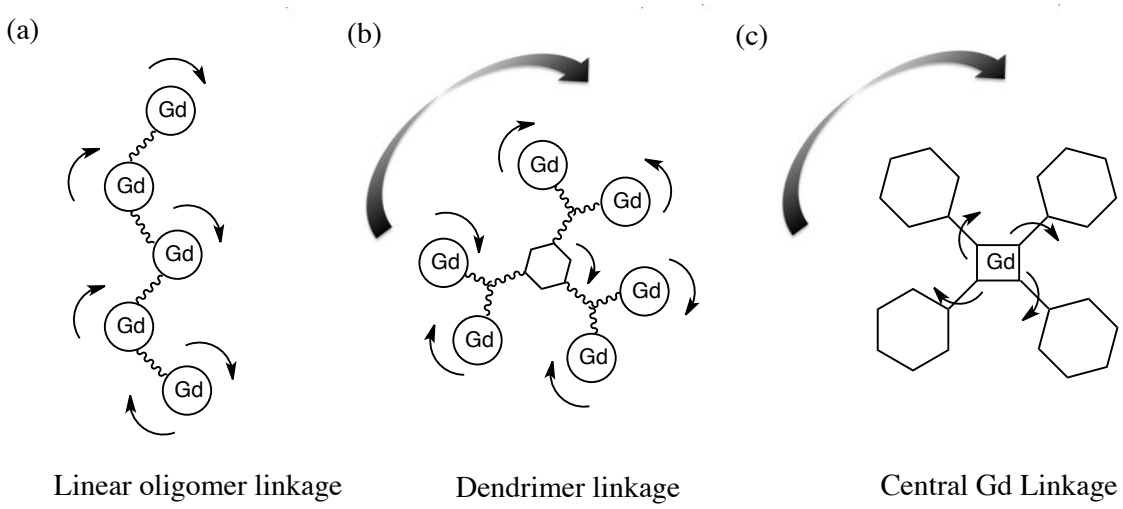


Fig. 1.8 Schematic representations of Gd chelate linkage and adduct rotation/conformational fluctuation. (a) linear oligomer linkage with anisotropic rotation where rotation about the short axis of the molecule is fast and limiting in terms of relaxivity enhancement; (b) dendrimer linkage with both isotropic rotation and internal motion around the core; the latter by virtue of the linkage flexibility and, again, limiting in terms of MR contrast; (c) Centralised Gd linkage where structure rigidification results in a remarkably high relaxivity.

Silica nanoparticles present one of the most ideal platforms by virtue of their controllable size, high surface area:volume ratio and highly engineerable internal and external chemistries[44, 91-98]. Studies have attempted to incorporate of Gd^{3+}-complexes onto silica particles to generate enhanced MR signal. In most cases the determined T_1 relaxivity is 5 - 10 times higher than that observed with the free chelate, an observation generally assigned to the reduced tumbling rate of the paramagnetic centre due to its association with bulky nanoparticle hosts[44, 91-98]. Significantly, from the perspective of maximising signal, it has been observed that relaxivities are limited by water access, most clearly when the paramagnetic payload is present in multilayers[95]. Conversely, in

related work, Gd-DOTA complexes have been deposited on Gd-DTTA (DTTA, diethylenetriamine tetraacetic acid) modified silica nanoparticles *via* electrostatic interactions between the complexes[94]. As the number of layers increased, the authors reported a proportional increase in T_1 relaxivity, suggesting significant water access through the hydrophilic multilayers. Mesoporous silica presents a means of greatly increasing Gd loading in a closely related platform. Lin and Reiter *et al*. have, for example, prepared 75 nm dye-doped MSNs and subsequently post-functionalised the particles with Gd-DTTA[96]. Significantly, the observations (at 3 T, T_1 relaxivity of 28.8 $mM^{-1}s^{-1}$ for MSNs) within this work are consistent with slower tumbling and facile water access to the paramagnetic centres on the particles. Notably, among critical parameters of inner-sphere relaxation in S.B.M. theory, increased rotational correlation time (τ_R), thus far, is the only one employed in the interpretation of enhanced relaxivity in these prior works regardless of different preparative procedures, Gd^{3+} loading, particle types (e.g. porous and nonporous) and field strength. Although τ_R has reasonably explained the relaxivity enhancement, it has not been able to differentiate the relaxivity variations in different works. Importantly, because an effective relaxivity enhancement relies on the match of overall correlation time of a contrast agent and proton Larmor frequency (Eq. 2), the ability to enhance relaxivity by increasing rotational correlation time is field-dependent (i.e. an imaging agent that produces a high contrast result at a specific field does not necessarily behave the same at different fields). Small, fast tumbling molecules like Gd-DTPA (~0.06 ns ≈ 10^4 MHz)[99] show a modest decrease in T_1 relaxivity with increasing field, while slow tumbling molecules

like serum albumin bound Gd-chelates (<10 ns ≈ 100 MHz)[100] have high relaxivity between 0.5 and 1.0 T (≈ 22 – 43 MHz) and then sharply drop with increasing field (due to proton Larmor frequency shifting away from the tumbling frequency of contrast agents)[87]. This, therefore, indicates that at very high fields slow tumbling species do not necessarily result in greater relaxivity. In addition, the strategy of markedly slowing rotation (through nanoparticle conjugation, for example) results in large gains in T_1 relaxivity at 1.5 T and below but at high fields this strategy is much less effective[87]. For example, Gd-DTTA doped MSNs exhibit a four-fold relaxivity enhancement compared with Gd-DTTA molecular agent at 3 T, whereas at 9.4 T only one-fold enhancement can be observed[95, 96]. Moreover, nanoparticles with sizes ranging from 50 to 400 nm demonstrate rotational correlation time in the range of ~10^4 – 10^5 ns and this size variation is ineffective in gaining greater relaxivity at high field[99]. From these selected examples and evidence, it is clear not only that increased rotational correlation time (inner-sphere mechanism) by particle conjugation is not the only cause of enhanced relaxivity across broad field ranges in the literature but also that there remains appreciable room for further understanding and optimisation.

1.2.2 Outer-sphere Relaxivity

Since in most cases only a small fraction of the protons are bound at or near the Gd^{3+}-centres, it is reasonable to consider the contribution to the observed relaxation times from the bulk water protons (outer-sphere relaxation). Outer-sphere relaxation arising from the translational diffusion of water molecules near the Gd^{3+}-chelate is a complex

function of the shortest distance of water approaching the Gd^{3+}-chelate, diffusional correlation time (τ_D) of water and diffusion coefficients of water and Gd^{3+}-chelate (Fig. 1.7). A direct determination of outer-sphere contribution alone is difficult. A common approach employed is the subtraction of $q = 0$ complex's relaxivity (such as Gd-TTHA and Gd-TETA where no coordinate water indicates no inner-sphere contribution) from the observed values (TTHA, triethylenetetraaminehexaacetic acid; TETA, 1,4,8,11-tetraazacyclotetradecane-1,4,8,11-tetraacetic acid)[75, 101]. Notably, at higher field (>0.25 T) or using slower tumbling contrast agents, the outer-sphere contribution is comparably insignificant (compared to inner-sphere contribution)[102]. However, recently some reports have indicated that the confinement of water in a nano-environment affects its mobility and hence alters the diffusional behaviour of water passing through Gd^{3+}-centres[101-105]. In these cases, outer-sphere contribution can be enhanced. Sethi *et al.*, for example, have loaded Gd-TTHA complex into porous silicon microparticles (pore sizes of 5 - 10 nm; note that the complex is physically loaded in the pore rather than chemically anchored on the pore wall)[101]. Gd-TTHA demonstrated a four-fold relaxivity enhancement when loaded in the microparticles. Since it is a $q = 0$ complex with no inner-sphere relaxation, this enhancement was assigned to the water confinement effect resulting in slower water diffusion and greater outer-sphere relaxivity.

Overall, the perturbation/enhancement of proton relaxation by a Gd^{3+}-complex consists of both inner-sphere and outer-sphere mechanisms. In general, for a slow tumbling

contrast agent (e.g. nanoparticle based paramagnetic materials) at a field >1.5 T, the inner-sphere mechanism plays a significant role in the relaxation processes. In this relaxation scheme (inner-sphere), the resulting relaxivity of a contrast agent is governed by the shortest correlation time in S.B.M. equation (see the theory above). Importantly, rotational correlation time (τ_R) is generally acknowledged to dominate the relaxivity of a nanoparticle based agent at high field (>1.5 T). These constitute the reason in the majority of prior works that τ_R of the inner-sphere relaxation is the only parameter employed in the rationalisation of relaxivity change resulting from nanoparticle conjugation. However, for a contrast agent and water confined in a nano-environment, the restricted mobility may make the relaxation processes much more complicated. Specifically, paramagnetic species anchored in porous structures of MSNs falls into this category and the investigation of this structural effect on the resulting relaxivity has been lacking. Bridging this fundamental gap in knowledge and understanding is critical and may pave the way for MRI contrast agents based on nanomaterials of unprecedentedly high relaxivity.

1.3 Drug Delivery with MSNs

In addition to their application in diagnosis imaging techniques, much effort has been invested in utilising MSNs from a therapeutic perspective. By virtue of their high surface area and large pore volume as well as their biocompatibility[106, 107], MSNs have provided potential platforms for therapeutic agent carriage. The delivery of the hydrophobic anti-inflammatory drug, ibuprofen, was the initial motivation of using MSNs as carriers[48, 49]. The first successful example of such ibuprofen-loaded MSNs conjugation was reported at the start of this century where the interaction between native unmodified MSNs and hydrophobic ibuprofen was assigned to hydrogen bonding[48]. Since this initial report, studies have been carried out to control this particle-drug interaction with well-developed silanol modification chemistry. In this way, loading/release and delivery of nanoparticles *in vitro* or *in vivo* has become controllable[47, 54, 108-110]. In physiological conditions (~pH 7), for example, electrostatic repulsion makes native unmodified MSNs (negatively charged) unable to efficiently encapsulate negatively charged drugs. By modifying particles with moieties that are positively charged at neutral pH (e.g. quaternary ammonium groups), the amount of negatively charged drugs being loaded has been reported to be proportional to the degree of modification[47]. On the other hand, this electrostatic interaction also has influence on the release of the charged drug, with negatively charged drugs being released at a decreasing rate with increasing modification[47]. However, there exists a common feature in these examples that the release of therapeutic agents occurred almost immediately after loaded MSNs were administrated either *in vitro* or *in vivo*.[48]

This rapid release (more often called premature release) is particularly undesirable in terms of drug efficacy which indicates a therapeutic effect of a given drug dosage[111]. In a more general sense, the drug efficacy of therapeutic agents based on MSNs is the highest if they are only released at the targeting site by the trigger of specific pathological changes[48, 112, 113]. Therefore, more sophisticated ways in which various methods to close the pore openings of MSNs have, accordingly, been established to encapsulate therapeutic agents[114-134]. In doing this, the opening of pores and the subsequent release of therapeutic drugs only occur by externally triggering stimuli, leading to minimised premature release. In addition, targeting moieties have also been appended on MSNs, which further secure the performance of their therapeutic effects only at the desired sites[65, 114, 135].

This capping concept employs surface modifications with either materials (e.g. nanoparticles, biomolecules or supramolecules) that are larger than the pore sizes[114-131] or chemicals that can undergo structural changes[132-134] (e.g. dimerisation) in specific conditions (e.g. UV irradiation or pH difference) resulting in pore blocking. These structural changes are normally reversible so that the decapping is viable. For example, since dimerised coumarin or thymine are large enough to close the mesopores, prior works have demonstrated using the reversible photo-dimerisation of these two organic molecules to fabricate photo-triggered controlled release systems[132, 133]. pH-responsive delivery systems based on the packing/agglomeration of multiamine groups on the mesoporous silica have been reported, wherein systems such as

propyldiethylenetriamine are protonated in acidic conditions, leading to electrostatic repulsion of neighbouring amine chains, closing the pores, but in neutral pH conditions hydrogen bonding between amine groups results in opening of gates and subsequent release of the guest molecules[134].

In examples where capping relies on the bulky size of molecules, the pore opening mechanisms are even more diverse depending on the linkages between the capping materials and particle pores. For example, the first MSNs based stimuli responsive delivery system was introduced by Lin's group[122]. In their work, CdS quantum dots (QDs) were chemically attached to MSNs through a disulfide linker, which is chemically labile and could be cleaved with various disulfide reducing agents, a concept proved through the loading and release of vancomycin and adenosine triphosphate (ATP) guest molecules.

The triggered decapping can also be affected by utilising pH-, photo- and enzymatic responsive linkers[126, 129, 130]. In addition to these cleavable covalent bonds, there have been prior works employing non-covalent bonds where the decapping was achieved by the exploiting the difference in binding strength of capping materials towards particles and external stimuli[125] or by a change in electrostatic interaction[124]. For example, positively charged Au nanoparticles appended with photosensitive molecules have capped negatively charged and loaded MSNs *via* electrostatic attraction, with light irradiation causing a charge conversion process in the photosensitive molecules,

creating an electrostatic repulsion from MSNs causing the removal of Au nanoparticles and the subsequent guest release[124]. The use of supramolecular motion is another interesting technique to achieve capping and release from MSNs. Such examples involve the conjugation of MSNs with axial molecules threaded with movable macrocycles which govern whether particle pores are open or closed according to movement triggered by their oxidation or reduction[126-128].

More recently biomolecules, including saccharides, proteins, antibodies and DNA[114-121], have been used as gatekeepers in order to improve the biocompatibility and biovectoring of MSNs. In the majority of these cases, cleavable linker chemistries such as those noted above (pH or redox responsive, for example) were employed in the decapping mechanisms. Very few prior works have investigated capping/decapping mechanisms utilising the specific properties of the biomolecules themselves. Amongst these, avidin has been capped onto MSNs using strong binding between avidin and biotin where the triggered removal of capping proteins is carried out with their specific proteases[118]. Lactose has also been conjugated onto the loaded nanoparticles releasing guests with their being achieved by the digestion of lactose with β-D-galactosidase[121]. Utilising the concept of competitive displacement, exploitation of a difference in binding affinity has also been employed in the development of responsive MSNs delivery systems[116]. For example, MSNs modified with hapten (a small molecule that can be recognised by sulfathiazole antibodies leading to pore closing[116]) can be decapped, in the presence of sulfathiazole which promotes the competition with

hapten, resulting in the removal of capping antibodies. Notably here, this competition exists in between two small organic molecules (i.e. it is not biological). Significantly, there has been no prior investigation in the purely biological competition between two proteins from the particle gating perceptive.

1.4 Physiology of Nanomaterials with Cells

1.4.1 Endocytosis

1.4.1.1 Mechanism

The route that cells take up macromolecules and particulate substances from the cell surface to lysosomes is called endocytosis[136, 137]. In this process, the material to be ingested is progressively enclosed by a small portion of the plasma membrane, which first invaginates and then pinches off to form an endocytic vesicle containing the ingested substance or particle. Two main types of endocytosis are distinguished on the basis of the size of the endocytic vesicles formed. Phagocytosis involves the ingestion of large particles, such as microorganisms or dead cells *via* large vesicles called phagosomes (generally >250 nm in diameter); pinocytosis is a process of ingestion of fluid and solutes *via* small pinocytic vesicles (about 100 nm in diameter)[137].

In mammals, three classes of white blood cells act as professional phagocytes - macrophages, neutrophils and dendritic cells, and defend against infection by ingesting invading microorganisms[137]. Macrophages also have an important role in scavenging cells which have died from apoptosis (a programmed cell death mechanism, described in more detail below). The ingested subjects are located in phagosomes which fuse with lysosomes inside the cell followed by the degradation of materials. Phagocytosis is a triggered process, requiring receptors to be activated that transmit signals to the cell interior and initiate the response[137]. Foreign materials, on the other hand, rely on

the attachment of serum proteins (opsonisation) which are recognised by cell receptors[137-139].

Unlike phagocytosis, which is a triggered process, virtually all eukaryotic cells continually ingest their plasma membrane in the form of small pinocytic vesicles (a receptor-independent pinocytosis)[137]. The pinocytosis often begins at clathrin-coated pits (clathrin is a protein that helps cells to shape rounded vesicles). The lifetime of the pit is short (< a minute); it invaginates into the cell and pinches off to form a clathrin-coated vesicle (Fig. 1.9). The lifetime of coated vesicles is even shorter than the coated pits, within seconds being rapidly fused with early endosomes, where materials are sorted before transportation to degradative lysosomes[136, 137]. Since extracellular fluid is trapped in clathrin-coated pits as they invaginate to form coated vesicles, any substance dissolved in the extracellular fluid is internalised, a process called 'fluid-phase endocytosis'. Another clathrin-mediated mechanism involving specific adsorptive pinocytosis is receptor-dependent and has been referred to as 'receptor-mediated endocytosis'. This mode of endocytosis is of importance not only for ligands, but also for many viruses and for nanoparticles bearing these ligands on their surfaces[136, 137]. In addition to clathrin-coated pits and vesicles, there are other, less well-understood mechanisms by which cells can form pinocytic vesicles, such as the caveolae pathway[136, 137]. Caveolae are present in the plasma membrane of most cell types, and in some of these they are seen as deeply invaginated flasks forming from

lipid rafts. The major protein in caveolae is caveolin, a multipass integral membrane protein that is a member of a heterogeneous protein family.

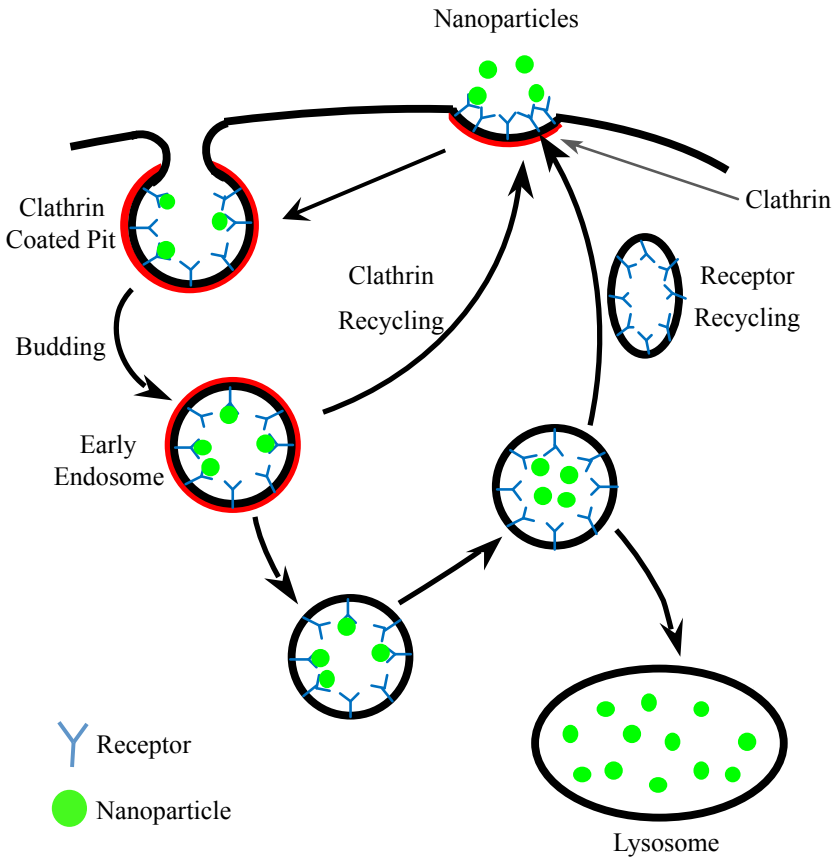


Fig. 1.9 Mechanism of clathrin-mediated endocytosis and subsequent vesicular pathways.

A common feature of phagocytosis and pinocytosis is that the ingested materials and their bound membrane receptors surrounded in phagosomes or pinocytic vesicles will fuse with acidic endosomes where they can be sorted into endocytic recycling compartments or matured into acidic lysosomes (where low pH promotes the degradation of ingested materials)[136, 137]. Most of the materials dissociate from their associated receptors (if internalised *via* phagocytosis or receptor-mediated

endocytosis) in the acidic environment of the endosome and eventually end up in lysosomes, while most of the receptors are recycled *via* endocytic recycling compartments back to the cell surface for reuse (Fig. 1.9). But receptor bound material complexes can follow other pathways from the endosomal compartment. In some cases, both the receptor and the ingested material end up being degraded in lysosomes, resulting in receptor down-regulation[136, 137]. In other cases, both are transferred to a different plasma membrane domain, and the ingested material is thereby released by exocytosis at a surface of the cell different from that where it originated, a process called transcytosis[136, 137]. Though the endocytic mechanism can be generalised as according to the processes described here, there is, by far, no conclusive report in the literature mean that there are parts of these complex biological processes which remain poorly understood. Cell-type specific variation can be one of the main reasons for significant differences in uptake, intracellular sorting, trafficking and localisation of materials. In addition, there still exist a number of variables depending on the characteristics of materials that would influence endocytosis. In dealing with nanotechnology in biomedical applications, these intrinsic variables must be considered. The major properties that can impact endocytosis include shape, size and surface chemistry of nanoparticles.

1.4.1.2 Influence of Geometry (Shape and Size) on Endocytosis

In understanding nanoparticle geometrical and surface properties' influence on cell endocytosis, a membrane-wrapping model is perhaps the easiest means of

description[65, 140] (Fig. 1.10). As noted previously, both phagocytosis and receptor-mediated pinocytosis require plasma membrane receptors to be activated by either serum proteins (opsonins) or specific ligands on the nanoparticles. This is then followed by membrane wrapping around the nanoparticles resulting in endocytic vesicles. The contact area between cell membrane and nanoparticles (geometry) and the opsonin/ligand density (surface chemistry) thus govern the communication of receptors and ligands[65, 140-143]. The cellular uptake can be considered as a result of competition between thermodynamic driving force for wrapping and the receptor diffusion kinetics[144]. The thermodynamic driving force refers to the amount of free energy required to drive the nanoparticles into the cell while the receptor diffusion kinetics refer to the kinetics of recruitment of receptors to the binding site. These two factors determine the rate and the quantity of nanoparticles taken up by cells.

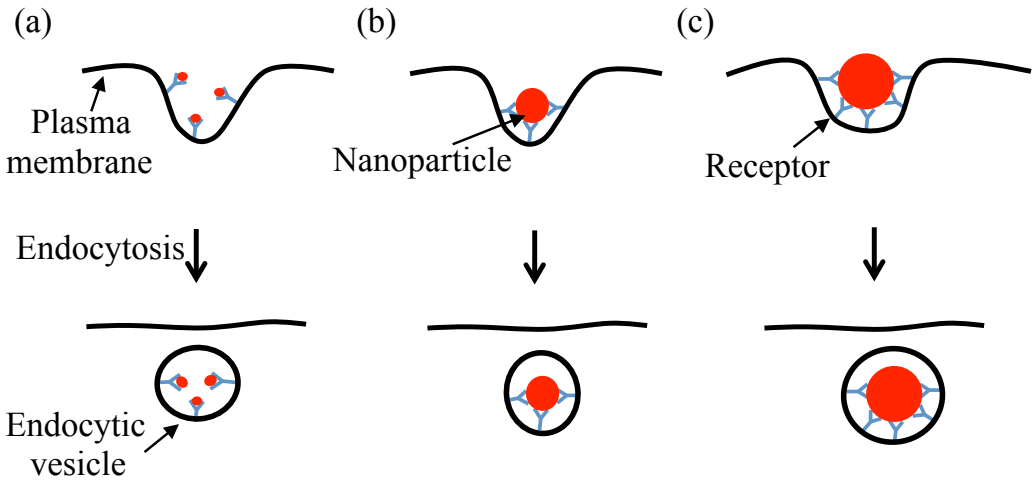


Fig. 1.10 Schematic representation of cell membrane wrapping. The particle (red sphere of varying size) endocytosis is determined by the numbers of receptors being bound (blue shapes) and the associated decrease in free energy as well as the deformation of membrane to recruit receptors. Scheme (a) – (c) indicates size-dependent cell uptake.

There has been evidence that, with a given geometric shape, nanoparticle's sizes have a strong effect on overall cell uptake[77, 164-167]. For spherical gold nanoparticles, silica nanoparticles and quantum dots, a 50 nm diameter is reported to be the optimal size which yields the fastest uptake rate and the highest intracellular concentration in mammalian cells investigated[140, 145, 146]. This size dependent uptake can be explained by a cell membrane wrapping processes (Fig. 1.10). The binding of nanoparticles to the receptors leads to a localised decrease in free energy which induces the membrane to wrap around the nanoparticle forming a closed vesicle. A single <50 nm nanoparticle may not be able to activate sufficient numbers of receptors and to induce enough free energy reduction and thus is less effectively internalised[140]. In order to provide enough free energy and to drive membrane wrapping, these small nanoparticles (<50 nm) are generally uptaken in a form of cluster that binds to multiple receptors. 14 nm nanoparticles, for example, have been reported to be uptaken as a group of at least six nanoparticles, while a single 50 nm nanoparticle is capable of recruiting and binding enough receptors to successfully produce membrane wrapping[140, 144, 147]. Though larger nanoparticles can act as a cross linker to cluster receptors and induce wrapping (uptake), for >50 nm nanoparticle the wrapping time is slower because of the requirement of receptor redistribution on the cell membrane *via* diffusion to compensate for local receptor depletion leading to ineffective cell uptake[140, 144, 147].

In addition to size, nanoparticle shape has been indicated to have direct influence on cell uptake behaviour. For >100 nm nanoparticle, rods show the highest uptake, followed by spheres, cylinders, and cubes[141]. In these works, the observation is assigned to the local curvature that affects ligand/opsonin adsorption and the degree to which particles fit the contours of cell membranes. It is the local shape of the particles (>100 nm) at the point where they attach to the cell that dictates the cell uptake rather than the overall shape. Conversely, in studies with sub 100 nm nanoparticles, spheres, however, demonstrate higher uptake than rods[143, 147]. Having said that, reports describing <100 nm rod shaped nanoparticles suggest that they may interact with more cell surface receptors inducing effective membrane wrapping if the long axis is in the right orientation[140]. These works imply, from an engineering perspective, that asymmetrical nanoparticles may provide another level of control in effecting cell uptake.

1.4.1.3 Influence of Surface Chemistries on Endocytosis

Since nanoparticle internalisation requires cell membrane wrapping and majority involves membrane receptor activation (phagocytosis and receptor-mediated pinocytosis, for example), the decoration of nanoparticles with targeting ligands has, accordingly, been reported to promote delivery to a specific cell population and/or to control the intracellular trafficking of the nanoparticles.

In addition to a nanoparticle's size, shape and targeting ligand decoration stated above, surface charge is also important in cell uptake. Since cell plasma membrane bears negative charges, positively charged nanoparticles are generally taken up at a faster rate (promoted by electrostatic attraction) compared with nanoparticles with a neutral or negative charge[106, 146, 148-150]. Particle surface charge not only influences the interaction with charged cell membrane, but also governs the serum protein attachment (opsonisation) and the subsequent cell recognition (phagocytosis). Studies have reported that the lower surface charge, the less protein association occurs and thus the slower phagocytosis[140, 147, 151].

The means to lessen endocytosis are not limited to the control of particle surface charge; particle coating with non-ionic hydrophilic polymers such as poly(ethylene) glycol (PEG) is also known to reduce protein adsorption and cell recognition[151-156]. Grafting nanoparticles with linear PEG (pegylation) is the most applied strategy to suppress non-specific protein adsorption by blocking protein-binding sites and creating a thermodynamic barrier to protein diffusion (facilitated by the interaction between hydrophobic particle surfaces and serum proteins), a factor that dominates the effectiveness of PEG stealth capability[155, 156]. Increasing PEG density generally decreases total serum protein adsorption[157]. Nanoparticle sizes also influence the protecting efficiency of grafted PEG due to the different surface curvatures that modulate PEG steric interaction with neighbouring PEG molecules and thus their conformational freedom[157]. PEG density and nanoparticle size together determine the

efficiency of protein adsorption and subsequent endocytosis. Another consideration is PEG chain length, where serum protein association decreases as PEG chain length increases, although in general the density remains the most important factor in preventing protein attachment and lessening cell uptake[155].

In summary, the routes that foreign materials can enter the cells are complex. In general, there are two relatively well-understood internalisation mechanisms for particulate materials – phagocytosis and clathrin-mediated pinocytosis distinguished by the size of foreign materials and the formed vesicles. Although cells can continuously ingest extracellular fluid by receptor-independent pinocytosis, particles typically are internalised by receptor-dependent pinocytosis and phagocytosis. As both processes rely on the activation of receptors by either biological ligands (pinocytosis) or adsorbed serum proteins (phagocytosis) on the particles, the plasma membrane wrapping model is widely employed in rationalising the internalisation driving force resulting from membrane deformation and receptor binding. In this model, the particle geometries (size and shape) and surface chemistries (ligand density, surface charge and modification) greatly determine the effectiveness of membrane wrapping and the subsequent particle uptake. For particle sizes ranging between 50 – 100 nm, spherical and positively charged nanoparticles can be uptaken at a faster rate. Conversely, particle internalisation can be suppressed by modifying the particle surfaces with non-ionic hydrophilic polymers such as PEG. Endocytosis involves fusion and maturation of a series of endocytic compartments, from early endosomes, late endosomes and

lysosomes. This process generally associates with the degradation of the ingested substances by the acidic endocytic environments.

1.4.2 Biodistribution, Clearance and Biocompatibility

1.4.2.1 General Behaviour

In the design of theranostic nanoparticles, knowledge of their pharmacokinetics and tissue distribution allows one to establish general synthetic guidelines for *in vivo* application. The distribution and the subsequent excretion of nanoparticles in animal bodies are closely related to their behaviours at the cellular level[139, 158-160]. In fact, the fate of nanoparticles in whole bodies is largely governed by the interaction with the cells resident in their administrated routes. This is particularly important in the understanding of nanoparticle theranostic efficiency as well as their excretion, where the efficiency can be considered as a consequence of the latter. For example, in the mononuclear phagocyte system (MPS) of the liver, kidney, spleen, or lymph nodes, nanoparticles can be rapidly taken up by phagocytes followed by the subsequent excretion process[161]. This greatly limits nanoparticles' traveling to the targeting sites/cells leading to a reduction in theranostic efficiency. Blood half-life is generally used in defining the duration of nanoparticles in blood circulation before their removal and excretion. Variations in half-lives appear to be a result of different nanoparticle surface chemistries[138, 161]. For example, blood half-life is the highest for neutral nanoparticles, whereas positively charged nanoparticles are cleared most quickly from

the blood (an observation consistent with that noted above wherein positive nanoparticles are taken up by cells at a faster rate)[162, 184].

As most nanomaterials, when administered into blood, are taken up within minutes or hours by the phagocytic cells of the MPS[161] and are eventually excreted, long blood circulation is desirable in order to maximise theranostic efficiency. In addition to particle surface charges, all the variables discussed at the cellular level that lessen cell endocytosis theoretically can be used in designing long circulating nanoparticles. A sub 100 nm rod nanoparticle, for example, is taken up by a cell at a rate slower than a sphere shaped nanoparticle with a comparable volume[143, 147]; similarly at a whole body level, the former have ten times longer circulation lifetime than that of the latter. Importantly, surface coating nanoparticles with PEG is perhaps the most popular technique to suppress rapid clearance and expand blood half-life[151-156]. Surfaces covered with PEG have been shown to be biocompatible and protein adsorption/biological degradation resistant. It has also been shown that, depending on the chain length and the coverage of PEG on the particle surface, the nanoparticle's blood half-life can be tuned across a broad range[150]. Indeed, though long circulation time is beneficial to theranostic efficiency, persistent circulation of nanoparticles in bodies may also cause potential toxicity concerns[162]. Any nanomaterials, after having performed their activity at the desired sites, need to be effectively excreted. The excretion of nanoparticles relies not only on their surface chemistries (that control the rate) but also on the selectivity of excretory organs (that determine the clearance

routes) such as the kidney, spleen and liver towards their physical sizes[158-160]. There thus exists a balance between surface chemistries (such as PEG length/density or charge) and particle sizes which must be reached in order to optimise theranostic efficiency without the cost of effective clearance. Generally, nanoparticles with diameters <6 nm can be cleared by kidney filtration and renal excretion; whereas particles >200 nm accumulate in the spleen and liver, where they are excreted *via* the hepatobiliary transport mechanism[158-160].

1.4.2.2 Biocompatibility of Silica

All the theranostic applications (including MRI and controlled drug delivery noted previously) of MSNs are viable because silica has been suggested to be a non-toxic, biocompatible and biodegradable material for a long time. The lack of toxicity of silica has been demonstrated at both the cellular[46, 106, 107, 122] and tissue level. For example, MSNs at concentrations below 100 μg/mL per 10^5 cells has been shown to have no effect on the viability and proliferation of various mammalian cells[46]. Cell membrane integrity is conserved after uptake of MSNs as determined by selective DNA staining followed by flow cytometry[106]. Microscopic analysis shows normal cell morphology upon uptake of MSNs. Mitochondrial activity remains at normal levels as determined by colorimetric assay with 3-[4,5-dimethylthiazol-2-yl]-2,5- diphenyltetrazolium bromide (MTT)[107]. Growth rates for cells exposed to MSNs are similar to those of cells grown in the absence of MSNs[106, 122].

The low toxicity of silica at the tissue level is reflective of its biodegradability. Silica has been reported to break into smaller particles that can be cleared by the kidneys in relatively short period and without causing any toxicity effect in a mouse model[163]. In addition, prior works have indicated that silica in physiological aqueous solutions can be hydrolytically degraded into orthosilicic acid ($Si(OH)_4$), which not only is a non-toxic species but also naturally exists in numerous tissues[164, 165]. Although high concentrations of orthosilicic acid may induce a cytotoxicity effect, it can be effectively removed from the body through diffusion in the blood stream or lymph system followed by urinal excretion at a rate of 1.8 mg silicon per day[165]. Notably, the degradation of silica is a structurally dependent process where the presence of porosity facilitates the silica matrix degradation[21, 162, 166-168]. The gradual dissolution of the porous silica increases the pore size and decreases the porosity and surface area. Significantly, prior work has demonstrated that highly porous silica made from sol-gel chemistry is more degradable than crystalline silica[18, 165]. This makes porous amorphous silica nanomaterials such as MSNs highly attractive for biomedical applications.

In summary, the nanoparticle's behaviour at a whole body level is closely related to those at cellular level. Significantly, the clearance of nanoparticles from bodies is important not only in determining the effectiveness of theranostic nanoparticles but also in safely excreting them after performing their activities. Pegylation is commonly employed to increase the blood circulation time of nanoparticles and to enhance the

likelihood of their delivery to the desired sites, whereas particle sizes govern the efficiency and the routes of excretion. In general, silica nanoparticles' highly modifiable surfaces and tailorable sizes as well as their biodegradability allow them to be easily pegylated, degraded and finally excreted. These features in combination with their lack of toxicity have made mesoporous silica nanoparticles an ideal candidate for biological application.

1.4.3 Apoptosis and Protein Therapeutics

The ultimate goals of theranostics are reliable detection and effective treatment. Reliable detection depends on precisely marking the pathological tissues/cells using MRI, for example; whereas triggered abnormal cell death by introducing therapeutic agents is significantly important in effective treatment at a cellular level. There have been at least eight different cell death pathways proposed in the literature[169-173]. Since cell biological processes are extremely complicated, the boundary among some of these pathways can be rather indefinitive. Necrosis and apoptosis are perhaps the most frequently seen cell death mechanisms in biological papers. The former is considered to be a toxic process where the cell is a passive victim and follows an energy-independent mode of death[169]. Apoptosis on the other hand is a programmed cell death mechanism that is considered to be an important component of various processes including normal cell turnover, proper development, functioning of the immune system, and chemically-induced cell death[169, 170]. From a morphological perspective, it involves cell shrinkage (cells are smaller in size, cytoplasm is dense and organelles are

more tightly packed), chromatin condensation and violent bubbling and blebbing from the plasma membrane followed by separation of the cell into a cluster of membrane-bounded bodies. Changes in several cell surface molecules also ensure that, in tissues, apoptotic cells are immediately recognised and phagocytosed by their neighbours to be degraded[169, 170]. From a biochemical point of view, apoptosis results from a collapse of the cellular infrastructure through internal proteolytic digestion[169, 170]. Apoptosis initiation, execution and regulatory pathways are governed by a member of the caspase family of proteases. Based on their structure and sequence in cell death pathways, caspases can be divided into upstream initiators (caspase-8, -9, and -10) and downstream effectors (caspase-3, -6, and -7)[169, 170].

Caspase activation is initiated by two major signaling routes: the extrinsic death receptor pathway and the intrinsic mitochondrial pathway[169, 170] (Fig. 1.11). Death receptor-mediated apoptosis plays a fundamental role in the maintenance of tissue homeostasis, especially in the immune system, whereas the mitochondrial pathway is used extensively in response to extracellular cues and internal insults such as DNA damage. All death receptors are characterised by a death domain responsible for transmitting the apoptotic signal. Upon ligand binding, the death receptors (e.g. Fas receptor, an apoptosis antigen) interact *via* their death domain with a corresponding protein motif in adapter proteins such as FADD (Fas-Associated protein with Death Domain). These adapters use their death effector domain to facilitate their binding to the precursor of the initiator caspase-8/10 (procaspase-8) resulting in the death-

inducing signaling complex (DISC) which activates caspase-8/10 through a dimerisation mechanism. At this point a high local concentration of dimerised caspase-8 leads to its autocatalytic activation and the subsequent activation of downstream effector caspases (caspase-3). Alternatively, this extrinsic pathway proceeds to an intrinsic one through the cleavage of proapoptotic Bid proteins by activated caspase-8/10.

Most cell death, however, proceeds *via* the mitochondrial pathway (Fig. 1.11), which integrates signals generated by a variety of stressors including DNA damage, loss of adhesion, growth factor withdrawal and others which provokes the activation of one or more proapoptotic BH3-only proteins[170, 174]. BH3-only proteins act as sensors for various death stimuli and can relieve the inhibitory action of antiapoptotic Bcl-2 proteins. The activation of BH3-proteins results in the oligomerisation of proapoptotic proteins, Bax and Bak, causing the release of cytochrome *c* from the mitochondrial intermembrane space into the cytosol. Upon binding of cytochrome *c*, the adaptor protein Apaf-1 oligomerises and binds to the precursor of caspase-9 (procaspase-9) to create a protein complex known as an apoptosome. The apoptosome then cleaves the procaspase-9 to its active form of caspase-9, which in turn activates the effector caspase-3 followed by a caspase cascade and final apoptotic cell death.

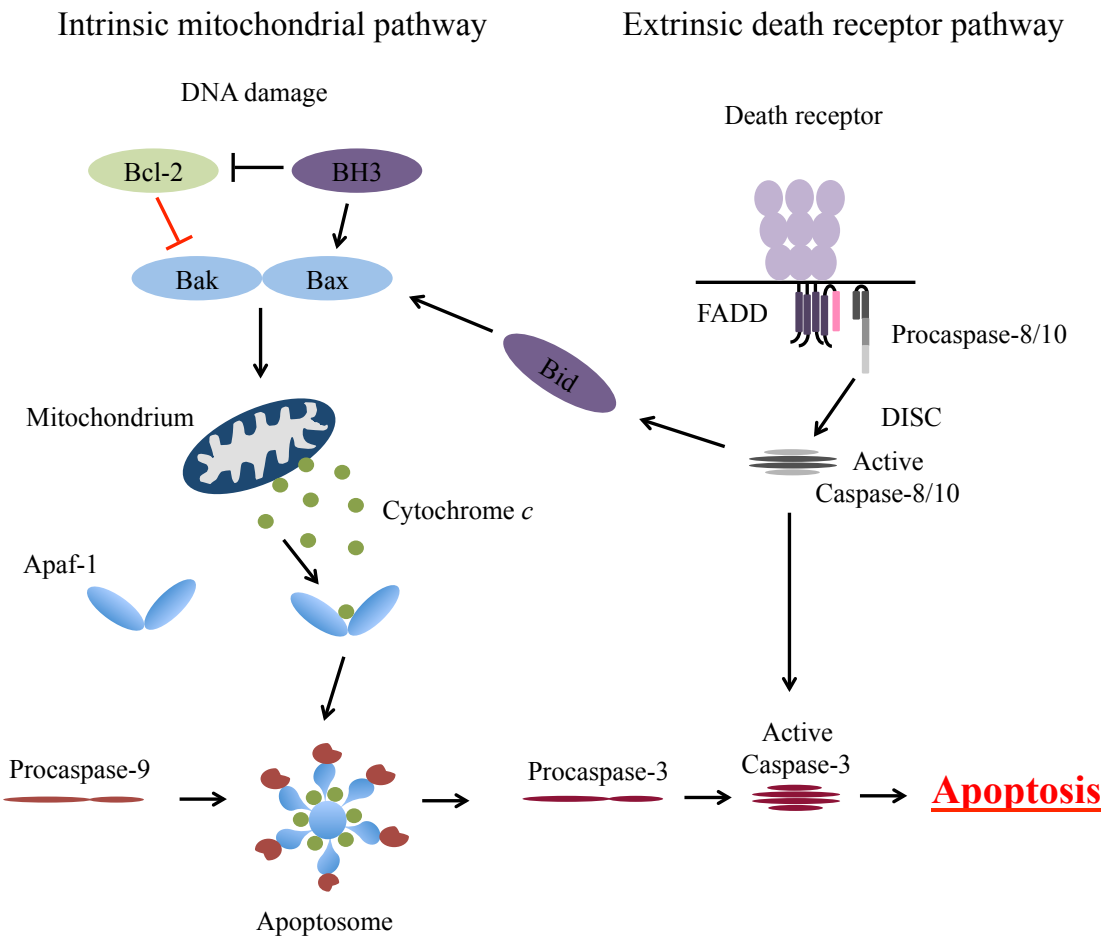


Fig. 1.11 The extrinsic death involves extracellular ligand binding to death receptors triggering the receptor-mediated pathway that can directly result in the activation of caspases without involvement of the mitochondria; the intrinsic mitochondrial pathway is triggered in response to various forms of cellular stress, such as DNA damage, which provokes the activation of one or more proapoptotic BH3-only proteins. The activation of BH3-proteins results in the oligomerisation of Bax and Bak causing the release of cytochrome *c* from mitochondrial. Subsequently, cytosolic cytochrome *c* binds to the adaptor protein Apaf-1 and initiates a series caspase cascade and the final apoptotic cell death.

Indeed, apoptosis is a common programmed cell death mechanism in many (or perhaps all) mammalian cells[169, 170, 174]. There have been, accordingly, increasing studies in triggering apoptotic death in tumour cells for cancer treatment. As endogenous release of cytosolic cytochrome *c* is the centre of apoptotic mechanism[192, 193, 197], some studies

have intended to induce apoptotic cell death by exogenous delivery of this small, membrane-impermeable protein into live cells[175-182]. However this impermeability and ready clearance from the circulation have limited the direct introduction by intravenous injection[183]. To allow its eventual interaction with corresponding targeted moieties in the cytoplasm of cells, exogenous cytochrome *c* must be directly injected into the cell cytosol or shielded from external deactivating influences such as MPS and subsequently be delivered to its site of action. The first successful attempt to induce Hela apoptosis by exogenously introducing cytochrome *c* employed microinjection into the cytosol[181]. Some other administration mechanisms based on delivery vehicles have also been investigated including membrane penetration peptides[175, 177], liposome[177], polyionic micelle nanoparticles[178] and carbon nanotubes[176]. Although in some cases apoptosis has been noted, this has generally been an ineffective means to induce apoptosis (overall cell death across literature is less than 30%). Attempts have also been made to use silica nanoparticles as delivery systems for this protein, though, thus far, this has been entirely without indication of cell death[179, 180]. In fact, in these works the only report of induced apoptosis is by released free cytochrome *c* rather than the bioconjugationed particle itself. This has resulted in, especially in the cases of delivery by nanoparticles, a lessened particle stabilisation effect (where particles no longer can prevent the released cytochrome *c* from proteolytic degradation), which decreases the apoptosis inducing ability[66, 84].

1.5 Project Aims

This project aims to explore the use of functionalised MSNs as effective theranostic agents for non-invasive MRI imaging and potent cell killing. Specifically, attempts will be made to optimise MSNs based MRI contrast agents and to induce programmed cell death in Hela cancerous cells.

The specific goals within this work were as follows:

1. To optimise the preparation of a mesoporous silica scaffold using a modified Stöber technique under basic catalytic conditions employing surfactant templates and the full structural characterisation of nanoparticles will be carried out using DLS, TEM, ζ-potential, TGA, BET and FTIR.
2. To control and characterise the location of functionalities within mesoporous silica nanoparticles. This will be achieved by varying conditions within the preparation procedure, including precursor concentration and reaction duration in order to yield particles with exclusively internally localised functionalities or with those on the both interior and exterior of particles. A post-grafting approach will also be employed to prepare MSNs with preferentially external modification. These location variations will then be confirmed by ζ-potential and MRI.
3. To investigate the effect of Gd^{3+} loading and location within nanoparticles on ^{1}H MRI relaxivity through the investigation of water accessibility, water mobility and the rigidity of the employed Gd^{3+}-complex. The preparation of

MSNs with high contrast and low Gd^{3+} loading will be carried out.

4. To design a vectorable and contrast switchable MSNs based contrast agent through covalent tethering of paramagnetic nanoparticles with targeting proteins. Subsequent tuning of their resulting relaxivities with retention of their vectoring capability will be investigated. The derivatives of those bioconjugated nanoparticles with non-covalently attached proteins will also be investigated to generate contrast switchable nanoparticles through competitive displacement of these proteins with their partner proteins.
5. To engineer particle interactions with live cells and to specifically manipulate the subcellular localisation of particles. The effect of pegylation and surface charge will be examined in controlling particle interaction with cells and the endocytosis. Particles coated with proton absorbing molecules will also be fabricated to study their endo/lysosomal escaping capabilities. A universal escaping formulation will additionally be proposed. Subsequently, the toxicity of these nanoparticles will be assessed.
6. To examine the delivery of small molecular model drugs using MSNs. Charged guest molecules will be loaded into nanoparticles and capped with bulky protein molecules. Their loading/release behaviours from these conjugates after triggered decapping of the proteins as well as the associated release kinetics will be discussed.
7. To facilitate the transportation of membrane impermeable therapeutic proteins into cells using a nanoparticle delivery vehicle and the subsequent induction of

apoptosis. Apoptosis inducing cytochrome *c* will be conjugated onto nanoparticle through either uncleavable or cleavable linkers. The internalisation of these protein modified nanoparticles into cells will be studied and compared to free proteins. The importance of nanoparticle retention of cytochrome *c*, as opposed to its release, will be assessed from a triggered cell killing perspective.

1.6 References

1. H. S. Sherry, *Clays and Clay Minerals*, 1979, **27**, 231-237.
2. E. M. Flanigen, L. B. Sand and American Chemical Society. Division of Colloid and Surface Chemistry., *Molecular Sieve Zeolites*, American Chemical Society, Washington, 1971.
3. P. B. Venuto, *Advances in Chemistry Series*, 1971, 260-283.
4. G. Q. Guan, K. Kusakabe and S. Morooka, *Microporous and Mesoporous Materials*, 2001, **50**, 109-120.
5. C. Platas-Iglesias, L. Vander Elst, W. Z. Zhou, R. N. Muller, C. F. G. C. Geraldes, T. Maschmeyer and J. A. Peters, *Chemistry – A European Journal*, 2002, **8**, 5121-5131.
6. M. Vallet-Regi, F. Balas, M. Colilla and M. Manzano, *Solid State Sciences*, 2007, **9**, 768-776.
7. N. Zarkovic, K. Zarkovic, M. Kralj, S. Borovic, S. Sabolovic, M. P. Blazi, A. Cipak and K. Pavelic, *Anticancer Research*, 2003, **23**, 1589-1595.
8. X. W. Xu, J. Wang and Y. C. Long, *Sensors*, 2006, **6**, 1751-1764.
9. G. A. Ozin, A. Kuperman and A. Stein, *Angewandte Chemie-International Edition in English*, 1989, **28**, 359-376.
10. M. Yu, S. G. Li, J. L. Falconer and R. D. Noble, *Microporous and Mesoporous Materials*, 2008, **110**, 579-582.
11. C. T. Kresge, M. E. Leonowicz, W. J. Roth, J. C. Vartuli and J. S. Beck, *Nature*, 1992, **359**, 710-712.
12. J. S. Beck, J. C. Vartuli, W. J. Roth, M. E. Leonowicz, C. T. Kresge, K. D. Schmitt, C. T. W. Chu, D. H. Olson, E. W. Sheppard, S. B. Mccullen, J. B. Higgins and J. L. Schlenker, *Journal of the American Chemical Society*, 1992, **114**, 10834-10843.
13. K. Moller, J. Kobler and T. Bein, *Advanced Functional Materials*, 2007, **17**, 605-612.
14. F. Hoffmann, M. Cornelius, J. Morell and M. Froba, *Angewandte Chemie-International Edition*, 2006, **45**, 3216-3251.
15. J. C. Vartuli, K. D. Schmitt, C. T. Kresge, W. J. Roth, M. E. Leonowicz, S. B. Mccullen, S. D. Hellring, J. S. Beck, J. L. Schlenker, D. H. Olson and E. W. Sheppard, *Chemistry of Materials*, 1994, **6**, 2317-2326.
16. D. Y. Zhao, J. L. Feng, Q. S. Huo, N. Melosh, G. H. Fredrickson, B. F. Chmelka and G. D. Stucky, *Science*, 1998, **279**, 548-552.
17. M. K. Naskar and M. Eswaramoorthy, *Journal of Chemical Sciences*, 2008, **120**, 181-186.
18. R. K. Iler and Knovel (Firm), *The Chemistry of Silica Solubility, Polymerization, Colloid and Surface properties, and Biochemistry,* Wiley, New York, 1979.
19. W. Stöber, A. Fink and E. Bohn, *Journal of Colloid and Interface Science*, 1968, **26**, 62-69.

20. K. Yano and Y. Fukushima, *Journal of Materials Chemistry*, 2003, **13**, 2577-2581.
21. H. Yamada, C. Urata, Y. Aoyama, S. Osada, Y. Yamauchi and K. Kuroda, *Chemistry of Materials*, 2012, **24**, 1462-1471.
22. C. J. Barbe, D. J. Cassidy, G. Triani, B. A. Latella, D. R. G. Mitchell, K. S. Finnie, K. Short, J. R. Bartlett, J. L. Woolfrey and G. A. Collins, *Thin Solid Films*, 2005, **488**, 153-159.
23. M. H. Yu, L. Zhou, J. Zhang, P. Yuan, P. Thorn, W. Y. Gu and C. Z. Yu, *Journal of Colloid and Interface Science*, 2012, **376**, 67-75.
24. J. N. Israelachvili, D. J. Mitchell and B. W. Ninham, *Journal of the Chemical Society-Faraday Transactions II*, 1976, **72**, 1525-1568.
25. J. N. Israelachvili and Hazel M. Hussong Fund., *Intermolecular and surface forces*, Academic Press, London ; San Diego, 1991.
26. S. T. Hyde, *Pure and Applied Chemistry*, 1992, **64**, 1617-1622.
27. U. Henriksson, E. S. Blackmore, G. J. T. Tiddy and O. Soderman, *Journal of Physical Chemistry*, 1992, **96**, 3894-3902.
28. K. Holmberg, *Surfactants and Polymers in Aqueous Solution*, Wiley, Chichester, 2003.
29. M. J. Lawrence, *Chemical Society Reviews*, 1994, **23**, 417-424.
30. J. C. Vartuli, C. T. Kresge, M. E. Leonowicz, A. S. Chu, S. B. Mccullen, I. D. Johnsen and E. W. Sheppard, *Chemistry of Materials*, 1994, **6**, 2070-2077.
31. K. Cassiers, T. Linssen, M. Mathieu, M. Benjelloun, K. Schrijnemakers, P. Van Der Voort, P. Cool and E. F. Vansant, *Chemistry of Materials*, 2002, **14**, 2317-2324.
32. S. K. Jana, R. Nishida, K. Shindo, T. Kugita and S. Namba, *Microporous and Mesoporous Materials*, 2004, **68**, 133-142.
33. A. Sayari, M. Kruk, M. Jaroniec and I. L. Moudrakovski, *Advanced Materials*, 1998, **10**, 1376-1379.
34. M. Eltohamy, U. S. Shin and H. W. Kim, *Materials Letters*, 2011, **65**, 3570-3573.
35. S. K. Jana, A. Mochizuki and S. Namba, *Catalysis Surveys from Asia*, 2004, **8**, 1-13.
36. P. A. Winsor, *Chemical Reviews*, 1968, **68**, 1-&.
37. H. E. Bergna and W. O. Roberts, *Colloidal Silica : Fundamentals and Applications*, CRC ;, Boca Raton, Fla. ; London, 2006.
38. J. Goldstein, *Scanning Electron Microscopy and X-ray Microanalysis : A Text for Biologists, Materials Scientists, and Geologists*, Plenum, New York ; London, 1992.
39. L. Reimer, H. Kohl and SpringerLink (Online service), in *Springer Series in Optical Sciences 36*, Springer, New York, NY, 5th edn., 2008, pp. xvi, 587 p.
40. B. J. Berne and R. Pecora, *Dynamic Light Scattering : with Applications to Chemistry, Biology, and Physics*, Wiley, New York, 1976.
41. J. Kecht, A. Schlossbauer and T. Bein, *Chemistry of Materials*, 2008, **20**, 7207-7214.

42. V. Cauda, A. Schlossbauer, J. Kecht, A. Zurner and T. Bein, *Journal of the American Chemical Society*, 2009, **131**, 11361-11370.
43. F. de Juan and E. Ruiz-Hitzky, *Advanced Materials*, 2000, **12**, 430-432.
44. F. Carniato, L. Tei, A. Arrais, L. Marchese and M. Botta, *Chemistry – A European Journal*, 2013, **19**, 1421-1428.
45. I. I. Slowing, B. G. Trewyn, S. Giri and V. S. Y. Lin, *Advanced Functional Materials*, 2007, **17**, 1225-1236.
46. I. I. Slowing, J. L. Vivero-Escoto, C. W. Wu and V. S. Y. Lin, *Advanced Drug Delivery Reviews*, 2008, **60**, 1278-1288.
47. C. H. Lee, L. W. Lo, C. Y. Mou and C. S. Yang, *Advanced Functional Materials*, 2008, **18**, 3283-3292.
48. M. Vallet-Regi, A. Ramila, R. P. del Real and J. Perez-Pariente, *Chemistry of Materials*, 2001, **13**, 308-311.
49. J. Andersson, J. Rosenholm, S. Areva and M. Linden, *Chemistry of Materials*, 2004, **16**, 4160-4167.
50. S. Huh, J. W. Wiench, J. C. Yoo, M. Pruski and V. S. Y. Lin, *Chemistry of Materials*, 2003, **15**, 4247-4256.
51. K. Moller, J. Kobler and T. Bein, *Journal of Materials Chemistry*, 2007, **17**, 624-631.
52. J. J. Davis, W. Y. Huang and G. L. Davies, *Journal of Materials Chemistry*, 2012, **22**, 22848-22850.
53. J. Xie, S. Lee and X. Y. Chen, *Advanced Drug Delivery Reviews*, 2010, **62**, 1064-1079.
54. M. Vallet-Regi, *ISRN Materials Science*, 2012, **2012**, 20.
55. G. T. Hermanson, *Bioconjugate Techniques*, Academic Press, San Diego ; London, 1996.
56. M. Aslam and A. Dent, *Bioconjugation : Protein Coupling Techniques for the Biomedical Sciences*, Macmillan, London, 1998.
57. A. Radzicka and R. Wolfenden, *Journal of the American Chemical Society*, 1996, **118**, 6105-6109.
58. P. Mccaldon and P. Argos, *Proteins-Structure Function and Genetics*, 1988, **4**, 99-122.
59. L. R. Hilliard, X. J. Zhao and W. H. Tan, *Analytica Chimica Acta*, 2002, **470**, 51-56.
60. D. P. Ferris, J. Lu, C. Gothard, R. Yanes, C. R. Thomas, J. C. Olsen, J. F. Stoddart, F. Tamanoi and J. I. Zink, *Small*, 2011, **7**, 1816-1826.
61. N. M. Green, *Methods in Enzymology*, 1990, **184**, 51-67.
62. J. H. Myung, K. A. Gajjar, J. Saric, D. T. Eddington and S. Hong, *Angewandte Chemie-International Edition*, 2011, **50**, 11769-11772.
63. P. I. Kitov and D. R. Bundle, *Journal of the American Chemical Society*, 2003, **125**, 16271-16284.
64. S. Hong, P. R. Leroueil, I. J. Majoros, B. G. Orr, J. R. Baker and M. M. B. Holl, *Chemistry & Biology*, 2007, **14**, 107-115.

65. W. Jiang, B. Y. S. Kim, J. T. Rutka and W. C. W. Chan, *Nature Nanotechnology*, 2008, **3**, 145-150.
66. E. V. Piletska and S. A. Piletsky, *Langmuir*, 2010, **26**, 3783-3785.
67. C. A. Ku and B. B. Lentrichia, *Journal of Colloid and Interface Science*, 1989, **132**, 578-584.
68. S. C. Huang, M. D. Stump, R. Weiss and K. D. Caldwell, *Analytical Biochemistry*, 1996, **237**, 115-122.
69. H. Harma, T. Soukka and T. Lovgren, *Clinical Chemistry*, 2001, **47**, 561-568.
70. P. J. Carter, *Experimental Cell Research*, 2011, **317**, 1261-1269.
71. E. Prieur, D. Betbeder, F. Niedergang, M. Major, A. Alcover, J. L. Davignon and C. Davrinche, *Vaccine*, 1996, **14**, 511-520.
72. W. Y. Huang and J. J. Davis, *Dalton Transactions*, 2011, **40**, 6087-6103.
73. T. F. Massoud and S. S. Gambhir, *Genes & Development*, 2003, **17**, 545-580.
74. R. A. Dwek, *Nuclear Magnetic Resonance (N.M.R.) in Biochemistry : Applications to Enzyme Systems*, Clarendon Press, Oxford, 1973.
75. P. Caravan, J. J. Ellison, T. J. McMurry and R. B. Lauffer, *Chemical Reviews*, 1999, **99**, 2293-2352.
76. K. N. Raymond and V. r. C. Pierre, *Bioconjugate Chemistry*, 2004, **16**, 3-8.
77. E. J. Werner, A. Datta, C. J. Jocher and K. N. Raymond, *Angewandte Chemie-International Edition*, 2008, **47**, 8568-8580.
78. C. Q. Tu, E. A. Osborne and A. Y. Louie, *Annals of Biomedical Engineering*, 2011, **39**, 1335-1348.
79. W. Xu, K. Kattel, J. Y. Park, Y. Chang, T. J. Kim and G. H. Lee, *Physical Chemistry Chemical Physics*, 2012, **14**, 12687-12700.
80. A. M. Hofer, *Journal of Cell Science*, 2005, **118**, 855-862.
81. M. A. Sieber, P. Lengsfeld, T. Frenzel, S. Golfier, H. Schmitt-Willich, F. Siegmund, J. Walter, H. J. Weinmann and H. Pietsch, *European Radiology*, 2008, **18**, 2164-2173.
82. A. N. Oksendal and P. A. Hals, *Journal of Magnetic Resonance Imaging*, 1993, **3**, 157-165.
83. J. J. Yang, J. H. Yang, L. X. Wei, O. Zurkiya, W. Yang, S. Y. Li, J. Zou, Y. B. Zhou, A. L. W. Maniccia, H. Mao, F. Q. Zhao, R. Malchow, S. M. Zhao, J. Johnson, X. P. Hu, E. Krogstad and Z. R. Liu, *Journal of the American Chemical Society*, 2008, **130**, 9260-9267.
84. I. Solomon, *Physical Review*, 1955, **99**, 559-565.
85. N. Bloembergen, E. M. Purcell and R. V. Pound, *Physical Review*, 1948, **73**, 679-712.
86. P. Caravan, *Chemical Society Reviews*, 2006, **35**, 512-523.
87. P. Caravan, C. T. Farrar, L. Frullano and R. Uppal, *Contrast Media & Molecular Imaging*, 2009, **4**, 89-100.
88. C. Casali, M. Janier, E. Canet, J. F. Obadia, S. Benderbous, C. Corot and D. Revel, *Academic Radiology*, 1998, **5**, S214-S218.
89. M. Rohrer, H. Bauer, J. Mintorovitch, M. Requardt and H. J. Weinmann, *Investigative Radiology*, 2005, **40**, 715-724.

90. M. Port, C. Corot, O. Rousseaux, I. Raynal, L. Devoldere, J. M. Idee, A. Dencausse, S. Le Greneur, C. Simonot and D. Meyer, *Magnetic Resonance Materials in Physics Biology and Medicine*, 2001, **12**, 121-127.
91. F. Carniato, L. Tei, M. Cossi, L. Marchese and M. Botta, *Chemistry – A European Journal*, 2010, **16**, 10727-10734.
92. F. Carniato, L. Tei, W. Dastru, L. Marchese and M. Botta, *Chemical Communications*, 2009, 1246-1248.
93. J. K. Hsiao, C. P. Tsai, T. H. Chung, Y. Hung, M. Yao, H. M. Liu, C. Y. Mou, C. S. Yang, Y. C. Chen and D. M. Huang, *Small*, 2008, **4**, 1445-1452.
94. J. S. Kim, W. J. Rieter, K. M. L. Taylor, H. An, W. L. Lin and W. B. Lin, *Journal of the American Chemical Society*, 2007, **129**, 8962-8963.
95. W. J. Rieter, J. S. Kim, K. M. L. Taylor, H. Y. An, W. L. Lin, T. Tarrant and W. B. Lin, *Angewandte Chemie-International Edition*, 2007, **46**, 3680-3682.
96. K. M. L. Taylor, J. S. Kim, W. J. Rieter, H. An, W. L. Lin and W. B. Lin, *Journal of the American Chemical Society*, 2008, **130**, 2154-2155.
97. K. M. L. Taylor-Pashow, J. D. Rocca and W. Lin, *Nanomaterials*, 2011, **2**, 1-14.
98. C. P. Tsai, Y. Hung, Y. H. Chou, D. M. Huang, J. K. Hsiao, C. Chang, Y. C. Chen and C. Y. Mou, *Small*, 2008, **4**, 186-191.
99. C. Tilcock, Q. F. Ahkong, S. H. Koenig, R. D. Brown, M. Davis and G. Kabalka, *Magnetic Resonance in Medicine*, 1992, **27**, 44-51.
100. P. Caravan, N. J. Cloutier, M. T. Greenfield, S. A. McDermid, S. U. Dunham, J. W. M. Bulte, J. C. Amedio, R. J. Looby, R. M. Supkowski, W. D. Horrocks, T. J. McMurry and R. B. Lauffer, *Journal of the American Chemical Society*, 2002, **124**, 3152-3162.
101. R. Sethi, J. S. Ananta, C. Karmonik, M. Zhong, S. H. Fung, X. W. Liu, K. Li, M. Ferrari, L. J. Wilson and P. Decuzzi, *Contrast Media & Molecular Imaging*, 2012, **7**, 501-508.
102. J. S. Ananta, B. Godin, R. Sethi, L. Moriggi, X. W. Liu, R. E. Serda, R. Krishnamurthy, R. Muthupillai, R. D. Bolskar, L. Helm, M. Ferrari, L. J. Wilson and P. Decuzzi, *Nature Nanotechnology*, 2010, **5**, 815-821.
103. S. Aime, L. Frullano and S. G. Crich, *Angewandte Chemie-International Edition*, 2002, **41**, 1017-1019.
104. K. Shirono and H. Daiguji, *Journal of Physical Chemistry C*, 2007, **111**, 7938-7946.
105. S. Takahara, N. Sumiyama, S. Kittaka, T. Yamaguchi and M. C. Bellissent-Funel, *Journal of Physical Chemistry B*, 2005, **109**, 11231-11239.
106. I. Slowing, B. G. Trewyn and V. S. Lin, *Journal of the American Chemical Society*, 2006, **128**, 14792-14793.
107. T. H. Chung, S. H. Wu, M. Yao, C. W. Lu, Y. S. Lin, Y. Hung, C. Y. Mou, Y. C. Chen and D. M. Huang, *Biomaterials*, 2007, **28**, 2959-2966.
108. B. Munoz, A. Ramila, J. Perez-Pariente, I. Diaz and M. Vallet-Regi, *Chemistry of Materials*, 2003, **15**, 500-503.
109. S. W. Song, K. Hidajat and S. Kawi, *Langmuir*, 2005, **21**, 9568-9575.

110. P. DeMuth, M. Hurley, C. W. Wu, S. Galanie, M. R. Zachariah and P. DeShong, *Microporous and Mesoporous Materials*, 2011, **141**, 128-134.
111. J. N. Soulakova and A. R. Sampson, *Statistics in Biopharmaceutical Research*, 2009, **1**, 39-47.
112. F. Alexis, E. M. Pridgen, R. Langer and O. C. Farokhzad, *Handbook of Experimental Pharmacology*, 2010, 55-86.
113. Q. Zhang, F. Liu, K. T. Nguyen, X. Ma, X. J. Wang, B. G. Xing and Y. L. Zhao, *Advanced Functional Materials*, 2012, **22**, 5144-5156.
114. Z. Luo, K. Y. Cai, Y. Hu, L. Zhao, P. Liu, L. Duan and W. H. Yang, *Angewandte Chemie-International Edition*, 2011, **50**, 640-643.
115. V. C. Ozalp and T. Schafer, *Chemistry – A European Journal*, 2011, **17**, 9893-9896.
116. E. Climent, A. Bernardos, R. Martinez-Manez, A. Maquieira, M. D. Marcos, N. Pastor-Navarro, R. Puchades, F. Sancenon, J. Soto and P. Amoros, *Journal of the American Chemical Society*, 2009, **131**, 14075-14080.
117. C. E. Chen, F. Pu, Z. Z. Huang, Z. Liu, J. S. Ren and X. G. Qu, *Nucleic Acids Research*, 2011, **39**, 1638-1644.
118. A. Schlossbauer, J. Kecht and T. Bein, *Angewandte Chemie-International Edition*, 2009, **48**, 3092-3095.
119. E. Climent, R. Martinez-Manez, F. Sancenon, M. D. Marcos, J. Soto, A. Maquieira and P. Amoros, *Angewandte Chemie-International Edition*, 2010, **49**, 7281-7283.
120. A. Schlossbauer, S. Warncke, P. M. E. Gramlich, J. Kecht, A. Manetto, T. Carell and T. Bein, *Angewandte Chemie-International Edition*, 2010, **49**, 4734-4737.
121. A. Bernardos, L. Mondragon, E. Aznar, M. D. Marcos, R. Martinez-Manez, F. Sancenon, J. Soto, J. M. Barat, E. Perez-Paya, C. Guillem and P. Amoros, *Acs Nano*, 2010, **4**, 6353-6368.
122. C. Y. Lai, B. G. Trewyn, D. M. Jeftinija, K. Jeftinija, S. Xu, S. Jeftinija and V. S. Y. Lin, *Journal of the American Chemical Society*, 2003, **125**, 4451-4459.
123. S. Giri, B. G. Trewyn, M. P. Stellmaker and V. S. Y. Lin, *Angewandte Chemie-International Edition*, 2005, **44**, 5038-5044.
124. J. L. Vivero-Escoto, I. I. Slowing, C. W. Wu and V. S. Y. Lin, *Journal of the American Chemical Society*, 2009, **131**, 3462-3463.
125. C. L. Zhu, C. H. Lu, X. Y. Song, H. H. Yang and X. R. Wang, *Journal of the American Chemical Society*, 2011, **133**, 1278-1281.
126. S. Angelos, Y. W. Yang, N. M. Khashab, J. F. Stoddart and J. I. Zink, *Journal of the American Chemical Society*, 2009, **131**, 11344-11346.
127. T. D. Nguyen, H. R. Tseng, P. C. Celestre, A. H. Flood, Y. Liu, J. F. Stoddart and J. I. Zink, *Proceedings of the National Academy of Sciences of the United States of America*, 2005, **102**, 10029-10034.
128. R. Hernandez, H. R. Tseng, J. W. Wong, J. F. Stoddart and J. I. Zink, *Journal of the American Chemical Society*, 2004, **126**, 3370-3371.

129. C. Park, H. Kim, S. Kim and C. Kim, *Journal of the American Chemical Society*, 2009, **131**, 16614-16615.
130. C. Park, K. Lee and C. Kim, *Angewandte Chemie-International Edition*, 2009, **48**, 1275-1278.
131. N. Singh, A. Karambelkar, L. Gu, K. Lin, J. S. Miller, C. S. Chen, M. J. Sailor and S. N. Bhatia, *Journal of the American Chemical Society*, 2011, **133**, 19582-19585.
132. N. K. Mal, M. Fujiwara and Y. Tanaka, *Nature*, 2003, **421**, 350-353.
133. D. G. He, X. X. He, K. M. Wang, J. Cao and Y. X. Zhao, *Langmuir*, 2012, **28**, 4003-4008.
134. Q. A. Gao, Y. Xu, D. Wu, W. L. Shen and F. Deng, *Langmuir*, 2010, **26**, 17133-17138.
135. D. Bartczak, T. Sanchez-Elsner, F. Louafi, T. M. Millar and A. G. Kanaras, *Small*, 2011, **7**, 388-394.
136. G. J. Doherty and H. T. McMahon, *Annual Review of Biochemistry*, 2009, **78**, 857-902.
137. B. Alberts, *Molecular Biology of Cell,* Garland Science, New York, 4th edn., 2002.
138. T. Cedervall, I. Lynch, S. Lindman, T. Berggard, E. Thulin, H. Nilsson, K. A. Dawson and S. Linse, *Proceedings of the National Academy of Sciences of the United States of America*, 2007, **104**, 2050-2055.
139. A. Albanese, P. S. Tang and W. C. W. Chan, *Annual Review of Biomedical Engineering, Vol 14*, 2012, **14**, 1-16.
140. B. D. Chithrani and W. C. W. Chan, *Nano Letters*, 2007, **7**, 1542-1550.
141. S. E. A. Gratton, P. A. Ropp, P. D. Pohlhaus, J. C. Luft, V. J. Madden, M. E. Napier and J. M. DeSimone, *Proceedings of the National Academy of Sciences of the United States of America*, 2008, **105**, 11613-11618.
142. J. A. Champion and S. Mitragotri, *Proceedings of the National Academy of Sciences of the United States of America*, 2006, **103**, 4930-4934.
143. Y. Qiu, Y. Liu, L. M. Wang, L. G. Xu, R. Bai, Y. L. Ji, X. C. Wu, Y. L. Zhao, Y. F. Li and C. Y. Chen, *Biomaterials*, 2010, **31**, 7606-7619.
144. H. J. Gao, W. D. Shi and L. B. Freund, *Proceedings of the National Academy of Sciences of the United States of America*, 2005, **102**, 9469-9474.
145. F. Lu, S. H. Wu, Y. Hung and C. Y. Mou, *Small*, 2009, **5**, 1408-1413.
146. H. Jin, D. A. Heller, R. Sharma and M. S. Strano, *Acs Nano*, 2009, **3**, 149-158.
147. B. D. Chithrani, A. A. Ghazani and W. C. W. Chan, *Nano Letters*, 2006, **6**, 662-668.
148. J. Wang, S. M. Tian, R. A. Petros, M. E. Napier and J. M. DeSimone, *Journal of the American Chemical Society*, 2010, **132**, 11306-11313.
149. D. L. J. Thorek and A. Tsourkas, *Biomaterials*, 2008, **29**, 3583-3590.
150. S. D. Perrault, C. Walkey, T. Jennings, H. C. Fischer and W. C. W. Chan, *Nano Letters*, 2009, **9**, 1909-1915.

151. R. Gref, M. Luck, P. Quellec, M. Marchand, E. Dellacherie, S. Harnisch, T. Blunk and R. H. Muller, *Colloids and Surfaces B-Biointerfaces*, 2000, **18**, 301-313.
152. P. Alexandridis and T. A. Hatton, *Colloids and Surfaces a-Physicochemical and Engineering Aspects*, 1995, **96**, 1-46.
153. K. Knop, R. Hoogenboom, D. Fischer and U. S. Schubert, *Angewandte Chemie-International Edition*, 2010, **49**, 6288-6308.
154. S. I. Jeon, J. H. Lee, J. D. Andrade and P. G. Degennes, *Journal of Colloid and Interface Science*, 1991, **142**, 149-158.
155. J. Satulovsky, M. A. Carignano and I. Szleifer, *Proceedings of the National Academy of Sciences of the United States of America*, 2000, **97**, 9037-9041.
156. V. P. Torchilin and V. S. Trubetskoy, *Advanced Drug Delivery Reviews*, 1995, **16**, 141-155.
157. C. D. Walkey, J. B. Olsen, H. B. Guo, A. Emili and W. C. W. Chan, *Journal of the American Chemical Society*, 2012, **134**, 2139-2147.
158. R. Kumar, I. Roy, T. Y. Ohulchanskky, L. A. Vathy, E. J. Bergey, M. Sajjad and P. N. Prasad, *Acs Nano*, 2010, **4**, 699-708.
159. A. A. Burns, J. Vider, H. Ow, E. Herz, O. Penate-Medina, M. Baumgart, S. M. Larson, U. Wiesner and M. Bradbury, *Nano Letters*, 2009, **9**, 442-448.
160. H. S. Choi, W. Liu, P. Misra, E. Tanaka, J. P. Zimmer, B. I. Ipe, M. G. Bawendi and J. V. Frangioni, *Nature Biotechnology*, 2007, **25**, 1165-1170.
161. I. Lynch and K. A. Dawson, *Nano Today*, 2008, **3**, 40-47.
162. V. Cauda, C. Argyo and T. Bein, *Journal of Materials Chemistry*, 2010, **20**, 8693-8699.
163. S. M. Haidary, E. P. Corcoles and N. K. Ali, *Journal of Nanomaterials*, 2012.
164. S. H. C. Anderson, H. Elliott, D. J. Wallis, L. T. Canham and J. J. Powell, *Physica Status Solidi a-Applied Research*, 2003, **197**, 331-335.
165. K. S. Finnie, D. J. Waller, F. L. Perret, A. M. Krause-Heuer, H. Q. Lin, J. V. Hanna and C. J. Barbe, *Journal of Sol-Gel Science and Technology*, 2009, **49**, 12-18.
166. V. Cauda, A. Schlossbauer and T. Bein, *Microporous and Mesoporous Materials*, 2010, **132**, 60-71.
167. Y. S. Lin, N. Abadeer and C. L. Haynes, *Chemical Communications*, 2011, **47**, 532-534.
168. Y. S. Lin, N. Abadeer, K. R. Hurley and C. L. Haynes, *Journal of the American Chemical Society*, 2011, **133**, 20444-20457.
169. S. Elmore, *Toxicologic Pathology*, 2007, **35**, 495-516.
170. A. Lawen, *Bioessays*, 2003, **25**, 888-896.
171. F. T. Andon and B. Fadeel, *Accounts of Chemical Research*, 2012.
172. G. Kroemer, W. El-Deiry, P. Golstein, M. E. Peter, D. Vaux, P. Vandenabeele, B. Zhivotovsky, M. V. Blagosklonny, W. Malorni, R. A. Knight, M. Piacentini, S. Nagata and G. Melino, *Cell Death and Differentiation*, 2005, **12**, 1463-1467.
173. G. Melino, R. A. Knight and P. Nicotera, *Cell Death and Differentiation*, 2005, **12**, 1457-1462.

174. X. J. Jiang and X. D. Wang, *Annual Review of Biochemistry*, 2004, **73**, 87-106.
175. M. P. Barnes and W. C. Shen, *International Journal of Pharmaceutics*, 2009, **369**, 79-84.
176. N. W. S. Kam and H. J. Dai, *Journal of the American Chemical Society*, 2005, **127**, 6021-6026.
177. S. K. Kim, M. B. Foote and L. Huang, *Biomaterials*, 2012, **33**, 3959-3966.
178. Y. Lee, T. Ishii, H. Cabral, H. J. Kim, J. H. Seo, N. Nishiyama, H. Oshima, K. Osada and K. Kataoka, *Angewandte Chemie-International Edition*, 2009, **48**, 5309-5312.
179. H. S. Park, C. Kim, H. J. Lee, J. H. Choi, S. G. Lee, Y. P. Yun, I. C. Kwon, S. J. Lee, S. Y. Jeong and S. C. Lee, *Nanotechnology*, 2010, **21**, 225101-225109.
180. I. I. Slowing, B. G. Trewyn and V. S. Y. Lin, *Journal of the American Chemical Society*, 2007, **129**, 8845-8849.
181. F. Li, A. Srinivasan, Y. Wang, R. C. Armstrong, K. J. Tomaselli and L. C. Fritz, *Journal of Biological Chemistry*, 1997, **272**, 30299-30305.
182. S. Santra, C. Kaittanis and J. M. Perez, *Molecular Pharmaceutics*, 2010, **7**, 1209-1222.
183. M. N. Hossen, K. Kajimoto, H. Akita, M. Hyodo, T. Ishitsuka and H. Harashima, *Molecular Therapy*, 2013, doi: 10.1038/mt.2012.1256.

Chapter 2 Experimental Section

2.1 Particle Preparation

Chemicals

All chemicals including proteins for particle synthesis were supplied by Sigma-Aldrich and used as received, unless otherwise specified.

General Washing Procedure

In the synthesis and functionalisation of silica nanoparticles, it was necessary, at various stages, to purify the as-synthesised particles for the next reaction steps or analyses achieved by a washing procedure. A general washing step for nanoparticles 'without biomodification' was carried out by dispersion in ethanol in a centrifuge tube *via* sonication at room temperature (the amount of ethanol required depends on the quantity of particle produced and the volume of centrifuge tubes ranging from 2 mL to 30 mL). Note that due to temperature increases associated with sonication, regular replacement of water in the sonic bath was required. The redispersed particle suspensions were then centrifuged for 20 min at 13200 rpm resulting in a particle pellet at the bottom of the tube and a supernatant solution. The supernatant was subsequently discarded or kept for the following analysis (e.g. Arsenazo test, see below for detail). The particle pellet was either resuspended using a sonicator and/or vortex in ethanol for further washing (if required), or in the desired solvents for the

subsequent reaction steps. The particles can also be resuspended in ultrapure water or buffer solutions or vacuum dried depending on the subsequent particle analyses (see below). For protein modified nanoparticles, the washing procedure was conducted in ultrapure water and in the steps where sonication was needed (otherwise gentler vortex was recommended), ice-cold water was always required in the sonicator. Note that biomodified nanoparticles were never sonicated for more than 10 min to prevent any destructive effect on proteins.

2.1.1 Preparation of Plain MSNs

Cetyltrimethylammonium bromide (CTAB; 0.64 g, 1.77 mmol) was dissolved by vigorous stirring into a mixture of ultrapure water (16.02 mL, 0.89 mol) and ethanol (1.84 mL, 0.04 mol). The solution was brought to 80˚C in an oil bath with a stirring hot plate. Triethanol amine (TEA; 1.03 g, 6.9 mmol) was subsequently added into the solution and mixed until dissolved. Finally, tetraethylorthosilicate (TEOS; 1.45 mL, 6.5 mmol) was added dropwise. The solution was reacted at 80˚C for 2 h. The resulting milky white solution (containing nanoparticles) was centrifuged (13200 rpm, 20 min) and redispersed by sonication into an acidified ethanol solution (15 mL HCl in 100 mL ethanol) to remove the surfactant. The surfactant removal was carried out by sonication for 30 min and repeated twice. The nanoparticles were then washed with ethanol (following the washing procedure stated above) 3 times and retained in a concentrated ethanol suspension[1, 2].

2.1.2 Preparation of Gd-DOTA MSNs by Post-grafting

The plain MSNs were aminated by dispersing 100 mg nanoparticles into a mixture of ultrapure water (5 mL) and ethanol (10 mL) using sonication. (3-aminopropyl)triethoxysilane (APTES; 0.59 µL, 2.6 µmol) was then added into particle suspension and stirred at room temperature for 24 h. After this time, the aminated particles were washed 3 times following the general washing procedure. Subsequently, the aminated MSNs were functionalised with 2,2',2''-(10-(2-((2,5-dioxopyrrolidin-1-yl)oxy)-2-oxoethyl)-1,4,7,10-tetraazacyclododecane-1,4,7-triyl)triacetic acid (DOTA-NHS ester, supplied by Macrocyclics) and chelated with Gd^{3+} (Fig. 2.1). Specifically, 50 mg aminated MSNs were dispersed into 15 mL anhydrous dimethylformamide (DMF) and stirred vigorously at room temperature for 24 h with DOTA-NHS ester (1.3 µmol) and 150 µL triethylamine. After this time, the nanoparticles were washed 3 times following the general washing procedure and redispersed into 10 mL ethanol. Two molar equivalents (with respect to DOTA-NHS ester) of $GdCl_3$ were added and stirred vigorously at room temperature for 24 h. The nanoparticles were then washed 8 times with ethanol and retained for characterisation.

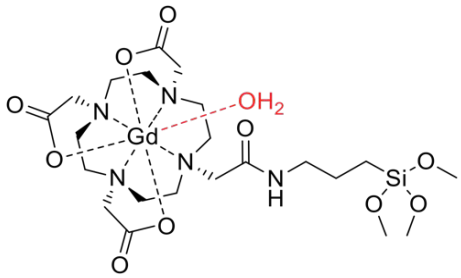


Fig. 2.1 Chemical structure of silaned Gd-DOTA with a single coordinated H_2O.

The presence of free Gd^{3+} ions in particle suspension was determined using arsenazo (III), a dye which forms a coloured complex when chelated with Gd^{3+}. A 10^{-5} M aqueous gadolinium solution was prepared by dissolving $GdCl_3$ (3 mg, 0.11 μmol) into ultrapure water (1 L). A 10^{-6} M aqueous arsenazo (III) solution was prepared by dissolving arsenazo (III) (0.8 mg, 1.03 μmol) into ultrapure water (1 L). A series of mixtures of gadolinium solution and arsenazo solution were prepared and their UV-Vis absorption spectra (UV PC-2401, Shimadzu) were collected which assessed the limit of detection of the arsenazo (III) to be 10 nmol $GdCl_3$ (see Appendix, Fig. A1). For particle analysis, the supernatants of particle suspensions obtained by the general washing procedure (see above) were mixed with the 10^{-6} M aqueous arsenazo (III) solution to assess the presence of free Gd^{3+} in the supernatants. Specifically, the general washing procedure and this analysis were repeated until no free Gd^{3+} in the supernatants capable of chelating with arsenazo (III). The same assessment was also repeated after different time periods to examine the long-term stability of Gd-DOTA chelate on the MSNs in ultrapure water suspensions (see Chapter 3).

2.1.3 Preparation of Gd-DOTA MSNs by Delayed Co-condensation

Aminated MSNs synthesised by delayed co-condensation were prepared following the procedure used in the synthesis of plain MSNs stated above with a slight modification. A mixture of 6.9 mmol TEA, 1.77 mmol CTAB, 0.89 mol H_2O, and 0.04 mol ethanol was heated to 80˚C in an oil bath with a stirring hot plate. TEOS was then added into

the mixture dropwisely under vigorous stirring (for amounts of TEOS used see Table 2.1).

Table 2.1 Total amounts of TEOS and APTES used in co-condensation amination experiments; amount of DOTA-NHS-ester and $GdCl_3$ used in contrast agent loading experiments. (Table generated based on ~400 mg MSNs).

Samples	Mol%** amination	Total TEOS (mmol)	APTES (μmol)	DOTA-NHS ester (μmol)	Delay time (min)
1.37 wt%* Gd-DOTA MSNs (long delay)	0.15	6.5	10	10	60
2.07 wt% Gd-DOTA MSNs	0.23	6.5	15	15	60
3.82 wt% Gd-DOTA MSNs	0.5	6.5	32.5	32.5	60
1.37 wt% Gd-DOTA MSNs (excess amine)	10	6.5	650	10	60
1.37 wt% Gd-DOTA MSNs (short delay)	0.15	6.5	10	10	10

*wt% refers to percentage weight ratio of final Gd^{3+} content determined by ICP-MS with respect to MSNs.
**mol% refers to percentage mole ratio of APTES with respect to TEOS.

Subsequently, a solution containing a 1:1 molar ratio of APTES and TEOS was prepared and added to the solution dropwise after 10 min ('short delay' co-condensation) or 1 h ('long delay' co-condensation); the reaction was then continued at 80˚C for a total time period of 2 h (for amounts of APTES used see Table 2.1). After this time, an opaque white solution remained which was then followed by the surfactant removal procedure as described in Section 2.1.1 above. The resulting surfactant free nanoparticles were subsequently washed 3 times following the general washing procedure and resuspended in anhydrous DMF for the next DOTA-NHS ester conjugation step. This conjugation was carried out using the same procedure employed in the preparation of Gd-DOTA MSNs (post-grafting) stated above (Section 2.1.2).

The amounts of DOTA-NHS ester needed depends on the quantity of APTES used (see Table 2.1). Finally, Gd^{3+} chelation was achieved by the addition of two molar equivalents (to DOTA-NHS ester) of $GdCl_3$ in ethanol at room temperature for 24 h. The obtained Gd-DOTA MSNs were collected by a series of ethanol washing and centrifugation steps following the general washing procedure[2, 3]. The relative amounts of TEOS, APTES and DOTA-NHS ester were varied depending on the desired loading of groups required, as summarised in Table 2.1.

2.1.4 Preparation of Protein Conjugated Gd-DOTA Doped MSNs with Various Linkages

2.1.4.1 Direct Protein Conjugation to MSNs

40 mg of Gd-DOTA MSNs (long delay, see Table 2.1) was mixed with 0.03 mmol of APTES in 1:2 H_2O:ethanol mixture (4 mL:8 mL) and reacted at room temperature for 24 h. After external amination, nanoparticles were washed twice following the general washing procedure and redispersed in 20 mL anhydrous DMF with 0.06 mmol of succinic anhydride to convert the amine groups to carboxyl groups overnight at room temperature followed by the general washing procedure (twice). The obtained externally carboxylated Gd-DOTA MSNs were coupled with biotin labelled bovine serum albumin (BSA) or Strep5 aptamer (consists of 5 strep-tags separated by a regular spacer peptide with sequence: WSHPQFEKGGGSGGGSGGGSWSHPQFEKGTGSGGGSGGGSWSHPQFEKGTG SGGGSGGSWSHPQFEKGTGSGGGSGGGSWSHPQFEK) by reacting with EDC [1-

ethyl-3-(-3-dimethylaminopropyl) carbodiimide hydrochloride] and NHS (N-hydroxysuccinimide) overnight (carbodiimide chemistry, for detailed mechanism see Chapter 1). Specifically, carboxylated MSNs were resuspended in 2 mL, 0.1 M, pH 5.5 2-(N-morpholino)ethanesulfonic acid (MES) buffer and activated with 7 nmol of EDC and 14 nmol of NHS for 20 min. After this time, a 8 mL, 0.1 M, pH 8.5 bicarbonate buffer solution containing 3.5 nmol of proteins was added to the pH 5.5 particle EDC/NHS solution to obtain a neutral mixture. This mixture was then stirred at room temperature overnight to conjugate the proteins and nanoparticles. Finally, the protein modified nanoparticles were washed in ice-cold water and collected with centrifugation (see above washing procedure for biomodified nanoparticles, Fig 2.2).

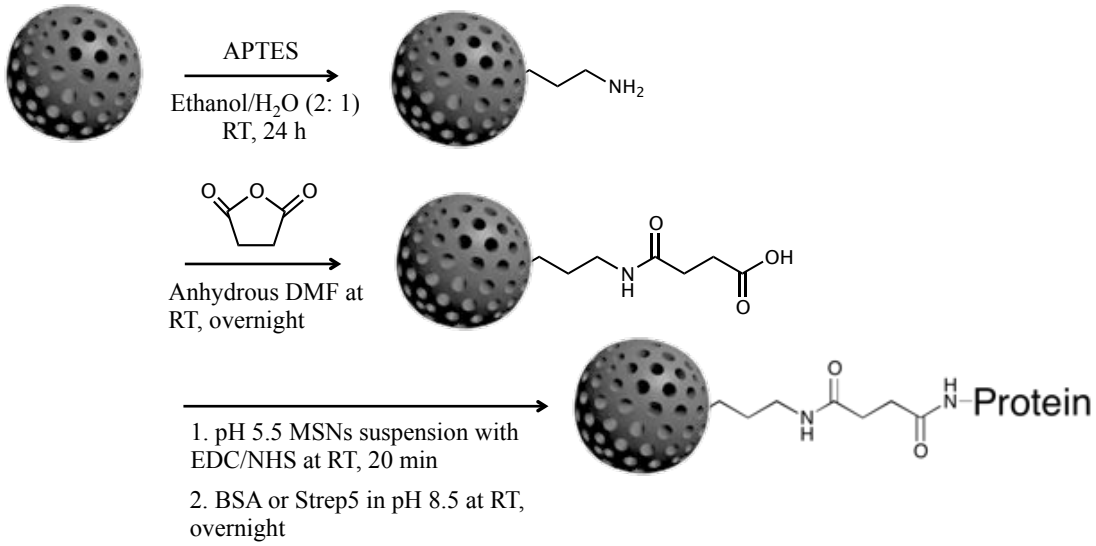


Fig. 2.2 Reaction scheme of protein directly conjugated Gd-DOTA MSNs.

2.1.4.2 Protein Conjugated MSNs *via* PEG Linker

For PEG5000 modified nanoparticles, 40 mg of Gd-DOTA MSNs (long delay, see Table 2.1) was mixed with 3.5 nmol (for low pegylated particles) [or 28 μmol (for

highly pegylated particles)] of silanised PEG5000 (amine-terminated, supplied by Nanocs) in 1:2 H_2O:ethanol mixture (4 mL:8 mL) at room temperature for 24 h followed by the conversion of amine to carboxylic groups through reaction with 7 nmol (or 56 nmol) of succinic anhydride in 20 mL anhydrous DMF at room temperature overnight. The carboxyl-terminated pegylated Gd-DOTA MSNs were resuspended in 2 mL, 0.1 M, pH 5.5 MES buffer and activated with 7 nmol (or 56 μmol) of EDC and 14 nmol (or 112 μmol) of NHS for 20 min. After this time, a 8 mL, 0.1 M, pH 8.5 bicarbonate buffer solution containing 3.5 nmol of proteins was added to the pH 5.5 particle EDC/NHS solution followed by stirring at room temperature overnight to conjugate the proteins and nanoparticles. Finally, the protein modified nanoparticles were washed in ice-cold water and collected with centrifugation (see above washing procedure for biomodified nanoparticles, Fig 2.3).

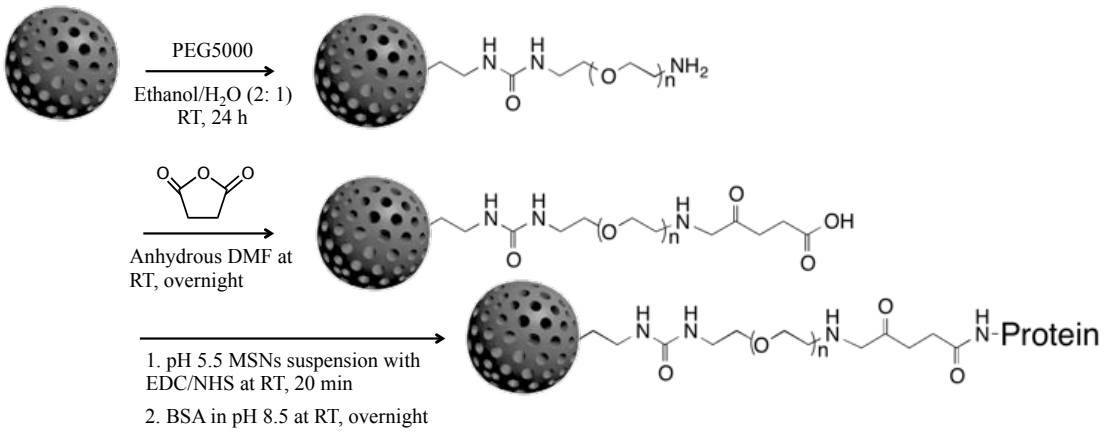


Fig. 2.3 Reaction scheme of PEG5000 linked protein conjugated Gd-DOTA MSNs.

For PEG2000 modified nanoparticles, 40 mg of Gd-DOTA MSNs (long delay, see Table 2.1) was mixed with 3.5 nmol (for low pegylated particles) [or 28 μmol (for

highly pegylated particles)] of APTES in 1:2 H_2O:ethanol mixture (4 mL:8 mL) at room temperature for 24 h followed by the conversion of amine to carboxyl groups with 7 nmol (or 56 nmol) of succinic anhydride in 20 mL anhydrous DMF at room temperature overnight. The carboxyl-terminated Gd-DOTA MSNs were resuspended in 2 mL, 0.1 M, pH 5.5 MES buffer activated with 7 nmol (or 56 μmol) of EDC and 14 nmol (or 112 μmol) of NHS for 20 min. After this time, a 8 mL, 0.1 M, pH 8.5 bicarbonate buffer solution containing 3.5 nmol (or 28 μmol) of bis-amino-PEG2000 (supplied by RAPP Polymere) was added to the pH 5.5 particle EDC/NHS solution followed by stirring at room temperature overnight to achieve pegylation (Fig. 2.4). [Note that this carbodiimide chemistry (EDC/NHS activation) was employed repetitively throughout the following preparations of different particles with a molar ratio of carboxyl groups (on nanoparticles or proteins):EDC:NHS of 1:2:4; from now on this step will be referred to as 'EDC/NHS activation'.]

After pegylation, the particles were washed in ethanol twice following the general washing procedure and redispersed in 20 mL anhydrous DMF with 7 nmol (or 56 nmol) of succinic anhydride at room temperature overnight to convert terminal amines to carboxyl groups. The carboxyl-terminated pegylated Gd-DOTA MSNs were collected by centrifugation after a general washing procedure and conjugated with 3.5 nmol of proteins promoted by EDC/NHS activation. Finally, the protein modified nanoparticles were washed in ice-cold water and collected with centrifugation (see above washing procedure for biomodified nanoparticles, Fig 2.4).

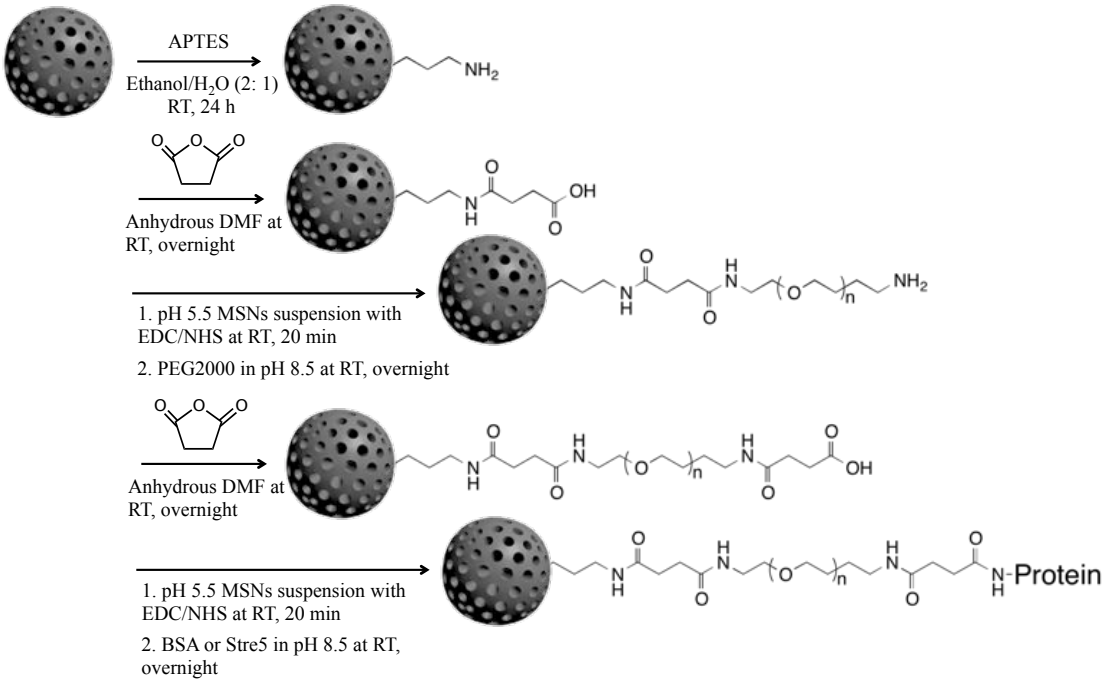


Fig. 2.4 Reaction scheme of PEG2000 linked protein conjugated Gd-DOTA MSNs.

2.1.4.3 Protein Conjugated MSNs *via* Disulfide Linker

40 mg of Gd-DOTA MSNs (long delay, see Table 2.1) was mixed with 3.5 nmol of APTES in 1:2 H_2O:ethanol mixture (4 mL:8 mL) at room temperature for 24 h and followed by the conversion of amine to carboxyl groups by reaction with 7 nmol of succinic anhydride in 20 mL anhydrous DMF at room temperature overnight. The obtained externally carboxylated Gd-DOTA MSNs were collected by centrifugation after a general washing procedure and conjugated with 3.5 nmol of cystamine promoted by EDC/NHS activation resulting in amine-terminated disulfide modified Gd-DOTA MSNs. 7 nmol of succinic anhydride then converted these to carboxyl-terminated particles in 20 mL anhydrous DMF at room temperature overnight followed by coupling with 3.5 nmol of streptavidin (STV)[4] (*via* carbodiimide chemistry, see

above). Finally, the protein modified nanoparticles were washed in ice-cold water and collected with centrifugation (see above washing procedure for biomodified nanoparticles, Fig 2.5). For subsequent disulfide cleavage and protein removal, the STV capped particles were redispersed in 2 mM (in ultrapure water) of reducing agent [dithiothreitol (DTT), 2-mercaptoethanol (2-ME), L-cysteine or tris(2-carboxyethyl)phosphine (TCEP)] with stirring for 2 h. After this cleavage process, the particles were resuspended in ethanol by sonication followed by the general washing procedure.

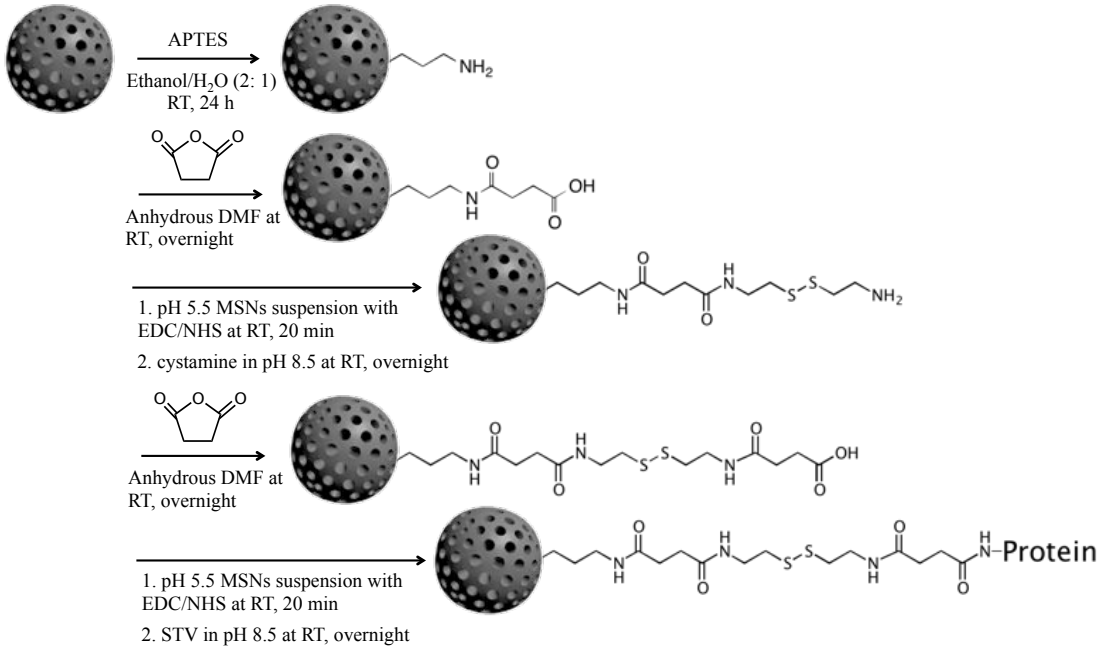


Fig. 2.5 Reaction scheme of disulfide linked protein conjugated Gd-DOTA MSNs.

2.1.4.4 Protein Conjugated MSNs *via* Biotin Linker

40 mg of Gd-DOTA MSNs (long delay, see Table 2.1) was mixed with 70 nmol (or 350 nmol) of APTES in 1:2 H_2O:ethanol mixture (4 mL:8 mL) at room temperature for

24 h followed by conjugation with 70 nmol (or 350 nmol) of biotin promoted by EDC/NHS activation. The as-synthesised biotinylated Gd-DOTA MSNs were then redispersed in 1.75 μM of STV aqueous solution to obtain streptavidin conjugated Gd-DOTA MSNs. In control experiments, the as-synthesised biotinylated Gd-DOTA MSNs were redispersed in 1.75 μM of molecular biotin, biotin quenched STV or native unmodified BSA aqueous solution. For competitive displacement with biotinylated BSA (see Chapter 4), the STV capped particles were redispersed in 7 μM of biotin-BSA solution with gentle stirring overnight.

2.1.5 Preparation of Gd-DOTA Doped Non-porous Silica Nanoparticles

Non-porous silica nanoparticles (SNPs) were synthesised by traditional Stöber methods[5]. A mixture of 1 mL NH_4OH, 20 mL ethanol and 1 mL TEOS was stirred at room temperature for 24 h. The resulting milky white solution (containing nanoparticles) was centrifuged (13200 rpm, 20 min) and washed following the general washing procedure. 116 mg of as-synthesised SNPs were mixed with 0.04 mL APTES in 10 mL toluene under stirring at 70˚C for 20 min. 90 mg of the resulting aminated nanoparticles were mixed with 160 μL triethylamine and 1.5 mg DOTA-NHS ester in 3 mL anhydrous DMF at room temperature for 24 h. After this time, the nanoparticles were washed 3 times following the general washing procedure and redispersed into 18 mL ethanol. The subsequent Gd^{3+} chelation was achieved by the addition of two molar equivalents (to DOTA-NHS ester) of $GdCl_3$ at room temperature for 24 h. The final

Gd-DOTA doped SNPs were collected by extensive washing in ethanol and centrifugation following the general washing procedure.

2.1.6 Preparation of Native FITC-MSNs, Primary Amine Modified MSNs and Rhodamine-MSNs

Native FITC-MSNs or rhodamine-MSNs were synthesised by exactly the same procedure as applied to the preparation 1.37 wt% Gd-DOTA MSNs (long delay, see Table 2.1) using NHS-fluorescein or NHS-rhodamine (supplied by Thermo Scientific) in the place of DOTA-NHS ester. The obtained tagged MSNs, possessing internalised dye molecules, were collected by a series of washing and centrifugation following the general washing procedure. Primary amine modified MSNs were prepared by post-grafting APTES (6.56 μmol, 32.8 μmol and 65.6 μmol for 1 mol%, 5 mol% and 10 mol% of amination, respectively) with 40 mg of the native FITC-MSNs in H_2O:ethanol mixture (4 mL:8 mL) at room temperature for 24 h followed by the general washing procedure (Fig. 2.6).

2.1.7 Preparation of Imidazole Modified MSNs

For imidazole-only and carboxyl/imidazole co-modified MSNs, 30 mg of the above 1 mol% of primary amine modified MSNs were first converted to carboxylated MSNs using 10 μmol of succinic anhydride in 15 mL anhydrous DMF at room temperature overnight. The resulting carboxylated MSNs were then conjugated with histamine or histidine (5 μmol) promoted by EDC/NHS activation followed by the general washing

procedure. For primary amine and imidazole co-modified MSNs, 30 mg of 1 mol% of primary amine modified MSNs were conjugated with histidine (5 μmol) promoted by EDC/NHS activation followed by the general washing procedure (Fig. 2.6).

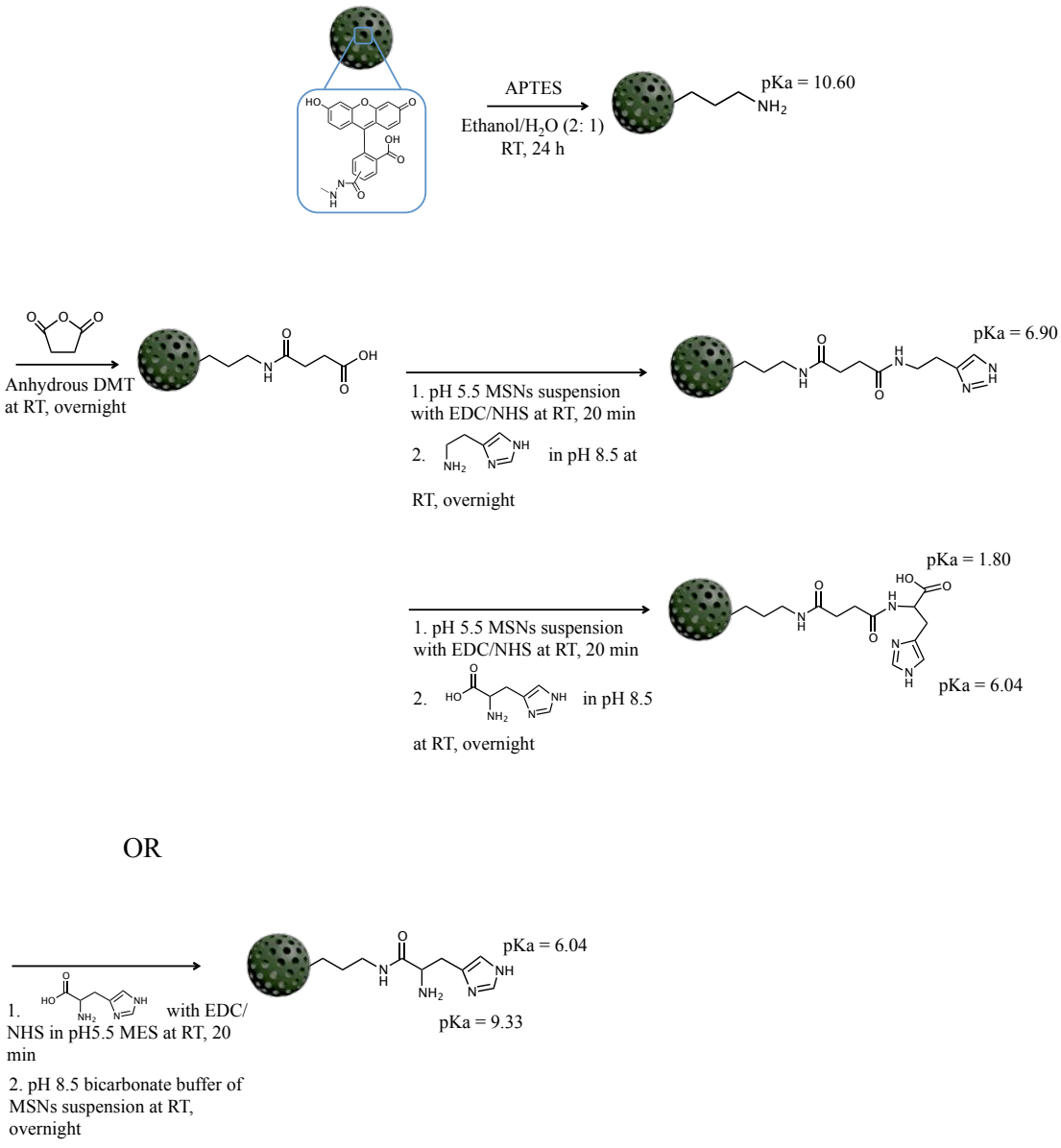


Fig. 2.6 Reaction scheme of various amine conjugated FITC-MSNs with pKa values of various acidic and basic groups noted.

2.1.8 Preparation of Cytochrome *c* Labelled MSNs & BSA Labelled MSNs

2.1.8.1 Protein Conjugated MSNs *via* Uncleavable Linker

40 mg of native FITC-MSNs were post-functionalised with 65.6 μmol of APTES in 1:2 H_2O:ethanol mixture (4 mL:8 mL) at room temperature for 24 h followed by 131.2 μmol of succinic anhydride carboxylation in 15 mL anhydrous DMF at room temperature overnight to produce 10 mol% carboxylated MSNs. 25 mg of the resulting carboxylated particles were then labelled with 2.19 nmol cytochrome *c* (from saccharomyces cerevisiae) promoted by EDC/NHS activation to produce type (b) particles in Chapter 6 ([Cyt *c*] = 87.5 pmol/mg MSNs). 25 mg of 1 mol% of primary amine modified MSNs were conjugated with 2.19 nmol cytochrome *c* or BSA promoted by EDC/NHS activation to produce type (b) cytochrome *c* or type (f) BSA particles in Chapter 6. For high cytochrome *c* dosage (41 nmol/mg MSNs) particles [type (c) in Chapter 6], the reaction was initiated with 0.5 mol% of aminated MSNs [40 mg of native FITC-MSNs with 3.28 μmol of APTES in 1:2 H_2O:ethanol mixture (4 mL:8 mL) at room temperature for 24 h] followed by 1.64 μmol of succinic anhydride carboxylation in 15 mL anhydrous DMF at room temperature overnight. 10 mg of the as-synthesised amine/carboxyl co-modified MSNs was then activated by 0.82 μmol EDC and 1.64 μmol NHS in 2 mL pH 5.5 MES buffer for 20 min followed by conjugation with 410 nmol of cytochrome *c* generating the type (c) particles in Chapter 6. Finally, the protein modified nanoparticles were washed in ice-cold water and collected with centrifugation (see above washing procedure for biomodified nanoparticles).

2.1.8.2 Protein Conjugated MSNs *via* Cleavable Linker

Acid-responsive hydrazone linked MSNs were prepared by modifying 50 mg of native FITC-MSNs with 4.38 nmol of triethoxysilylbutyraldehyde in 1:2 H_2O:ethanol mixture (5 mL:10 mL) at room temperature for 24 h followed by nucleophilic addition of succinic dihydrazide in 5 mL pH 8.5 bicarbonate buffer overnight. The resulting hydrazone modified MSNs were then reacted with 8.76 nmol succinic anhydride in 15 mL anhydrous DMF at room temperature overnight followed by post-functionalisation with APTES at the 1 mol% level in 1:2 H_2O:ethanol mixture (5 mL:10 mL) at room temperature for 24 h. The generated hydrazone and primary amine co-modified MSNs were subsequently conjugated with 4.38 nmol cytochrome *c* promoted by EDC/NHS activation (Fig. 2.7)[6].

Redox-responsive disulfide linked MSNs were prepared by modifying 50 mg of FITC-MSNs with 4.38 nmol of APTES in 1:2 H_2O:ethanol mixture (5 mL:10 mL) at room temperature for 24 h followed by 8.76 nmol succinic anhydride carboxylation in 15 mL anhydrous DMF at room temperature overnight. The resulting carboxylate particles were conjugated with 8.76 nmol cystamine promoted by EDC/NHS activation. The obtained cystamine MSNs were subsequently carboxylated by 8.76 nmol succinic anhydride in 15 mL anhydrous DMF at room temperature overnight followed by post-grafting with APTES at 1 mol% level in 1:2 H_2O:ethanol mixture (5 mL:10 mL) at room temperature for 24 h. Subsequently, 4.38 nmol cytochrome *c* was conjugated on the nanoparticles promoted by EDC/NHS activation. Finally, the protein

modified nanoparticles were washed in ice-cold water and collected with centrifugation (see above washing procedure for biomodified nanoparticles).

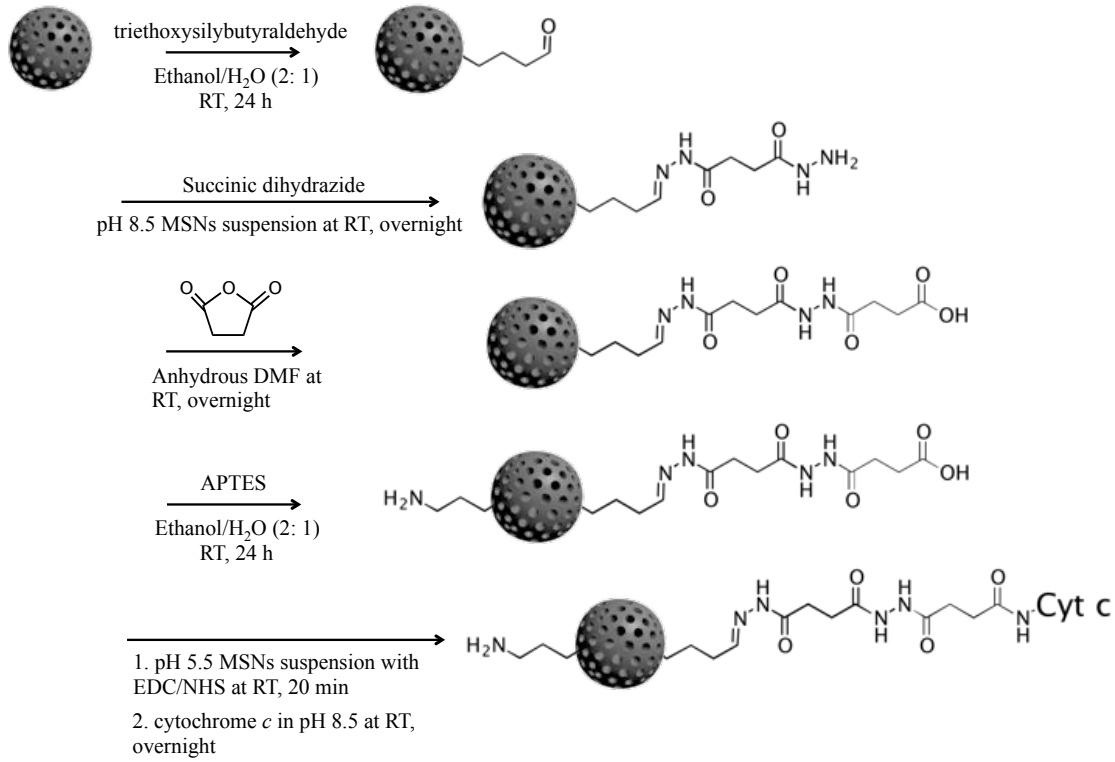


Fig. 2.7 Reaction scheme of hydrozone linked cytochrome *c* conjugated 1 mol% NH_2-MSNs.

2.1.9 Preparation of Rhodamine 6G Loaded MSNs and Capping with BSA through Disulfide Linker

100 mg of plain MSNs were post-grafted with APTES followed by conversion of amine groups to carboxyl groups by succinic anhydride (the amounts of APTES and succinic anhydride needed depend on the desired coverage, 5 mol% and 10 mol%). 80 mg of the resulting carboxylated MSNs were conjugated with equimolar (compared to carboxyl groups) of cystamine promoted by EDC/NHS activation resulting in amine-terminated disulfide modified MSNs (see Fig 2.5). These particles can be then further

converted to carboxyl-terminated disulfide modified MSNs. For loading of 3 mg rhodamine 6G (R6G), 40 mg NH_2-terminated MSNs and COOH-terminated MSNs were redispersed in 5 mL pH 8.5 bicarbonate buffer and pH 5.5 MES buffer, respectively. The R6G and nanoparticle mixtures were then stirred at room temperature for 24 h.

For the subsequent BSA capping on NH_2-terminated MSNs, 5 mol% (2.1 g, 31.8 μmol) [or 10 mol% (4.2 g, 63.6 μmol)] of BSA was activated by 63.6 μmol (or 127.2 μmol) of EDC and 127.2 μmol (or 254.4 μmol) of NHS in 20 mL pH 5.5 MES buffer at room temperature for 20 min followed by mixing with the R6G loaded NH_2-terminated MSNs suspension (5 mL in pH 8.5 bicarbonate buffer). An additional 75 mL of pH 8.5 bicarbonate buffer was then added to this 25 mL particle suspension and stirred at room temperature overnight. For the subsequent BSA capping on COOH-terminated MSNs, the R6G loaded COOH-terminated MSNs suspension (5 mL) was activated by 63.6 μmol (or 127.2 μmol) of EDC and 127.2 μmol (or 254.4 μmol) of NHS at room temperature for 20 min followed by mixing with a 20 mL pH 8.5 bicarbonate buffer solution containing 5 mol% (2.1 g, 31.8 μmol) [or 10 mol% (4.2 g, 63.6 μmol)] of BSA. Additional 15 mL of MES buffer and 60 mL of bicarbonate buffer were then added to this 25 mL particle suspension and stirred at room temperature overnight. The following R6G (479.2Da) release studies were conducted using a 0.5 mL filter device (molecular weight cut-off of 10000Da; Fig. 2.8) and at the desired time points the disulfide bonds were cleaved using tris(2-

carboxyethyl)phosphine (TCEP) with constant stirring (700 rpm). The release of R6G was monitored through its absorption at 530 nm by UV-Vis spectrometry (see Chapter 6).

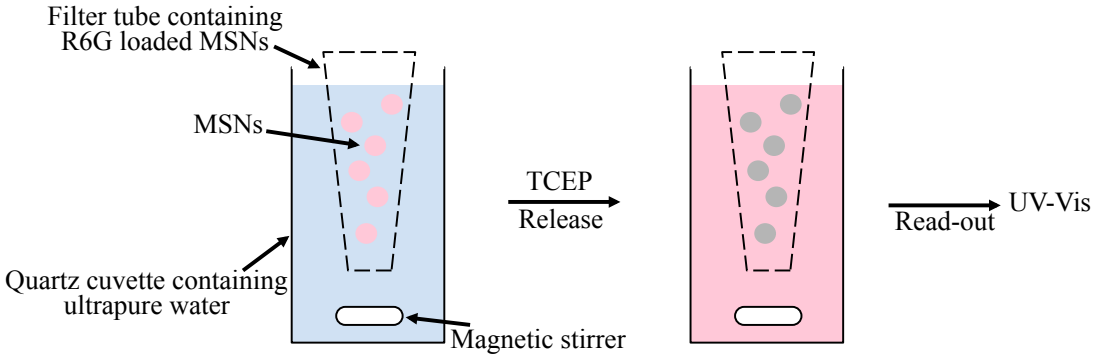


Fig. 2.8 Experimental setup for R6G release study. A filter tube (molecular weight cut-off of 10000Da to prevent diffusion of nanoparticles) containing 0.5 mL of R6G loaded MSNs suspension (0.4 mg/mL) was placed in a quartz cuvette containing 2 mL ultrapure water. The release was triggered *via* the cleavage of disulfide linked BSA by TCEP. By virtue of the filter permeability to R6G (479.2Da), it then diffused into quartz cuvette which was subsequently monitored by UV-Vis spectrometry.

2.2 Microarray Spotting

Buffer Solutions

To prepare print buffer for protein spotting, 0.1 g of tween 20 was dissolved in 99.9 g of 20 mM of phosphate buffered saline (PBS) which were designated as 2x PBST buffer. 20 g of glycerol was then dissolved in 80 g of this PBST buffer to obtain the final 'print buffer'. To prepare blocking buffer for blocking the non-specific area of a spotting slide (see below), 5 g of tween 20 was dissolved in 95 g of 20 mM PBS. The blocking buffer was obtained by mixing 1 g of BSA protein with 99 g of the tween 20 PBS solution.

Spotting Procedure

25 μL of 1 g/L streptavidin and 10 μL of 0.4 M EDC were dissolved in 5 μL of print buffer (final [streptavidin] = 10 μM). The resulting streptavidin solution was then place in a 96 plate well followed by printing in 3 x 3 features, across 9 repetitions on amine modified glass slides (supplied by Genetix) by a BioOdyssey Calligrapher MiniArrayer (humidity controlled at 50%, temperature 4°C). The spotted volumes were allowed to incubate on the slide for 60 min (for the binding of streptavidin to slides) prior to a blocking step (to block areas without streptavidin spots). Specifically, the blocking was carried out by soaking the slides in the blocking buffer for 60 min. After this time, the slides were rinsed with fresh PBS buffer. Subsequently, the slides were incubated with protein modified luminescent MSNs suspensions (in PBS; proteins were fluorescently labelled with Atto655 NHS ester supplied by ATTO-TEC

Gmbh with concentration >7 nM) for 2 h to test the particle vectoring toward the streptavidin spots (see Chapter 4). Finally, the vectored slides were rinsed in PBS for 10 min and ultrapure water for 2 min twice. After this, the slides were dried under a stream of nitrogen and scanned at a pixel resolution of 5 μm with 633 nm lasers under the Cy5 detection protocol (ScanArray Express, Perkin Elmer).

2.3 Cell Experiments

Chemicals

All ingredients and cell stain solutions for Hela cell culture and confocal microscopy were supplied by Life Technologies, unless otherwise specified. To prepare Hoechst33342 working solution (nucleus stain), 4 μL of the stock solution (used as received from the supplier) was diluted with 10 mL Dulbecco's Phosphate-Buffered Saline (DPBS). To prepare LysoTracker Red or LysoTracker Green working solution (late endosome and lysosome stains), 1 μL of the stock solution was diluted with 15 mL DPBS. To prepare 100 μL/mL of propidium iodide (PI) working solution (dead cell indicator), 5 μL of 1 mg/mL stock solution was diluted with 45 μL of 1x annexin-binding buffer.

2.3.1 Fluorescent Labelling of Cellular Organelles

To stain the adhered and fixed cells, the fixation solution (4% paraformaldehyde, see below) was discarded and the cells were rinsed with 2 mL DPBS twice. After this, 1 mL of the desired working stain solutions (Hoeshst33342, LysoTracker Red and Green) were added into the cell dishes and allowed to incubate at room temperature for 15 – 20 min (occasionally checking the staining quality with a confocal microscope). After this time, the stain solutions were discarded and the cells were washed with 2 mL DPBS twice. Finally, the cells were left in 2 mL DPBS for the following imaging. To stain unfixed floating cells with apoptotic stains [PI and Annexin V (AnnV)], the cells were detached by trypsinisation and resuspended in 100 μL of 1x annexin-binding

buffer (see below) followed by the addition of 2 μL PI working solution and 10 μL Pacific blue conjugated AnnV (used as received) at room temperature for 15 min. After this, the cell suspension was centrifuged (1200 rpm, 5 min) and resuspended into 100 μL of 1x annexin-binding buffer for the following programmed cell death determination (see below).

2.3.2 Cell Culture Procedure and Sample Preparation for Confocal Microscopy

Human cervical carcinoma Hela cells were grown in 2 mL Dulbecco's Modified Eagle Medium (DMEM) with 10% fetal bovine serum (FBS, supplied by Sigma-Aldrich) and 1% penicillin-streptomycin (the cultural medium) in 3.5 cm glass-bottom petri dishes (supplied by Fluorodish, WPI) for 24 h at 37°C in an atmosphere of 5% CO_2. (Note in general cell experiments several dishes were cultured in the same conditions simultaneously; some dishes were used for the following particle experiments while others were used to determine cell density after incubation.) After 24 h, Hela cells adhered onto the glass bottom of the culture dishes so that the culture medium could be separated and discarded by pipetting. Subsequently, the adhered cells were rinsed with 2 mL DPBS twice. For cell number determination, cells were detached with 0.5 mL Trypsin-EDTA and resuspended in DPBS and transferred into a haemocytometer (a slide containing 10 chambers where each constitutes 160 grids with total volume of 1 μL; supplied by Immune Systems). Typically, 10^3 – 10^4 cells were used per dish in this work. The cells for particle experiments were then incubated with MSNs suspensions (200 μg/mL, in 0.5 mL PBS and 1.5 mL cultural medium) for the desired incubation

time. In the experiments which require chloroquine to release nanoparticles from the endocytic route, 0.5 mL of 200 μM chloroquine was added into the culture (see Chapter 5).

For confocal imaging, the medium containing nanoparticles were discarded after the incubation and the cells were rinsed with 2 mL DPBS twice (so that the fluorescent particles seen in the images are exclusively from the cell bodies). Subsequently, 2 mL of 4% paraformaldehyde was added into the dishes for cell fixation at room temperature for 20 min. The fixed cells were then labelled with fluorescent tags using the protocols stated above followed by mounting onto an A1 confocal microscope (Nikon) for cell imaging (see below). For cell death determination, after incubation, the cells were detached with Trypsin-EDTA and suspended in 100 μL of 1x annexin-binding buffer followed by the apoptotic stain protocols (PI and AnnV) stated above. The stained cell suspensions were subsequently transferred to a haemocytometer mounted onto A1 confocal microscope. Programmed cell death was then determined from the PI and AnnV staining ratio.

2.3.3 Confocal Microscopy

Cell fluorescent confocal images were obtained using a Nikon Eclipse Ti-E inverted microscope with an attached A1 confocal laser microscope system. The microscope was fitted with a Plan Fluor 10x objective, a S Fluor 20x objective and a Plan Apo 100x oil immersion objective. The system was equipped with a LU4 4-laser unit,

which provides four laser lines (with options of 400 - 405 nm, 457 - 514 nm, 561 nm and 639 nm). NIS-Elements AR 64bit 3.00 SP6 software was used to capture and manipulate images. On the software setting, the scan area and pinhole size were generally set as 512 x 512 and <60 μm, respectively. Practically, scan speed [typically <1/2 (frame/s)], laser power and image gain were tunable depending on the image quality. (Note laser power should be kept as low as possible to prevent the quenching of fluorescent labels and the potential cell death.) For imaging fixed adhered cell, the stained cells were immersed in DPBS and imaged with the 100x oil immersion objective using the 404 nm laser for Hoechst33342 stained nucleus, 488 nm for FITC tagged nanoparticles and LysoTracker Green stained endo/lysosomes, and 561 nm for rhodamine tagged nanoparticles and LysoTracker Red stained endo/lysosomes. The obtained images were then demonstrated as three individual channels or a merged image (see Chapters 5 and 6). For programmed cell death determination, the stained cell suspensions were loaded into a haemocytometer and imaged with 20x objective using the 561 nm laser to visualise PI stained dead cell nucleus and 404 nm for AnnV stained apoptotic cell membrane. The percentages of necrotic cells and apoptotic cells were then determined by counting PI-positive cells and AnnV-positive cells (see Chapter 6).

2.4 Particle Characterisation

All characterisation techniques and measurements were carried out on at least two different batches of nanoparticles of each sample type.

2.4.1 Physical Properties of Particles (Size, Morphology and Surface Charge)

The above nanoparticles (with concentration of 1 mg/mL) were characterised with dynamic light scattering (DLS)/ ζ-potential (Zetasizer Nano, Malvern Instruments) at 20°C to assess particle distribution and surface charge. DLS was recorded using a 532 nm laser with the light source detected at angle of 173^{o} in ultrapure water over 5 repetitions providing the hydrodynamic size (d_{hyd}) and polydispersity index (PDI). In combination with the evidence from Transmission Electron Microscopy (TEM; see below), nanoparticles in this work possessed d_{hyd} <200.0 nm with PDI <0.3, indicative of highly stable and monodisperse suspensions. ζ-potentials were assessed in ultrapure water and different pH buffers over 5 repetitions providing information about particle surface charge and colloidal stability [pH 3.0 and pH 4.1 in formate acid buffer; pH 5.5 in MES buffer; pH 7.1 in phosphate buffer; pH 8.5 in 2-amino-2-hydroxymethyl-propane-1.3-diol (tris base) buffer]. In addition, ζ-potential measurement was also employed to assess the success of the introduction of different surface functional groups on nanoparticles (see results chapters). TEM images were obtained at the Research Complex at Harwell, Oxford using a JEOL JEM-2100 LaB_6 microscope operated at 120 kV with a beam current of about 65 mA for particle size and morphology assessment. Samples for TEM were prepared by deposition and drying of

a drop of the nanoparticles dispersed in water (1 mg/mL) onto a formvar-coated 300-mesh copper grid. Diameters were measured using the ImageJ version 1.40 software; average values were calculated by counting a minimum of 100 particles. Nitrogen adsorption-desorption analyses (BET) were carried out on a CE Instruments Sorptomatic 1990 instrument in Department of Chemistry, Oxford for determining particle pore size distribution. Specifically, 100 mg of dried nanoparticle sample was degassed at 200°C for at least 12 h before running adsorption measurements and subsequently cooled by liquid nitrogen. Known amounts of nitrogen gas were then released into the sample holder followed by the adsorption of nitrogen onto the particle sample accompanying slowly decreased pressure. After the saturation pressure, the particle sample was removed from the nitrogen atmosphere and heated to cause the desorption of nitrogen. Thereafter, the PC automatically correlated this pressure change to surface area or pore size distribution.

2.4.2 Chemical Properties of Particles

Thermogravimetric analysis (TGA) measurements were performed to study the removal of surfactant CTAB using Netzsch TGA instrument in Department of Chemistry, Oxford. For the analysis, 20 mg of dried nanoparticle sample was placed in a ceramic specimen holder and the temperature was then increased at a rate of 5°C/min starting at room temperature to a maximum of 600 - 800°C under an inert argon atmosphere. Through monitoring the characteristic temperatures at which a functional groups are removed, the presence of a given functional group and its relative weight to

the particle sample was determined (see Chapter 3). IR spectra were recorded to determine the presence of functional groups on the FTS-6000 Fourier Transform IR spectrometer built by Bio-Rad in Department of Chemistry, Oxford (see Chapter 6). Specifically, prior to sample analysis, a DuraSamplIR diamond ATR (Attenuated Total Reflection) accessory (used to analyse nanoparticle samples) was installed and purged with liquid nitrogen for several hours for the removal of moisture. After this, a background scan was carried out before the sample analysis. Subsequently, 2 mg of solid nanoparticle sample was placed on the diamond detector and mechanically pressed into contact with the crystal to achieve optical contact followed by a spectrum scan ranging 800 - 4000 cm^{-1}.

2.4.3 Relaxivity Assessment

Samples for MRI measurements were prepared by dispersing a known amount of nanoparticles or Gd^{3+}-complex into ultrapure water in a 2 mL eppendorf tube. Several different concentrations were prepared and measured for each sample. T_1 relaxivity values were calculated from curves plotted of $1/T_1$ (s^{-1}) vs. [Gd] concentration (mM; analysis of gadolinium concentration was carried out using ICP-MS and samples were measured by $LiBO_2$ fusion by Viridian Partnership, Surrey) and analysis of the slope of the line of best fit for each sample, with error measured from the average of a minimum of 2 measurements for each concentration point. The water ^1H longitudinal relaxation rates of these aqueous samples were measured at 20°C at 300 MHz (7 T) using a Varian Inova (Varian Inc., Palo Alto, CA) and 128 MHz (3 T) using a Siemens

Verio (Siemens AG, Munich, Germany) (see Chapter 3 and 4). Prior to T_1 measurement, FID shim was performed to obtain spectrum with <60Hz line width. After this, a 90^o pulse calibration was carried out with RF (radio frequency) pulse set between 10 and 900 MHz and power set at 60 dB. During the calibration, the repetition time (TR) was adjusted (typically started with 500 ms) until the 90^o pulse width closed to 250 μs. For the measurement of the relaxation rates, the standard inversion-recovery method was employed with a typical 90^o pulse calibration of 250 μs. To derive a proper T_1 value, a TR array was set (typically this should be at least 3 times of the expected T_1 value) and the resulting signal of each inversion time (ti) was fitted based on exponential growth. T_1-weighted phantom images were captured on aqueous samples with [Gd] concentrations of 0.04 mM using TR = 30 ms; TE = 5 ms; a slice thickness of 2 mm and a matrix of 256 x 256.

2.5 References

1. K. Moller, J. Kobler and T. Bein, *Advanced Functional Materials*, 2007, **17**, 605-612.
2. J. J. Davis, W. Y. Huang and G. L. Davies, *Journal of Materials Chemistry*, 2012, **22**, 22848-22850.
3. J. Kecht, A. Schlossbauer and T. Bein, *Chemistry of Materials*, 2008, **20**, 7207-7214.
4. Z. Luo, K. Y. Cai, Y. Hu, L. Zhao, P. Liu, L. Duan and W. H. Yang, *Angewandte Chemie-International Edition*, 2011, **50**, 640-643.
5. W. Stöber, A. Fink and E. Bohn, *Journal of Colloid and Interface Science*, 1968, **26**, 62-69.
6. C. H. Lee, S. H. Cheng, I. P. Huang, J. S. Souris, C. S. Yang, C. Y. Mou and L. W. Lo, *Angewandte Chemie-International Edition*, 2010, **49**, 8214-8219.

Chapter 3 Synthesis of Mesoporous Silica Nanoparticles and Location-tuned MRI Contrast

3.1 Introduction

The preparation of mesoporous materials is well-documented in the literature, with silica being formed in the micro- and nano-size particle ranges by a variety of techniques, from classical aqueous and emulsion techniques to spray drying[1-4]. The most popular synthetic route involves a surfactant templation in an aqueous solution based on Stöber method[3-5]. In this approach, a porous network within the silica particle matrix will be obtained after removing the templating surfactant. Fine-tuning the reaction conditions allows particle morphology and pore size to be controlled[4, 6, 7].

Depending on the desired application, the outer surface of nanoparticles or the internal surface of mesopores may need to be modified. Modification generally can be achieved by two different approaches; *in situ* co-condensation, where functionalisation is carried out during the synthesis of the particles[4, 8]; and post-grafting, where modification is performed after particle formation[8, 9]. Importantly, the latter produces particles with preferentially external modifications, whereas the former has better control over the location of functionalities depending on their concentrations and the duration of co-condensation[8, 10] (Fig. 3.3). Indeed, a means to control loading and selective functionalisation of internal and external surfaces was first described by

Cauda *et al*.[8, 10] In their work, different silanised functional groups were added sequentially during the co-condensation reaction. Depending on the addition time, functional groups can be localised at different depths along the pore channels of mesoporous silica nanoparticles (MSNs). The introduction of each functional group after certain time intervals (time delay) allowed the complete reaction of the previous functional group, a technique referred to as 'delayed' co-condensation. This method has been adapted herein for the preparation of location-tuned Gd-loaded MSNs.

The traditional applications of mesoporous silica materials mainly occupy the fields of catalytic chemistry[11], analytic chemistry[12] and purification[13, 14]. Recently, the lack of toxicity and biocompatibility has made these silica materials ideal candidates for biomedical applications, focussing on utilising MSNs' porosity and extraordinarily high surface to volume ratio[15-18]. From a therapeutic perspective, MSNs have also been investigated for drug delivery[16, 19-26]; further, diagnostic studies have attempted to integrate multiple imaging agents on their high surface area for multimodal imaging[27, 28].

Proton magnetic resonance imaging (MRI) provides imaging information by mapping the spatial distribution of ^{1}H signal intensity with high resolution[29, 30]. There exist a number of studies focussed on increasing the signal intensity, *i.e.* contrast, including advancing the hardware employed and introducing a contrast enhancing agent[27, 30, 31]. Contrast agents enhance the image quality by reducing T_1 or T_2 relaxation times of the

surrounding water; their effectiveness in doing this can be represented in a quantitative way, as relaxivity[29, 30] (normally in the unit of $mM^{-1}s^{-1}$). This work has focused on the effect of using Gd^{3+} based agents on protic T_1 relaxation. Prediction of suitability of a material as a contrast agent is best described by S.B.M. theory[31-33] (see Chapter 1). In this, the inner-sphere relaxation of a contrast agent is correlated to the number of water molecules (q) coordinated to the agent and a variety of correlation times (τ_c), including rotational correlation time (τ_R), electronic relaxation time (T_e) and water residence time (τ_M), associated with motion of the agent; the outer-sphere relaxation is governed by diffusional correlation time (τ_D, correlated to the diffusion of bulk water near the Gd^{3+}-centre)[30, 32, 33]. Notably, in inner-sphere relaxation scheme, the relaxation enhancement approaches a maximum as the inverse of the correlation time, $1/\tau_c$, approaches the Larmor precession frequency, ω_H (see Eq. 2 in Chapter 1). In addition, previous reports generally acknowledged that at common clinical field strength (1.5 T and 3T, ~64 MHz and 128 MHz proton frequency, respectively), the dominant correlation time is almost always rotational[34], i.e. when $1/\tau_R$ (tumbling rate) of a contrast agent approaches the ω_H at these fields, the effectiveness of contrast enhancement (relaxivity) of this agent will be the greatest. Importantly, for a simple monomeric gadolinium complex, its molecular motion under these fields is too fast to result in an efficient resonance and relaxation [τ_R is in the order of 0.1 ns (~10^4 MHz)] leading to the limitation of contrast enhancement (typical molecular agents have relaxivities ranging ~2 – 4 $mM^{-1}s^{-1}$ that are relatively insensitive to field strengths; see Chapter 1)[28, 33]. Slowing down the rotation of these gadolinium complexes is thus potentially

beneficial to the increase in relaxation/relaxivity. Some prior works have, accordingly, attempted to achieve this by conjugating Gd^{3+}-complexes on silica nanoparticles[27, 35, 36].

There are several methods of loading Gd^{3+}-chelates onto MSNs, including layer-by-layer incorporation and direct coupling of the agent using silane chemistry. The layer-by-layer coating technique employs the assembly of oppositely charged ions through electrostatic interactions[37]; however, the leakage of the attracted Gd^{3+}-complexes over time is a major concern in this approach. Covalent loading provides a reliable and convenient method of producing Gd^{3+} loaded contrast agents. To date, the most popular approach to covalently introduce Gd^{3+} is post-grafting of Gd^{3+}-chelates onto nanoparticles[9, 36, 38, 39]. In this way, Gd-DTTA, for example, have been loaded onto MSNs with high percentages of Gd^{3+} chelates (15 – 20 wt% loading) yielding high T_1 relaxivity (28.8 $mM^{-1}s^{-1}$ at 3 T and 10.2 $mM^{-1}s^{-1}$ at 9.4 T)[36]. Gd-DOTA has also been conjugated to MSNs and assessed at lower fields resulting in 26.6 $mM^{-1}s^{-1}$ at 0.47 T[38] (Note that the fields investigated in the literature is rather diverse leading to the difficulty in direct comparison; generally, a contrast agent demonstrates greater relaxivity number at lower field; see Chapter 1). Importantly, the majority of these works uses very high loading of Gd^{3+} which is a potential toxicity concern[40-42]. In addition, as high loadings (>40 wt% by post-grafting, for example) can cause a reduction in pore size leading to inhibition of water access to the internalised Gd^{3+}, the active number of paramagnetic centres decreases[39]. Indeed, it has been reported that

increasing the amount of Gd^{3+}-complex on a per particle basis does not necessarily increase the relaxivity values of the composites, as the inner Gd^{3+} centres are not as readily accessible to surrounding water molecules[9, 39]. Underpinning this restricted water access to inner Gd^{3+}-centres and the limited relaxivity enhancement is the use of the post-grafting synthetic procedure, which preferentially functionalises outer surfaces of nanoparticles and thus eventually reduces porosity.

Although these works have demonstrated the advantage of increased rotational correlation time (reflected in the enhanced contrast), the relaxivities obtained from particles with comparable size at similar field strength have been inconsistent. For example, the relaxivities for non-porous silica nanoparticles (SNPs) and MSNs with similar size at 3 T have been reported to be 19.7 $mM^{-1}s^{-1}$ and 28.8 $mM^{-1}s^{-1}$ respectively in two separate works[35, 36] where these values are both assigned to the effect of increased rotational correlation time. This has clearly indicated that the size effect (and associated τ_R from inner-sphere relaxation) alone can not explain the difference in these two relaxivity values. The investigation in the (structural) cause of greater relaxivity in porous particles has been lacking in the literature. Indeed, when designing molecular agents, the importance of water exchange (τ_M) has been stressed, suggesting it may be accelerated by the increase of negative charge and steric congestion of the molecules[43, 44]. It will be postulated within this thesis that the facilitated water exchange may also exist in sterically crowded mesoporous structures. In addition, on the basis of altered water mobility in a confined nano-environment[45-47], the diffusion

correlation time (τ_D) within the outer-sphere relaxation scheme[41, 42] was also hypothesised to have further contribution to the observed relaxivity. Overall, it will be proposed within this chapter that the markedly enhanced relaxivity observed with MSNs contrast agents is the result of the beneficial effect of slow tumbling (τ_R) and rapid water exchange (τ_M) (both belonging to inner-sphere relaxation) in combination with slow water diffusion (τ_D) (related to outer-sphere relaxation).

Although Gd^{3+}-chelates have been covalently tethered to MSNs recently, high contrast relaxivities have only been possible at very high Gd^{3+} loading and no attempt has been made to tune Gd^{3+} location or optimise its interaction with water. Herein, a 'delayed' co-condensation technique was employed to counter the problem of potential pore blocking resulting from post-grafting as previously described. In doing this, an extremely high T_1 relaxivity was achieved by (structurally) controlling the location of Gd^{3+} in the nanoparticles on the basis of S.B.M.'s prediction rather than by chemical incorporation of high Gd^{3+} dosage as commonly employed in prior works (Fig. 3.3). The ^1H T_1 relaxivity of nanoparticles was measured at 7 T to elucidate the relaxation activity of internally and externally loaded contrast agents and to provide insight into the interaction of water molecules with these nanopore confined paramagnetic centres. The ^1H contrast of the MSNs was further tuned by varying the percentage loadings of the Gd^{3+}-centres.

3.2 Results and Discussion

3.2.1 Optimisation of Functionalised MSNs Preparation

MSNs were prepared using an aqueous Stöber technique of the hydrolysis and condensation of an ethoxysilane precursor under basic triethanol amine catalysis employing a surfactant Cetyltrimethylammonium bromide (CTAB) template that was subsequently removed to yield a porous network. Thermogravimetric analysis (TGA) shown in Fig. 3.1 indicated some residual surfactant CTAB (<5%; the weight loss between 200°C and 300°C)[48]. A broad region of weight loss after 300°C is likely to be the result of dehydroxylation of silanol groups during the thermal treatment[49, 50].

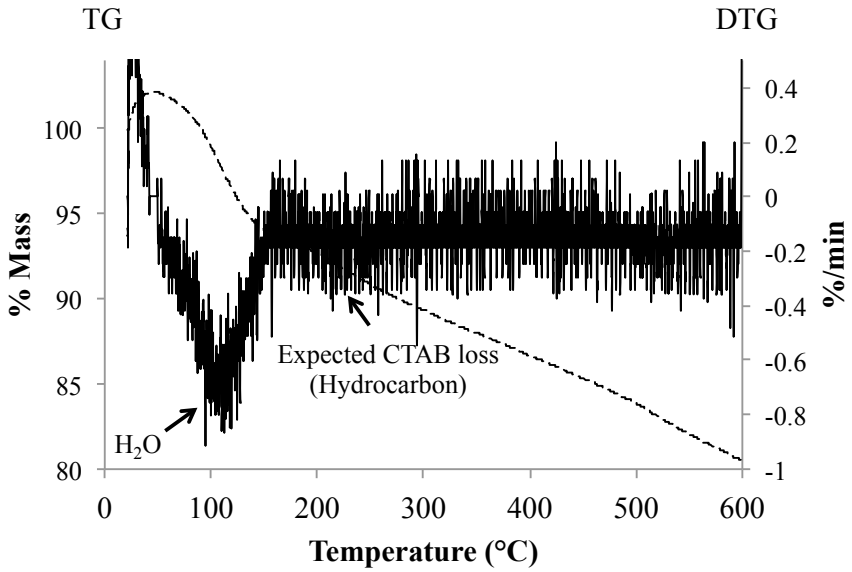


Fig. 3.1 Thermogravimetric (TG) and differential (DTG) curves for unfuntionalised MSNs after templating CTAB removal. A weight loss at 100°C indicates the removal of moisture. The weight loss (<5%) due to some residual CTAB was seen between 200°C and 300°C. A broad region of weight loss after 300°C is likely to be the result of dehydroxylation of silanol groups during the thermal treatment.

Initially, experiments carried out in which all reaction ingredients were mixed simultaneously at room temperature, including the silanol source, tetraethylorthosilicate (TEOS), resulting in suspensions with some sedimentation. Subsequent heating at 80°C for 2 h resulted in a large degree of particle aggregation as confirmed by DLS (d_{hyd}: 1364.0 nm, PDI: 0.38). A similar result has been observed by Bein[3] and Amoros *et al*.[51] where resulting nanoparticles appeared as morphologically rough intergrown structures rather than discrete primary nanoparticles. Modifying the reaction conditions to carry out the addition of TEOS at 80°C led to a much more satisfactory preparation without agglomeration (d_{hyd}: 157.0 nm, PDI: 0.12; additionally confirmed by TEM shown Fig. 3.2). In order to prepare amine-functionalised nanoparticles for subsequent reactions, (3-aminopropyl)triethoxysilane (APTES) can be employed during the hydrolysis and condensation procedure. Notably, this protocol of silane addition can not be directly adapted to prepare aminated MSNs (i.e. partial TEOS substitution with APTES; co-condensation). The simultaneous addition of TEOS and APTES yielded very broad particle size distribution (PDI: 0.92) with d_{hyd} of 584.7 nm presumably due to the difference in electrostatic interaction with surfactant CTAB in basic condition and thus reactivity yielding heterogeneous reaction[4]. A 'delayed' co-condensation reaction was thus performed, involving a two-step reaction, where APTES was added after the initial condensation of TEOS, resulting in well dispersed aminated MSNs (d_{hyd}: 148.4 nm, PDI: 0.14 for 10 min-delay and d_{hyd}: 144.4 nm, PDI: 0.14 for 60 min-delay). (Note that the 'delay time' refers to the time interval between the addition of TEOS and the subsequent addition of APTES; 10 min-delay

and 60 min-delay denote 'short delay' and 'long delay' respectively throughout this chapter.)

3.2.2 Control of Amine and Gd^{3+}-chelate Location

The amine groups in aminated MSNs (and non-porous silica nanoparticles, SNPs) were used as anchor points for Gd^{3+}-complexes conjugation to generate nanoparticles with high MR image contrast. The influence of their locations on the properties of the final particles was examined. Initially, a control over the molar ratio of TEOS and APTES and the co-condensation duration (delay time) was investigated (and tracked through ζ-potential; Table 3.1). The silanol-rich surfaces of the particles were partially aminated by either co-condensing or post-grafting APTES onto their surfaces. Neither amination nor the route of amination affected the size, morphology or structure of the MSNs (see the TEM images of their resulting Gd^{3+}-doped particles shown in Fig. 3.2). Partial functionalisation of the negatively charged terminal silanol groups on the nanoparticles with positively charged amine groups was confirmed by the observation of a progressive increase in positive surface charge of the particles with increasing degree of amination (Table 3.1). (Note that mol% refers to the percentage mole ratio of APTES with respect to TEOS employed in the reaction.)

Table 3.1 Total amounts of APTES used in co-condensation and post-grafting amination experiments; delay time employed in the amination experiments; the ζ-potentials after amination (errors derived from the average of five repetitions); the resulting Gd^{3+}-complexes conjugated products, hydrodynamic size (d_{hyd}), polydispersity index (PDI) and their associated Gd^{3+} locations.

Samples	Mol% amination	Delay time (min)	ζ-potential in H_2O (mV)	Final products	d_{hyd} (nm) & PDI	Interpretation
plain-MSNs	-	-	-29.0 (± 0.5)	-		-
0.15 mol% NH_2-MSNs (long delay)	0.15	60	-26.3 (± 0.8)	1.37 wt%* Gd-DOTA MSNs (long delay)	138.9 (0.08)	Internally but pore-opening localised Gd^{3+}
10 mol% NH_2-MSNs (long delay)	10	60	-1.6 (± 0.5)	1.37 wt% Gd-DOTA MSNs (excess amine)	135.4 (0.06)	Externally localised Gd^{3+}
0.15 mol% NH_2-MSNs (short delay)	0.15	10	-28.1 (± 1.1)	1.37 wt% Gd-DOTA MSNs (short delay)	148.0 (0.17)	Deeply internalised Gd^{3+}
0.15 mol% NH_2-MSNs (post-grafting)	0.15	-	-22.0 (± 0.6)	1.37 wt% Gd-DOTA MSNs (post-grafting)	146.2 (0.13)	Externally localised Gd^{3+}
0.15 mol% NH_2-SNPs	0.15	-	-	1.37 wt% Gd-DOTA SNPs	115.5 (0.08)	Externally localised Gd^{3+}

*wt% refers to percentage weight ratio of final Gd^{3+} content with respect to MSNs.

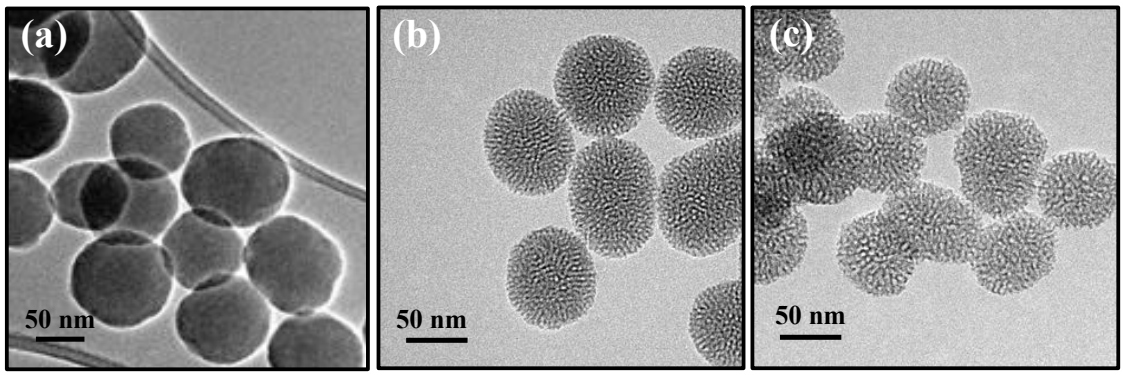


Fig. 3.2 Typical TEM images of (a) functionalised non-porous silica nanoparticles [1.37 wt% Gd-DOTA SNPs (80.9 ± 7.7 nm)]; (b) functionalised MSNs prepared by co-condensation [1.37 wt% Gd-DOTA (long delayed) (68.3 ± 7.2 nm)]; and (c) functionalised MSNs prepared by post-grafting [1.37 wt% Gd-DOTA MSNs (post-grafting) (64.3 ± 6.0 nm)]. [Note that pore size was controlled by surfactant chain length and was expected to be unchanged after such a low modification degree; Pore size distribution of MSNs was confirmed by nitrogen adsorption anaylsis (BET) to be 1.6 ± 0.7 nm in radius; see Appendix, Fig. A2].

The ζ-potential measurements provided not only information on the presence of amine groups but also insight into the location of functional groups. During the two-step condensation process (a total 2 h reaction), varying the delay time for the addition of APTES enables the location of amine groups to be controlled. Post-grafting was known to yield preferentially external amination [0.15 mol% NH_2-MSNs (post-grafting)] that would clearly result in progression in positive surface charge compared with unmodified plain-MSNs (Table 3.1; the difference in ζ-potential is ~7 mV after amination). It was expected that the same molar ratio of amine (0.15 mol%) introduced by co-condensation can only lead to a marginal increase in ζ-potential (<3 mV) due to internally localised functional groups [0.15 mol% NH_2-MSNs (long delay) and 0.15 mol% NH_2-MSNs (short delay)]. It should be noted that this is true on the basis of 100% amination yield [which is confirmed by the consistent concentrations of Gd^{3+}

theoretically calculated by the concentration of linker amines and those by ICP-MS elemental analysis (13982 ± 162 μg of Gd per g of MSNs; note that the error (~1%) associated with this is not translatable to MRI imaging contrast, the typical representation of relaxivity is thus not affiliated with error]. Therefore, this marginal increase in ζ-potential is not the result of lack of amination, but rather localisation, whereby internalised amines contribute less to the overall particle surface charge. The determination of the amine locations of the two particle types which were both prepared using co-condensation but with different delay times [0.15 mol% NH_2-MSNs (long delay) and 0.15 mol% NH_2-MSNs (short delay)], is more difficult to monitor by ζ-potential. However, the markedly different MR contrasts of their resulting Gd^{3+} incorporated products have facilitated the proposal of the location variation of functional groups (see next section). On the other hand, higher amination (10 mol%, long delay) drastically increased the corresponding ζ-potential resulting in highly external modification (see Table 3.1 and Fig. 3.3 schematic representation of amine location). Importantly, ζ-potential also reflects the particle colloidal stability, whereby the electrostatic repulsion makes charged particles much better dispersed in solutions. Indeed, all the aminated particles exhibit highly charged surfaces indicating their excellent colloidal stability with the exception of 10 mol% particles (~-2 mV only). This low surface charge and thus stability will additionally affect the following MR characteristics.

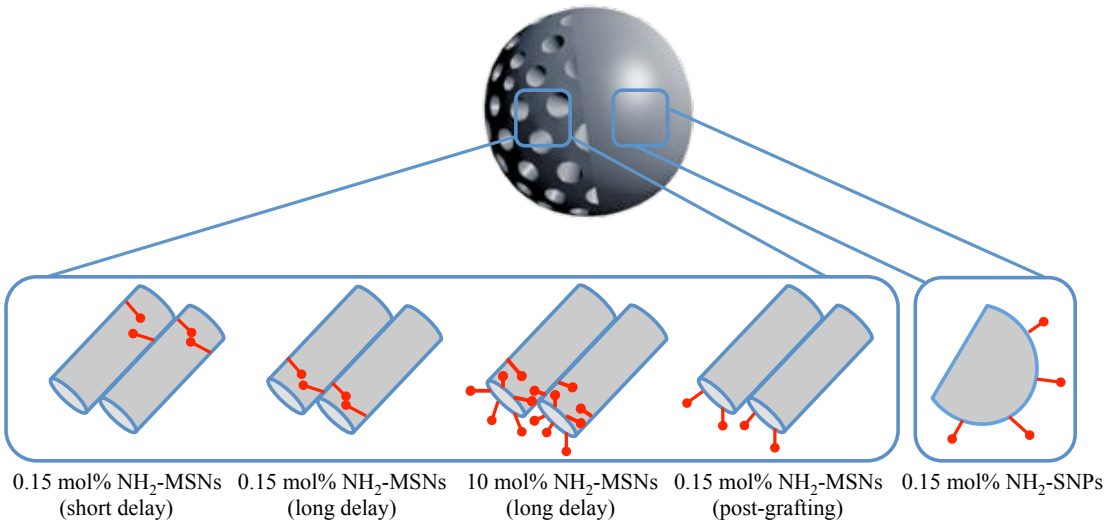


Fig. 3.3 Schematic representation of amine location (red rods represent amine groups). (Left to right): short delay co-condendation led to deeply internalised amination; long delay co-condensation resulted in internal amination but close to the pore opening; 10 mol% amination using long delay co-condensation produced both internal and external amination; and post-grafting technique yielded external functionalisation.

In summary, a careful control over APTES concentration and the delay time of co-condensation procedure have been confirmed to alter the location of linker amine groups by ζ-potential change (Table 3.1 and Fig. 3.3). This location control could subsequently be utilised in tuning Gd^{3+} location and particle MR characteristics (see the following discussion).

3.2.3 Relaxivity Assessments

3.2.3.1 Gd Stability

To confirm the suitability of Gd^{3+} doped MSNs for biological applications, the amount of free Gd^{3+} present in any dispersion of the nanoparticles should ideally be negligibly small by the end of the synthesis (due to the toxicity of the free ion to biological

tissues)[40-42]. The arsenazo test (see experimental section in Chapter 2) was carried out to detect free Gd^{3+}. Arsenazo III is a dye which forms a coloured complex with Gd^{3+} giving a characteristic absorption at 605 nm and 653 nm, while the free dye has a strong visible absorption at 548 nm. The relative intensity of the complexed dye peaks (605 nm and 653 nm) and free dye peak (548 nm) accordingly report on the presence and the absence of free Gd^{3+}.

The UV-vis spectra (Fig. 3.4) of two standard solutions, pure arsenazo III solution and arsenazo-Gd^{3+} complexed solution, were measured and compared with that of supernatant of Gd-DOTA MSNs and control colloidal solutions collected by centrifugation (all the solutions were prepared in ultrapure water). In order to confirm that the washing procedure was adequate for removal of free Gd^{3+}, a control solution was prepared by mixing $GdCl_3$ with aminated MSNs (the parent particles of Gd-DOTA MSNs) followed by washing using centrifugation and subsequent absorption testing. The absorption of the supernatant of Gd-DOTA MSNs solution (blue line, Day 1 in Fig. 3.4) and control solution showed similar spectra as the pure arsenazo solution. This indicated that there is no free Gd^{3+} capable of chelating with arsenazo in the solution. These analyses were repeated at 1 week, 2 weeks and 4 weeks showing there is no detectable level of Gd^{3+} leaking from the particles over at least a 4 week period (particles were stored in ethanol and re-dispersed in ultrapure water before analysis). Note that Fig. 3.4 was the representative result from 1.37 wt% Gd-DOTA MSNs (long delay) (optimised particles, see below) and their parent 0.15 mol% NH_2-MSNs (long

delay); other particle types were washed under the same protocol prior to the following MR assessments to ensure the signals are exclusively resulted from the chelated Gd^{3+} on nanoparticles.

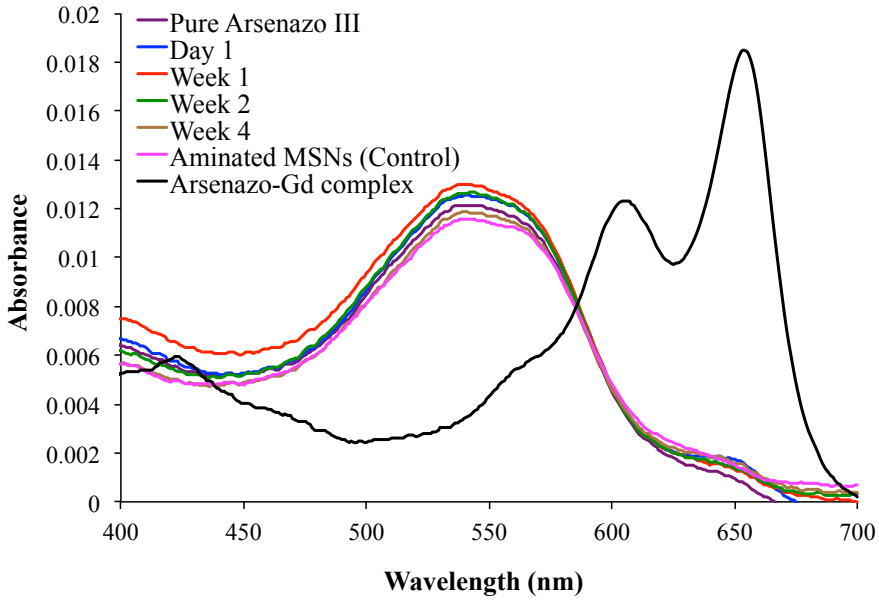


Fig. 3.4 UV-vis spectra of 10^{-6} M aqueous arsenazo (III) with washed Gd-DOTA MSNs and aminated MSNs supernatant solutions (Ultrapure water) and a $GdCl_3$ solution control. Gd-DOTA-MSNs demonstrated excellent stability and no leakage of Gd ions over a 4 week period.

3.2.3.2 Influence of Gd Location on Relaxivity

In order to prepare nanomaterials with ^1H T_1 MRI contrast, aminated MSNs synthesised using *in situ* co-condensation or post-grafting techniques were functionalised with DOTA-NHS ester using carbodiimide chemistry and finally metallated with Gd^{3+} ions to yield MSNs functionalised with Gd-DOTA chelates loaded on the internal or external surfaces (Fig. 3.5). All samples were prepared using the same percentage loading of Gd-DOTA complexes [1.37 wt% (percentage ratio of weight of Gd^{3+} content confirmed by ICP-MS with respect to the weight of MSNs);

Table 3.1]. The ^{1}H MRI relaxivity of these Gd-DOTA-loaded MSNs was calculated by observing the change in the relaxation rate ($1/T_1$, s^{-1}) of water protons per mM concentration of the contrast agent.

The longitudinal relaxivity measured at 7 T for samples of nanoparticles prepared using different loading techniques is presented in Fig. 3.5. The relaxivities of all loaded-nanoparticle samples was higher than for free Gd-DOTA complexes in solution (2.01 $mM^{-1}s^{-1}$). This is consistent with expectation of slower rotational correlation time (τ_R) of the chelate due to its association with large, slowly moving nanoparticles in suspension[30, 31, 35, 36]. Importantly, the Gd-DOTA MSNs prepared using the delayed co-condensation method with low amine content (17.14 $mM^{-1}s^{-1}$ and 33.57 $mM^{-1}s^{-1}$ for 'short' and 'long' delay reactions respectively), provided relaxivities significantly higher than those from post-grafted (10.77 $mM^{-1}s^{-1}$) MSNs and non-porous silica (SNPs, 9.56 $mM^{-1}s^{-1}$).

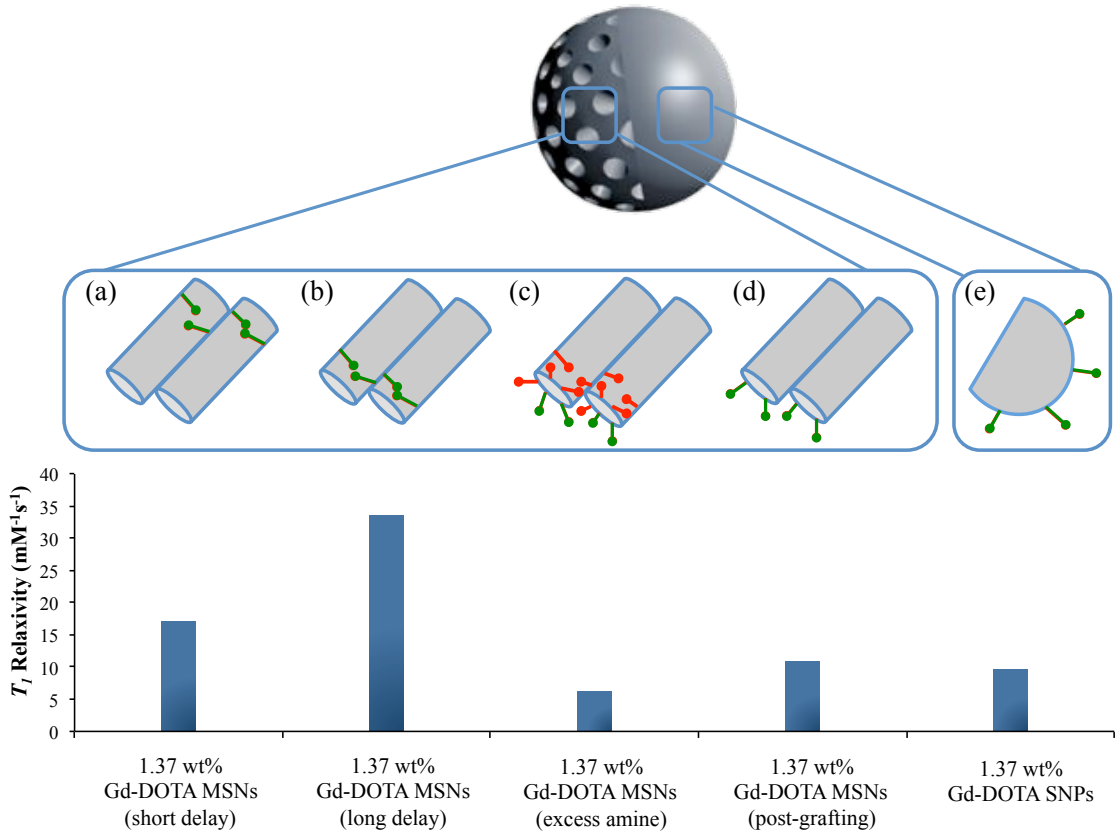


Fig. 3.5 Schematic representation of Gd-DOTA MSNs (where red rods represent the amine groups and green rods indicate the location of Gd-DOTA) prepared using (a) 'Short delay' co-condensation, where functionalities are internalized deeply in the structure (17.14 $mM^{-1}s^{-1}$); (b) 'long delay' co-condensation, where functionalities are internalised nearer to the porous openings (33.57 $mM^{-1}s^{-1}$); (c) 'long delay' co-condensation but with excess of amine, where functionalities are loaded preferentially on external surfaces (6.13 $mM^{-1}s^{-1}$); and (d) post-grafting, where functionalities are loaded on external surfaces (10.77 $mM^{-1}s^{-1}$). (d) Post-grafted Gd-DOTA-non-porous silica nanoparticles (9.56 $mM^{-1}s^{-1}$). The chart displays T_1 relaxivities of corresponding nanoparticle samples, measured at 7 T, 20°C over three repetitions.

It was postulated that the location of the paramagnetic contrast agents would have an effect on the resulting relaxivity and contrast of the nanoparticles, due to the accessibility of water molecules and their interactions with the Gd^{3+}-centres. To rationalise these variations in relaxivities, the difference in loading location based on the different preparative conditions is represented in the schematics in Fig. 3.5 (red

rods refer to the linker amines and green rods indicate the location of Gd-DOTA; also see Table 3.1). MSNs prepared using the post-grafting technique preferentially have external surface Gd^{3+} functionalisation as their linker amines are presented on the exterior of particles [Fig. 3.5 (d)]. Those prepared using the co-condensation technique have functionalisation on the internal or external surfaces of the particles depending on the delay time and the loading of amine linker (Table 3.1, Fig. 3.3 and Fig. 3.5). Preparation with 'excess' amine loading [10 mol%; note that Gd^{3+} concentration is only 0.15 mol% (= 1.37 wt%)] using 'long' delay resulted in highly external amination and thus external Gd^{3+} localisation only (as external amines are more accessible than the internal ones) [Fig. 3.5 (c)]. Importantly, at this point the Gd^{3+} locations of particles prepared employing 'short' or 'long' delay co-condensation in combination with 'low' amine loading (0.15 mol%) can not be determined yet. As it is known that the particle growth starts from the centre of a spherical nanoparticle, it was hypothesised that the 'short' delay led to deeply internalised Gd^{3+}-centres [Fig. 3.5 (a)] and 'long' delay yielded localisation closer to the pore openings [Fig. 3.5 (b)]. The subsequent MR characteristics perfectly fitted into this location assumption and followed the theoretical prediction of S.B.M. theory and confined water mobility.

To evaluate the influence of mesoporous structure on relaxivity, it is worth considering the behaviour of water in the pores and in bulk solvent. The diffusion of water molecules into porous silica structure have been studied both experimentally and theoretically[45-47, 52]. In these studies, water molecules confined in hydrophilic pore

walls has been determined to have a diffusion coefficient significantly smaller than that of the free bulk water. In addition, the diffusion coefficient of confined water decreases as the pore size reduces. Specifically, it can decrease by an order of magnitude in 4 nm pore from 3.3×10^{-9} m^2s^{-1} for bulk water to 2.3×10^{-10} m^2s^{-1} for confined water[53]. Such behaviour is mainly associated with the strong interaction of water molecules with hydroxyl groups on the pore surfaces resulting in a limitation of water mobility. From an MR perspective, this confined water diffusion and its relative motion to paramagnetic centres (diffusion correlation time, τ_D) are closely related to the outer-sphere relaxation of the latter (see above and Chapter 1)[52, 53]. Hence, the significantly higher relaxivity values observed for MSNs with Gd-DOTA housed inside their porous networks [(a) and (b) in Fig 3.5] was assigned to the contribution of enhanced diffusion correlation time (τ_D) resulting from water confined in the porous structures. In addition, confined water molecules surrounding the Gd^{3+}-complexes and exchangeable protons trapped on the particle silanol walls (presumably through hydrogen bonding) that are in the proximity of the complexes may have further contribution to inner-sphere relaxation by affecting water residence time (τ_M)[54, 55]. Overall, the beneficial effect of increased rotational correlation time (τ_R) by particle conjugation, accelerated water exchange (τ_M) and slower diffusion correlation time (τ_D) by water confinement all are responsible for the markedly high relaxivities of MSNs with internalised Gd^{3+}-centres [17.14 $mM^{-1}s^{-1}$ and 33.57 $mM^{-1}s^{-1}$ for 1.37 wt% Gd-DOTA MSNs (short delay) and 1.37 wt% Gd-DOTA MSNs (long delay) respectively; (a) and (b) in Fig 3.5]. Notably, the lower relaxivity of 'short delay' particles,

indicative of inefficient water exchange with the bulk solvent[39], reflected more deeply internalised contrast agent groups that is consistent with the location proposal stated above.

Non-porous SiO_2 nanoparticles post-grafted with Gd-DOTA that yields particles with external surface functionalisation only have provided further evidence in confirming the importance of porous structure in maximising relaxivity [Fig. 3.5 (e)]. The relaxivity value observed for non-porous nanoparticles (9.56 $mM^{-1}s^{-1}$) was similar to that of post-grafted Gd-DOTA MSNs (10.77 $mM^{-1}s^{-1}$) and 1.37 wt% Gd-DOTA MSNs (excess amine) (6.13 $mM^{-1}s^{-1}$) due to the dominant presence of externally localised Gd-DOTA limiting the interaction with water (and thus contrast enhancement). The somewhat reduced relaxation enhancement for 1.37 wt% Gd-DOTA MSNs (excess amine) was assigned to the slightly poorer colloidal stability of this highly aminated MSNs suspension (confirmed by a lack of surface charge, Table 3.1).

These results clearly demonstrate that the structural design of nanoparticles in exclusively confining Gd-DOTA inside the porous networks by tuning the preparative conditions allows the interaction of water with the paramagnetic complex in this restricted environment to be altered. This confinement results in the changes in correlation times associated with diffusion of bulk water (τ_D), lifetime of bound water (τ_M) and rotation of contrast particle (τ_R) in the critical relaxation processes. Strictly, for the optimised particles [1.37 wt% Gd-DOTA MSNs (long delay)], τ_R is increased

by particle conjugation and the enhanced τ_D and reduced τ_M result from water confinement in mesoporous structures.

3.2.3.3 Influence of Gd Loading on Relaxivity

To further investigate and optimise the relaxivity of MSNs by varying Gd^{3+} loading, the 'long' delay co-condensation technique was employed and samples with different loadings of Gd-DOTA on both internal and external surfaces were prepared. Electron microscopy confirmed the morphology of the nanoparticles with highly porous nature and narrow size distributions; no change in structure or morphology was observed after grafting of the Gd^{3+}-chelate onto the particle surface. The surface charges of the particles were negative, with the charges becoming slightly less negative (a contribution from the positively charged Gd^{3+} ions) with increasing loadings of Gd-DOTA chelates (-11 ± 1.1 mV, -11.4 ± 0.5 mV and -10.2 ± 0.4 mV for 1.37 wt%, 2.07 wt% and 3.82 wt% respectively).

The ^1H MRI relaxivity of the nanoparticles measured at 7 T are summarised in Fig. 3.6; all Gd-DOTA-loaded MSN samples demonstrated significant enhancements compared to free Gd-DOTA complexes in solution.

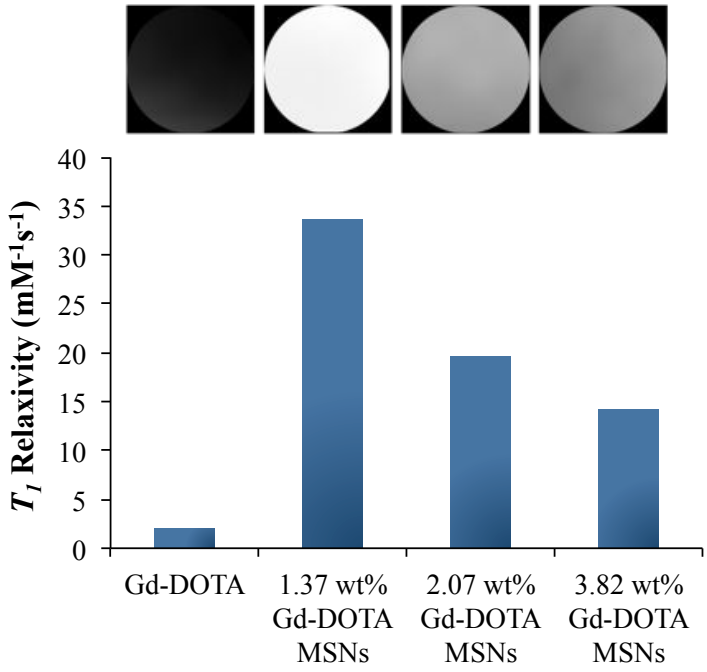


Fig. 3.6 Relaxivities of Gd-DOTA complex in solution (2.01 $mM^{-1}s^{-1}$) and Gd-DOTA-MSNs prepared with different percentage Gd loadings (1.37 wt% Gd: 33.57 $mM^{-1}s^{-1}$; 2.07 wt% Gd: 19.6 $mM^{-1}s^{-1}$; 3.82 wt% Gd: 14.22 $mM^{-1}s^{-1}$) measured at 7 T, 20°C (errors originated from three repetitions). Upper inset shows corresponding T_1-weighted phantom images of aqueous MSNs samples with [Gd^{3+}] 0.04 mM (TR = 30 ms; TE = 5 ms; slice thickness = 2 mm; matrix = 256 × 256).

Increasing the percentage loading of Gd^{3+} further, to 2.07 wt% and 3.82 wt%, yielded particles with lower r_1 relaxivity (19.6 $mM^{-1}s^{-1}$ and 14.22 $mM^{-1}s^{-1}$ respectively). This lessened contrast enhancement, despite increased concentrations of contrast agent, was assigned to the result of externally localised Gd^{3+}. As previously discussed, the use of the 'long' delay co-condensation method promotes loading of both the internal and external surfaces of the MSNs. As the concentration of the functionalities increased, the external modification is expected to increase, leading to more Gd-DOTA chelates residing on the external surfaces of the particles (where the advantages of water confinement are reduced). Phantom T_1-weighted MRI images shown in Fig. 3.6 clearly

demonstrated the difference in contrast obtained for MSNs with different loadings of Gd-DOTA chelates. In addition, relaxivity was also measured at clinically relevant field strengths (3 T) with the optimal Gd-DOTA MSNs (1.37 wt%, long delay) resulting in an significantly high value of 39.26 ± 1.29 $mM^{-1}s^{-1}$ (cf. highest literature value of 28.8 $mM^{-1}s^{-1}$ at 3 T[36]).

Therefore it is clear that through the ability to tune sub-particle location, water access, water mobility and rotational rigidity, it has been possible to prepare colloidal stable contrast agents with unprecedentedly high relaxivity and low Gd^{3+} loading at clinically relevant field strength.

3.3 Conclusions

The preparation of MSNs has been investigated and optimised herein demonstrating the addition of silanol sources including TEOS and APTES plays an important role in the quality of the resulting nanoparticles depending on the temperature and the delay co-condensation time. Confinement of Gd-DOTA contrast agents within the internal surfaces of mesoporous silica by tuning the preparative procedure yielded nanoparticulate contrast agents with extremely high T_1 MRI relaxation (33.57 $mM^{-1}s^{-1}$ for 'long' delay and 17.14 $mM^{-1}s^{-1}$ for 'short' delay at 7 T). These particles demonstrated a marked enhancement compared to free Gd-DOTA (2.01 $mM^{-1}s^{-1}$ at 7 T) and a three-fold enhancement over non-confined externally-loaded Gd-DOTA MSNs (10.77 $mM^{-1}s^{-1}$ at 7 T) and Gd-DOTA-loaded non-porous silica nanoparticles (9.56 $mM^{-1}s^{-1}$). This extraordinary improvement in T_1 contrast resulted from the tailoring of loading location of contrast agents and their interaction with water housed within a nanospace, leading to changes in the correlation times of the critical dynamic properties of molecules with the paramagnetic centres.

The results here also demonstrated that careful tuning of the percentage loading of the contrast agent can affect the resulting contrast enhancement and can yield nanoparticles with extremely high relaxivities at very low concentrations, 39.26 $mM^{-1}s^{-1}$ at 3 T and 33.57 $mM^{-1}s^{-1}$ at 7 T for MSNs loaded with 1.37 wt% Gd^{3+}. These nanoparticles provided relaxivity values which were markedly higher than those of previously reported MSNs-based contrast agents, at Gd^{3+} loadings which were

significantly lower. The use of lower loadings of contrast agents is an important consideration in biomedical applications, where there are concerns over the toxicity of free Gd^{3+} ions. Due to their size, colloidal stability and surface properties, these MSNs, despite their very low percentages of Gd^{3+} loading with just 87 μmol/g MSNs, provide impressive MRI relaxation enhancement and excellent potential for a variety of biological applications.

3.4 References

1. Y. S. Lin, K. R. Hurley and C. L. Haynes, *Journal of Physical Chemistry Letters*, 2012, **3**, 364-374.
2. M. Grun, I. Lauer and K. K. Unger, *Advanced Materials*, 1997, **9**, 254-257.
3. K. Moller, J. Kobler and T. Bein, *Advanced Functional Materials*, 2007, **17**, 605-612.
4. S. Huh, J. W. Wiench, J. C. Yoo, M. Pruski and V. S. Y. Lin, *Chemistry of Materials*, 2003, **15**, 4247-4256.
5. W. Stöber, A. Fink and E. Bohn, *Journal of Colloid and Interface Science*, 1968, **26**, 62-69.
6. K. Yano and Y. Fukushima, *Journal of Materials Chemistry*, 2003, **13**, 2577-2581.
7. Z. A. Qiao, L. Zhang, M. Y. Guo, Y. L. Liu and Q. S. Huo, *Chemistry of Materials*, 2009, **21**, 3823-3829.
8. J. Kecht, A. Schlossbauer and T. Bein, *Chemistry of Materials*, 2008, **20**, 7207-7214.
9. F. Carniato, L. Tei, A. Arrais, L. Marchese and M. Botta, *Chemistry – A European Journal*, 2013, **19**, 1421-1428.
10. V. Cauda, A. Schlossbauer, J. Kecht, A. Zurner and T. Bein, *Journal of the American Chemical Society*, 2009, **131**, 11361-11370.
11. A. T. Dickschat, F. Behrends, M. Bühner, J. Ren, M. Weiß, H. Eckert and A. Studer, *Chemistry – A European Journal*, 2012, **18**, 16689-16697.
12. J. Y. Lei, L. Z. Wang and J. L. Zhang, *Chemical Communications*, 2010, **46**, 8445-8447.
13. G. J. D. Soler-illia, C. Sanchez, B. Lebeau and J. Patarin, *Chemical Reviews*, 2002, **102**, 4093-4138.
14. K. K. Unger, D. Kumar, M. Grun, G. Buchel, S. Ludtke, T. Adam, K. Schumacher and S. Renker, *Journal of Chromatography A*, 2000, **892**, 47-55.
15. T. H. Chung, S. H. Wu, M. Yao, C. W. Lu, Y. S. Lin, Y. Hung, C. Y. Mou, Y. C. Chen and D. M. Huang, *Biomaterials*, 2007, **28**, 2959-2966.
16. C. Y. Lai, B. G. Trewyn, D. M. Jeftinija, K. Jeftinija, S. Xu, S. Jeftinija and V. S. Y. Lin, *Journal of the American Chemical Society*, 2003, **125**, 4451-4459.
17. I. Slowing, B. G. Trewyn and V. S. Lin, *Journal of the American Chemical Society*, 2006, **128**, 14792-14793.
18. I. I. Slowing, J. L. Vivero-Escoto, C. W. Wu and V. S. Y. Lin, *Advanced Drug Delivery Reviews*, 2008, **60**, 1278-1288.
19. E. Climent, A. Bernardos, R. Martinez-Manez, A. Maquieira, M. D. Marcos, N. Pastor-Navarro, R. Puchades, F. Sancenon, J. Soto and P. Amoros, *Journal of the American Chemical Society*, 2009, **131**, 14075-14080.
20. E. Climent, R. Martinez-Manez, F. Sancenon, M. D. Marcos, J. Soto, A. Maquieira and P. Amoros, *Angewandte Chemie-International Edition*, 2010, **49**, 7281-7283.

21. V. C. Ozalp and T. Schafer, *Chemistry-a European Journal*, 2011, **17**, 9893-9896.
22. A. Schlossbauer, J. Kecht and T. Bein, *Angewandte Chemie-International Edition*, 2009, **48**, 3092-3095.
23. A. Schlossbauer, S. Warncke, P. M. E. Gramlich, J. Kecht, A. Manetto, T. Carell and T. Bein, *Angewandte Chemie-International Edition*, 2010, **49**, 4734-4737.
24. N. Singh, A. Karambelkar, L. Gu, K. Lin, J. S. Miller, C. S. Chen, M. J. Sailor and S. N. Bhatia, *Journal of the American Chemical Society*, 2011, **133**, 19582-19585.
25. J. L. Vivero-Escoto, I. I. Slowing, C. W. Wu and V. S. Y. Lin, *Journal of the American Chemical Society*, 2009, **131**, 3462-3463.
26. Z. Luo, K. Y. Cai, Y. Hu, L. Zhao, P. Liu, L. Duan and W. H. Yang, *Angewandte Chemie-International Edition*, 2011, **50**, 640-643.
27. W. Y. Huang and J. J. Davis, *Dalton Transactions*, 2011, **40**, 6087-6103.
28. S. Santra, R. P. Bagwe, D. Dutta, J. T. Stanley, G. A. Walter, W. Tan, B. M. Moudgil and R. A. Mericle, *Advanced Materials*, 2005, **17**, 2165-2169.
29. R. A. Dwek, *Nuclear magnetic resonance (N.M.R.) in biochemistry : applications to enzyme systems*, Clarendon Press, Oxford, 1973.
30. P. Caravan, J. J. Ellison, T. J. McMurry and R. B. Lauffer, *Chem Rev*, 1999, **99**, 2293-2352.
31. P. Caravan, *Chemical Society Reviews*, 2006, **35**, 512-523.
32. I. Solomon, *Physical Review*, 1955, **99**, 559-565.
33. N. Bloembergen, E. M. Purcell and R. V. Pound, *Physical Review*, 1948, **73**, 679-712.
34. P. Caravan, C. T. Farrar, L. Frullano and R. Uppal, *Contrast Media & Molecular Imaging*, 2009, **4**, 89-100.
35. W. J. Rieter, J. S. Kim, K. M. L. Taylor, H. Y. An, W. L. Lin, T. Tarrant and W. B. Lin, *Angewandte Chemie-International Edition*, 2007, **46**, 3680-3682.
36. K. M. L. Taylor, J. S. Kim, W. J. Rieter, H. An, W. L. Lin and W. B. Lin, *Journal of the American Chemical Society*, 2008, **130**, 2154-2155.
37. J. S. Kim, W. J. Rieter, K. M. L. Taylor, H. An, W. L. Lin and W. B. Lin, *Journal of the American Chemical Society*, 2007, **129**, 8962-8963.
38. F. Carniato, L. Tei, M. Cossi, L. Marchese and M. Botta, *Chemistry-a European Journal*, 2010, **16**, 10727-10734.
39. F. Carniato, L. Tei, W. Dastru, L. Marchese and M. Botta, *Chemical Communications*, 2009, 1246-1248.
40. A. M. Hofer, *Journal of Cell Science*, 2005, **118**, 855-862.
41. C. Lin, T. Kadono, K. Yoshizuka, T. Furuichi and T. Kawano, *Zeitschrift Fur Naturforschung C-a Journal of Biosciences*, 2006, **61**, 74-80.
42. A. N. Oksendal and P. A. Hals, *Journal of Magnetic Resonance Imaging*, 1993, **3**, 157-165.
43. S. Laurent, L. V. Elst, F. Botteman and R. N. Muller, *European Journal of Inorganic Chemistry*, 2008, 4369-4379.

44. P. Lebduskova, P. Hermann, L. Helm, E. Toth, J. Kotek, K. Binnemans, J. Rudovsky, I. Lukes and A. E. Merbach, *Dalton Transactions*, 2007, 493-501.
45. S. Takahara, N. Sumiyama, S. Kittaka, T. Yamaguchi and M. C. Bellissent-Funel, *Journal of Physical Chemistry B*, 2005, **109**, 11231-11239.
46. K. Shirono and H. Daiguji, *Journal of Physical Chemistry C*, 2007, **111**, 7938-7946.
47. P. H. Fries and E. Belorizky, *Journal of Chemical Physics*, 2010, **133**.
48. N. S. Singh, H. Kulkarni, L. Pradhan and D. Bahadur, *Nanotechnology*, 2013, **24**.
49. L. T. Zhuravlev, *Colloids and Surfaces a-Physicochemical and Engineering Aspects*, 2000, **173**, 1-38.
50. S. Guggenheim, Y. H. Chang and A. F. K. Vangroos, *American Mineralogist*, 1987, **72**, 537-550.
51. J. El Haskouri, D. O. de Zarate, C. Guillem, J. Latorre, M. Caldes, A. Beltran, D. Beltran, A. B. Descalzo, G. Rodriguez-Lopez, R. Martinez-Manez, M. D. Marcos and P. Amoros, *Chemical Communications*, 2002, 330-331.
52. J. S. Ananta, B. Godin, R. Sethi, L. Moriggi, X. W. Liu, R. E. Serda, R. Krishnamurthy, R. Muthupillai, R. D. Bolskar, L. Helm, M. Ferrari, L. J. Wilson and P. Decuzzi, *Nature Nanotechnology*, 2010, **5**, 815-821.
53. R. Sethi, J. S. Ananta, C. Karmonik, M. Zhong, S. H. Fung, X. W. Liu, K. Li, M. Ferrari, L. J. Wilson and P. Decuzzi, *Contrast Media & Molecular Imaging*, 2012, **7**, 501-508.
54. S. Aime, M. Botta, S. G. Crich, G. B. Giovenzana, R. Pagliarin, M. Piccinini, M. Sisti and E. Terreno, *Journal of Biological Inorganic Chemistry*, 1997, **2**, 470-479.
55. S. Aime, L. Frullano and S. G. Crich, *Angewandte Chemie-International Edition*, 2002, **41**, 1017-1019.

Chapter 4 Biological T_1 Contrast Gating

4.1 Introduction

Recently, much effort has been made towards the development of non-invasive diagnostic imaging techniques, specifically for the early detection of a pathological event for effective therapeutic intervention. The introduction of imaging probes to produce a signal is essential to some available modalities such as nuclear and optical techniques. Such nuclear and optical probes are particularly useful for the utility in molecular imaging, due to their low background signals resulting from the lack of naturally existent probes in living tissues[1]. Conventional MRI, on the other hand, differentiates healthy and abnormal tissues by the signal variations from water protons in tissues. Although the application of an imaging agent, such as clinically approved Gd-DTPA and Gd-DOTA can enhance image contrast, the background signal is still relatively high due to the low effectiveness of these imaging agents (in terms of relaxivity) and the lack of target specificity[1]. In order to improve image quality of MRI and to provide information at the cellular or molecular level, the development of better imaging agents has been the central focus of this field[1, 2]. The strategies of relaxivity enhancement introduced in Chapter 3 are among the most widely used approaches[3-6]. However, it should be noted that these can only passively and non-specifically enhance signal. The more appreciable approach to specifically enhance image contrast is those in combination with an improvement in target specificity and will be discussed in this

chapter.

Active targeting involves the use of biomarkers such as antibodies or small peptides to encourage site-specific binding[7-9]. Initial efforts to create targeted contrast agents for MRI involved direct conjugation of a clinically approved molecular contrast agent onto an antibody. Bioconjugation effectively takes not only the advantages afforded by increased molecular bulk (longer rotational correlation time, as discussed in Chapter 3) but also those engendered by natural biological targeting[7]. A range of DOTA and DTPA derivatives have, for example, been bound to peptides, monoclonal antibodies or proteins capable of targeting specific cell receptors[10-12]. Lauffer *et al*. have reported a protocol for the reaction of DTPA-dianhydride with a variety of proteins where an enhancement in MR contrast is observed[11]. However, in terms of practical application this method is still limited by relatively low sensitivity of MRI and low concentration of most cellular receptors/targets[2]. More recent studies have focused on increasing local concentration of contrast agents (to counter the low inherent MRI sensitivity) by conjugating multiple Gd^{3+}-complexes on a single antibody or targeting moiety[7-9]. For example, Artemov *et al.* have developed Gd-based avidin/biotin system for MR molecular imaging of HER-2/neu receptors (overexpressed in breast cancer)[7]. In this work, the extracellular domain of HER-2/neu-overexpressing breast cancers was pre-labeled with biotinylated HER-2/neu antibody. An avidin with ~13 Gd-DTPA conjugated can thus actively target to this biotinylated antibody which defines the location of HER-2/neu receptors.

In addition, owing to their high surface areas (offering the ability to support a great number of paramagnetic centres) and their longer rotational correlation times (resulting from larger sizes compared to molecular imaging agents), particulate contrast agents have become powerful tools that can induce a large change in contrast upon binding to targets by increasing the local concentration of contrast agents[13-15]. Perfluorocarbon nanoparticles, for example, formulated with greater than 50000 gadolinium-containing molecules and targeting moieties in their outer layers have been used for *in vivo* imaging of angiogenic regions in tumors and in vessels with early-stage atherosclerosis[16, 17]. Silica nanoparticles with concentrated Gd^{3+}-complexes tethered to their surfaces have also been conjugated with RGD peptides[18]. These peptide-conjugated nanoparticles demonstrated a high affinity to their targeted $\alpha_v\beta_3$ integrin overexpressed cancer cells. The development of targeting agents (both molecular and particulate) to date relies on high local concentration of paramagnetic centres to overcome the low sensitivity of MRI, but leads to potential concerns about toxic Gd^{3+} leakage. It is clear that there remains appreciable room for further improvement. In addition, although these prior works have married the advantageous features of biological targeting and non-invasive MRI, no prior work has addressed the influence of targeting agents (proteins) steric bulk on contrast enhancement.

The initial motivation in this chapter thus was to employ the previously developed MSNs based contrast agent with low Gd^{3+} loading (Chapter 3) in the development of targeting MR agents by external conjugation with vectoring proteins. Significantly,

since the diffusive access of water through particle nanopores to internalised magnetic elements is both theoretically expected and experimentally confirmed, an ability to cap the particle apertures with vectoring proteins whilst maintaining facile water access was investigated (Fig. 4.1). Once this had been understood, both the response of this external protein to its binding partners and the potential utility in gating contrast was to be investigated (Fig. 4.1).

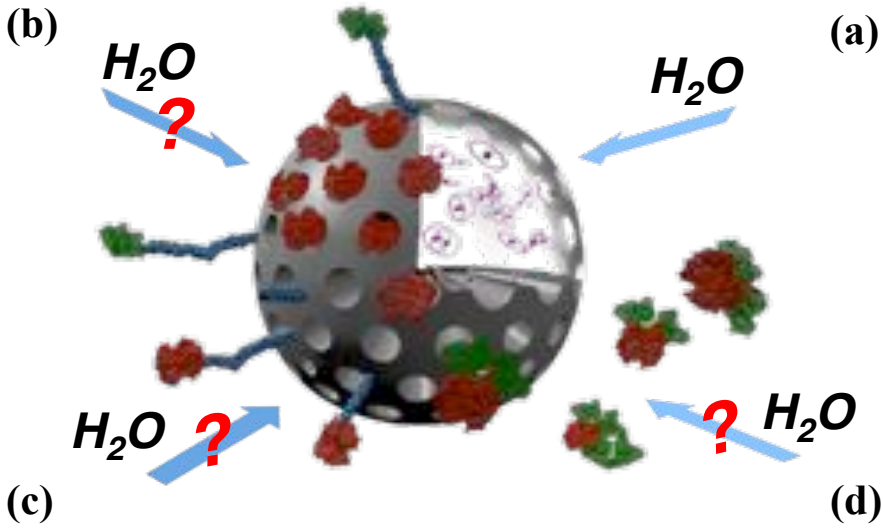


Fig. 4.1 Schematic concepts investigated herein. (a) Internalised Gd^{3+}-complexes within unmodified MSNs enjoy excellent water access and impressive relaxivity (noted in Chapter 3); (b, c) MSNs with biomolecules attached w/o PEG spacers on the surfaces towards the understanding of bioconjugation's influence on water accessibility and the subsequent relaxivity; and (d) the consequence on 'switchable' MRI contrast after the removal of surface proteins by the competition of higher affinity partner proteins or by the external redox-stimuli.

4.2 Results and Discussion

4.2.1 Particle Preparation and Biomodification

As previously described in Chapter 3 a 'delayed' co-condensation procedure was capable of tuning the location of covalently bound Gd-DOTA and its resulting T_1 relaxivity[19, 20], this methodology was employed herein to generate bio-vectored imaging agents with markedly high relaxivities and, importantly, internalisation of the Gd^{3+}-chelate species within the pores of the nanoconstruct. The bioconjugation of outer surfaces of nanoparticles was conducted *via* a stepwise post-grafting procedure employing silanol chemistry (to attach linker groups on the particle surface, amine or carboxylate) and subsequent carbodiimide conjugation chemistry (to conjugate biotin and proteins). The successful modification of the particles and the presence of vectoring proteins were confirmed by changes in ζ-potentials (see Table 4.1) and microarray spotting (Fig. 4.3). The native silica nanoparticles, due to the exposed acid silanol groups, bear negative charges (Table 4.1). Modification with amine terminated molecules [APTES, amino polyethylene glycol (PEG) and cystamine] due to the basic nature of NH_2 in water leads to an increase in surface charges; acidic carboxyl groups (succinic anhydride) results in charge changes in an opposite direction. Due to the isoelectric point (pI) of protein bovine serum albumin (BSA) and streptavidin (STV) being pH 4.7[21] and pH 6.3[22], respectively, the presence of these proteins on the nanoparticles was also successfully confirmed by the increase in negative ζ-potentials (Table 4.1 and also see experimental section in Chapter 2). Importantly, these modifications were associated with negligible perturbation of particle

stability/dispersion or size as confirmed by dynamic light scattering (DLS) determined polydispersity indices (PDI) <0.3[23] (Table 4.1).

Table 4.1 ζ-potential summary monitored stepwise through nanoparticle surface coupling reactions (see reaction procedures and schemes in Chapter 2). Hydrodynamic size (d_{hyd}) and polydispersity index (PDI) of the final resulting particles are also indicated. (Errors derived from the average of five repetitions).

BSA-MSNs reaction steps d_{hyd} (PDI) = 128.9 (0.09) (nm)	ζ-potentials (mV) in H_2O
Gd-DOTA MSNs	-24.9 (± 0.2)
Amination	0.9 (± 0.3)
Carboxylation	-21.2 (± 1.2)
BSA conjugation	-41.0 (± 0.6)

BSA-PEG2000-MSNs reaction steps d_{hyd} (PDI) = 135.6 (0.07) (nm)	ζ-potentials (mV) in H_2O
Gd-DOTA MSNs	-27.0 (± 1.5)
Amination	-25.7 (± 1.3)
Carboxylation	-28.2 (± 1.7)
Pegylation	-26.5 (± 1.2)
BSA conjugation	-38.6 (± 2.1)

BSA-PEG5000-MSNs reaction steps d_{hyd} (PDI) = 140.9 (0.08) (nm)	ζ-potentials (mV) in H_2O
Gd-DOTA MSNs	-24.9 (± 0.2)
Pegylation	-20.5 (± 0.3)
BSA conjugation	-34.5 (± 1.2)

Strep5-PEG2000-MSNs reaction steps d_{hyd} (PDI) = 138.2 (0.10) (nm)	ζ-potentials (mV) in H_2O
Gd-DOTA MSNs	-27.0 (± 1.5)
Amination	-25.7 (± 1.3)
Carboxylation	-28.2 (± 1.7)
Pegylation	-26.5 (± 1.2)
Strep5 conjugation	-34.0 (± 0.8)

STV-SS-MSNs reaction steps d_{hyd} (PDI) = 142.2 (0.11) (nm)	ζ-potentials (mV) in H_2O
Gd-DOTA MSNs	-30.7 (± 0.5)
Amination	-29.3 (± 0.7)
Cystamine conjugation	-36.5 (± 0.5)
STV conjugation	-40.4 (± 0.9)

STV-MSNs reaction steps d_{hyd} (PDI) = 144.3 (0.17) (nm)	ζ-potentials (mV) in H_2O
Gd-DOTA MSNs	-30.7 (± 0.5)
Amination	-27.1 (± 1.0)
Biotinylation	-25.6 (± 1.2)
STV conjugation	-38.1 (± 2.5)

Notably, the dispersity of STV conjugated MSNs through non-covalent biotin linkers depended on the ratio of particle surface biotin and STV. Excessive particle biotinylation (biotin:STV = 100:1) was observed to cause particle aggregation due to the multivalent nature of STV (d_{hyd}: 3440.0 nm, PDI: 0.47; also see below). To minimise this aggregation, the biotin concentration was reduced to a ratio of 1:20 (biotin:STV), which equates to 0.04 wt% (mass equivalent with respect to MSNs mass) and confirmed to be monodisperse (d_{hyd}: 144.3 nm, PDI: 0.17). Fig. 4.2 show

typical electron micrographs of protein modified MSNs that further confirmed the particles' monodispersed sizes.

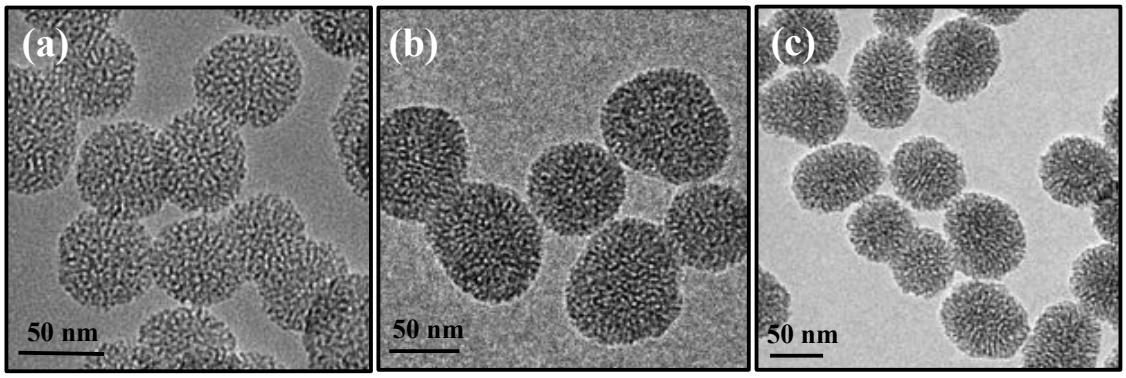


Fig. 4.2 Typical TEM images of protein conjugated MSNs with (a) short APTES linker; (b) PEG linker and (c) biotin linker.

4.2.2 Bio-vectoring Assessments

Three different vectoring proteins were investigated in this chapter – biotinylated BSA (that for simplicity will from now on only be referred to as BSA), synthetic Strep5 aptamer and STV (streptavidin). The high affinity of biotin to STV results from the tetrameric nature of the latter that allows it to bind with four biotins through a cooperative binding mechanism with extremely high stability and low dissociation constant (K_d) in the order of 10^{-14} M[24-26]. Strep5 aptamer has been developed to target the protein STV with K_d of ~3×10^{-7} M[27].

As well as the use of ζ-potential to determine modification, the success of protein conjugation to the nanoparticles was also validated by the retention of its vectoring capability. The effectiveness of protein modification in mediating clean particle

vectoring to target proteins was analysed in a microarray format on amine modified glass slides (Fig. 4.3).

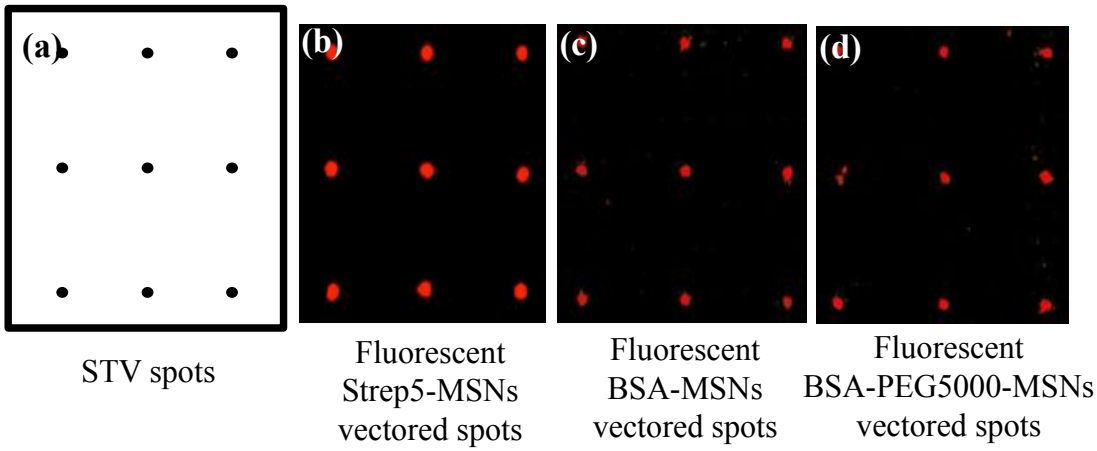


Fig. 4.3 (a) Schematic representation of ordered STV arrays; microarray images of (b) vectored fluorescent Strep5-MSNs to STV spots; (c) BSA-MSNs vectored spots; and (d) BSA-PEG5000-MSNs vectored spots. The clean ordered fluorescent spots after nanoparticle targeting clearly indicated vectoring nanoparticles to a target protein is possible with the appendage of its partner proteins.

Fig. 4.3 (a) shows the printed non-fluorescent STV spots on an aminated glass slide which will become fluorescent after incubation and successful targeting by luminescent vectoring nanoparticles [Fig 4.3 (b, c, d)]. In order to minimise non-specific surface association, the STV slides were blocked with native BSA and intensively washed before reading. The fluorescent Strep5 and BSA modified nanoparticles with Gd-DOTA covalently loaded inside the porous network [Strep5-MSNs and BSA-MSNs derivatised from the optimised 'long delay' nanoparticles in Chapter 3; Fig. 4.3 (b, c)] were targeted on the STV spots to examine the affinity of these nanoparticles toward STV. The fluorescence array was also recorded with BSA conjugated MSNs separated by a PEG linker [BSA-PEG5000-MSNs, Fig. 4.3 (d)]

showing specific binding to the spots. These results clearly indicated that vectoring proteins have been successfully tethered onto nanoparticles with retention of their targeting capabilities.

4.2.3 Relaxivity Assessments

The above results have demonstrated high contrast Gd^{3+}-complexes loaded MSNs can be reliably vectored to a specific protein by bioconjugation with its partner protein. The relaxivity change (if any) of nanoparticles after this bioconjugation was examined to determine the effect of these biomaterials on the outer particle surfaces. The T_1 relaxivity (at 7 T) of parent MSNs with Gd-DOTA covalently localised inside the porous structures in this chapter was determined to be 22.25 $mM^{-1}s^{-1}$ (with $[Gd^{3+}]$ analysised using ICP-MS to be 8070 ± 250 μg of Gd per g of MSNs). These Gd-DOTA complexes enjoy the beneficial MR enhancing effects resulting from their localisation inside the porous network [see schematics in Fig. 4.1 (a)] as discussed in the previous chapter and demonstrated a ten-fold and a three-fold relaxation enhancement compared with molecular Gd-DOTA and Gd-DOTA loaded non-porous silica nanoparticles (Gd-DOTA SNPs) respectively (Fig. 4.4). The corresponding MR images of particle aqueous solutions were also acquired, demonstrating Gd-DOTA MSNs contrast enhancement has been successfully achieved [Fig. 4.4 (b)].

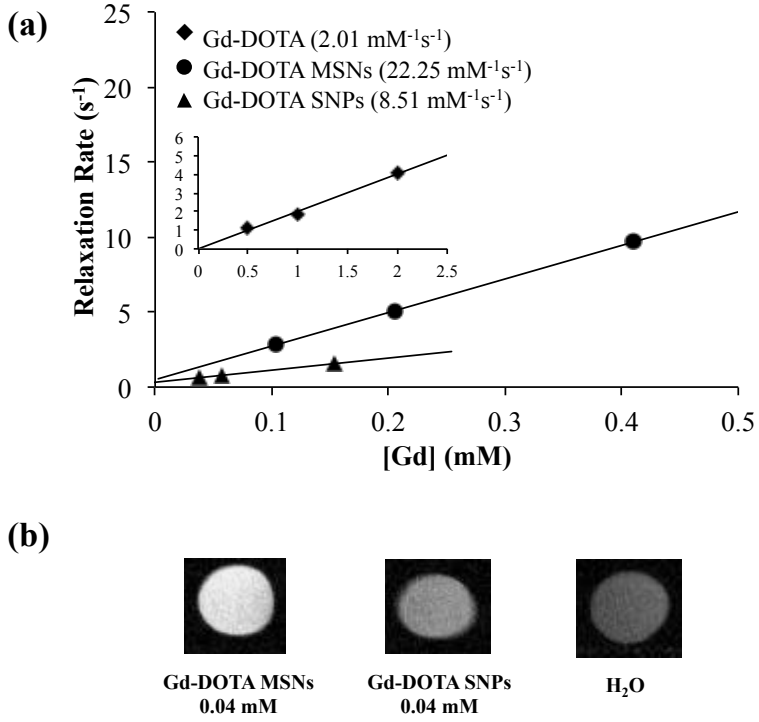


Fig. 4.4 (a) Plots of relaxation rate ($1/T_1$) (s^{-1}) versus concentration (mM) measured at 7 T magnetic field and 20°C. A linear fit of the data points yielded relaxivity, shown in brackets; (b) MR images of Gd-DOTA MSNs, Gd-DOTA SNPs and H_2O taken with an inversion recovery Spin-Echo with repetition time (TR) set to 9000ms (~3x longest T_1 value) and 1 s inversion recovery times (Acquisition number = 1).

In seeking to analyse the effects of biomodification on the particle MR contrast characteristics one may, in the first instance, consider the effects of suface biomodification on particle rotational correlation time according to $\tau_c = \frac{4\pi\eta r^3}{3kT}(s)$

where τ_c: rotational correlation time, r: radius, η: viscosity of solvent, 8.94×10^{-4} kg•m^{-1}s^{-1} (H_2O at 298K), k: 1.38×10^{-23} kg•m^{2}s^{-2}K^{-1}, T: 298K[3]. The surface modification of these particles with ~ 6 nm biomolecules (BSA, 66000Da)[28] is, thus, expected to change τ_c from ~3 x 10^4 ns to 9 x 10^4 ns. This is, of course, a negligible (and experimentally undetectable) change. Significantly, however, the direct anchoring of

BSA through a 'short' APTES linker [BSA-MSNs; see schematics in Fig. 4.5] generated a 78.8% drop in relaxivity compared to the native Gd-DOTA MSNs (Fig. 4.5). In considering that rapid water exchange is important in yielding high MR contrast[3] (Chapter 3). The particle pore size of native Gd-DOTA MSNs has been determined from gas adsorption measurement (BET) to be 1.6 ± 0.7 nm in radius (see Appendix Fig. A2 for pore size distribution graph). Coating these nanoparticles with ~6 nm BSA through a 'short' APTES linker (i.e. protein is close to the particle surface), of course, would easily block this small pore size. The relaxivity reduction is thus likely to be the result of the steric capping of particle pores leading to heavily restricted diffusional water access to internalised Gd^{3+}-centres. To confirm this theory of hindered water accessibility, two approaches were investigated; namely PEG spacing and the chemical/biological removal of protein.

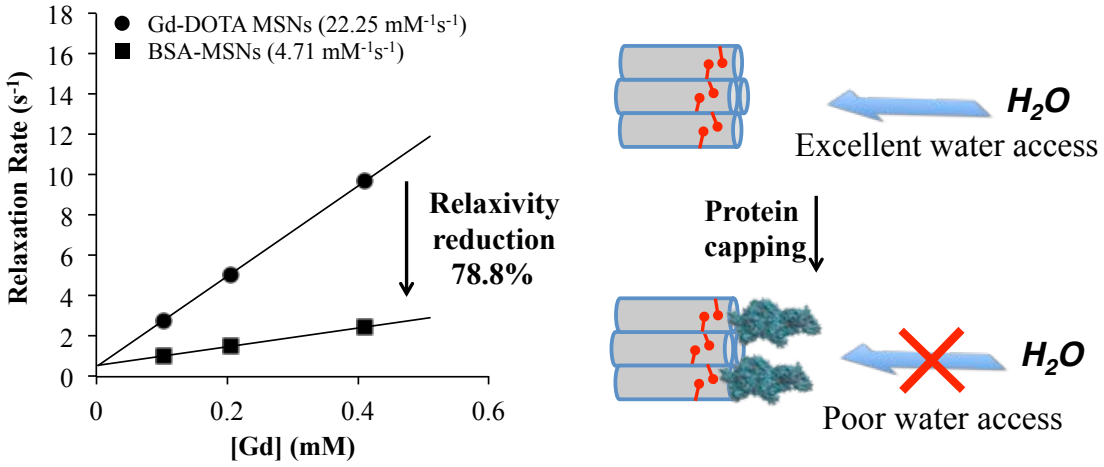


Fig. 4.5 Plots of relaxation rate ($1/T_1$) (s^{-1}) versus concentration (mM) measured at 7 T magnetic field and 20°C. The numbers in the brackets are the corresponding relaxivity values, obtained from a linear fit of the data points. Direct anchoring of BSA *via* a short APTES linker leads to a dramatic reduction in relaxivity (4.71 $mM^{-1}s^{-1}$; 78.8% of original value). The schematics on the right represents that protein capping through a short linker results in restricted water access and thus lower relaxivity.

4.2.3.1 PEG Tuned Relaxivity

Influence of Linker Length on Relaxivity

In order to examine the protein blocking hypothesis whilst retaining both stability and biological vectoring capability, PEG chains of different lengths (PEG2000 and PEG5000 with average molecular weights of 2000 and 5000 g mol^{-1}, respectively) were introduced as spacers between the particle surface and BSA (Fig. 4.6 and Fig. 4.7). Both the DLS particle size distribution noted above and the microarray spotting images (Fig. 4.3) clearly indicated that bioconjugation through a PEG linker affects neither particle colloidal stability nor successful protein vectoring. An initial assessment confirmed that the PEG modification alone (whether using PEG5000 or PEG2000) has negligible effect on relaxivity (<3% relaxivity change, cf. ~78% change for BSA-MSNs with respect to native Gd-DOTA MSNs) as shown in Fig. 4.6 with relaxivity of 22.50 $mM^{-1}s^{-1}$ and 21.50 $mM^{-1}s^{-1}$ for PEG5000-MSNs and PEG2000-MSNs, respectively (native parent Gd-DOTA MSNs have relaxivity of 22.25 $mM^{-1}s^{-1}$).

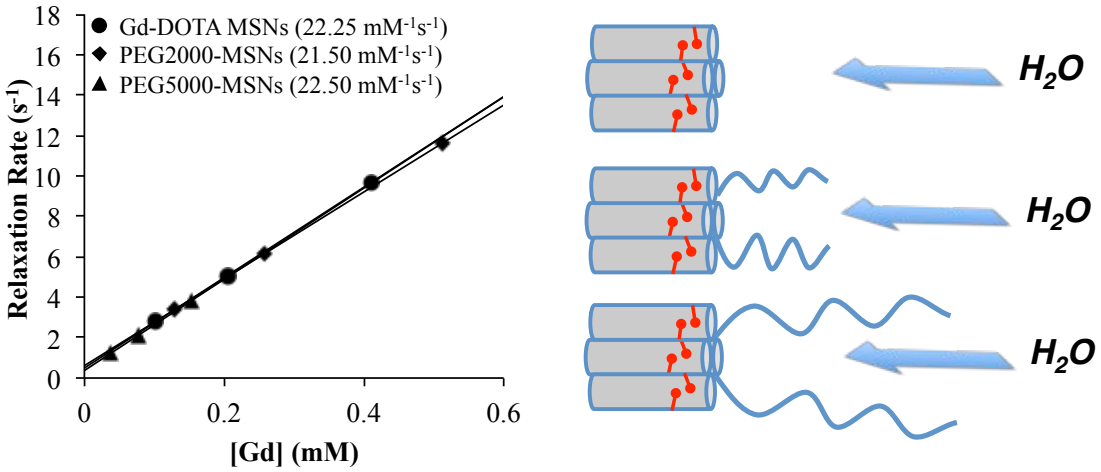


Fig. 4.6 Plots of relaxation rate ($1/T_1$) (s^{-1}) versus concentration (mM) measured at 7 T magnetic field and 20°C. The numbers in the brackets are the corresponding relaxivity values, calculated from a linear plot of the data points. Relaxivity assessments showing that the introduction of PEG alone has negligible effect on particle relaxivity. The schematics on the right represents that water access is not hindered by PEG modification.

Upon insertion of a PEG5000 spacer between the particle and protein, the high relaxivity was retained (Fig. 4.7; BSA-PEG5000-MSNs; 17.34 $mM^{-1}s^{-1}$, 77.9% of the value obtained for non protein capped particles). This ~80% relaxivity recovery is fully consistent with the assumption that in keeping BSA protein away from particle pore opening, the internalised Gd^{3+}-centres would continue to enjoy facile water access and efficient relaxation enhancement (Fig. 4.7). Notably, the ~20% relaxivity decrease observed is assigned to the physisorption of non-covalently conjugated BSA to non-sterically protected areas of the particle surface during the biomodification steps. The use of a shorter PEG2000 spacer leads to a reduced retention of relaxivity (BSA-PEG2000-MSNs; 14.90 $mM^{-1}s^{-1}$, 67.0% of native value), an observation reflective of its lower efficiency at reliably keeping the protein coating away from the particle pores (Fig. 4.7).

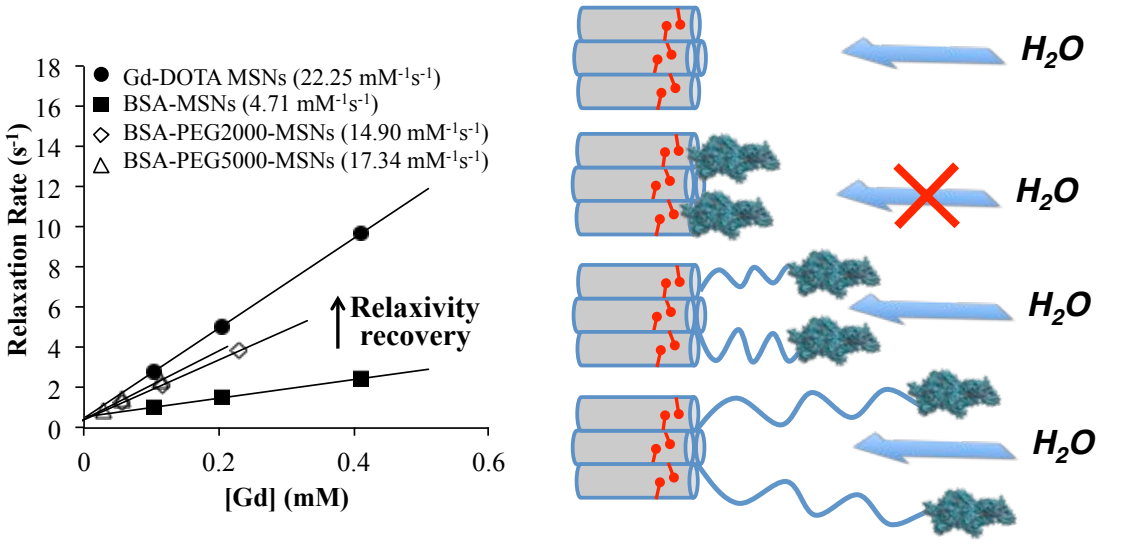


Fig. 4.7 Plots of relaxation rate ($1/T_1$) (s^{-1}) versus concentration (mM) measured at 7 T magnetic field and 20°C. The numbers in the brackets are the corresponding relaxivity values, calculated from a linear plot of the data points. Relaxivity assessment of BSA modified MSNs with PEG5000 and PEG2000 as spacers. PEGs were confirmed to be able to keep proteins away from particle surface and high relaxivity retained (14.90 $mM^{-1}s^{-1}$ for PEG2000 and 17.34 $mM^{-1}s^{-1}$ for PEG5000). The schematics on the right represents that water access is tunable by varying linker length.

Influence of Protein Size on Relaxivity

In order to demonstrate the general applicability of high contrast targeted MRI imaging, the investigation of other proteins with different sizes was carried out. To study the pore blocking and the resulting reduced water access of a smaller protein, vectoring Strep5 aptamer (25418Da) was conjugated onto nanoparticles through short APTES and PEG2000 linkers. On the basis of protein size being proportional to its molecular weights[29], the size of Strep5 is approximately 2 nm [calculated by correlating to the size and molecular weight of BSA (66000Da and 6 nm)]. Accordingly, it is clearly smaller than the nanoparticle pore size (~3.2 nm in diameter). Microarray results (Fig. 4.3) demonstrated that, Strep5 was successfully conjugated on

the particle periphery and retained its vectoring capability towards STV. Significantly, both Strep5 conjugated particles (linked through either APTES or PEG2000) demonstrated decreases in relaxivity [Fig. 4.8; 5.91 $mM^{-1}s^{-1}$ and 4.74 $mM^{-1}s^{-1}$, respectively; a four-fold lower than the value of the native Gd-DOTA MSNs].

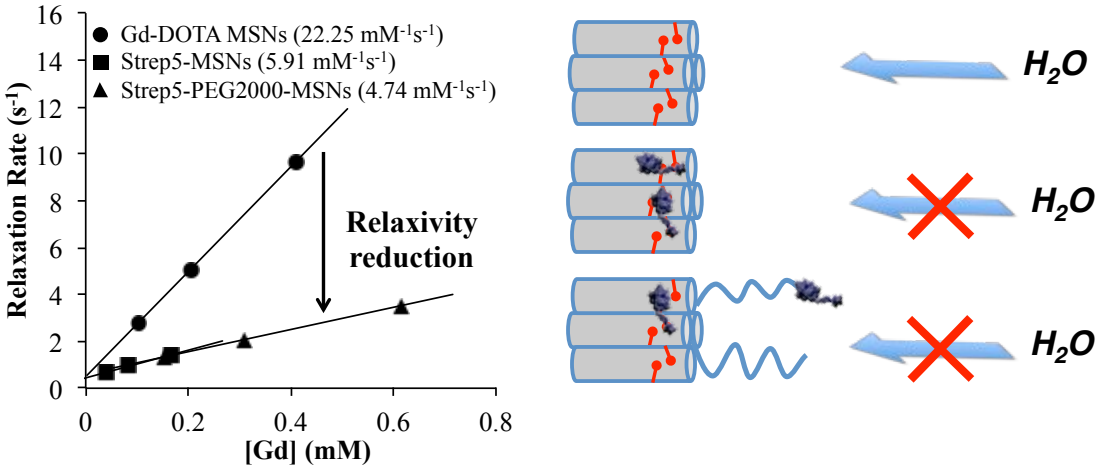


Fig. 4.8 Plots of relaxation rate ($1/T_1$) (s^{-1}) versus concentration (mM) measured at 7 T magnetic field and 20°C. The numbers in the brackets are the corresponding relaxivity values, calculated from a linear plot of the data points. Data shown indicates Strep5 was small enough to be immobilized in the porous network during the bioconjugation steps and low pegylated layer was thus incapable of keeping small protein from diffusing into the pores. The schematics on the right represents that small proteins are immobilised inside the porous network through physisorption and restricted water access.

Indeed, this was an expectable observation that the larger pores are permeable to the smaller Strep5[30] leading to their uncontrollable physisorption inside the porous walls during the bioconjugation steps and the eventual restriction in water access (resulting in low relaxivity). It should be emphasised here that even the low pegylation does not provide sufficient protection to prevent Strep5 from partially diffusing into the pores (It is known that for a 90 nm nanoparticle, a minimum density of PEG coating with a molecular weight >1000 to effectively prevent protein physisorption onto

nanoparticles is >1 PEG/nm^2; cf. the density employed in this work is <1 PEG per 20000 nm^2 of particle surface[31]). To confirm this reduced relaxivity resulted from ~2 nm of Strep5 immobilised inside the porous network, two control experiments were carried out. Gd-DOTA MSNs suspensions were stirred with Strep5 (control I) or BSA (control II) aqueous solution overnight followed by intensive washing by centrifugation and redispersion in water and their relaxivities monitored (Fig. 4.9). Particles stirred with Strep5 (~2 nm) showed significant reduction in relaxivity compared to the parent particles, whereas those stirred in the presence of larger BSA (~6 nm) only resulted in a slight decrease in relaxivity (due to some surface physisorption). These relaxivity results were fully consistent with the permeability of pores to smaller Strep5 resulting in a pore blocking effect and hence lower relaxivity.

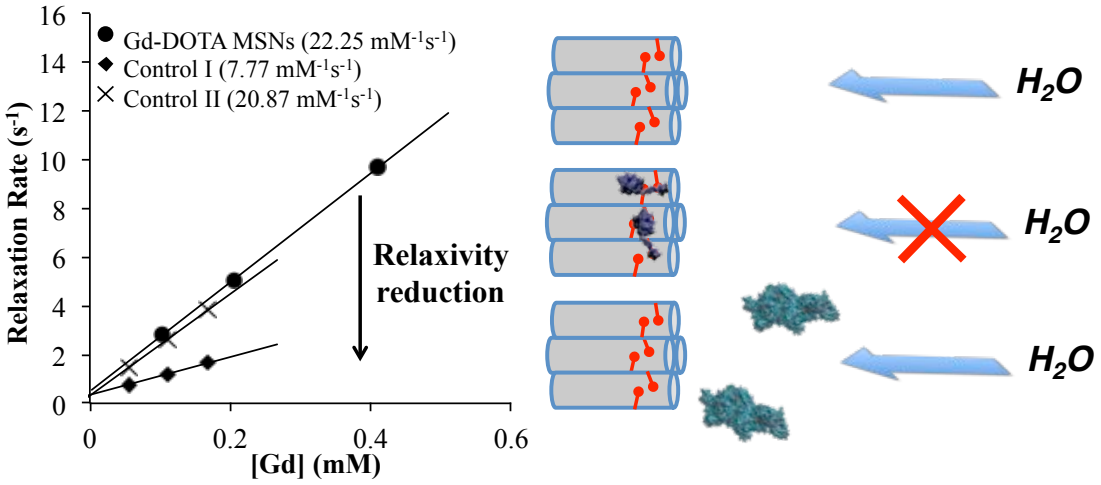


Fig. 4.9 Plots of relaxation rate ($1/T_1$) (s^{-1}) versus concentration (mM) measured at 7 T magnetic field and 20°C. The numbers in the brackets are the corresponding relaxivity values, calculated from a linear plot of the data points. Control I and II are the results from Strep5 and BSA, respectively showing smaller Strep5 resulted in a significant reduction in relaxivity, presumably due to their immobilised inside the pores, whereas BSA with size larger than pores is unable to access into the pores.

In summary, conjugation of a vectoring protein directly anchored onto native Gd-DOTA MSNs possessing markedly high relaxivity *via* a short linker demonstrated a significant detrimental effect on relaxivity. In the case of proteins larger than pores, this can be avoided by inserting long PEG spacers between nanoparticles and proteins to improve diffusional water access to the internalised Gd^{3+}-centres. Importantly, the degree of relaxivity retention is proportional to the length of PEG linker (Fig. 4.10).

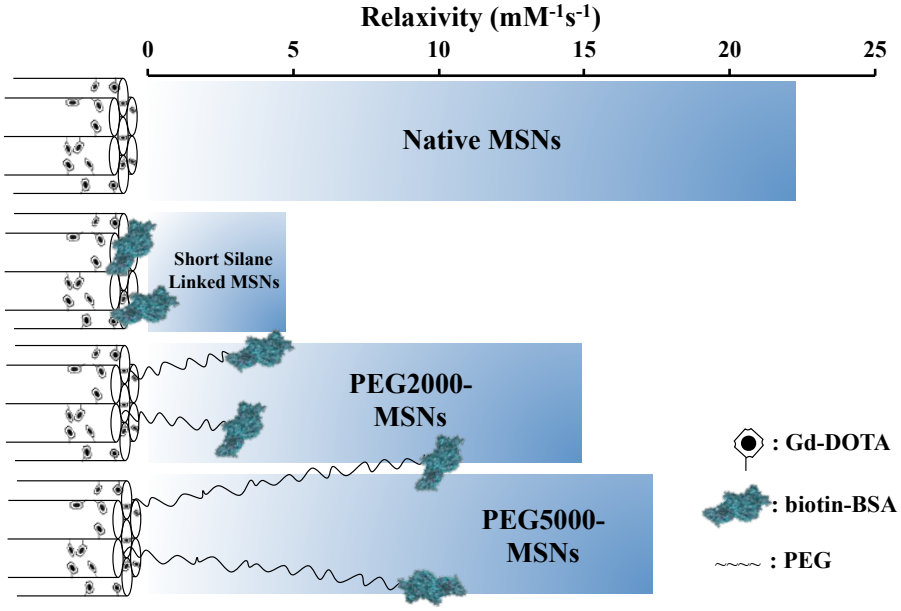


Fig. 4.10 Schematic summary of PEG tuned relaxivity.

4.2.3.2 Responsive and Switchable Relaxivity

Redox-responsive Relaxivity

It has been shown that Gd^{3+} doped MSNs can be prepared with a protein coating that retains or blocks water access as required (i.e. the removal of these water-access blocking proteins should cause a transition from weak to strong relaxivity state). This hence was ultilised in the following section to design a novel activatable/switchable

contrast agent in response to the changes in biological events/environments. As the level of glutathione in a cell cytosol (disulfide reductive environment) is important in a variety of physiological activities[21, 32], signal changes of a contrast agent responsive to glutathione can be potentially indicative of the activities of its associated biological events. Therefore, Gd^{3+}-doped MSNs specifically designed to achieve this were constructed using a capping protein streptavidin (STV; 5 nm[33]) *via* a short reducible disulfide linker (STV-SS-MSNs, Fig. 4.11). The presence of this disulfide linker was confirmed by ζ-potential changes (Table 4.1). The native Gd-DOTA MSNs possessed good water accessibility and thus demonstrated high relaxivity (22.25 $mM^{-1}s^{-1}$). STV attachment was associated with restricted water access, as expected from earlier investigations and confirmed by the reduction in relaxivity (STV-SS-MSNs; 8.45 $mM^{-1}s^{-1}$, 62.0% reduction compared to parent particles; Fig. 4.11). To examine the effectiveness of protein removal, various reducing agents including dithiothreitol (DTT), 2-mercaptoethanol (2-ME), L-cysteine and tris(2-carboxyethyl)phosphine (TCEP) have been employed under the same conditions (the success of protein capping and its removal were qualitatively demonstrated *via* microarray spotting towards biotinylated BSA spots on an amine glass slide shown in Appendix, Fig. A3).

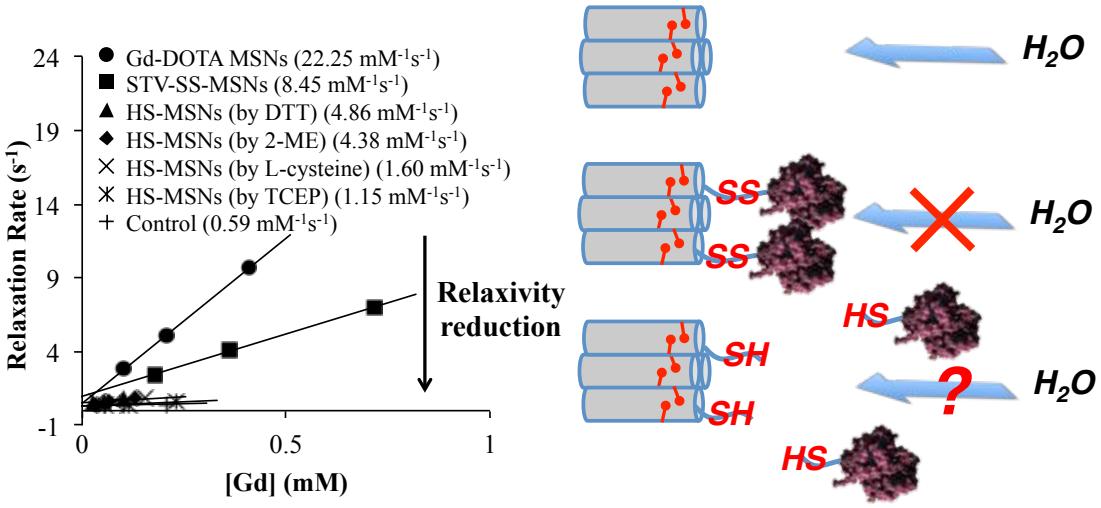


Fig. 4.11 Plots of relaxation rate ($1/T_1$) (s^{-1}) versus concentration (mM) measured at 7 T magnetic field and 20°C. The numbers in the brackets are the corresponding relaxivity values, calculated from a linear plot of the data points. Data shown indicates STV conjugated onto disulfide modified MSNs inducing a reduced relaxivity as the result of restrict water access. Particles treated with reducing agents resulted in even lower relaxivities.

However, surprisingly, all the agents had a detrimental effect on particle relaxivity. A further decrease in relaxivity was observed even after intensively washing the reductant-treated nanoparticles (Fig. 4.11; a nearly 100% reduction). Indeed, a control experiment (mixing the native Gd-DOTA MSNs with TCEP followed by intensive washing as employed in the cleavage of disulfide bonds, Fig. 4.11) has confirmed that these commonly used disulfide reducing agents, to some extent, interacted with either the nanoparticle or Gd-DOTA complexes and led to a reduced relaxivity. Although the mechanistic origin of this reduction could not be determined, this observation was highly reproducible and this approach accordingly abandoned. Focus then moved to an approach to reversibly gate water access in a purely biological means.

Biologically Switchable Relaxivity

As previously outlined, STV capped particles could be controllably prepared such that internal water access was reduced. A careful control over the biotin and STV ratio is essential for the synthesis of stable and monodispersed nanoparticles. The optimal ratio of biotin (nanoparticle bound) and STV during the reaction was determined to be 20:1 with which the STV driven particle aggregation (due to the tetrameric nature of STV) can be avoided (Table 4.1 and Fig. 4.2). In the first instance native Gd-DOTA MSNs were biotin modified with retention of facile water access (Biotin-MSNs, Fig. 4.12). In the presence of low molar equivalents of STV such particles could be robustly capped (STV-MSNs) with a dramatic (>60%) decrease in relaxivity (Fig. 4.12).

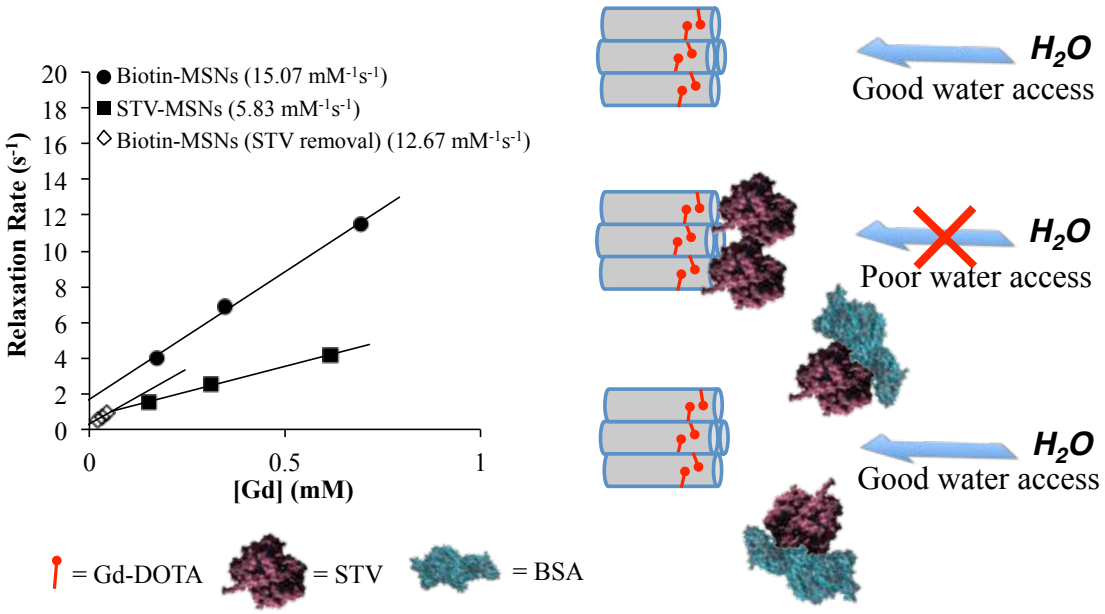


Fig. 4.12 Plots of relaxation rate ($1/T_1$) (s^{-1}) versus concentration (mM) measured at 7 T magnetic field and 20°C. The numbers in the brackets are the corresponding relaxivity values, calculated from a linear plot of the data points. Externally biotinylated Gd^{3+}-doped MSNs enjoy good water accessibility and a high relaxivity (15.07 $mM^{-1}s^{-1}$) that can be reversibly capped by the steric bulk of a bound STV (5.83 $mM^{-1}s^{-1}$). In presence of low μM of biotinylated BSA, the gating protein is competed off the particles surface and relaxivity recovers to 12.67 $mM^{-1}s^{-1}$ (84.1% of original value).

These STV capped particles display long-term stability, with their colloidal and relaxivity characteristics remaining unchanged throughout three months of storage in water [Fig. 4.13 (a)], the latter observation being consistent with negligible leakage of Gd-species. To confirm the specificity of this image contrast capping, the relaxivity characteristics of biotinylated Gd-doped MSNs remained unchanged in the presence of molecular biotin, biotin saturated STV and natively unmodified BSA [Fig. 4.13 (b)].

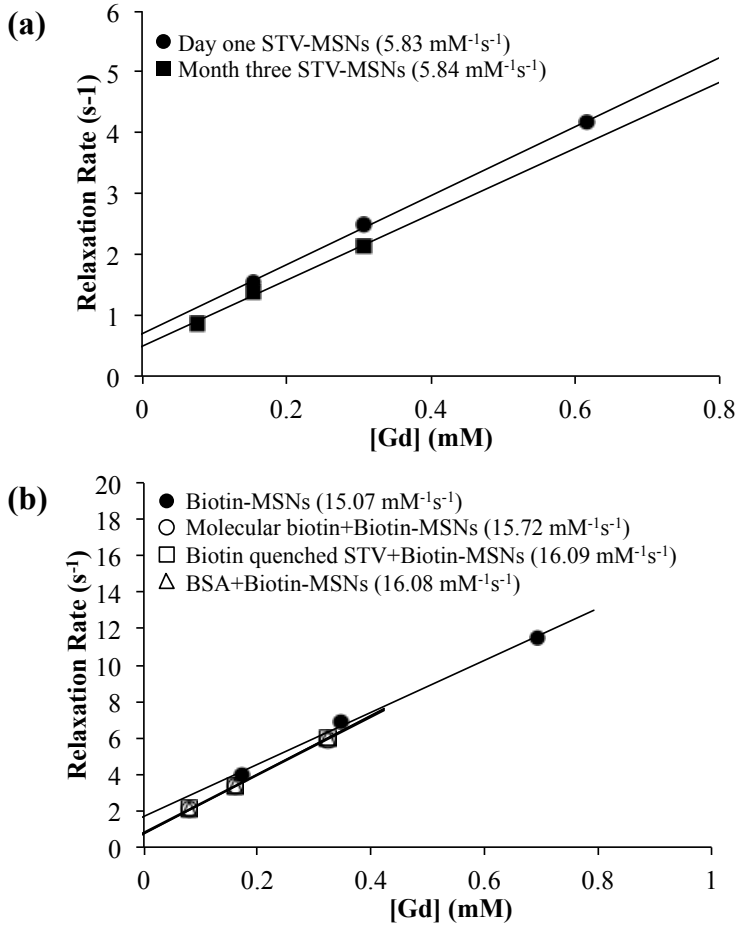


Fig. 4.13 (a) Relaxivity assessment of STV-MSNs at day-one and month-three after particle synthsised. The data indicates the relaxivity characteristics of protein capped particles is highly stable for at least three months; (b) Relaxivity assessment of biotinylated Gd^{3+}-doped MSNs in the presence of molecular biotin, biotin saturated STV or natively unmodified BSA. Data indicates these three controls have negligible effect on relaxivity, showing high specificity towards STV (7 T, 20°C).

Though the solution phase affinity of biotin for STV is very high[24] as stated above, a substantial size dependent decrease in this at nanoparticle surfaces has been previously noted as has the competitive displacement of STV by solution phase biotin[33-35]. In the presence of 1000 fold excess (7 μM) of biotinylated BSA, the gating STV is displaced and particle relaxivity recovers to 84.1% of its original value (Fig. 4.12 and Fig. 4.14). Significantly the associated image contrast shown in Fig. 4.14 can be reversibly 'switched on/recovered' in the presence of competitive proteins.

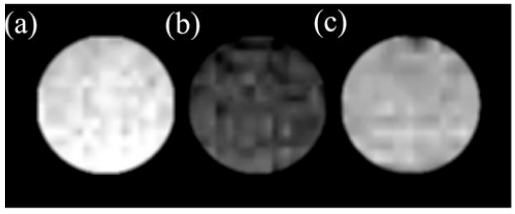


Fig. 4.14 T_1-weighted phantom images of (a) Biotin-MSNs; (b) STV-MSNs; (c) Biotin-MSNs after the competitive removal of capping STV in the presence of low micromolar biotinylated BSA. (TR = 30 ms, TE = 5 ms, slice thickness = 2 mm, matrix = 256 × 256, and T = 20° C, 7 T).

In summary, a contrast activatable nanoparticle based MR contrast agent is successfully demonstrated employing a competitive displacement concept. Streptavidin can be non-covalently gated on the periphery of Gd^{3+}-doped MSNs where it sterically restricts water access to internalised Gd^{3+}-centres. These streptavidin moieties can then be specifically removed in the presence of biotinylated target molecules. Once particle pores have thus been 'decapped', the internalised Gd^{3+}-centres once again enjoyed excellent water access, improved relaxivity and the associated imaging contrast were activated/switched on (Fig. 4.15). This proof of principal, introduced here, immediately suggests numerous analogous applications

where MR contrast can be dramatically switched on in the presence of specific proteins, that may be, for example, disease markers.

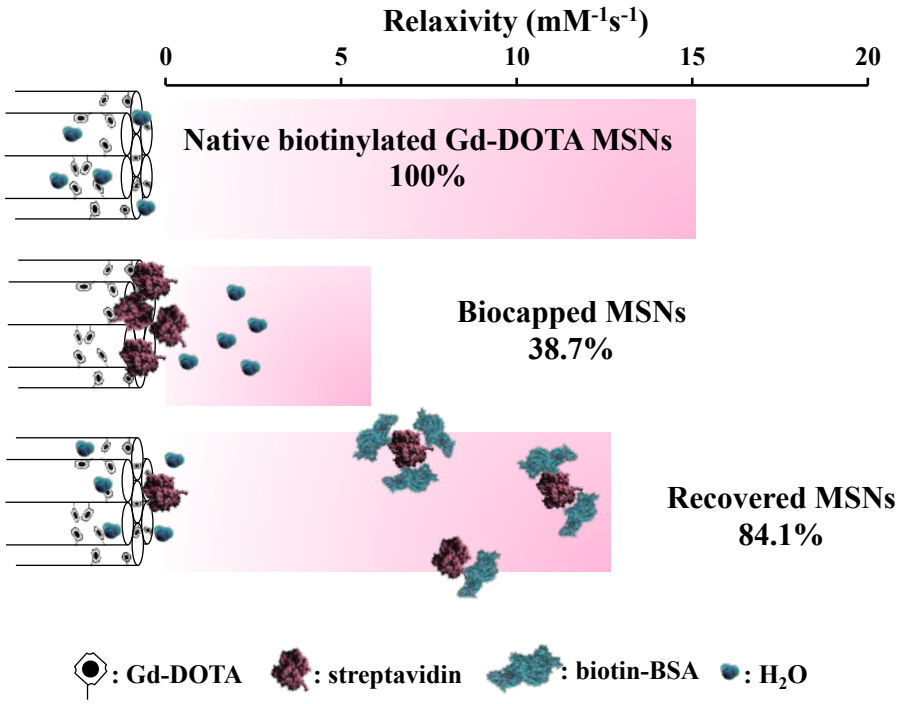


Fig. 4.15 Schematic summary of biologically switchable relaxivity.

4.3 Conclusions

In the present work the synthesis of stable, MR responsive and biologically vectorable MSNs is reported. Through appropriate surface chemistry, nanoparticles can be externally modified without loss of very high relaxivity. Significantly, the internally biased Gd^{3+} loading can be sterically gated at the particle periphery. The introduction of suitably long PEG spacers enables protein conjugation to be achieved with retention of an open gate and good water accessibility; conjugation with short spacers restricts this and dramatically reduces. In the presence of solution phase protein partners the sterically bulky gate can be competed off and high image contrast returns. The work herein not only identifies and utilises the importance of water access, but also constitutes the first example of reversible T_1 contrast gating exploiting protein recognition. This proof of principal is of significant potential value in furthering the application of nanoparticle chemistry to functional MR imaging.

4.4 References

1. W. Y. Huang and J. J. Davis, *Dalton Transactions*, 2011, **40**, 6087-6103.
2. A. M. Morawski, G. A. Lanza and S. A. Wickline, *Current Opinion in Biotechnology*, 2005, **16**, 89-92.
3. P. Caravan, J. J. Ellison, T. J. McMurry and R. B. Lauffer, *Chemical Reviews*, 1999, **99**, 2293-2352.
4. S. Aime, M. Botta, S. G. Crich, G. B. Giovenzana, R. Pagliarin, M. Piccinini, M. Sisti and E. Terreno, *Journal of Biological Inorganic Chemistry*, 1997, **2**, 470-479.
5. P. Caravan, *Chemical Society Reviews*, 2006, **35**, 512-523.
6. S. Laurent, L. V. Elst, F. Botteman and R. N. Muller, *European Journal of Inorganic Chemistry*, 2008, 4369-4379.
7. D. Artemov, N. Mori, R. Ravi and Z. M. Bhujwalla, *Cancer Research*, 2003, **63**, 2723-2727.
8. R. M. Botnar, A. Buecker, A. J. Wiethoff, E. C. Parsons, M. Katoh, G. Katsimaglis, R. M. Weisskoff, R. B. Lauffer, P. B. Graham, R. W. Gunther, W. J. Manning and E. Spuentrup, *Circulation*, 2004, **110**, 1463-1466.
9. S. Laurent, L. Vander Elst, Y. J. Fu and R. N. Muller, *Bioconjugate Chemistry*, 2004, **15**, 99-103.
10. L. M. De Leon-Rodriguez, A. Ortiz, A. L. Weiner, S. R. Zhang, Z. Kovacs, T. Kodadek and A. D. Sherry, *Journal of the American Chemical Society*, 2002, **124**, 3514-3515.
11. R. B. Lauffer and T. J. Brady, *Magnetic Resonance Imaging*, 1985, **3**, 11-16.
12. H. X. Guo, H. Q. Yang, F. Gallazzi, E. R. Prossnitz, L. A. Sklar and Y. B. Miao, *Bioconjugate Chemistry*, 2009, **20**, 2162-2168.
13. G. von Maltzahn, Y. Ren, J. H. Park, D. H. Min, V. R. Kotamraju, J. Jayakumar, V. Fogal, M. J. Sailor, E. Ruoslahti and S. N. Bhatia, *Bioconjugate Chemistry*, 2008, **19**, 1570-1578.
14. D. Kim, Y. Y. Jeong and S. Jon, *Acs Nano*, 2010, **4**, 3689-3696.
15. R. Kumar, I. Roy, T. Y. Hulchanskyy, L. N. Goswami, A. C. Bonoiu, E. J. Bergey, K. M. Tramposch, A. Maitra and P. N. Prasad, *Acs Nano*, 2008, **2**, 449-456.
16. P. M. Winter, A. M. Morawski, S. D. Caruthers, R. W. Fuhrhop, H. Y. Zhang, T. A. Williams, J. S. Allen, E. K. Lacy, J. D. Robertson, G. M. Lanza and S. A. Wickline, *Circulation*, 2003, **108**, 2270-2274.
17. A. M. Morawski, P. M. Winter, X. Yu, R. W. Fuhrhop, M. J. Scott, F. Hockett, J. D. Robertson, P. J. Gaffney, G. M. Lanza and S. A. Wickline, *Magnetic Resonance in Medicine*, 2004, **52**, 1255-1262.
18. K. M. L. Taylor-Pashow, J. D. Rocca and W. Lin, *Nanomaterials*, 2011, **2**, 1-14.
19. J. J. Davis, W.-Y. Huang and G.-L. Davies, *Journal of Materials Chemistry*, 2012, **22**, 22848-22850.

20. V. Cauda, A. Schlossbauer, J. Kecht, A. Zurner and T. Bein, *Journal of the American Chemical Society*, 2009, **131**, 11361-11370.
21. S. R. Ge, K. Kojio, A. Takahara and T. Kajiyama, *Journal of Biomaterials Science-Polymer Edition*, 1998, **9**, 131-150.
22. Y. Takakura, N. Oka, H. Kajiwara and M. Tsunashima, *Journal of Bioscience and Bioengineering*, 2012, **114**, 485-489.
23. L. Mazzarino, C. Travelet, S. Ortega-Murillo, I. Otsuka, I. Pignot-Paintrand, E. Lemos-Senna and R. Borsali, *Journal of Colloid and Interface Science*, 2012, **370**, 58-66.
24. N. M. Green, *Methods in Enzymology*, 1990, **184**, 51-67.
25. T. Sano and C. R. Cantor, *Journal of Biological Chemistry*, 1990, **265**, 3369-3373.
26. J. Strömqvist, L. Nardo, O. Broekmans, J. Kohn, M. Lamperti, A. Santamato, M. Shalaby, G. Sharma, P. Trapani, M. Bondani and R. Rigler, *The European Physical Journal Special Topics*, 2011, **199**, 181-194.
27. M. Busby, L. K. J. Stadler, P. K. Ferrigno and J. J. Davis, *Biophysical Chemistry*, 2010, **152**, 170-177.
28. J. W. Anderegg, W. W. Beeman, S. Shulman and P. Kaesberg, *Journal of the American Chemical Society*, 1955, **77**, 2927-2937.
29. H. P. Erickson, *Biological Procedures Online*, 2009, **11**, 32-51.
30. H. S. Park, C. Kim, H. J. Lee, J. H. Choi, S. G. Lee, Y. P. Yun, I. C. Kwon, S. J. Lee, S. Y. Jeong and S. C. Lee, *Nanotechnology*, 2010, **21**.
31. C. D. Walkey, J. B. Olsen, H. B. Guo, A. Emili and W. C. W. Chan, *Journal of the American Chemical Society*, 2012, **134**, 2139-2147.
32. S. E. Moriarty-Craige and D. P. Jones, *Annual Review of Nutrition*, 2004, **24**, 481-509.
33. E. V. Piletska and S. A. Piletsky, *Langmuir*, 2010, **26**, 3783-3785.
34. K. Aslan, C. C. Luhrs and V. H. Perez-Luna, *Journal of Physical Chemistry B*, 2004, **108**, 15631-15639.
35. X. X. Duan, Y. Li, N. K. Rajan, D. A. Routenberg, Y. Modis and M. A. Reed, *Nature Nanotechnology*, 2012, **7**, 401-407.

Chapter 5 Engineering Cell-nanoparticle Interactions

5.1 Introduction

The entry of foreign materials into cell bodies is a complex process which can be affected by properties of the materials, including size, solubility, geometry, and chemical characteristics amongst others. There are three main entrance pathways, the simplest of which is passive diffusion across the cell membrane lipid bilayer[1]. This is the process by which small membrane-permeable species such as O_2, CO_2 and small, uncharged polar molecules (urea and ethanol, for example) are transported into cells, driven by diffusion down a concentration gradient by random thermal motion into the cell cytoplasm (without the need of transport proteins). The solubility and molecular weight of these materials have the greatest effect on their diffusion efficiency, which decreases as molecular weight increases and at extremes of hydrophobicity and hydrophilicity. The second pathway is active transport which moves substances into the cell against a concentration gradient, and requires energy either from adenosine triphosphate (ATP) or from an electrochemical gradient[1]. This is normally mediated by a channel protein that spans the cell membrane e.g. the sodium-potassium pump which has an enzyme bridging the membrane which pumps sodium and potassium ions in opposite directions against their respective concentration gradients with the help of ATP. The third pathway is endocytosis, active for macromolecules and particulate substances[1-3]. There are various sub-divisions of endocytosis; the most notable of

which is receptor-mediated endocytosis that makes use of the proteins that decorate the outer cell membrane. The other endocytic pathways vary only subtly but the majority, including those which are receptor mediated, cause the molecule transported across the membrane to be localised inside a vesicle membrane formed from the surface lipid bilayer. These vesicles have two roles that govern the associated fates of internalised species; through which they can be exocytosed or transported/maturated from early, late endosomes to lysosomes with acidification occurring in these vesicles and enzymatic degradation thereafter.

The internalisation of nanoparticles into the cells thus, is generally by endocytosis[2, 3]. As discussed in Chapter 1, a series of structural and chemical characteristics can influence endocytosis. Among these, the inherent difficulty in controlling the orientation of the nanoparticle being uptaken has made the effects of particle geometries relatively unclear. Conversely, due to their highly tailorable surfaces, the influences of nanoparticles' surface chemistries (through their surface charges[4-8] and the characteristics of surface groups[5, 9]) are relatively well understood. Outer Cell membranes possess a negative charge which is considered to play a role in interacting with nanoparticles and the associated uptake behaviours. Positively charged nanoparticles are generally acknowledged to be internalised at a faster rate than those with a neutral or negative charge[4-8]. In addition to this electrostatic interaction, particle surface functionalities can also alter cell uptake patterns. Most nanomaterials are taken up rapidly after serum protein association (opsonisation)[10], which aids the recognition

of nanoparticles by cells. However, this process can be reduced by adding poly(ethylene) glycol (PEG) to the surface of nanomaterials[9]. PEG is a water soluble polymer composed of repeating ethylene oxide units. Structurally, PEG's polar character provides its hydrophilicity, prevention from protein adsorption and thus slower cell uptake.

Nanoparticles that are uptaken *via* endocytosis involve endosomal/lysosomal organelles (see Fig. 1.9 in Chapter 1), cellular degradation of membrane-bound acidic compartments which are the central mechanism of foreign materials[11, 12]. In the vast majority of cases, particles uptaken in this way are subsequently trapped within these compartments, unable access the cytoplasm or nucleus or to directly influence cellular physiology[13-15]. From either gene transfection or protein delivery perspectives payload access to the cytosol is a vital requirement[15, 16]. A number of approaches have been examined to facilitate the escape of nanoparticles or therapeutic agents from this endocytic pathway, generally involving their destructive interaction with the endosomal/lysosomal membranes[17-27]. Photosensitisers, for instance, release singlet oxygen species after endocytosis and excitation, which oxidises amino acids, fatty acids and cholesterol and thus damaging membranes[18]. Cationic amphiphilic peptides, after binding to the lipid bilayer, lead to internal membrane tension and can subsequently create pores in the membrane, facilitating cytosol access[24]. The pH-buffering effect ('proton sponge' effect), on the other hand, is perhaps the most widely used mechanism and is generally employed with inorganic nanoparticles[17, 22, 25-27]. The

effect is mediated by agents with high buffering capacity which creates a difference in osmotic pressure, inflow of ions and water and subsequent endo/lysosomal membrane rupturing. Various amine-containing molecules have been reported to demonstrate this pH-buffering capacity due to their basic functionalities. Among these, the introduction of chloroquine to induce endo/lysosomal rupturing is perhaps the simplest protocol[17, 19]; its inherent cytotoxicity, however, has made it less attractive[28]. Tertiary amines, such as polyethyleneimine (PEI), have been proven to be able to enhance particle uptake (through electrostatic attraction effects) and facilitate endo/lysosomal escape[22]. Similarly, imidazole or histidine-rich molecules have been shown to exhibit a buffering effect upon protonation, resulting in endo/lysosomal disruption[20, 26]. In addition to the above amine derivatives, cationisation (charge conversion) of poly(lactide) particles caused by a change in pH was also reported to bypass endosomal entrapment[27]. Though there exist some studies now where these agents have been utilised to release particles from the acidic and destructive endocytic compartments, their design criteria or mechanism of operation has generally not been addressed and cytosol access remains, in general, highly inefficient and poorly reproducible.

Indeed, not only is particle endocytosis an extremely complicated process but it also varies depending on particle and cell types. To engineer cell-nanoparticle interactions, the initial study in this work was to examine the capability of Hela cells to endocytose MSNs. The effect of pegylation of these nanoparticles was then investigated to

determine the influence of this modification on cell uptake characteristics. Subsequent studies examined the electrostatic interaction between the charged cell membrane (lipid bilayer) and nanoparticles. Additionally, the ability to rupture the resulting endocytic vesicles from this lipid bilayer of Hela cells was tested using chloroquine, a common proton sponge. On the basis of these results, the influences of specially designed surface amine functionalities (and their associated charges) on nanoparticle subcellular distributions were systematically studied through examining their pKas and surface coverage. Most importantly, their interactions with acidic endocytic compartments were assessed and towards facilitating endo/lysosomal escape.

5.2 Results and Discussion

The ultimate objective of this work was to design nanoparticles that would be reliably endocytosed by Hela cells and can subsequently escape from this acidic and destructive route into cell cytosols once internalised, in order to enable to use of these particles as cytosolic drug delivery agents. Importantly, in any manner of cell work, there are several variations (e.g. different cell types, particle chemistries or culture conditions) that may influence the final observations. Therefore, despite prior reports that acknowledge the capability of cancer cells to uptake silica nanoparticles, it is reasonable to consider and establish a basic knowledge of cell-nanoparticle systems in this work prior to any further investigation and particle engineering.

5.2.1 General Interactions of MSNs with Hela Cells

The assessment of cell-particle interaction in this chapter was carried out with luminescent MSNs and Hela cells using fluorescent confocal microscopy. Hela cells are the oldest and the most commonly used immortalised human cancer cell line in scientific research and their basic structure is much the same as healthy making them a popular cell model for studying both cell biology and cancer therapy[29]. To confirm Hela cells can efficiently endocytose the MSNs synthesised within this work, the particles were fluorescently labelled with green fluorescein (FITC) and the cell organelles were stained with blue nucleus dye and red endo/lysosome dye [using Hoescht33342 and LysoTracker Red respectively; note that LysoTracker is specifically designed to tag the late compartments of endocytic pathway (late endosomes and

lysosomes)[44, 45]. A variety of nanoparticles were employed to investigate the influence of pegylation and particle charge on the efficiency of endocytosis (Table 5.1).

Table 5.1 Summary of surface charges and hydrodynamic sizes of MSNs employed in the investigation of cell-nanoparticle interactions (errors derived from the average of five repetitions).

MSNs	Mean ζ-potential (mV) at pH 7.1*	d_{hyd} (nm) & PDI**
Native FITC-MSNs	-30.3 (± 1.6)	185.8 (0.05)
10 mol% COOH-MSNs	-45.4 (± 1.9)	176.2 (0.07)
10 mol% NH_2-MSNs	2.5 (± 0.2)	198.3 (0.05)
10 mol% COOH-PEG2000-MSNs	-43.9 (± 1.1)	186.8 (0.06)

* Samples measured at pH 7.1 using phosphate buffer (10 mM, salt free).
** d_{hyd}: hydrodynamic size; PDI: polydispersity index.

Neither pegylation nor amination/carboxylation changed the resulting particle size or size distribution (see d_{hyd} in Table 5.1), therefore the size-dependent variations in cell uptake can be ruled out here. Initially, nanoparticles were incubated with cells for a period of 24 h to confirm the endocytic pathway of MSNs uptake, their subcellular distribution and their colocalisation with late vesicles of endocytosis. Confocal images of native FITC-MSNs after incubation with Hela cells for 24 h [Fig. 5.1 (a1 – a3)] clearly show that the nanoparticles were internalised *via* the endocytic mechanism as confirmed by the colocalisation of the green nanoparticles and red endo/lysosomes (showing yellow in the figure). In order to subsequently investigate the possibility of altering the uptake behaviours, PEG2000 was conjugated onto these native FITC-MSNs through a series of carboxylation and pegylation steps (see experimental section in Chapter 2). As prior work suggested that particle surface charges can change endocytic efficiency[4-8], highly negatively charged carboxyl-terminated peglyated

MSNs (10 mol% COOH-PEG2000-MSNs; Table 5.1) and carboxyl-terminated MSNs without pegylation (10 mol% COOH-MSNs; Table 5.1) were investigated to examine the effect of pegylation specifically. The images again demonstrated that both carboxylated particle types were taken up endocytically [Fig. 5.1 (b1 – b3) and Fig. 5.1 (c1 – c3)] (as shown by the perfect overlap of the green particles and red endo/lysosomes); however, Hela cells clearly internalised pegylated particles much less efficiently [Fig. 5.1 (c1 – c3)], with qualitatively fewer nanoparticles observed inside the cells. It should be noted that the magnification of confocal microscopy and its recorded fluorescent intensities can only provide information from the nanoparticles within a given focal plane therefore cannot accurately quantify the number of internalised particles.

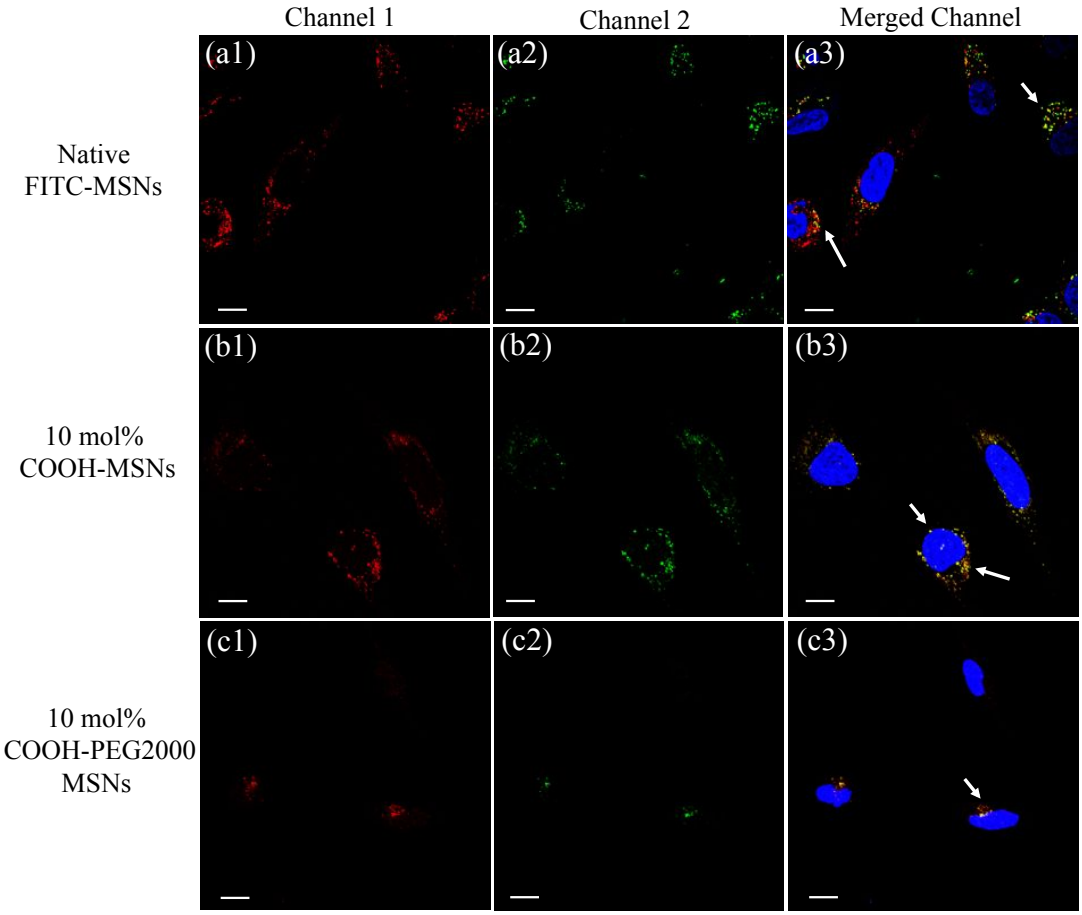


Fig. 5.1 Confocal fluorescent images after 24 h incubation of Hela (~3×10^3) with 200 μg/mL of nanoparticles of (a1 – a3) native FITC-MSNs; (b1 – b3) 10 mol% COOH-MSNs; and (c1 – c3) 10 mol% COOH-PEG2000-MSNs, showing nanoparticles were internalised *via* endocytosis confirmed by the overlap of green nanoparticles and red endo/lysosomes (showing yellow; arrows indicated). Note that pegylation is capable of suppressing cell uptake (fewer green particles in figure (c), a qualitative imaging result). Channel 1: endo/lysosomes stained with LysoTracker Red; Channel 2: green FITC tagged particles; and Channel 3: merged images of channel 1, channel 2 and nucleus stained with blue Hoest33342 (Scale: 10μm; lasers used: 404 nm, 488nm and 561nm for nucleus, nanoparticles and endo/lysosomes, respectively).

In order to qualitatively further confirm the uptake retardation by pegylation of MSNs, the particle incubation time was extended to 48 h, with the resulting confocal images shown in Fig. 5.2. These images clearly show that, within the same size of viewing area, the cell number and particle density increased in the both cases (with and without

pegylation). Once again, however, after particle incubation with cells for 48 h, more non-pegylated particles appeared to have been internalised demonstrating once more that a PEG coating on nanoparticle surfaces can suppress uptake.

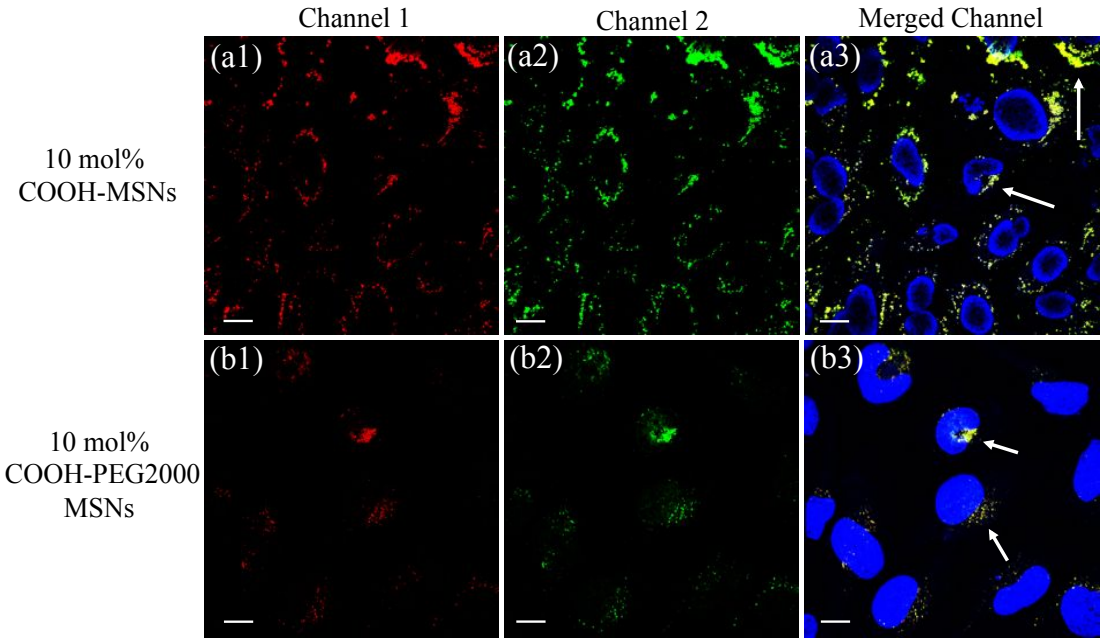


Fig. 5.2 Confocal fluorescent images after 48 h incubation of Hela (~3×10^3) with 200 μg/mL of nanoparticles (a1 – a3) 10 mol% COOH-MSNs; and (b1 – b3) 10 mol% COOH-PEG2000-MSNs, showing pegylated nanoparticles were internalised less effectively confirmed by the qualitatively fewer green nanoparticles prescent in figure (b). Channel 1: endo/lysosomes stained with LysoTracker Red; Channel 2: green FITC tagged particles; and Channel 3: merged images of channel 1, channel 2 and nucleus stained with blue Hoest33342 (Arrows indicated the endo/lysosomal colocalised nanoparticles) (Scale: 10μm; lasers used: 404 nm, 488nm and 561nm for nucleus, nanoparticles and endo/lysosomes, respectively).

Literature suggests that negatively charged nanoparticles will be less efficiently internalised to cells than positively charged particles, due to their stronger electrostatic repulsion with the negatively charged cell membrane. However, on comparing 24 h incubation of native FITC-MSNs and FITC-MSNs with 10 mol% COOH-MSNs (-30.3 ± 1.6 mV and -43.9 ± 1.1 mV respectively), no apparent difference in cell uptake was

observed herein, despite their different surface charges [Fig. 5.1 (a1 – a3) and Fig. 5.1 (b1 – b3)]. Significantly, this lack of particle surface charge effect was consistently observed, even upon cell incubation for 24 h with nanoparticles with a slightly positive surface charge [10 mol% NH_2-MSNs, 2.5 ± 0.2 mV; Table 5.1 and Fig. 5.3 (a1 – a3)]. In considering the mechanism by which a cell recognises nanoparticles, which relies on the serum proteins/amino acids adsorption on particles (see Chapter 1), any charged amino acid in the culture medium may associate with particles having an opposite surface charge. Indeed, the medium used here contains amino acids with a variety of isoelectric points (pI, which determined their charges in neutral pH conditions). Anionic glutamine and cationic lysine (whose pIs are 5.65 and 9.74 respectively[30]), for example, may facilitate the cell uptake for positively and negatively charged nanoparticles respectively, hence leading to the lack of difference in particle internalisation observed in this work.

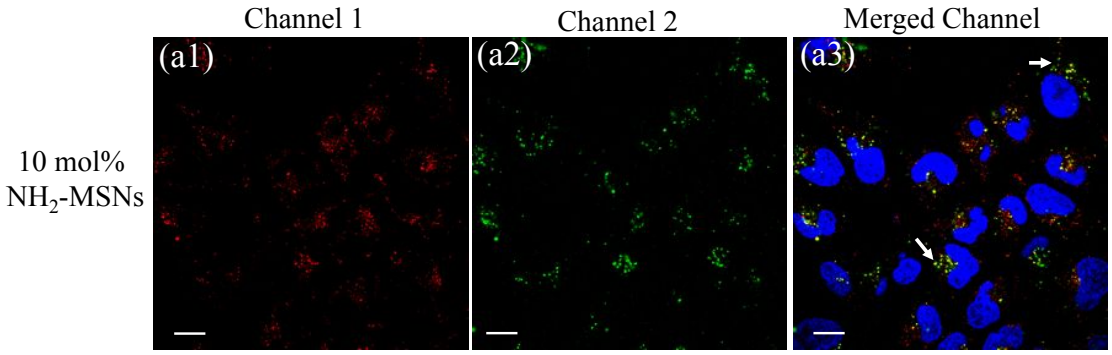


Fig. 5.3 Confocal fluorescent images after 24 h incubation of Hela (~3×10^3) with 200 μg/mL of nanoparticles showing slightly positively charged NH_2 nanoparticles were also internalised *via* endocytosis confirmed by the overlap of green nanoparticles and red endo/lysosomes (showing yellow; arrows indicated). Channel 1: endo/lysosomes stained with LysoTracker Red; Channel 2: green FITC tagged particles; and Channel 3: merged images of channel 1, channel 2 and nucleus stained with blue Hoest33342 (Scale: 10μm; lasers used: 404 nm, 488nm and 561nm for nucleus, nanoparticles and endo/lysosomes, respectively).

Although the overall 24 h incubation results here have indicated that the only obvious difference in cell-nanoparticle interaction is facilitated by using pegylated nanoparticles, it should be emphasised that the interactions of cells with nanoparticles are not necessarily completely charge-independent. To investigate this further by studying their interaction over shorter time periods, 5 h incubation of particles with cells was also carried out. Significantly, native particles (FITC-MSNs), highly negatively charged carboxylated particles (10 mol% COOH-MSNs) and slightly positively charged aminated particles (10 mol% NH_2-MSNs) demonstrated different interactions with Hela cells [Table 5.1 and Fig. 5.4 (a1 – a3), Fig. 5.4 (b1 – b3) and Fig. 5.4 (c1 –c3)]. 10 mol% NH_2-MSNs exhibited a strong membrane-association [pink arrow in Fig. 5.4 (c3)]. Significantly fewer 10 mol% COOH-MSNs were internalised within 5 h compared with native FITC-MSNs and NH_2-MSNs exhibited a strong membrane-association [pink arrow in Fig. 5.4 (c3)], with a similar amount of particles internalized as native FITC-MSNs. These results clearly indicated that there are some short-term differences in the cellular uptake between nanoparticles with differing surface charges (within 5 h incubation), resulting from electrostatic interactions, however, these are relatively insignificant for long-term observations (24 h incubation periods).

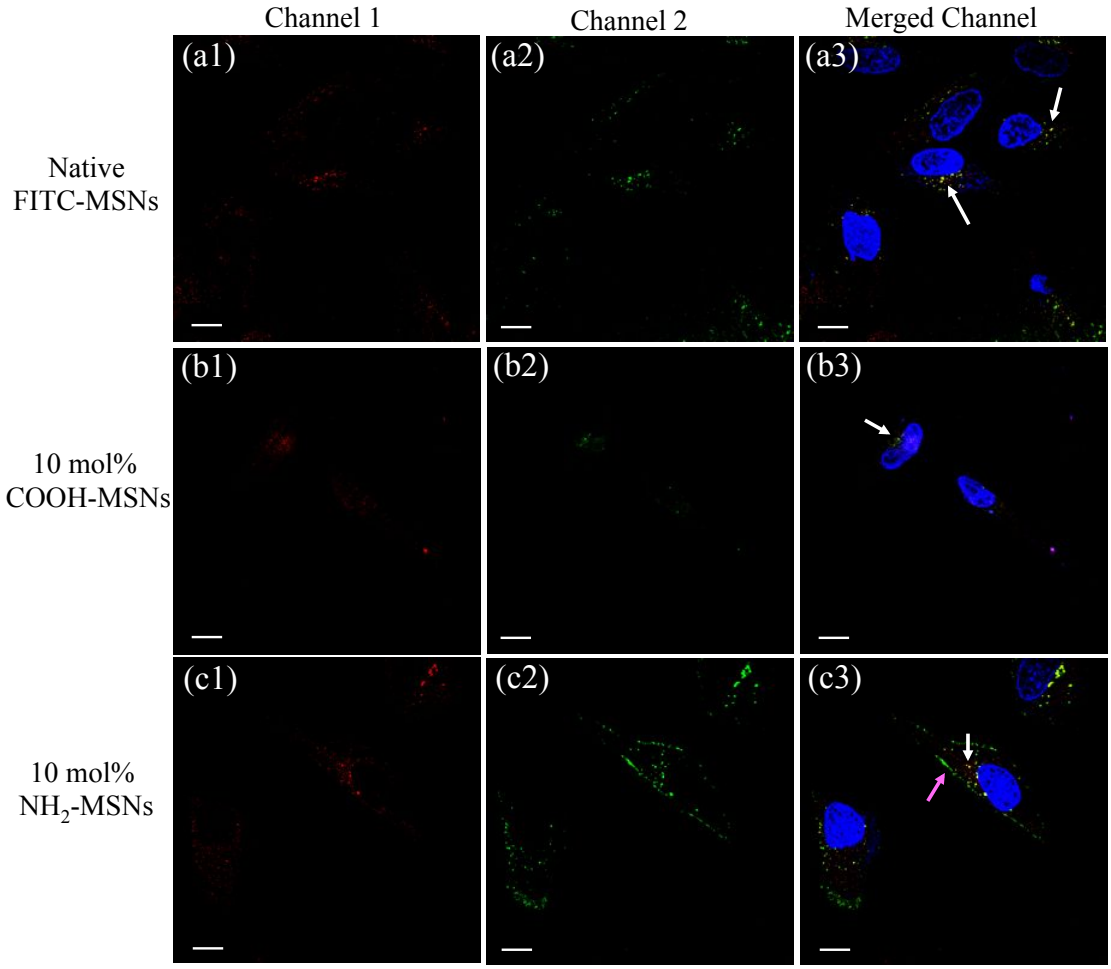


Fig. 5.4 Confocal fluorescent images showing different cell-nanoparticle associations (~3×10^3 Hela with 200 μg/mL MSNs) resulting from electrostatic interactions at a shorter incubation (5 h). (a1 – a3) native FITC-MSNs show typical endo/lysosomal colocalisation (indicated by white arrows); (b1 – b3) 10 mol% COOH-MSNs showing ineffective cell-nanoparticle interaction and endocytosis presumably due to electrostatic repulsion; and (c1 – c3) 10 mol% NH_2-MSNs clearly showing particle association with the cytoplasm membrane (pink arrow; possibly resulting from the electrostatic attraction to the negative cell membrane). Channel 1: endo/lysosomes stained with LysoTracker Red; Channel 2: green FITC tagged particles; and Channel 3: merged images of channel 1, channel 2 and nucleus stained with blue Hoest33342 (Scale: 10μm; lasers used: 404 nm, 488nm and 561nm for nucleus, nanoparticles and endo/lysosomes, respectively).

In summary, the MSNs synthesised in this work can be readily internalised by Hela cells *via* endocytosis within 24 h incubation. Pegylation can significantly slow down the particle internalisation whereas particle surface charges have negligible effect on

cell uptake over this incubation time. Importantly, electrostatic forces can still play a role in affecting the interaction of the negatively charged lipid bilayer with nanoparticles at shorter time periods. It is possible, then that any endocytic vesicle originating from this plasma lipid bilayer could also be influenced by this nanoparticle electrostatic interaction. This theory was tested and subsequently employed in the following sections to control the subcellular distribution after particle internalisation.

5.2.2 Confirmation of Endo/lysosomal Escapability

As the release of theranostic or transfection agents into the cytosols or nucleus of a cell (their sites of action) is often a requirement[15, 16], the escape of their carrier MSNs from destructive endocytic compartments is thus particularly valuable. Among various escape mechanisms described in the prior works, the proton sponge effect (pH buffering) is perhaps the most widely employed method[17, 22, 25-27]. In this, the acidic endocytic vesicles can be destroyed by a proton sponge that creates osmotic pressure between endo/lysosomes and the cytosols and the subsequent endo/lysosomal membrane rupturing. Chloroquine, which possesses a quinoline nitrogen with pKa ~8.5 is well known amongst these pH buffering agents. It has been shown to stop the acidification of endosomes, and to cause swelling and release of encapsulated proteins in rat cells[31]. Since reliable endocytosis of MSNs has been confirmed above, initial studies allowed examination of the endo/lysosomal escape capability of MSNs using chloroquine. To facilitate the escape of MSNs, two different approaches of chloroquine addition were investigated.

5.2.2.1 Co-incubation of Chloroquine and Luminescent MSNs with Hela Cells

Fluorescent MSNs are normally uptaken by cells *via* an endocytic route within a 5 h period, as described above (Section 5.2.1). Surprisingly, however, a preliminary 5 h co-incubation of MSNs (red rhodamine-MSNs; d_{hyd}: 173.3 nm; PDI: 0.10) with chloroquine (200 μM; involving the simultaneous addition of nanoparticles and chloroquine into a Hela culture) demonstrated that no particles were internalised to cells [Fig. 5.5 (a1 – a3)]. On extending the co-incubation period to 24 h, MSNs were internalised by cells and were observed to be present in the cytosol, albeit with a lower degree of uptake compared with those cultured in the absence of chloroquine [Fig. 5.1 and Fig. 5.5 (b1 –b3)]. Although there is no direct evidence that the slightly toxic chloroquine has an influence on cellular activity and endocytosis in this work, this lower degree of uptake was a reproducible observation. Significantly, co-incubation of MSNs with chloroquine successfully prevented the endo/lysosomal localisation of MSNs and their presence in the cytosol of the cells (Fig. 5.5).

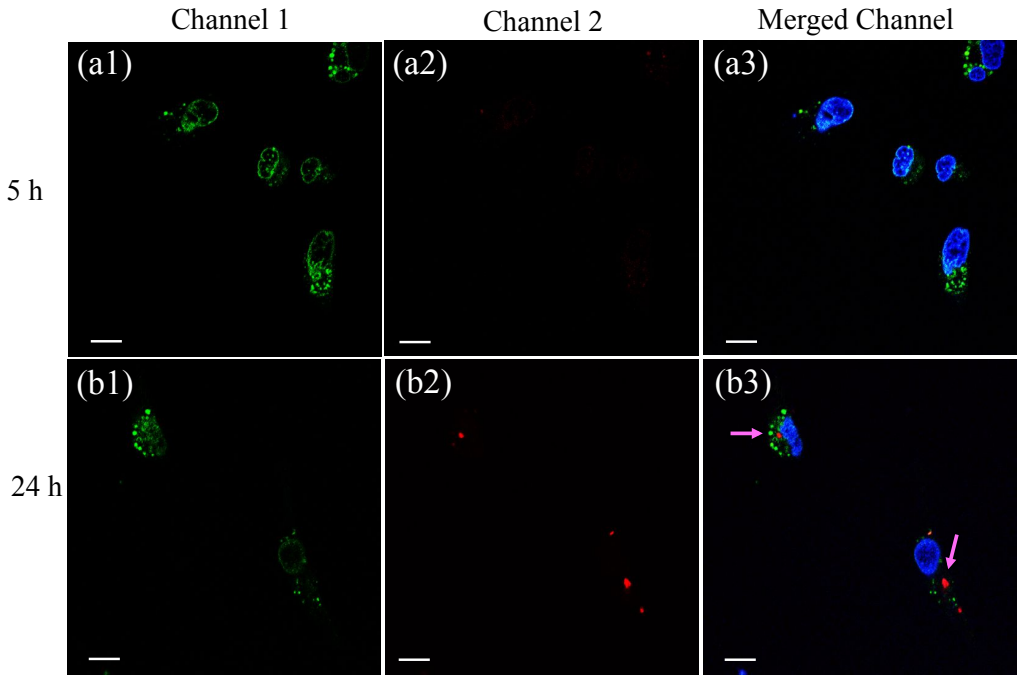


Fig. 5.5 Confocal fluorescent images showing nanoparticles which have bypassed endo/lysosomal localisation [observed as red; arrows indicated in figure (b)]. (a1 – a3) after 5 h incubation of Hela (~3×10^3) with 200 µg/mL red rhodamine-MSNs and 200 µM chloroquine (note that almost no red particles were taken up at this timeframe, likely due to toxic chloroquine affect cellular activity). (b1 – b3) after 24 h incubation of Hela (~3×10^3) with 200 µg/mL red rhodamine-MSNs and 200 µM chloroquine showing a lack of endo/lysosomal colocalisation (free red particles indicated with pink arrows). Channel 1: endo/lysosomes stained with LysoTracker Green; Channel 2: red rhodamine tagged particles; and Channel 3: merged images of channel 1, channel 2 and nucleus stained with blue Hoest33342 (Scale: 10µm; lasers used: 404 nm, 488nm and 561nm for nucleus, endo/lysosomes and nanoparticles, respectively).

5.2.2.2 MSNs Incubation Followed by Chloroquine Addition

Although co-incubation of MSNs and chloroquine has shown the capability to bypass MSNs' endo/lysosomal localisation, the degree of internalisation is relatively low even after a long incubation period (24 h). In order to increase the uptake of particles, the incubation procedure was modified, wherein cells were incubated for 24 h with MSNs only followed by the administration of 200 µM chloroquine and subsequent 2 h

incubation. As the first step of this process involved incubation with particles alone, the cell-nanoparticle interaction was comparable to that reported in the above section [Fig. 5.1 (a1 – a3)]. Upon a further 2 h incubation after the addition of chloroquine, a significant proportion of MSNs were released from the endo/lysosomes [Fig. 5.6 (a1 – a3), pink arrow; chloroquine was thought to permeate the cell membrane and endo/lysosomal compartments of the cells and facilitate particle escape *via* the proton sponge effect[31]]. Extending this incubation period further, to 4 h, showed a marginally greater proportion of particles were not localised with the endo/lysosomes [Fig. 5.6 (b1 – b3)]; after a total 24 h incubation with chloroquine, no further increase in MSNs located in cytosol was observed [Fig. 5.6 (c1 – c3)]. It is worth noting again that despite the images reported here representing only qualitative results, the release of nanoparticles from endocytic pathway by chloroquine was microscopically demonstrated clearly.

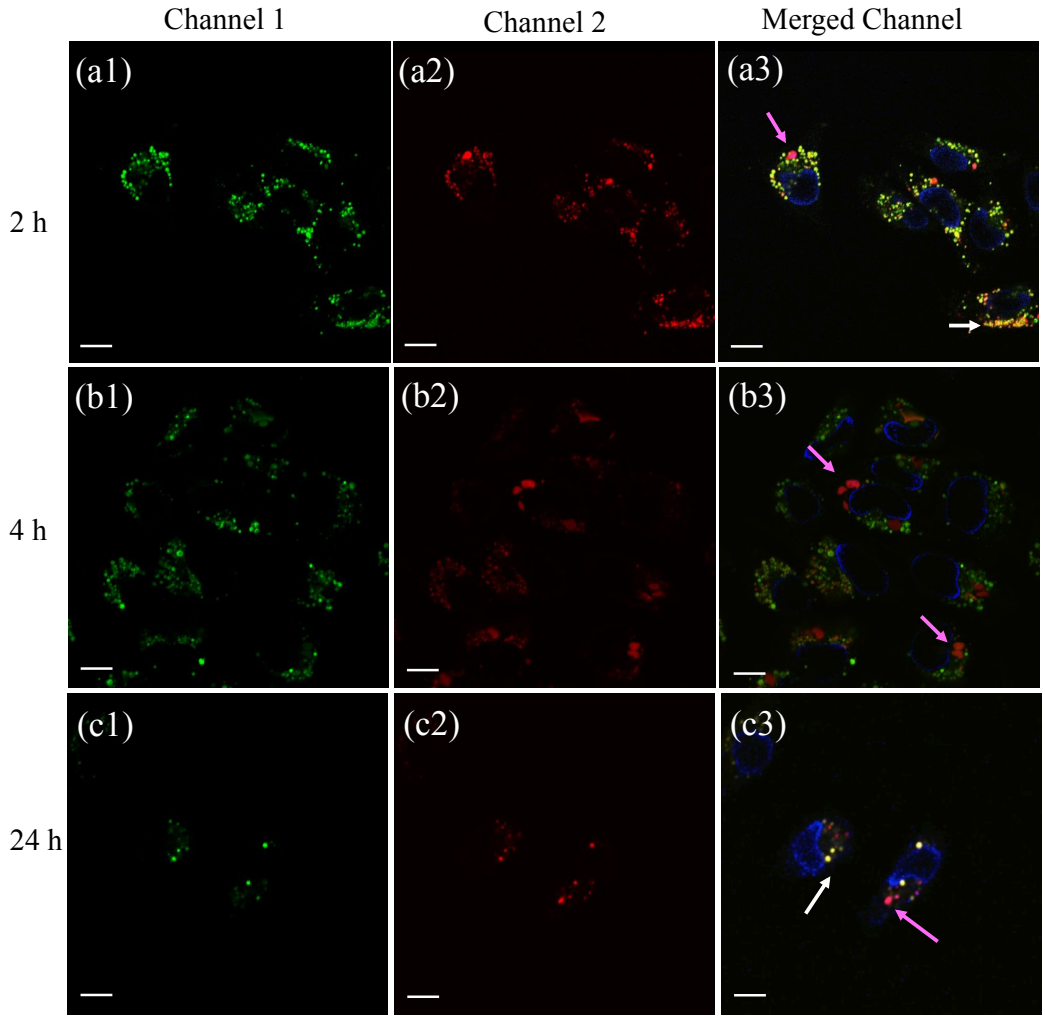


Fig. 5.6 Confocal fluorescent images showing nanoparticles escaped from endocytic pathway (showing red; arrows indicated) after 24 h Hela (~3×10^3) incubation with 200 μg/mL of rhodamine-MSNs followed by the incubation with 200 μM chloroquine for (a1 – a3) 2 h; (b1 – b3) 4 h; and (c1 – c3) 24 h. Channel 1: endo/lysosomes stained with LysoTracker Green; Channel 2: red rhodamine tagged particles; and Channel 3: merged images of channel 1, channel 2 and nucleus stained with blue Hoest33342 (Scale: 10μm; lasers used: 404 nm, 488nm and 561nm for nucleus, endo/lysosomes and nanoparticles, respectively).

5.2.3 Formulation of Novel Endo/lysosomal Escaping Nanoparticles

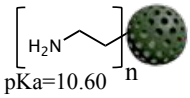
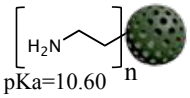
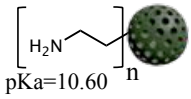
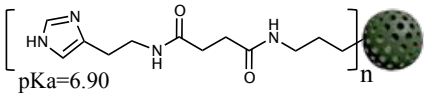
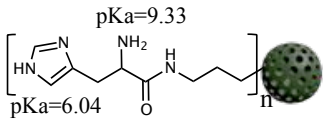
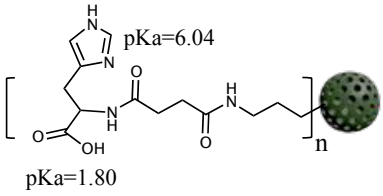
Although the presence of weakly basic chloroquine has been shown to facilitate the release of internalised endo/lysosomally-entrapped MSNs to the cytosols, the previous results have also indicated it lowered the efficiency of particle internalisation,

presumably due to its inherent toxicity that influences cellular activity[28]. In addition, the influence that chloroquine and other weak basic agents that are widely used in nonviral vector designs have on endo/lysosomal escape are typically rationalised based on a 'hypothesised' proton sponge effect associated with a large pH buffering capability[17, 22, 25-27]. No prior work has attempted to systematically investigate the relationship between this capability and the types of basic functional groups as well as their surface concentrations on nanoparticles. Therefore, herein, much effort was invested to propose a more universal formula to facilitate the endo/lysosomal escape of nanoparticles, correlating surface concentrations and functional groups to the effectiveness of escape to the cytosol.

5.2.3.1 Surface Concentration Effect

In the first instance, one may consider the effect of surface concentration of pH-buffering coating (amine groups in this work) on endo/lysosomal escape. Three different mol% of APTES were post-grafted onto native FITC-MSNs to produce type (a) particles [1 mol%, 5 mol% and 10 mol% with respect to TEOS designated as type (a1), (a2) and (a3), respectively; Table 5.2; see experimental section in Chapter 2]. The final nanoparticle size, hydrodynamic diameter or colloidal stability was unaffected by the surface modifications (Table 5.2). The success of varying surface amine coverage was confirmed by the progressive increase in ζ-potential at pH 7.1 (Table 5.3).

Table 5.2 Structural representations, calculated molar percentage ratio of amine functional groups with respect to TEOS and hydrodynamic sizes of native FITC-MSNs with primary amine modification [type (a1- a3)], 1 mol% imidazole modification [type (b)], 1 mol% primary amine and imidazole co-modification [type (c)] and 1 mol% imidazole and carboxyl co-modification [type (d)]. Functional group pKa values are also indicated.

MSN type	Structure	Molar percentage raito*	d_{hyd} (nm) & PDI
Type (a1)		1 mol%	177.5 (0.14)
Type (a2)		5 mol%	182.5 (0.15)
Type (a3)		10 mol%	198.4 (0.18)
Type (b)		1 mol%	189.3 (0.05)
Type (c)		1 mol%	176.1 (0.05)
Type (d)		1 mol%	172.2 (0.08)

* Molar percentage ratio calculated from the concentration of amine functional groups with respect to silanol source, TEOS, during the reaction

Table 5.3 Summary of ζ-potential monitored stepwise throughout all nanoparticle surface coupling reactions (see reaction procedures and schemes in Chapter 2). Through the changes of ζ-potential towards a positive direction, the successful introduction of amine-terminated groups is confirmed; carboxylation leads to changes in a negative direction. (Errors derived from the average of five repetitions).

Type (a) reaction steps	Mean ζ-potential (mV) pH 7.1
Native FITC-MSNs	-30.3 (± 1.6)
1% Amination	-17.5 (± 0.8)
5% Amination	-4.2 (± 0.6)
10% Amination	2.5 (± 0.2)

Type (b) reaction steps	Mean ζ-potential (mV) pH 7.1
Native FITC-MSNs	-30.3 (± 1.6)
Amination	-17.5 (± 0.8)
Carboxylation	-44.9 (± 1.5)
Imidazole conjugation	-39.1 (± 2.2)

Type (c) reaction steps	Mean ζ-potential (mV) pH 7.1
Native FITC-MSNs	-30.3 (± 1.6)
Amination	-17.5 (± 0.8)
Carboxylation	-44.9 (± 1.5)
Histidine conjugation	-38.5 (± 3.1)

Type (d) reaction steps	Mean ζ-potential (mV) pH 7.1
Native FITC-MSNs	-30.3 (± 1.6)
Amination	-17.5 (± 0.8)
Histidine conjugation	-28.7 (± 1.4)

Fig. 5.7 show confocal fluorescent images of Hela cells after with 24 h MSNs incubation with these different particle types. All three particles are reliably internalised within this timeframe by endocytosis [note the perfect overlap of green particles with red endo/lysosomes for type (a2) and type (a3) nanoparticles]. On examining the co-localisation of MSNs with cellular and endosomes/lysosomes, one may expect that a higher degree of amination would be associated with a better proton sponge ability and hence more effective endo/lysosomal escape. Significantly, only the lowest mol% of aminated MSNs [1 mol%, type (a1)] were able to escape from endo-lysosomal compartments within 24 h incubation [Fig. 5.7 (a1 – a3)].

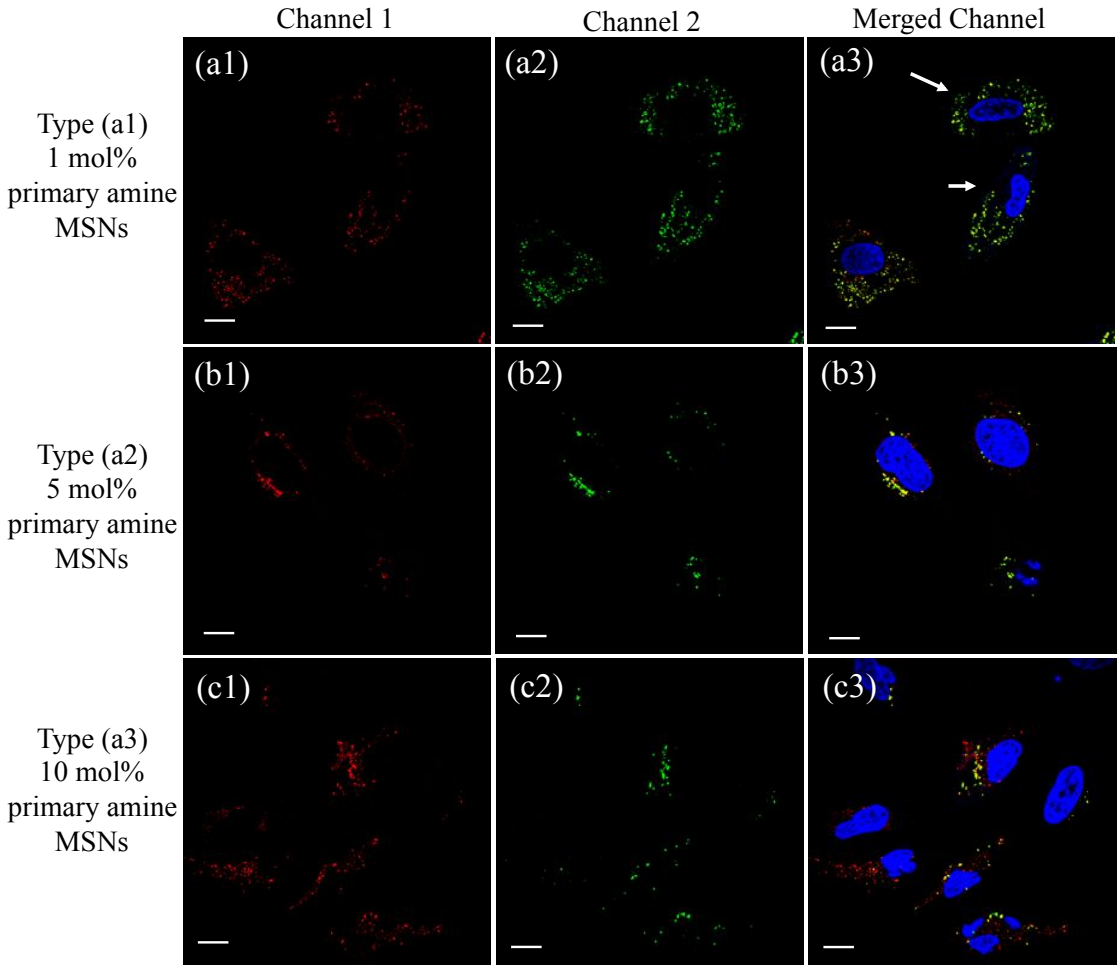


Fig. 5.7 Confocal fluorescent images of Hela cells 24 h after incubation (~$3x10^3$ cells with 200 μg/mL of MSNs) summarising the effects of amine surface density on subcellular localisation. Images from (a) to (c) are the corresponding results of type (a) particles with 1 mol%, 5 mol% and 10 mol% of primary amine modification, respectively. The green colour represents functionalised FITC-MSNs; red areas are indicative of endo/lysosomes; yellow colour shows co-localisation of MSNs and endo/lysosomes. Arrows in image (a3) indicate MSNs having escaped endo/lysosomal entrapment (green). The data confirms only 1 mol% primary amine modified MSNs [type (a1)]are capable of effective endo/lysosomal escape. Channel 1: endo/lysosomes stained with LysoTracker Red; Channel 2: green FITC tagged particles; and Channel 3: merged images of channel 1, channel 2 and nucleus stained with blue Hoest33342 (Scale: 10μm; lasers used: 404 nm, 488nm and 561nm for nucleus, nanoparticles and endo/lysosomes, respectively).

In considering that the interior of an endosome/lysosome is known to be highly acidified, becoming more so with fusion/maturation (where internal pH changes from

~6 to 4 from early endosomes through late endosomes to lysosomes[32]). The ζ-potentials of nanoparticles were screened across a broad pH range (Fig. 5.8) in order to examine more closely the relationship between particle amine concentration and subcellular distribution. Herein a 'charging capacity' is defined as the ζ-potential change between pH 4.1 and pH 7.1 (the shaded window in Fig. 5.8). This pH range was chosen as it is representative of the range of pHs within the endo/lysosomal pathway[32] through which endocytosed materials will progress upon internalisation to cells. Importantly, 1 mol%, (a1), and 10 mol%, (a3), of aminated MSNs demonstrated the highest and the lowest charging capacities respectively among three type (a) particles. This behaviour, inverse to the degree of amination, is attributed to the movement of particles's pI towards higher pH with increasing of amination (ascribed to the substitution of surface silanol groups, of pKa ~6.7, with primary APTES amine, pKa ~10.6)[33, 34] and is closely associated with a progressive decrease in the magnitude of the charging capacity within the pH window of interest (pH 7.1 – pH 4.1, Fig, 5.8). This lower charging capacity of the particles with the highest degree of amination [type (a3)] indicated that the lower degree of proton absorption within the endocytic pH window (pH 7.1 – pH 4.1) and thus built weaker osmotic pressure between endocytic compartments and cytoplasm, leading to the entrapment of nanoparticles. Conversely, the particles with high charging capacity are capable of soaking up protons and resulting in endo/lysosomal rupturing.

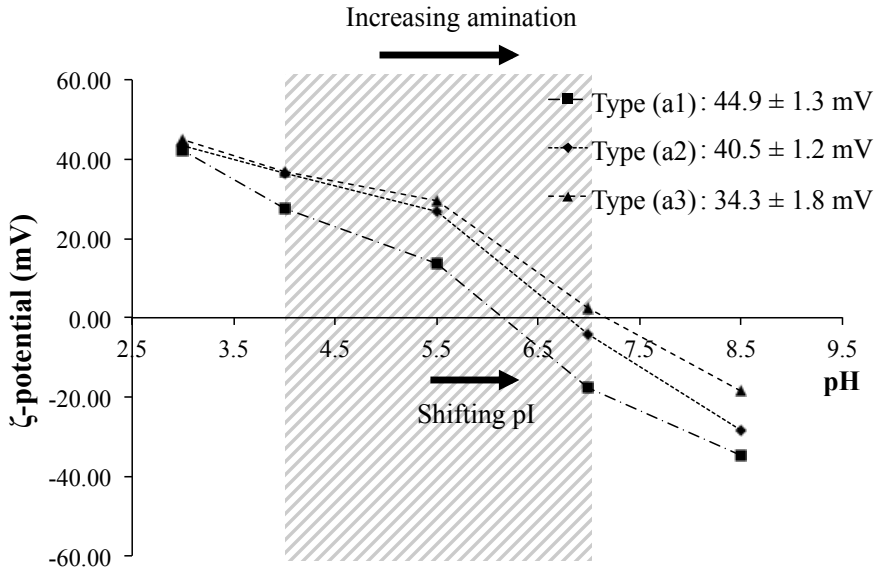


Fig. 5.8 Particle ζ-potentials as a function of solution pH. Graph data points are the mean zeta values across five repetitions. The shaded area highlights the ζ-potential changes associated with the particles moving between pH 7.1 and pH 4.1. The charging capacities of each particle type are stated top right. A higher degree of amination pushes the pI towards higher pH and the associated surface charge changes within the shaded window drops.

5.2.3.2 Effect of Surface Functionalities

To further examine if high charging capacity is the only criteria necessary to facilitate efficient escape, different types of basic groups were conjugated onto the primary amine of this 1 mol% type (a1) particles (Table 5.2; see experimental section in Chapter 2). Imidazole was introduced by post-carboxylation of type (a1) MSNs and subsequent N-(3-dimethylaminopropyl)-N'-ethylcarbodiimide (EDC) and N-hydroxysucciminide (NHS) promoted histamine conjugation [resulting in a 1 mol% imidazole modified surface; type (b); Table 5.2]. A substitution of histamine with histidine generated type (d) particles (particles with both a carboxyl and imidazole moiety, the former moving the pI to lower values). Direct histidine conjugation onto

type (a1) particles generated (c) bearing surface primary amine and imidazole groups at a 1 mol% loading (Molar percentage ratio calculated from the concentration of amine functional groups with respect to silanol source, TEOS, during the reaction). The success of introduction of each functional group was confirmed by tracking the ζ-potential change [Table 5.3; note that the histidine conjugation steps for type (c) and (d) led to the surface charge changes in different directions resulting from the presence of primary amines or carboxyl groups in the final products (see structures in Table 5.2)] and FTIR during each reaction step (Fig. 5.9 – 5.10).

The introduction of various surface amines was monitored by FTIR throughout every step of the reaction (Fig. 5.9 – 5.10). Note that as l mol% modification was too low for detection by FTIR, the data presented are the results of 20 mol% of surface modification. FTIR spectra of native FITC-MSNs, aminated (NH_2-MSNs), carboxylated (COOH-MSNs) and imidazole containing particles [type (b), type (c) and type (d); see Table 5.2] are shown in Fig. 5.9 – 5.10. All MSN samples displayed strong absorption signals at 1065 cm^{-1} and 963 cm^{-1}, characteristic of asymmetric stretching of Si-O-Si bridges and skeletal vibration of the C-O bond stretching, respectively. Additional peaks at 1600 cm^{-1} assigned to the $–NH_2$ bending, were observed for NH_2-MSNs. Conjugation of NH_2 with histidine resulted in an additional peak at 1678 cm^{-1}, assigned to amide I band for the secondary amide, indicative of the success of histidine introduction [Type (c); Fig. 5.10 (a)]. Conversion of NH_2 to COOH led to the emergence of a distinctive absorption at 1719 cm^{-1} representing C=O

(COOH-MSNs). Peaks at 1647 cm^{-1} and 1552 cm^{-1} were assigned to the amide I band and amide II band for the secondary amide after carboxylation [Fig. 5.9 and 5.10 (b)]. After imidazole conjugation [type (b)] or histidine conjugation [type (d)], the carbonyl peak (at 1719 cm^{-1}) of carboxylic acid disappeared, indicating the successful introduction of the imidazole/histadine functional groups onto the nanoparticles.

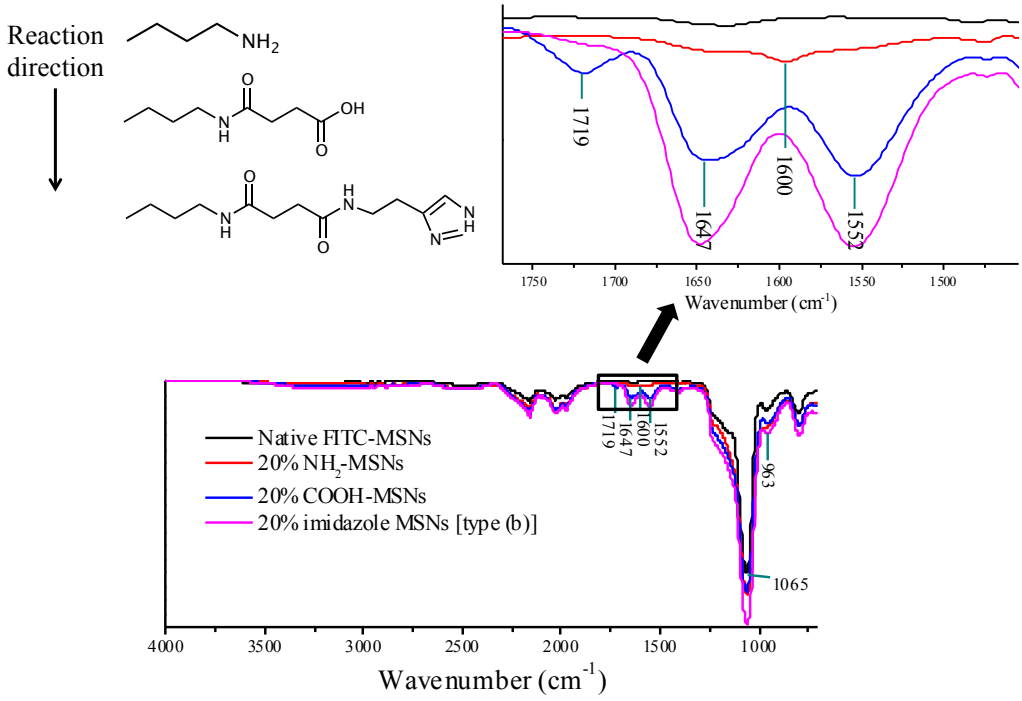


Fig. 5.9 FTIR spectra of native FITC-MSNs, 20 mol% NH_2-MSNs, 20 mol% COOH-MSNs and 20% of type (b) particles. Top-left show chemical structures of the particle surface modifications; top-right spectrum shows highlighted area.

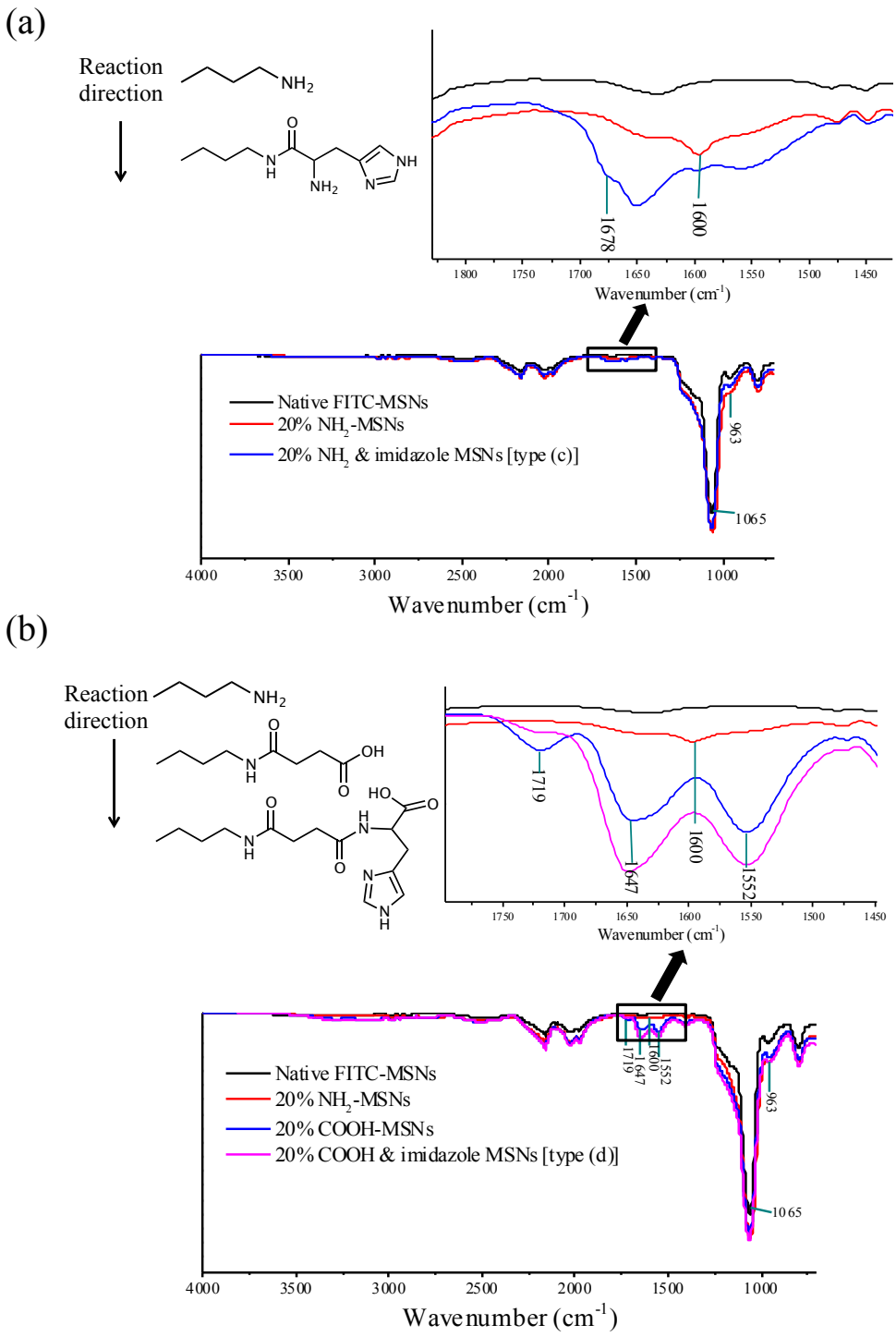


Fig. 5.10 FTIR spectra of (a) native FITC-MSNs, 20 mol% NH_2-MSNs and 20% of type (c) particles; (b) native FITC-MSNs, 20 mol% NH_2-MSNs, 20 mol% COOH-MSNs and 20% of type (d) particles. Top-left show chemical structures of the particle surface modifications; top-right spectrum shows highlighted area.

The specific ζ-potential changes with pH of these particles are summarised in Fig. 5.11. As expected, due to the lack of basic groups, native FITC-MSNs demonstrated the lowest charge change within the pH window. For the other nanoparticles, shifting of pI towards higher pH occurs in the order of particle type (d), (b), (c), (a1) (Fig. 5.11), a trend which can be explained by considering the functional group pKa (where APTES > histidine primary amine > imidazole > histidine imidazole > histidine carboxyl)[33, 35, 36]. Most significant here is the fact that type (c) particles have a pI located at the centre of the pH window of interest (~pH 5.7) and accordingly exhibit the greatest charging capacity (the charging capacities of other particles fall as their pI's move away from this central point).

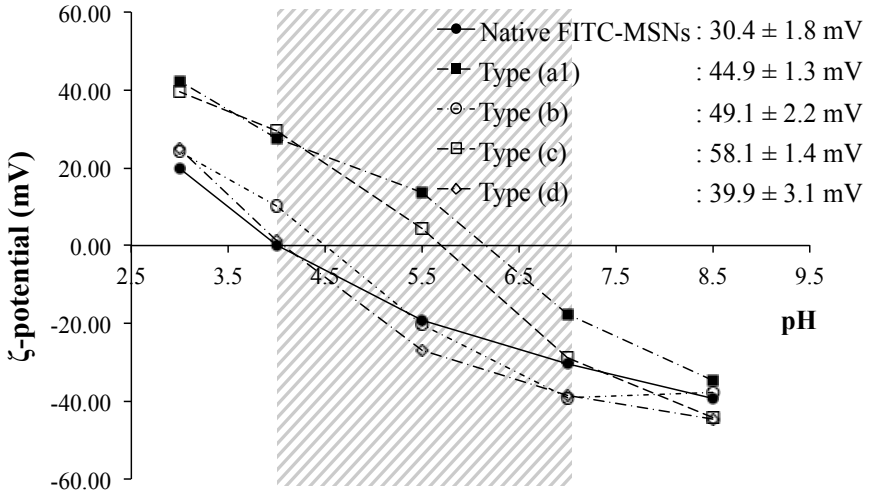


Fig. 5.11 Particle ζ-potentials as a function of solution pH. Graph data points are the mean zeta values across five repetitions. The central shaded area highlights the ζ-potential changes across the pH 7 - pH 4 window. The values next to the particle numbers in the legend are the resulting charging capacities. pI increases through the particle series according to (d) < (b) < (c) < (a1).

Fig. 5.12 summarises the uptake and subcellular distribution characteristics of amine modified nanoparticles (where yellow indicates the co-localisation of MSNs and

endo/lysosomes). It is evident that particles without possession of a basic moiety (native FITC-MSNs) are endo/lysosomally trapped [Fig. 5.12 (a1 – a3)]. Particles with high charging capacities (>40 mV across pH 4.1 – 7.1), including type (a1) and type (c) readily access the cell cytosol [Fig. 5.7 (a1 – a3) and Fig. 5.12 (c1 – c3)] as expected. Significantly, particle types (b) and (d), though exhibiting a large (>40 mV) charge change do not access the cytosol [Fig 5.12 (b1 – b3) and Fig. 5.12 (d1 – d3)] presumably because the lack of significant cationisation (between pH 7.1 to pH 4.1), and thus association with the anionic membrane, even at pH 4.1, is limited [ζ-potentials at pH 4.1 are 10.0 ± 0.2 mV and 1.4 ± 0.2 mV respectively compared to 29.4 ± 0.2 mV for type (c)]. These observations strongly indicated that the induction of endo/lysosomes rupturing and the subsequent particle release resulted from both high osmotic pressure built from the proton absorption and strong electrostatic force between nanoparticles and the membrane of endocytic compartments that presumably creates membrane tension and instability.

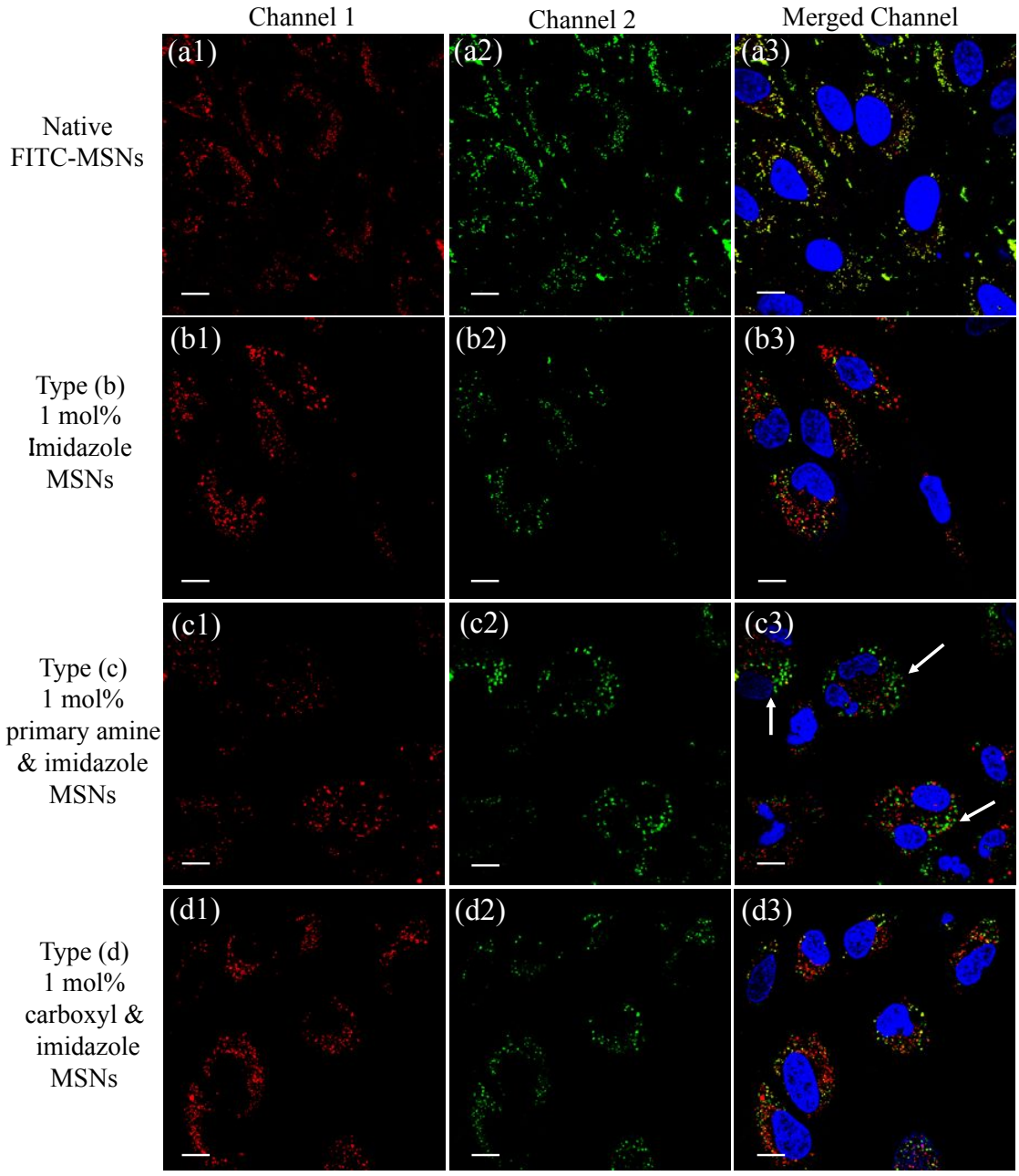


Fig. 5.12 Confocal fluorescent images of Hela cells after 24 h incubation (~$3x10^3$ cells incubated with 200 µg/mL of MSNs) confirming that only 1 mol% primary amine and imidazole co-modified MSNs [type (c)] are capable of escape into the cytosol [showing green and indicated with arrows in image (c3)]. Images from (a) to (d) are the corresponding characteristic results associated with native FITC-MSNs, type (b), type (c) and type (d) particles, respectively. Yellow colour represents co-localised MSNs (green) and endo/lysosomes (red). Scale: 10 µm.

To conclude, 95 ± 8 nm spherical MSNs are readily endocytosed by Hela cells. By default these are endosomally confined. In a comparatively simple consideration of functional group surface density and pKa, one can generate particles for which such entrapment is associated with both substantial (>40 mV change in ζ-potential) charging and cationisation prior to cytosol release. Such changes, and the combination of interparticle repulsion and particle-membrane association that subsequently develops, are suggested to be responsible for mediating a highly effective particle release into the cell cytosol. For nanoparticles which exhibit the appropriate charging and high levels of cationisation [types (a1) and (c)], uptake and endo/lysosomal escape is clearly observed after 24 h imaging.

5.2.3.3 Time-dependent Endo/lysosomal Escape

In order to further examine the time-dependency of this endo/lysosomal escaping process, the subcellular distribution of escapable particles [type (a1) and type (c)] after shorter incubation timeframes (30 min, 5 h) were subsequently monitored and summarised in Fig. 5.13. After 30 min incubation (that typical of early endosome confinement of internalised materials[37-39]), the lack of co-localisation of some type (a1) and type (c) particles with late endosome/lysosomes (observed as green) indicated that the particles have not yet been transported or maturated into these late compartments of the endocytic pathway. After 5 h, the yellow colour demonstrating the perfect overlap of green particles and red endo/lysosomes indicated their fusion into these late compartments and particle entrapment therein. It is, thus, clear that the particles access

the cell cytosol *via* the expected endocytotic pathway, being uptaken within 30 minutes (Fig. 5.13), ultimately localising in lysosomes after some 5 hours prior to escape into the cell cytosol [Fig. 5.7 (a) and Fig. 5.12 (c)] which occurs within 24 h.

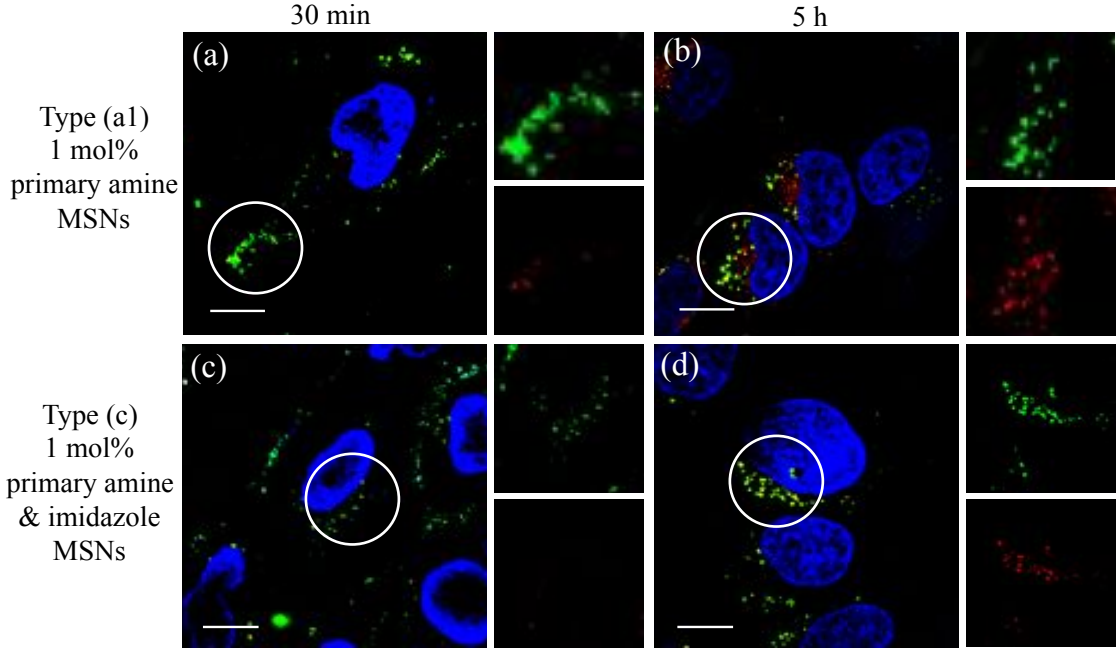


Fig. 5.13 Merged confocal fluorescent images of Hela cells after various incubation times (~3x10^3 cells with 200 μg/mL of MSNs). (a) Type (a1) particles after 30 min incubation; (b) Type (a1) particles after 5 h incubation; (c) Type (c) particles after 30 min incubation and (d) Type (c) particles after 5 h incubation. The spectrally resolved components of the circled regions are magnified and shown on the top-right and bottom-right for FITC tagged MSNs (green) and late endosome/lysosomes (red, stained with LysoTracker Red). After 30 min incubation, the lack of co-localisation of some type (a1) and (c) particles with late endosome/lysosomes (observed as green) indicates that the particles have not yet been transported or maturated into these late compartments of the endocytic pathway. After 5 h, the yellow colour demonstrating the perfect overlap of green particles and red endo/lysosomes indicates their fusion into these late compartments and particle entrapment therein. Scale: 10 μm.

A proposed model for the proton sponge effect facilitated escape of nanoparticles from the endocytic pathway is depicted in Fig. 5.14, where escapable MSNs (>40 mV charging capacity with significant cationisation) are readily endocytosed within 30 min

of incubation[37-39] (Fig. 5.13) and encapsulated in early endosomes (pH ~6.3[32, 40], at which particles are negatively charged as confirmed by ζ-potential and the lack of overlap with LysoTracker Red, a dye which stains late endosomes and lysosomes[41, 42]). Maturation into late endosomes (pH ~5 - 6[36, 44]) was confirmed by the overlap of LysoTracker Red staining and particles, as shown by confocal imaging after 5 h nanoparticle incubation periods, shown in Fig. 5.13. Eventual fusion with lysosomes (pH ~4.6 - 5[36, 44]) is followed by a surge in protonation/cationisaton, and osmotic pressure that results in rupturing of these organelles and cytosolic release [Fig. 5.7 (a) and Fig. 5.12 (c)].

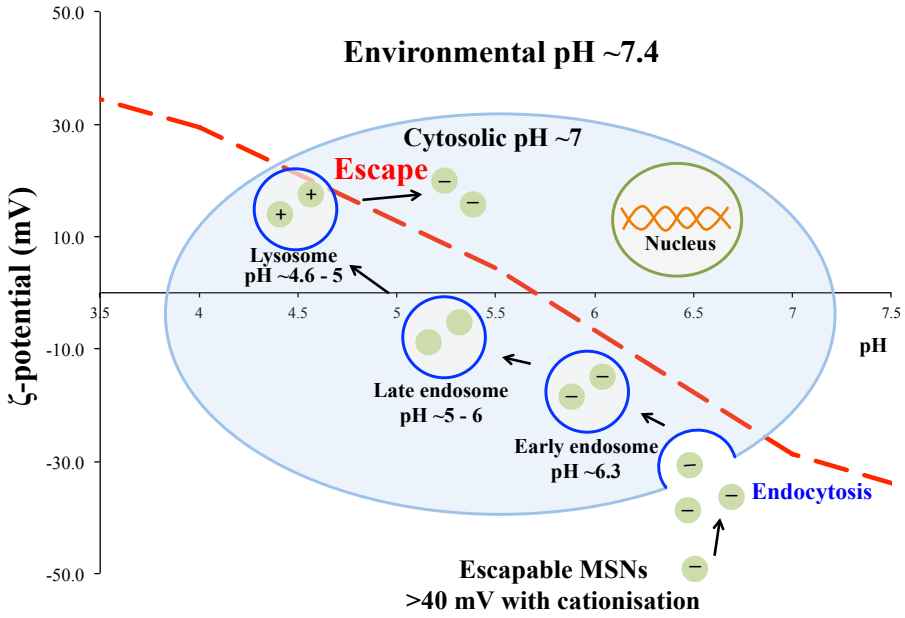


Fig. 5.14 A schematic model of particulate endo/lysosomal escaping process. The red pH profile shown is that of the optimised escapable nanoparticle, type (c). Particles initially exhibit a negative surface charge at pH ~ 7.4. After endocytosis, they are entrapped in acidic early endosomes (pH ~ 6.3) and then late endosomes (pH ~ 5 - 6), during which their surface charge becomes increasingly positive charge. When late endosomes fuse into lysosomes (pH ~ 4.6 - 5) the particle surface is highly cationic and escape occurs [see arrow indications in Fig. 5.12 (c)].

5.3 Conclusions

The interactions of various types of mesoporous silica nanoparticles with Hela cells have been investigated and engineered herein. MSNs can be internalised within 30 min by Hela cancerous cells following an endocytic route. In identifying the colocalisation of unfunctionalised nanoparticles with the late compartments of this internalisation pathway (late endosomes and lysosomes) at 24 h incubation periods, it is evident that MSNs were taken up endocytically. Significantly, variation of the surface charge of the nanoparticles was shown to have little effect on the uptake capability of the cells over 24 h incubation periods, despite some prior reports emphasising the importance of charge-dependent cell uptake. On incorporating a PEG polymer onto nanoparticle surfaces, one can greatly slow down the process of endocytosis, a potentially important feature in the design of long blood-circulated nanoparticles for the applications in monitoring long-term physiological activities. Indeed, cell-nanoparticle interactions over 24 h incubation periods can only be affected by pegylation regardless of surface charges. Shorter 5 h incubation periods of cells with nanoparticles of different surface charges, however, demonstrated different interactions with the negatively charged cell membrane. For slightly positively charged particles (2.5 ± 0.2 mV), strong outer membrane association was observed, attributed to electrostatic attraction, whereas electrostatic repulsion appeared to reduce the endocytosis of highly negatively charged nanoparticles (-43.9 ± 1.1 mV) [both observations were made in comparison to their parent nanoparticles (-30.3 ± 1.6 mV)].

The results here have also demonstrated that through the incorporation of proton buffering agents, such as chloroquine, or through careful tuning of the surface chemistry of nanoparticles, their subcellular distribution upon internalisation can be controlled. Specifically, their escape from the endocytic pathway and release into the cell cytosols was studied. Facilitating endo/lysosomal escape is not only important in preventing uptaken substances from enzymatic degradation but also in their delivery to the necessary sites of action (often in the cytosols and nucleus). In the initial studies herein, a proton sponge agent, chloroquine, was employed to examine the escape of MSNs. This agent resulted in rupturing of the endocytic vesicles of Hela cell, causing the release of trapped nanoparticles. The observations, however, have also demonstrated that the toxic chloroquine has some apparent impact on cell uptake behaviour, leading to inefficient particle uptake. To overcome this, the most significant result within this work has demonstrated the specific design and engineering of nanoparticles with various amine-containing functional groups, which can lead to reliable endo/lysosomal escape without inducing toxicity (see Chapter 6) With a simple consideration of the pKa of the surface amine coating, one can develop a nanoparticle possessing high charging capacity (exceeding 40 mV) with cationisation occurring between pH 7.1 and pH 4.1. Significantly, this pH range is associated with the fusion/maturation of early endosomes to late endosomes/lysosomes of the endocytic pathway, indicating the strong electrostatic interaction between highly cationic particles (as a result of cationisation) and those late endocytic vesicles potentially responsible for the resulting escape. The subcellular localisation of the

nanoparticles was monitored after 30 min, 5 h and 24 h incubation periods, with the lack of late endosomal/lysosomal localization of particles after a shorter 30 min incubation period further indicating that the internalisation of nanoparticles began by encapsulation in early endosomes (30 min), followed by fusion into late endosomes to eventual maturation in lysosomes (5 h to 24 h), a typical endocytosis process. For the most appropriately prepared escapable particles, their internalisation into cells followed this pathway with cytosol access at 24 h incubation. Overall, a high charging capacity originating from the basic amine groups present on the nanoparticle surfaces soaking up protons and the subsequently generated high osmotic pressure in combination with interparticle repulsion and endocytic vesicle membrane association all are thought to contribute to the mediation of effective endo/lysosomal escape. In the next chapter, this endo/lysosomal escaping formulation was employed to deliver therapeutic proteins to the cytosols of Hela cells, resulting in triggered cancer cell death.

5.4 References

1. H. F. Lodish, *Molecular Cell Biology*, W.H. Freeman, New York, 2008.
2. S. Elmore, *Toxicologic Pathology*, 2007, **35**, 495-516.
3. A. Lawen, *Bioessays*, 2003, **25**, 888-896.
4. H. Jin, D. A. Heller, R. Sharma and M. S. Strano, *Acs Nano*, 2009, **3**, 149-158.
5. S. D. Perrault, C. Walkey, T. Jennings, H. C. Fischer and W. C. W. Chan, *Nano Letters*, 2009, **9**, 1909-1915.
6. I. Slowing, B. G. Trewyn and V. S. Lin, *Journal of the American Chemical Society*, 2006, **128**, 14792-14793.
7. D. L. J. Thorek and A. Tsourkas, *Biomaterials*, 2008, **29**, 3583-3590.
8. J. Wang, S. M. Tian, R. A. Petros, M. E. Napier and J. M. DeSimone, *Journal of the American Chemical Society*, 2010, **132**, 11306-11313.
9. K. Knop, R. Hoogenboom, D. Fischer and U. S. Schubert, *Angewandte Chemie-International Edition*, 2010, **49**, 6288-6308.
10. T. Cedervall, I. Lynch, S. Lindman, T. Berggard, E. Thulin, H. Nilsson, K. A. Dawson and S. Linse, *Proceedings of the National Academy of Sciences of the United States of America*, 2007, **104**, 2050-2055.
11. G. J. Doherty and H. T. McMahon, *Annual Review of Biochemistry*, 2009, **78**, 857-902.
12. T. G. Iversen, T. Skotland and K. Sandvig, *Nano Today*, 2011, **6**, 176-185.
13. Y. J. Kwon, *Accounts of Chemical Research*, 2012, **45**, 1077-1088.
14. A. M. Sauer, A. Schlossbauer, N. Ruthardt, V. Cauda, T. Bein and C. Brauchle, *Nano Letters*, 2010, **10**, 3684-3691.
15. V. Sokolova and M. Epple, *Angewandte Chemie-International Edition*, 2008, **47**, 1382-1395.
16. X. J. Jiang and X. D. Wang, *Annual Review of Biochemistry*, 2004, **73**, 87-106.
17. J. B. Delehanty, C. E. Bradburne, K. Boeneman, K. Susumu, D. Farrell, B. C. Mei, J. B. Blanco-Canosa, G. Dawson, P. E. Dawson, H. Mattoussi and I. L. Medintz, *Integrative Biology*, 2010, **2**, 265-277.
18. S. Febvay, D. M. Marini, A. M. Belcher and D. E. Clapham, *Nano Letters*, 2010, **10**, 2211-2219.
19. N. W. S. Kam and H. J. Dai, *Journal of the American Chemical Society*, 2005, **127**, 6021-6026.
20. S. Mishra, J. D. Heidel, P. Webster and M. E. Davis, *Journal of Controlled Release*, 2006, **116**, 179-191.
21. A. K. Varkouhi, M. Scholte, G. Storm and H. J. Haisma, *Journal of Controlled Release*, 2011, **151**, 220-228.
22. T. A. Xia, M. Kovochich, M. Liong, H. Meng, S. Kabehie, S. George, J. I. Zink and A. E. Nel, *Acs Nano*, 2009, **3**, 3273-3286.
23. S. T. Yang, E. Zaitseva, L. V. Chernomordik and K. Melikov, *Biophysical Journal*, 2010, **99**, 2525-2533.

24. H. W. Huang, F. Y. Chen and M. T. Lee, *Physical Review Letters*, 2004, **92**, 198304-198307.
25. S. R. Bhattarai, E. Muthuswamy, A. Wani, M. Brichacek, A. L. Castaneda, S. L. Brock and D. Oupicky, *Pharmaceutical Research*, 2010, **27**, 2556-2568.
26. R. Mo, Q. Sun, J. Xue, N. Li, W. Li, C. Zhang and Q. Ping, *Advanced Materials*, 2012, **24**, 3659-3665.
27. J. Panyam, W. Z. Zhou, S. Prabha, S. K. Sahoo and V. Labhasetwar, *Faseb Journal*, 2002, **16**, 1217-1226.
28. I. A. Khalil, K. Kogure, H. Akita and H. Harashima, *Pharmacological Reviews*, 2006, **58**, 32-45.
29. R. Rahbari, T. Sheahan, V. Modes, P. Collier, C. Macfarlane and R. M. Badge, *Biotechniques*, 2009, **46**, 277-284.
30. A. L. Lehninger, D. L. Nelson and M. M. Cox, *Lehninger Principles of Biochemistry*, W.H. Freeman, New York, 2013.
31. P. O. Seglen, B. Grinde and A. E. Solheim, *European Journal of Biochemistry*, 1979, **95**, 215-225.
32. N. A. Bright, M. J. Gratian and J. P. Luzio, *Current Biology*, 2005, **15**, 360-365.
33. S. Wang, J. Xue, X. Ge, H. Fan, H. Xu and J. R. Lu, *Chemical Communications*, 2012, **48**, 9415-9417.
34. R. K. Iler and Knovel (Firm), Wiley, New York, 1979.
35. F. A. Smith and J. Whittington, *Journal of Experimental Botany*, 1988, **39**, 1549-1560.
36. D. Voet and J. G. Voet, *Biochemistry*, J. Wiley & Sons, New York, 1995.
37. I. I. Slowing, J. L. Vivero-Escoto, C. W. Wu and V. S. Y. Lin, *Advanced Drug Delivery Reviews*, 2008, **60**, 1278-1288.
38. A. Vonderheit and A. Helenius, *Plos Biology*, 2005, **3**, 1225-1238.
39. K. J. Zhou, Y. G. Wang, X. N. Huang, K. Luby-Phelps, B. D. Sumer and J. M. Gao, *Angewandte Chemie-International Edition*, 2011, **50**, 6109-6114.
40. A. Sorkin and M. von Zastrow, *Nature Reviews Molecular Cell Biology*, 2002, **3**, 600-614.
41. F. Belleudi, L. Leone, L. Aimati, M. G. Stirparo, G. Cardinali, C. Marchese, L. Frati, M. Picardo and M. R. Torrisi, *Faseb Journal*, 2006, **20**, 395-397.
42. K. K. Huynh, E. L. Eskelinen, C. C. Scott, A. Malevanets, P. Saftig and S. Grinstein, *Embo Journal*, 2007, **26**, 313-324.

Chapter 6 Nanoparticles for Therapeutic Delivery

6.1 Introduction

Since the discovery of the M41S type of molecular sieves by the Mobil Oil Corporation, a great deal of progress has been made in the synthesis of silica-based mesoporous materials[1, 2]. This porous silica is characterised by extraordinarily high surface areas (> 1000 cm^2g^{-1}), ordered pore systems and well-distributed pore sizes (3 – 5 nm)[1, 2]. A variety of mesoporous materials have been developed, investigated and classified based on structural criteria such as Mobil Composition of Matter silica (MCM-41)[1, 2], Santa Barbara amorphous silica (SBA)-15[3], Michigan State University silica (MSU)-n[4], folded sheet-derived mesoporous silica (FSM)-16[5], and Korean Institute of Technology silica (KIT)-1[6]. These materials were initially used for catalytic and absorption/purification purposes[7-9]. More recently, mesoporous silica nanoparticles (MSNs), due to their high surface areas, large cavity volumes and low native toxicity, have been reported to carry high payloads including both synthetic and biological molecules[10]. Significantly, these constitute not only promising delivery means but also targeting therapies[11-19].

A clear advantage of using MSNs to administer therapeutic agents (specifically hydrophobic drugs) is their ability to allow such agents to overcome their poor water solubility and rapid clearance, that are the main obstacles in their *in vivo* application[10].

In addition, the silane chemistry, which offers the potential for a wide variety of relatively straight forward surface functionalisation provides the possibility of controlled drug release in a cell-specific manner, which could reduce a therapeutic agent's side effects on other healthy cells. Various techniques have been proposed to effectively store drug models within the mesoporous hosts, among which electrostatic interaction might be the simplest method to load and retain the guest drugs[20-23]. The use of MCM-41 materials to study controlled drug delivery of ibuprofen was first investigated by Vallet-Regi and co-workers[10]. Since this initial study, subsequent works have demonstrated that surface functionalities[24, 25], pore sizes[26, 27], pore structures[27], loading conditions[28], as well as the chemical characteristics of the loaded cargos[28, 29] affect both the loading and release of the payloads into and out of porous silica nanoparticles. Importantly, these studies have shown that attractive and repulsive electrostatic interactions as well as hydrophobic effects between the entrapped molecules and the silica surfaces influence the corresponding drug release rate. Ng *et al*., for example, have recently reported that the affinity of charged molecules for the negatively charged silica surface result in variable release profiles depending on the cationic or anionic characteristics of the loaded molecules[29].

While the above systems utilise pore sizes and electrostatic interactions for controlling drug release, others have developed more sophisticated conjugations in which stimuli responsive capping materials are instead employed[11-19, 30-38]. Fujiwara *et al.*, for example, have demonstrated the potential of stimuli-responsive release devices by

controlling the uptake and release of guest molecules from coumarin-functionalised mesoporous nanoparticles using UV radiation[30]. Lin and co-workers have reported a series of nano-caps as gatekeepers for MSNs, including CdS, Au, Fe_3O_4 and polymer nanoparticles, which could be removed by external redox, light or magnetic stimulation leading to the release of loaded drugs[13, 19, 32]. In addition, supramolecular nanomachines, such as 2-pseudorotaxane and 2-rotaxane, have been used as nano-valves[33-35]. Polymers have also been used to cap loaded nanoparticles[18]. You and co-workers, for instance, have reported temperature-controlled release systems utilising a surface bound temperature-responsive polymer[37], while Hong has created a system in which release is governed by a pH-responsive polymer[36]. Recently, the selection of gatekeepers has been shifted to biological materials such as proteins[14, 16, 17, 38], antibodies[11] or peptide aptamers[12, 15] to increase biocompatibility and bio-vectoring. Lin *et al.* have used gluconic acid-modified insulin to cap phenylboronic acid-modified MSNs where the gluconic acid and phenylboronic acid form a cyclic ester which can then be cleaved by saccharides leading to the release of insulin[38]. MSNs have also been end-capped with collagen conjugated through disulfide bonds which respond to the external reducing agents[14].

There are various parameters of MSNs that needs to be evaluated when particles are being designed to deliver internally loaded drugs: 1) loading efficiency, 2) surface charge-dependent drug release efficiency, and 3) the effect of surface modification on release kinetics. Though MSNs' high volume is beneficial in allowing a high payload,

their high surface area is not necessarily an advantageous feature, if, for instance, the loaded drug has a strong interaction with such a high surface area (electrostatic attraction of loaded drugs bearing opposite charges to those on particle pores, for example) which leads to an ineffective release[29]. In addition, a vital requirement for the application of these materials *in vivo* is prevention of premature release[10]. This is particularly important in increasing therapeutic efficiency and minimising side effects[10, 39, 40]. Capping techniques, such as those described earlier, are hence significantly valuable especially if they are responsive to specific external stimulations occurring at the target sites.

The utility of MSNs in therapeutic delivery is not limited to carrying small synthetic drugs. Recently, high specificity and fewer adverse effects[41-45] have made protein therapeutics an attractive topic. The delivery of therapeutic proteins or nucleic acids (DNA, RNA, and oligonucleotides) into live cells have been shown to be potential powerful tools for novel therapeutics and gene transfection. Owing to poor permeability and potentially proteolytic degradation, the introduction of these biomolecules into cells, however, is generally acknowledged to be a challenge[46, 47]. Studies attempting to stabilise proteins and reliably transport them across cell membrane barriers using nanoparticles have been documented with various degrees of success[48-52]. Therapeutic proteins can be delivered by either physical entrapment or chemical attachment on MSNs[52, 53]. For the latter, the conjugation methods are generally adapted from those employed in particle biological capping stated above.

The treatment of cancer currently relies primarily on the use of various forms of 'cytotoxic' chemotherapy and radiation therapy[54]. These interventions can have profound positive results on many hematologic malignancies and a few solid tumours. However, tumours usually consist of mixed populations of malignant cells, some of which are sensitive to chemotherapy while others are resistant, resulting in inefficient therapy[54]. Dose escalation using high-dosage chemotherapy may yield a modest improvement in responses but the side effects of these agents on normal tissues and cells remain serious concerns of these cytotoxic treatments. Significantly, recent accomplishments in the understanding of mechanisms of growth regulation, stress response and programmed cell death of mammalian cells have allowed the development of novel cancer therapy at the cellular or molecular level[54-57]. Indeed, detailed investigations into the apoptosis (or programmed cell death) mechanism noted in Chapter 1 have provided significant insight into the processes involved in cell killing more specifically. Significantly, the release of cytosolic cytochrome *c* from mitochondria is central to the activation of caspase cascade and the subsequent apoptosis. Therefore, it is a proposal in this chapter that exogenous introduction of this protein into cell cytosols could also induce the activation of apoptotic cell death.

Herein, as biologically switchable MRI (magnetic resonance imaging) agents have been developed earlier in Chapter 4 using protein gating to tune the water accessibility to the internalised paramagnetic centres, the same gating concept was also employed in the delivery of internally loaded synthetic drug. The influence of particle surface

functional groups (and their associated charges) and charged model drugs on their loading and release from redox-responsive BSA capped MSNs was assessed. Specifically, the stimuli-triggered release model and its kinetics were subsequently investigated. Significantly, MSNs were also investigated as specific cancer therapeutic delivery vehicles. The delivery of bioconjugated MSNs to cells was explored with the aim of affecting subcellular machineries (such as cytosolic proteins) and monitoring the corresponding apoptotic physiology. Specifically, the utility of MSNs capable of internalisation by live cells and subsequent reliable and rapid escape into the cellular cytosol (using the formulation described in Chapter 5) as scaffolds for surface modification with cytochrome *c* and the examination of their ability to effect an apoptotic response is investigated. Finally the importance of nanoparticle retention of the cytochrome *c*, as opposed to its release, was also assessed in terms of its effectiveness in eliciting a cancerous cell death response.

6.2 Results and Discussion

6.2.1 Drug Loading and Release Studies

To study triggered delivery of internally loaded small synthetic drugs, BSA (bovine serum albumin) was chosen as a nanoparticle mesopore capping agent, due to its bulky size (~6 nm in comparison to the nanoparticle pore radius of 1.6 ± 0.7 nm, see Appendix, Fig. A2 for pore size distribution)[58]. Rhodamine 6G (R6G) was selected as a model drug due to its small molecular size, solubility and characteristic strong optical properties. Plain native MSNs were prepared with excellent colloidal stability (d_{hyd}: 157.0 nm, PDI: 0.12). A variety of R6G-loaded MSNs were subsequently prepared and capped with BSA *via* a disulfide linkage (Fig. 6.1 and Table 6.1).

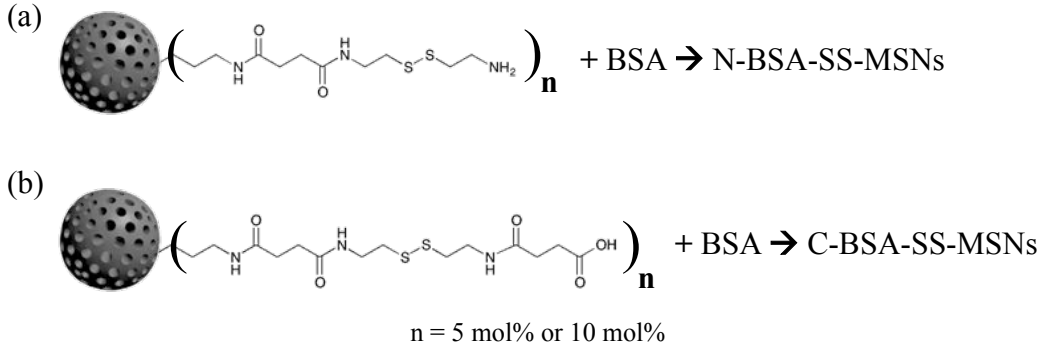


Fig. 6.1 Surface chemistries/structures of disulfide bound MSNs with BSA capping. "n" represents the molar percentage ratio of disulfide linkers and BSA with respect to TEOS during the reaction. Particles made from amine-terminated MSNs and from carboxyl-terminated MSNs are designated as (a) N-BSA-SS-MSNs and (b) C-BSA-SS-MSNs, respectively.

This disulfide linkage was then reductively cleaved by a reducing agent [tris(2-carboxyethyl)phosphine, TCEP] and the release of R6G was monitored. Amine-terminated disulfide linker and carboxyl-terminated disulfide linker were post-

functionalised onto unmodified MSNs with 5 mol% and 10 mol% coverage to investigate the effect of surface charges/functional groups on drug loading and release (mol% was calculated on the basis of the molar percentage ratio of linker groups with respect to silanol source, TEOS, during the reaction). Resulting BSA functionalised amine-terminated MSNs and carboxyl-terminated MSNs are designated as (a) N-BSA-SS-MSNs and (b) C-BSA-SS-MSNs, respectively (Fig. 6.1). Successful disulfide modification was confirmed by FTIR analysis and monitored throughout every step of the reaction (see reaction scheme in Chapter 2)[14]. FTIR spectra of plain, aminated (NH_2-MSNs), carboxylated (COOH-MSNs) and disulfide linked aminated (NH_2-SS-MSNs) and carboxylated (COOH-SS-MSNs) particles are shown in Fig. 6.2. All MSN samples displayed strong absorption signals at 1065 cm^{-1} and 963 cm^{-1}, characteristic of asymmetric stretching of Si-O-Si bridges and skeletal vibration of the C-O bond stretching, respectively. Additional peaks at 1597 cm^{-1} assigned to the $–NH_2$ bending, were observed for NH_2-MSNs. Conversion of NH_2 to COOH led to the emergence of a distinctive absorption at 1719 cm^{-1} representing C=O (COOH-MSNs). Peaks at 1632 cm^{-1} and 1557 cm^{-1} were assigned to the amide I band and amide II band for the secondary amide after carboxylation. After cystamine conjugation, the carbonyl peak (at 1719 cm^{-1}) disappeared indicating the successful introduction of the cystamine linker (NH_2-SS-MSNs). A further conversion of NH_2 end group of cystamine to COOH resulted in an increase in the intensity of the C=O peak (1719 cm^{-1}) (COOH-SS-MSNs).

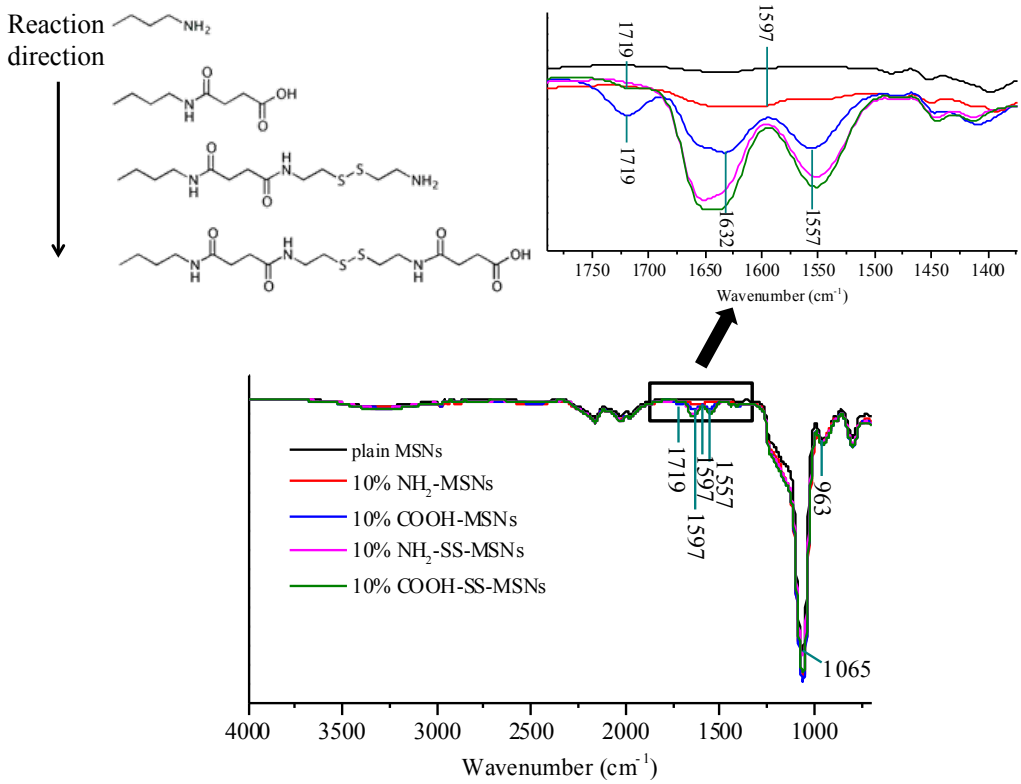


Fig. 6.2 FTIR spectra of plain MSNs, 10 mol% NH_2-MSNs, 10 mol% COOH-MSNs, 10 mol% NH_2-SS-MSNs and 10 mol% COOH-SS-MSNs. Top-left show chemical structures of the particle surface modifications; top-right spectrum shows highlighted area.

Both the loading and release efficiency of the model drug are expected to be influenced by the surface charges or the characteristics of functionalities on the MSNs carriers. It is important to consider both efficiencies when designing a drug-nanoparticle conjugation; however, the release efficiency is more important in determining the effectiveness of therapeutic drugs (as this decides the actual dosage being administrated). Therefore to assess the influence of particle characteristics on release only, it is necessary to maintain consistent loading efficiency across all the particle samples. To eliminate or at least minimise the effect of particle surface charge

on loading behaviour, amine-terminated particles were loaded with R6G in pH 8.5 bicarbonate buffer, whereas loading of carboxyl-terminated particles were carried out in pH 5.5 MES buffer. In this way, the particle surface charges are comparable across all generated samples (-31.0 ± 2.4 mV, -35.3 ± 1.4 mV, -29.9 ± 1.5 mV and -31.7 ± 2.3 mV for 5 mol% aminated, 10 mol% aminated, 5 mol% carboxylated and 10 mol% carboxylated particles). Additionally, the basic R6G molecules are expected to be protonated and thus positively charged under both pH conditions (pH 8.5 and pH 5.5); the variation of loading efficiency (if any) is therefore minimised by keeping electrostatic interaction consistent across samples (Table 6.1).

Table 6.1 Loading and release summaries.

	Loading[a] (μg/mg MSNs)	Release[b] (μg/mg MSNs)	% Release	Event 1 k[c] (%/min$^{1/2}$) (washing)	Event 2 k (%/min$^{1/2}$) (burst release)	Event 3 k (%/min$^{1/2}$) (steady release)
5% modification						
NH_2-terminated MSNs	40.58	6.00	14.78	0.023 ± 0.002	0.450 ± 0.030	0.021 ± 0.001
COOH-terminated MSNs	45.67	3.25	7.12	0.023 ± 0.001	0.403 ± 0.004	0.023 ± 0.002
10% modification						
NH_2-terminated MSNs	33.77	6.93	20.52	0.021 ± 0.001	0.096 ± 0.005	0.021 ± 0.002
COOH-terminated MSNs	41.61	1.78	4.28	0.026 ± 0.000	0.476 ± 0.024	0.030 ± 0.003

[a] amine-terminated MSNs were loaded at pH 8.5 and carboxyl-terminated MSNs were loaded at pH 5.5; [b] Release was carried out in ultrapure water; [c] Release rate constant derived from Peppas equation.

Fig. 6.3 show the corresponding release profiles of four samples as detailed in Table 6.1. The profiles are divided into three regions/events (in order to allow kinetics fitting, described below): 1) release of physically absorbed R6G drug models (a washing procedure, where fast initial release is observed followed by slow and steady diffusion defined by concentration gradient); 2) phase-one release after reducing agent, TCEP, triggered disulfide decapping (the steepest region in the profile, associated with diffusional concentration-gradient controlled release); and 3) phase-two release (final part of the release process, where the release rate is reduced due to internal and external R6G concentration reaching an equilibrium). The loading efficiency (or encapsulation efficiency of BSA capping here) was determined by the difference between initial input drug concentration and the total release concentration in the first event (release of physisorbed R6G only) leading to 40.58 μg, 33.77 μg, 45.67 μg, and 41.61 μg per mg MSNs for 5 mol% NH_2-terminated, 10 mol% NH_2-terminated, 5 mol% COOH-terminated and 10 mol% COOH-terminated particles, respectively (Table 6.1). The data indicated that these loading efficiencies varied <12% (in relative standard deviation), which, as noted above, is presumably the result of lack of difference in particle surface charges in the loading buffers employed. The profiles clearly demonstrated that the first event of release initially had a fast release rate (of physisorbed R6G) due to concentration-controlled diffusion which slowed over time and finally resulted in a plateau where the loaded R6G remained stably within the BSA capped MSNs. Notably here, this steady state (plateau) can be extended to as long as 24 h indicating the likelihood of premature release in the absence of an external-

stimulus (a reducing agent in this work) is low. This is a particularly desirable feature in designing targeting therapy where the therapeutic agents are expected to perform at the targeting site only without any side effect when passing though the administrative routes.

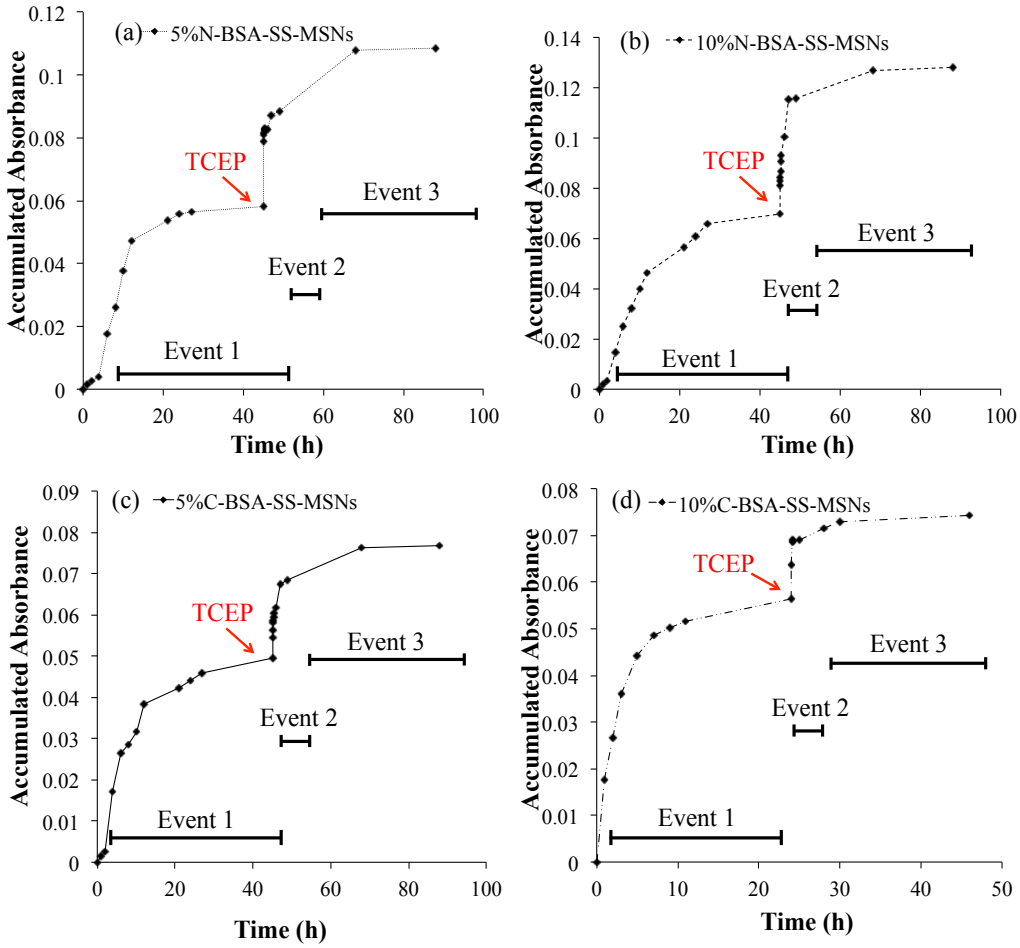


Fig. 6.3 Release profile of (a) 5 mol% N-BSA-SS-MSNs; (b) 10 mol% N-BSA-SS-MSNs; (c) 5 mol% C-BSA-SS-MSNs; (d) 10 mol% C-BSA-SS-MSNs with R6G loading and BSA capping determined by UV-vis spectroscopy. The entire profile can be divided into three events. The first event refers to a washing procedure allowing removal of physisorbed R6G and the second and third events are the TCEP triggered release.

The triggered R6G release was carried out in water by administering a reducing agent (TCEP). The corresponding release efficiency was determined by the total amount released in the second and third events in the profiles (Fig. 6.3). After event 1 release/washing process, R6G was robustly encapsulated in the nanoparticles; upon the addition of TCEP, disulfide cleavage and BSA decapping proceeded almost immediately (where TCEP selectively and completely reduced even the most water-soluble alkyl disulfides over a wide pH range requiring less than 5 min at room temperature[59]). This part of the release profiles consisted of 2 events, a so-called phase-one event (event 2), where the internally trapped R6G diffused out at a steady rate, followed a phase-two event (event 3), when the entire triggered release process finally reached an equilibrium. The resulting release efficiencies of 5 mol% NH_2-terminated, 10 mol% NH_2-terminated, 5 mol% COOH-terminated and 10 mol% COOH-terminated particles were 14.78%, 20.52%, 7.12% and 4.28% with respect to the loading amounts, respectively. These significantly different values (difference > 60% in relative standard deviation) indicate that the release efficiencies of the model drug form MSNs in water are strongly influenced by either surface functionality or surface charge. Nanoparticles bearing acidic carboxyl groups exhibited more negatively charged surfaces than those with basic surface amine groups in water; these thus influence their interaction with positively charged R6G (Fig. 6.4). For all samples, R6G was trapped within the pores by the attraction of between negatively charged particle surfaces and positive R6G. The capping procedure of BSA on the nanoparticles was carried out at neutral pH conditions, resulting in residual internal

positive charges for amine functionalised particles and negative charges for carboxylated particles. Therefore, upon decapping and release, the strong electrostatic repulsion between the positively charged R6G and the amine groups leads to more effective release of cargo, compared to its electrostatic attraction with negative carboxyl groups resulting in less efficient diffusion (5-fold and 2-fold increased release compared with carboxyl-terminated particles for 10 mol% and 5 mol% of surface modification, respectively, Table 6.1).

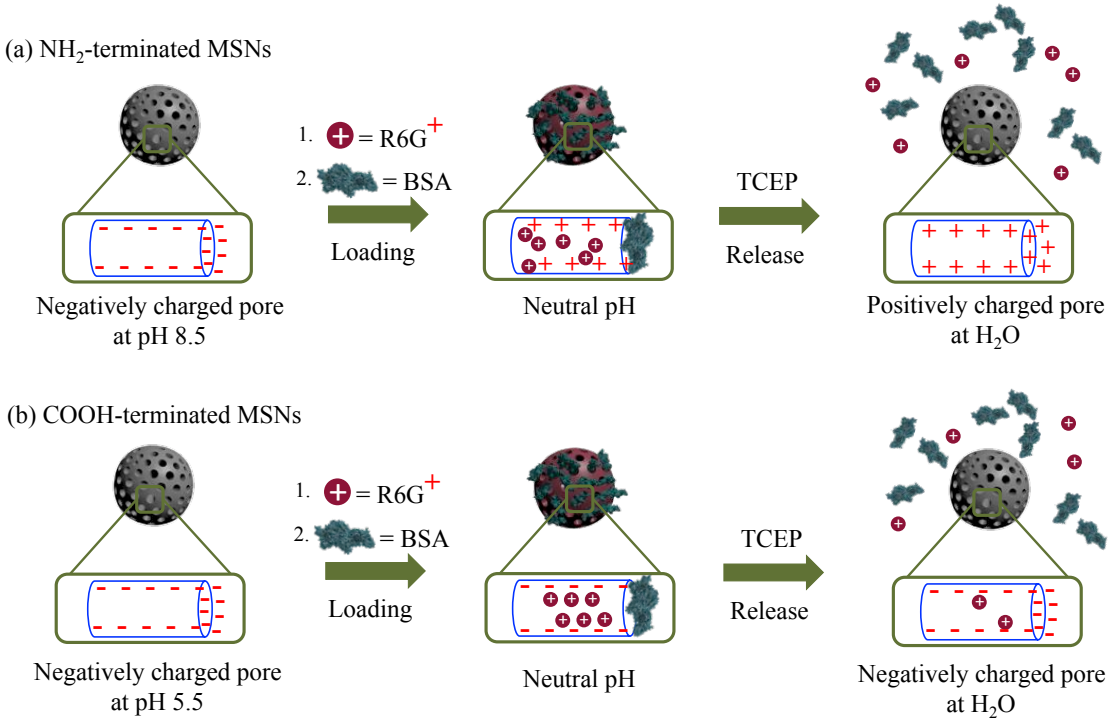


Fig. 6.4 Schematic model of loading and release. Both (a) and (b) particles were negatively charged in buffers, which led to their consistent interaction with positively charged R6G and comparable loading. The capping procedure was carried out at neutral pH conditions and subsequent release was carried out in water using a reducing agents TCEP. Under these conditions the particles possessed positive and negative charge for (a) and (b) respectively and thus demonstrated different interactions with R6G molecules. In (a), the electrostatic repulsion promoted the release; and in (b), the electrostatic attraction made the release inefficient.

Indeed, this surface charge effect has been previously noted in the studies of different release mechanisms[20, 21, 29]. DeShong and co-workers, for example, have investigated pH-sensitive release of R6G from unmodified MSNs and aminated MSNs where in regardless of modification total release in acidic conditions was greater than those obtained in neutral pH 7 conditions[20]. Mou and co-workers, on the other hand, used quaternary ammonium groups to produce positively charged particles loaded with negatively charged drugs (sulfasalazine and salvianolic acid B)[21]. Their results indicated that the highest positively charged MSNs exhibited the slowest release rate, confirming that the nanoparticle vehicle charge plays a significant role in the uptake and release of charged payloads.

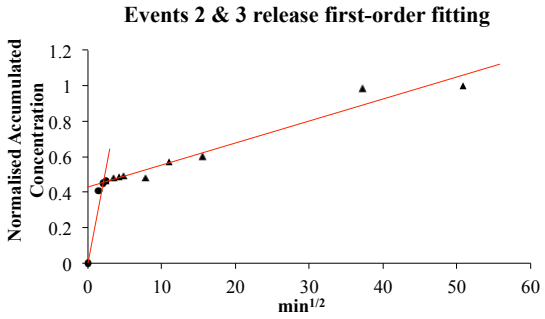
The three-stage releasing mechanism, described thus far in terms of 'events' (Fig. 6.3), can be rationalised by considering drug release kinetics analysed with Peppas equation (Eq. 1)[60, 61].

$$\frac{M_t}{M_\infty} = kt^n \qquad (1)$$

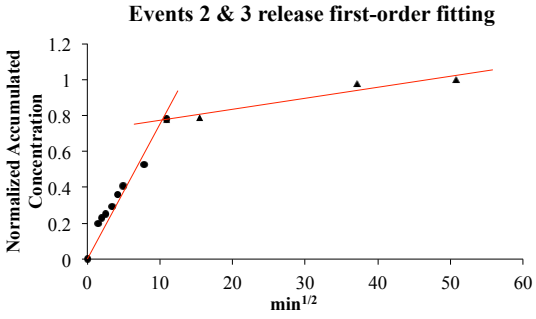
where M_t is the total concentration of guest released at a given time t, M_∞ is the total amount released as time goes to infinity (i.e. complete release), k is a release rate constant, and n is the exponential characteristic of the release mechanism. When $n = 1$, the release mechanism is dissolution-controlled following zero-order kinetics; when $n = 1/2$, the mechanism is diffusion-based following first-order kinetics[60, 61]. It is generally acknowledged that the delivery of covalently bound molecules *via* bond

cleavage follows a dissolution-controlled release mechanism (n = 1 in the Peppas equation), whereas the delivery of physically absorbed molecules *via* a diffusion-based release mechanism (n = 1/2 in the Peppas equation). The release of internally physically entrapped R6G in this chapter therefore follows Eq. 1, with n = 1/2, which was used herein to derive the release rate constant k (which reflects the release rates). By plotting normalised accumulated release concentrations versus square root of times, the corresponding release kinetics constant (k in %/min$^{1/2}$) of each release event can be determined from the slope of the linear fit (Fig. 6.5 and Table 6.1).

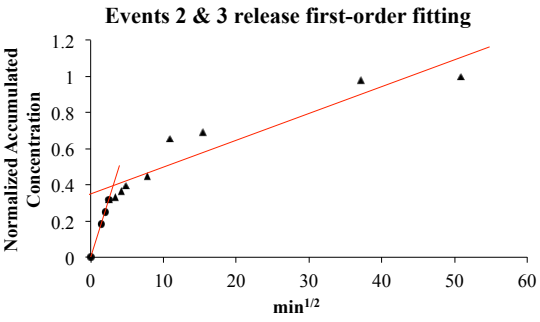
(a) 5 mol% N-BSA-SS-MSNs



(b) 10 mol% N-BSA-SS-MSNs



(c) 5 mol% C-BSA-SS-MSNs



(d) 10 mol% C-BSA-SS-MSNs

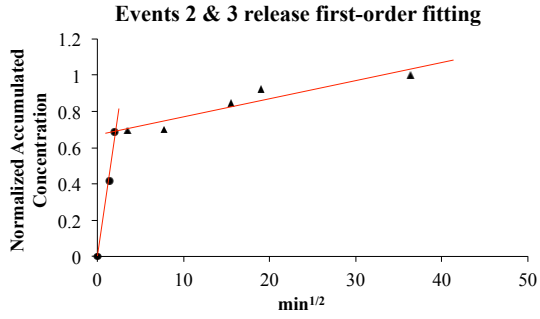


Fig. 6.5 Release kinetics fitting of (a) 5 mol% N-BSA-SS-MSNs; (b) 10 mol% N-BSA-SS-MSNs; (c) 5 mol% C-BSA-SS-MSNs and (d) 10 mol% C-BSA-SS-MSNs according to Peppas equation using first-order fitting. In performing two separate linear fittings (red lines), the release rate constants of events 2 and 3 were obtained.

In event 1, since the process is simply the diffusive release of physisorbed R6G from the outer surface silanol groups and BSA caps, the release rate constants are ~0.02 %/min$^{1/2}$ and are consistent across all samples with standard deviation <0.003 %/min$^{1/2}$ (Table 6.1). Notably, after the removal of the protein caps, carrying out a fitting assuming that the release remains a single process as that in event 1 yielded extremely unacceptable results. Indeed, the plots (concentration vs. time$^{1/2}$) clearly indicated that there exist two diffusive release steps (bimodal release; events 2 and 3) during the process after decapping. In performing linear fitting separately [the two red fitting lines in Fig 6.5], much more satisfactory results and the associated release rate constants (of event 2 and event 3, Fig 6.2; Table 6.1) were determined. Importantly, event 2 demonstrated larger release rate constants compared with those from event 3. This larger release rate constant (or faster release rate) in the beginning of the release of entrapped drugs from MSNs is often called burst release and can be explained as R6G molecules released from the external surface/pore-opening, whereas the slower rate in event 3 was attributed to the result of the release of deeply internalised R6G in combination with a reduced concentration gradient over time (resulting in a steady release). Notably, 10 mol% amine-terminated MSNs demonstrated the slowest burst release rate (0.096 ± 0.005 %/min$^{1/2}$) while the others release at a 5-fold faster rate. This behaviour is thought to be related to high coverage of positively charged functional groups, where the amine groups attract fewer positively charged R6G molecules to the pore entrances, resulting in increases diffusion distance that, in turn, reduces the overall diffusion rate of this step.

In summary, the loading and release of a model drug, R6G, from the internal mesoporous network of MSNs with varying surface functionalities and loading was investigated. In order to prevent premature release the loaded MSNs were then end-capped with proteins *via* redox-responsive disulfide linkers. The encapsulation efficiencies can be kept consistent (<12% in relative standard deviation) across all the investigated samples by carrying out the loading procedures in different pH buffer systems, facilitating control of the particle charges depending on the surface functionalities. The triggered release of R6G from BSA capped MSNs occurred almost immediately after the removal of the capping protein. Importantly, the release demonstrated a bimodal mechanism starting with a burst release indicating the release of pore-entrance localised R6G followed by a steady release of deeply internalised molecules. The release efficiencies were controlled by the electrostatic interactions between cationic R6G and charged nanoparticles, with the most positively charged particles providing the most efficient release (20.52% release) and the most negatively charged particles prohibiting efficient drug release (4.28% release).

6.2.2 Therapeutic Cytochrome *c* Delivery and Programmed Cell Death

This work has invested much effort in studying the delivery of physically entrapped synthetic model drugs within protein capped MSNs which can be released in a triggered stimuli-responsive fashion. Clearly, the delivery system proposed in this chapter can be easily adapted to carry chemotherapeutic drugs (e.g. doxorubicin), which however mainly makes use of 'cytotoxic effect' to induce cancer cell death[62].

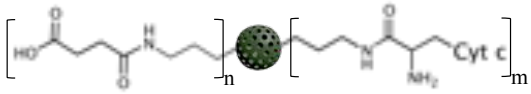
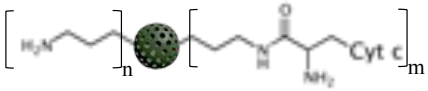
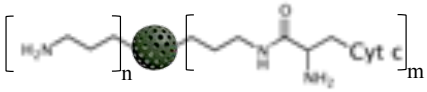
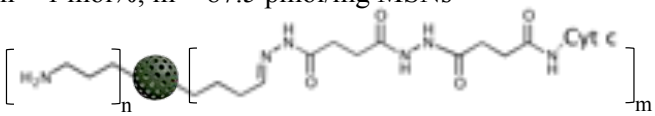
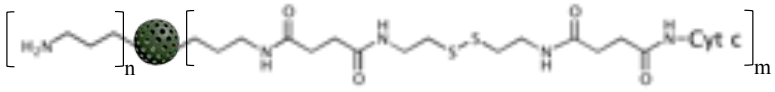
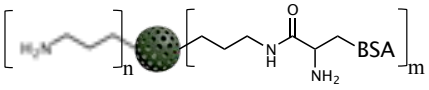
This cytotoxicity not only is less target-specific (due to an association with necrotic cell death, see Chapter 1) but also has significant impact on healthy cells[54, 62]. To kill cells in a more specific way, the induction of programmed cell death (apoptosis) is likely to be a more efficient mechanism. As noted in Chapter 1, the release of cytosolic cytochrome *c* (Cyt c) by mitochondria is central to the caspase cascade and the resulting apoptosis[57]; in the following section the focus was therefore placed on the delivery of 'cytosol accessible' cytochrome *c* and its efficiency in inducing apoptosis in Hela cancer cells. In an effort to effect programmed cell death, there have been several reported approaches to facilitate the delivery of cytochrome *c* to cells. These have included the incubation of loaded nanostructures (carbon nanotubes[48] or MSNs[51, 52]), pH-responsive polyionic micelles[63], or membrane penetration peptide containing liposomes[49, 64]. The observations made across these works are highly varied; in some cases no cell death has been noted, even at comparatively high dose[51] [750 pg/cell, more than 5-fold higher than that used in this work (140 pg/cell)] where the protein supposedly has cytosol access.

Herein, the cytochrome *c* was covalently conjugated onto FITC fluorescently labelled MSNs (Table 6.2; for simplicity the fluorescent MSNs from now on are referred to as MSNs only) rather than physically loaded in the porous networks as reported in the literature where no apoptosis was noted[52]. In doing this, one can prevent the release of free proteins which are susceptible to proteolytic degration (one of the main challenges in protein therapeutics). Importantly, as the activation of cytosolic caspase

is a requirement for triggering apoptosis, the cytochrome *c* carring MSNs have to be localised in the cell cytoplasm[65]. Typically, MSNs are internalised into cells through endocytosis and entrapped in acidic endocytic compartments[66, 67] (noted in Chapter 1 and Chapter 5). To facilitate their escape from this endocytic pathway, the endo/lysosomal escaping formulation developed in Chapter 5 was employed herein. In this formulation, the endo/lysosomal escape is the most efficient when particle surface properties fulfil cationisation and charging capacity exceed 40 mV (achievable based on its pKa by coating 1 mol% of primary amine on particles, for example) across the pH range 4.1 – 7.1. Both endo/lysosomal escapable and entrapped MSNs were prepared by varying the mol% coating of primary amine groups. These particles were labelled with cytochrome *c* using a range of linker chemistries (post grafted on external particle surfaces) *via* standard carbodiimide chemistry (see experimental section in Chapter 2; Table 6.2; for typical electron micrograph see Chapter 3 and 4). The surface density cytochrome *c* was kept very low (87.5 pmol/mg MSNs; protein to amine molar ratio <0.1%) in order to minimise its effect on particle surface charges and endo/lysosomal escape capability (Table 6.3) and was consistent across the investigated samples unless otherwise stated. [See absorbance ratiometric data in Appendix, Fig. A4, where the ratio is determined from the absorbance of protein induced bicinchoninic acid-cuprous complexes (BCA assay) with respect to that of FITC on particles, indicating particle type (a), (b) and (f) containing a comparable protein level on particles whereas type (c) bearing a much higher degree of protein coating. The protein levels on type (d) and (e) can not be directly compared with those

on other particle types, as the linkages employed can interfere with BCA absorption. Note that this technique is only designed for qualitative comparison.]

Table 6.2 Structural representations and hydrodynamic sizes of type (a) cytochrome labelled MSNs with 10 mol% carboxyl coating; type (b) cytochrome labelled MSNs with 1 mol% primary amine coating; type (c) cytochrome labelled MSNs with 0.25 mol% primary amine coating; type (d) acid-responsive cytochrome labelled MSNs with 1 mol% primary amine coating; type (e) redox-responsive cytochrome labelled MSNs with 1 mol% primary amine coating; type (f) BSA labelled MSNs with 1 mol% primary amine coating.

MSN type	Structure	d_{hyd} (nm) & PDI
Type (a)	n = 10 mol%*; m = 87.5 pmol/mg MSNs 	172.2 (0.05)
Type (b)	n = 1 mol%; m = 87.5 pmol/mg MSNs 	177.3 (0.05)
Type (c)	n = 0.25 mol%; m = 41 nmol/mg MSNs 	145.9 (0.09)
Type (d)	n = 1 mol%; m = 87.5 pmol/mg MSNs 	168.6 (0.06)
Type (e)	n = 1 mol%; m = 87.5 pmol/mg MSNs 	171.4 (0.04)
Type (f)	n = 1 mol%; m = 87.5 pmol/mg MSNs 	179.4 (0.12)

*Molar percentage ratio calculated from the concentration of amine functional groups with respect to silanol source, TEOS, during the reaction.

Table 6.3 ζ-potential summaries of biomodified MSNs at different pH.

MSN type	Mean ζ-potential (mV) pH 4.1	Mean ζ-potential (mV) pH 5.5	Mean ζ-potential (mV) pH 7.1	Charging capacity (mV)
(a)	-16.5	-39.7	-49.0	32.5 ± 2.4
(b)	29.3	16.1	-23.5	52.8 ± 1.8
(c)	20.4	16.6	-13.3	33.7 ± 1.1
(d)	39.4	26.3	-13.0	52.4 ± 1.3
(e)	28.0	14.3	-23.8	51.8 ± 2.6
(f)	23.5	11.5	-21.6	45.1 ± 2.4

*Charging capacity is defined as the ζ-potential change between pH 4.1 and pH 7.1.

Type (a) particles, used as negative controls here (endosomal 'entrapment'; capacity <40 mV), were prepared by carboxylating 10 mol% of aminated MSNs followed by 87.5 pmol/mg MSNs of cytochrome coupling, and were the only carboxyl functionalised MSNs of all those generated herein. The same proportion of cytochrome *c* or BSA (87.5 pmol/mg MSNs) was coupled onto 1 mol% of primary amine modified MSNs, to give particle forms (b) and (f) respectively. MSNs particles with a higher cytochrome dose [type (c), 41 nmol/mg MSNs] but without endo/lysosomal escape capability were also produced to further examine the necessity of cytosolic access of cytochrome *c*. Notably, the protein is attached to all of these particles *via* an uncleavable APTES linker. To investigate the importance or otherwise of the release of cytochrome *c* from the particles, acid-responsive hydrazine and redox-responsive disulfide chemistries were used to create cleavable protein linkers [type (d) and (e), respectively; Table 6.2]. The synthesis of disulfide conjugated nanoparticles employed the same protocol used in the preparation of redox-responsive MSNs described earlier. The prescence of hydrozone bonds were also confirmed by FTIR[68] (Fig. 6.6). Note that as l mol% modification was too low for detection by FTIR, the data presented are the

results of 10 mol% of surface modification. The successful functionalisation of MSNs was monitored throughout every step of the reactions. FTIR spectra of plain, aldehyde functionalised and hydrozone functionalised particles are shown in Fig. 6.6. All MSN samples displayed strong absorption signals at 1065 cm^{-1} and 963 cm^{-1}, characteristic of asymmetric stretching of Si-O-Si bridges and skeletal vibration of the C-O bond stretching, respectively. An emerging stretch at 1721 cm^{-1} was observed for aldehyde modified particles, which can be assigned to the C=O stretching (CHO-MSNs). Conjugation of succinic dihydrazide led to the evolution of two additional stretches at 1356 cm^{-1} (CH_2 deformation) and 858 cm^{-1} (primary amine wagging; $CNNH_2$-MSNs).

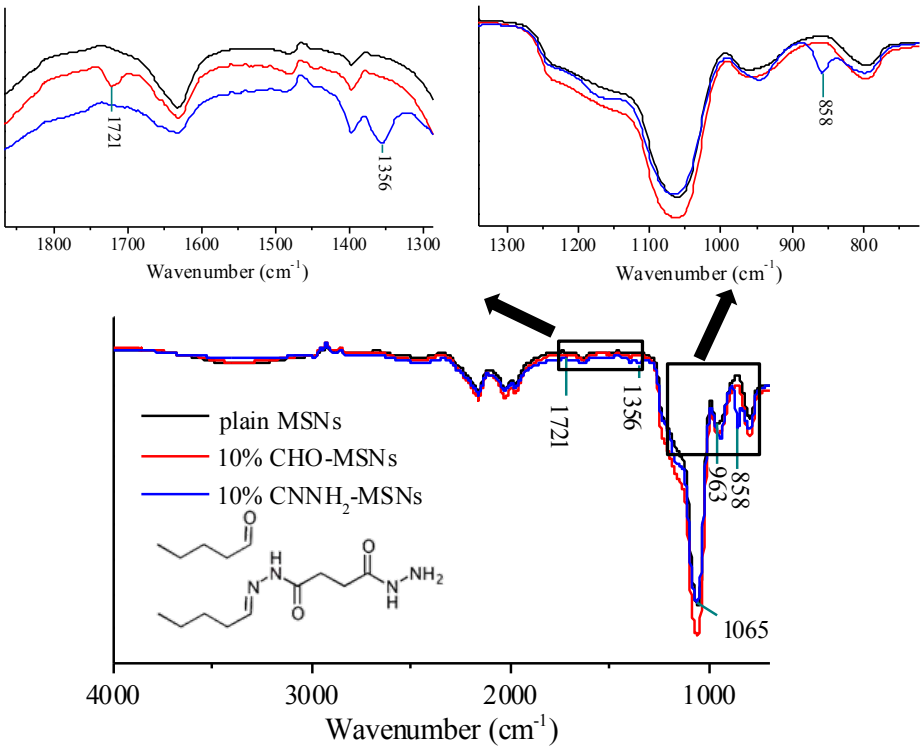


Fig. 6.6 FTIR spectra of plain MSNs, 10 mol% CHO-MSNs and 10 mol% $CNNH_2$-MSNs. Insert are representations of the chemical modifications present on the nanoparticles; top-left and top-right spectra show highlighted areas.

Significantly, in line with the previously identified importance of nanoparticle charging capacity (Chapter 5), protein modified particles (b), (d), (e) and (f) exhibited facile cytosol access (due to their high charging capacity >40 mV accompanied by cationsation across the pH range 4.1 – 7.1) whilst those of (a) and (c) do not (Table 6.3 and Fig. 6.7).

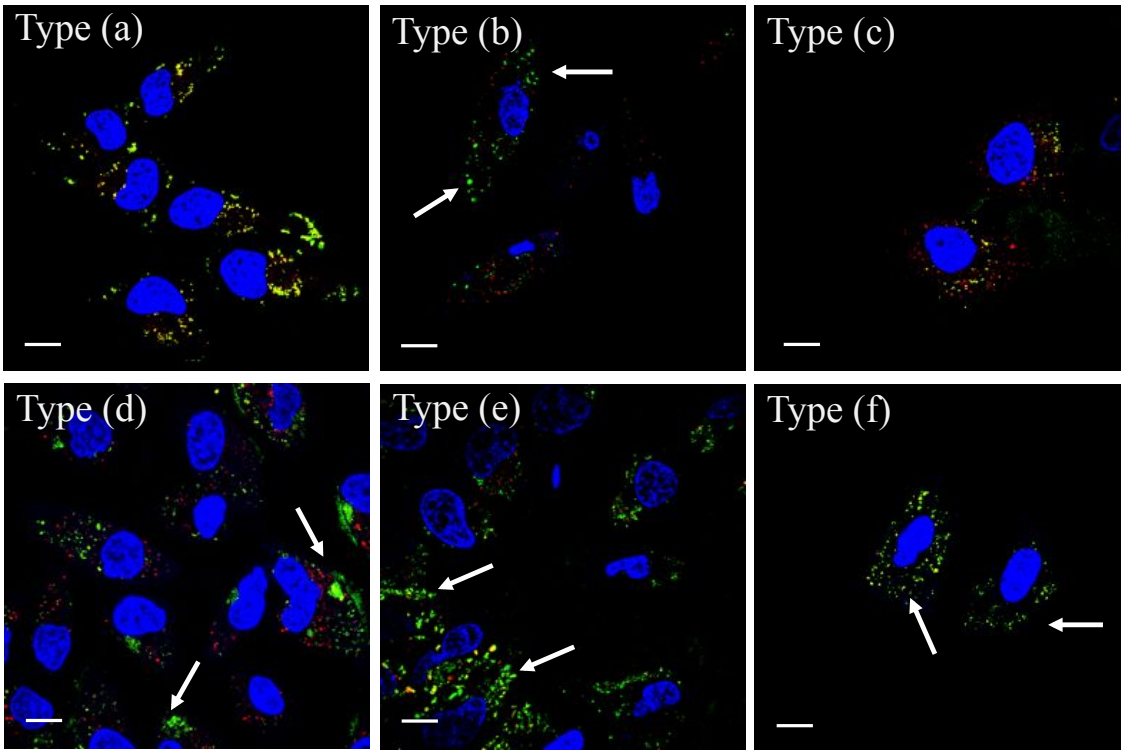


Fig. 6.7 Merged confocal fluorescent images of Hela cells after 24 h incubation with endo/lysosomally entrapped type (a) and type (c) particles and endo/lysosomally escapable type (b), type (d), type (c) and type (f) particles (~$3x10^3$ cells with 200 μg/mL of MSNs) showing endocytic entrapped nanoparticles [yellow in type (a) and type (c)] and cytosol localised (escaped) nanoparticles [green, indicated by white arrows in type (b), type (d), (e) and (f)]. (Scale: 10μm; lasers used: 404 nm, 488nm and 561nm for nucleus stained with Hoechst33342, nanoparticles and endo/lysosomes stained with LysoTracker Red, respectively).

The physiological effects of these particles (with ~$3x10^3$ at 200 μg/mL for 24 h) were examined using propidium iodide (PI), a dead cell stain, where the percentage of cells

having undergone programmed cell death determined from the ratio of PI positive and negative cells, and the results are summarised in Fig. 6.8 and Table 6.4. Notably, native FITC-MSNs exhibit low cytotoxicity, according to PI staining assessment at up to 200 μg/mL dosage compared to nanoparticle-free cell controls. Particles capable of effective endosomal escape but without appended cytochrome (1 mol% NH_2-MSNs) exhibited slightly increased cellular toxicity. To examine the ability of cytochrome *c* to induce apoptosis, the cells were initially incubated with an 140 pg/cell dosage of cytochrome *c* alone led to undetectable uptake and no significant increase in cell death due to the impermeability of cell membrane to this protein. The cells incubation with an equivalent cytochrome *c* modified particles, type (a), incapable of endosomal escape also leads to limited cell death (14.93 ± 5.11%) even for non-escapable particles (c) for which cytochrome loading is markedly increased (500 fold to 41 nmol per mg MSNs; where cell death 9.80 ± 7.21% of cell death). Most striking are the observations made with type (b) particles, which exhibit the greatest endosomal escaping capacity (Table 6.3) coupled with cytochrome *c* functionalisation, where cell death is dramatic (82.13 ± 9.78% across 6 repetitions and 2 separately prepared batches of particles), indicating the necessity of cytosolic access of cytochrome *c*, a fully consistent observation with the cytosolic caspase cascade triggered apoptotic mechanism.

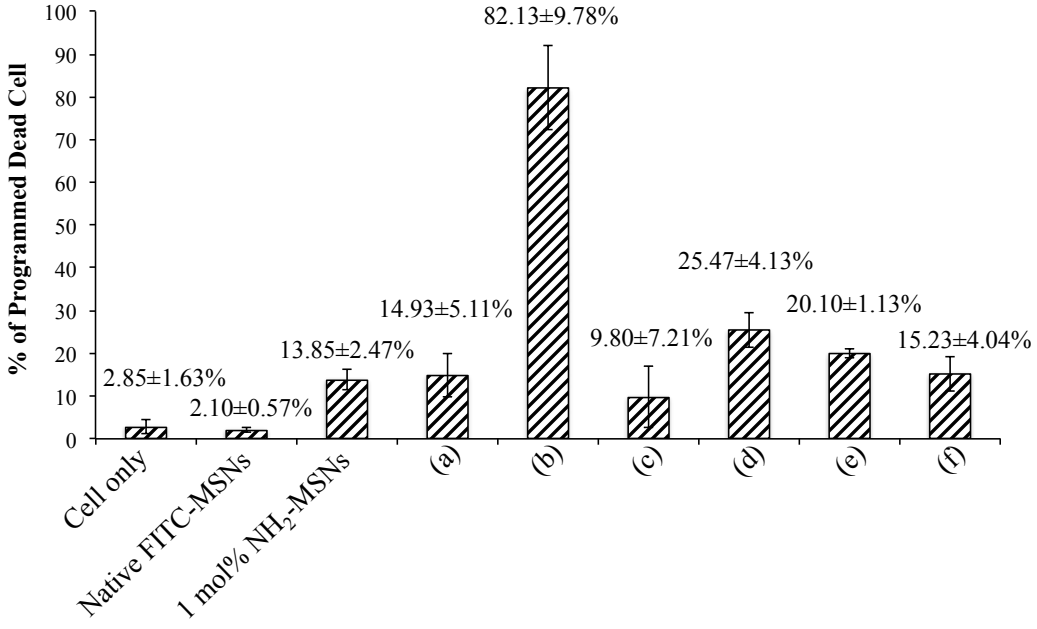


Fig. 6.8 Percentage of programmed cell death (numbers on chart determined from the ratio of PI positive and negative cells) as effected by dosing with different nanoparticle formulations (each dosage ~3x10^3 cells with 200 μg/mL MSNs, 24 h incubation). Data shown are the results of three repetitions across two separately prepared batches of particles (6 repetitions in total).

To further confirm that the triggered death here follows an apoptotic mechanism (and is not based on any innate native nanoparticle toxicity), the cells were co-stained with Annexin V (AnnV), a standard apoptotic cell indicator that binds to phosphatidylserine on the outer membrane leaflet (resulting from membrane inversion, a morphological feature indicative of entry into an apoptotic phase)[56, 69, 70]. As shown in Fig. 6.9, early apoptotic cells are AnnV-positive/PI-negative; late apoptotic cells are AnnV-positive/PI-positive; and necrotic cells are AnnV-negative/PI-positive[69]. These images clearly demonstrate that cells treated with escapable cytochrome labelled particles [type (b)] follow the apoptotic pathway of programmed cell death [Fig. 6.9 (2) and (3)]. As apoptosis is initiated by a series of caspase cascade activated by cytochrome *c*

introduction, the cells were also treated with caspase 3/7 reporter [based on fluorescent inhibitor of caspases (FLICA) technique[71]] at a earlier incubation period (9 h) to confirm the induction of caspase cascade prior to the entry of apoptotic phase by cytochrome labelled nanoparticles [Fig. 6.9 (4)]. The confocal fluorescent image shown in Fig. 6.9 (4) clearly demonstrated that the caspase cascade has been initiated by the red expression of caspase 3/7 resulting from the binding with fluorescent caspase 3/7 reporters.

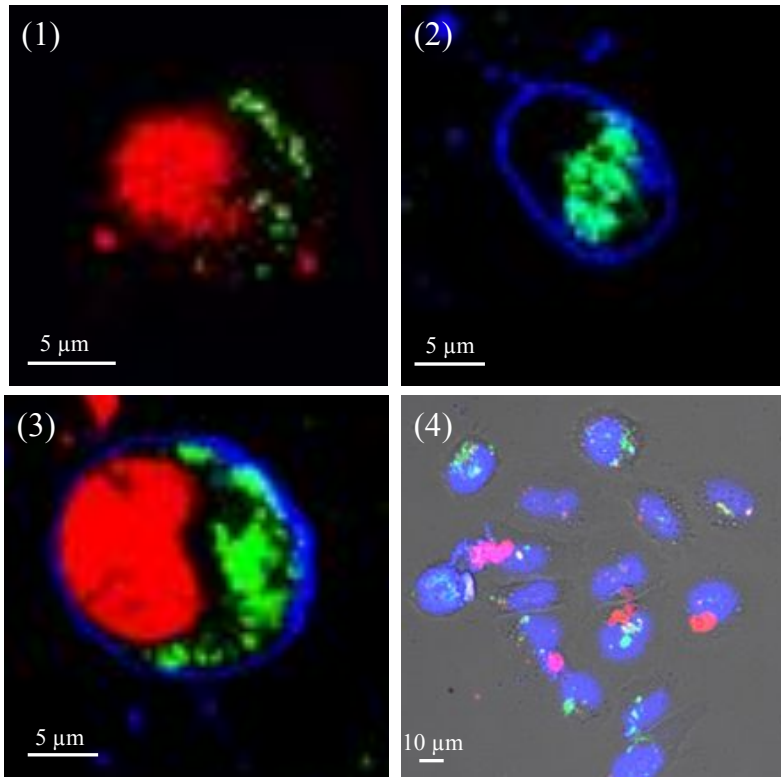


Fig. 6.9 Confocal fluorescent images of HeLa cell suspensions after 24 h incubation with (1) 1 mol% NH_2-MSNs which is only PI-positive indicating these particles having induced necrosis cell death; (2, 3) escapable cytochrome labelled particles type (b) which are AnnV-positive/PI-negative (early apoptosis) and AnnV-positive/PI-positive (late apoptosis), respectively. AnnV (blue) binds phosphatidylserine on the outer membrane leaflet of apoptotic cells and indicates the cell boundary within which MSNs are clearly internalised (green). The dead cell indicator, PI (red), binds to nucleic acids (nucleus). (4) Merged image with bright field, blue nucleus, green escapable cytochrome labelled type (b) particles and red caspase 3/7 at 9 h, indicating these particles having triggered caspase cascade.

Fig. 6.10 summarises the percentages of AnnV-positive cells and PI-positive cells to the total cell number. Significantly, escapable cytochrome labelled particles [type (b)] which induce the highest percentage of cell death show a correspondingly high percentage of AnnV-positive cells (compared to PI-positive cells), confirming, once more, that the cells died apoptotically.

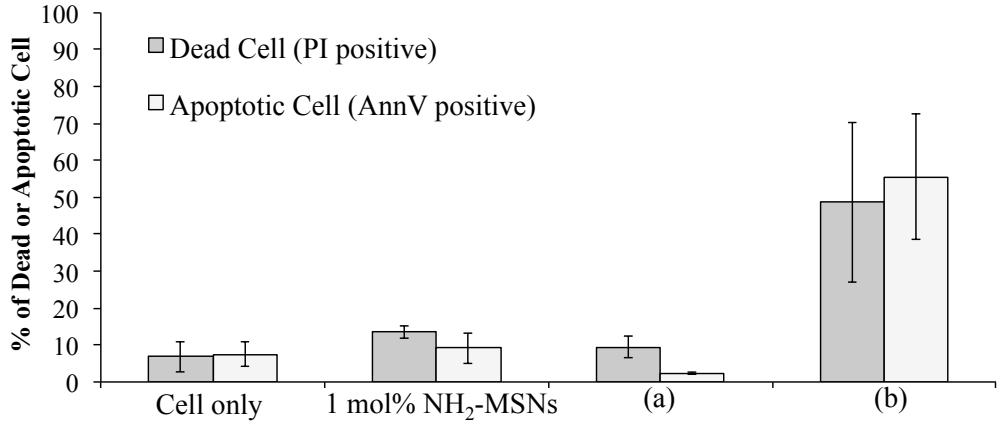


Fig. 6.10 Percentage of programmed cell death of Hela treated with 1 mol% NH_2-MSNs, unescapeable cytochrome labelled particles type (a) and escapable cytochrome labelled particles type (b) determined from the ratio of PI positive and negative cells, indicating cell death and the ratio of AnnV positive and negative cells, indicating an apoptotic mechanism of cell death (each dosage ~$3x10^3$ cells with 200 μg/mL MSNs, 24 h incubation). Data shown are the results of two repetitions. High percentage of AnnV-positive cells (compared to PI-positive cells), confirming that the cells died apoptotically.

To confirm that innate nanoparticle toxicity is not a general feature of any protein decorated MSNs capable of accessing the cellular cytosol i.e. cytochrome *c* was specifically responsible for the observed cell death was, an equivalent dose of BSA (a protein which is not associated with an apoptotic cell death mechanism) labelled particles capable of endosomal escape were examined [type (f)] where only low toxicity levels (15.23 ± 4.04%) are seen (Fig. 6.8). Worth noting again here is the fact that these potent particles are associated with uncleavable anchored cytochromes.

As noted earlier, loss of free protein or peptide activity through proteolytic degradation is well documented[46, 47, 49, 72, 73] and the potential stabilising effect of tethering protein to nanoparticles have been noted[74, 75]. To examine the potential role of this nanoparticle stabilisation in this work, particles were generated with protein bound through a pH or reductively cleavable linker [type (d) and (e)] and examined in terms of their impact on cellular exposure upon bond cleavage and subsequent release of the cytochrome *c* into the cell. Prior work has demonstrated the facile manner in which redox-responsive disulfide bonds are cleaved by cytosol glutathione[76] and hydrazone linkages hydrolysed by the acidic endosomal compartment[50] [also see Appendix Fig. A4, indicating the protein levels on particles are clearly reduced after cleavage using a reducing agent (TCEP) and an acidic pH 4.1 buffer solution (a comparable pH to that in lysosomes) for type (e) and (d) respectively]. Significantly, these particles, though exhibiting high levels of charge change and resulting in efficient cytosol access (see Table 6.3 and Fig. 6.7), induce only limited degrees of cell death (25.47 ± 4.12% and 20.10 ± 1.13% respectively), consistent with the detrimental effects of rapid proteolytic degradation of released cytochrome and, consequently, a markedly reduced efficiency of caspase cascade triggering[46, 64, 72, 77].

It is clear then from these observations that confinement of the apoptosis-triggering protein on MSNs surfaces is vital in stabilising the cytochrome against degradation (by either local pH as the particle moves through the endosomal pathway or cytosolic proteases as cytosol access is finally secured). Significantly, the physiological activity

of the protein in triggering a cell killing caspase cascade is retained in its tethering to the nanoparticle surface, resulting in stabilisation (Table 6.4).

Table 6.4 Summary of programmed cell death (24 h, 200 μg/mL dose), where +: presence of MSNs properties, -: absence of MSNs properties.

MSN type	Charging capacitiy >40 mV*	Highly cationic at pH 4.1*	Endo/lysosomal escape	Immobilised cytochrome *c*	Apoptosis
Native FITC-MSNs	-**	-	-	-	-
1 mol% NH_2-MSNs	+**	+	+	-	-
(a)	+	-	-	+	-
(b)	+	+	+	+	+
(c)	-	+	-	+	-
(d)	+	+	+	-	-
(e)	+	+	+	-	-
(f)	+	+	+	-	-

*Charging capacity is defined as the ζ-potential change between pH 4.1 and pH 7.1.

6.3 Conclusions

In the present work the delivery of physically loaded or chemically conjugated model therapeutic drugs using MSNs has been described. In the former, the delivery of internally loaded small R6G molecules has been studied towards understanding the importance of the influence of electrostatic interaction on drug encapsulation and release. R6G molecules were loaded within the mesoporous networks of MSNs and physically entrapped with removable protein BSA caps. The different linkers employed in protein capping determined the loading/encapsulation efficiency which can also be controlled using different buffer systems to manipulate the electrostatic interaction between R6G and nanoparticles (whose surface charges are controlled by silanol and functional linker groups). Through the use of protein caps, premature release has been successfully prevented and the loaded R6G can stably remain within nanoparticles for as long as 24 h, an important feature in improving drug efficacy. The release of R6G can be effectively achieved by reducing the linker disulfide bonds, facilitating decapping and opening of the porous network. This release is comprised of two phases with different releasing rates – an initial burst release and a final steady release. From a kinetic perspective, both processes followed a diffusion-controlled mechanism described by the Peppa's first order equation. Qualitatively, the release rate is decided by particle-drug electrostatic interaction. In the case of particles with concentrated amine groups localised on outer particle surfaces (positively charged), the electrostatic repulsion between cationic R6G and amine groups led to the slowest release rate among all the investigated samples in this chapter. Significantly, these

results have not only indicated the importance of electrostatic interaction in controlling the effectiveness of drug delivery but also suggested the great potential that MSNs have in designing novel triggered delivery systems.

The results here have also demonstrated that covalently conjugation of therapeutic proteins can be reliably delivered to the cytosolic cellular machinery of cancer cells where they can efficiently affect cellular physiology. Notably, this protein-nanoparticle conjugation is able to robustly stabilise and protect the carried proteins from rapid degradation whilst retaining their activity. Specifically, nanoparticle vehicles capable of entering the cytosol have allowed membrane impermeable cytochrome *c* to be administrated to trigger a caspase cascade within the Hela cytoplasm and to induce the eventual programmed cell death. On incorporating a low dose (140 pg/cell) of this protein onto the surface of optimised fluorescent MSN formulations it is possible to induce programmed cell death with remarkable efficacy (82.13 ± 9.78%), considerably exceeding those observed on other means of translocation of this cytochrome[44, 64] in Human cervical carcinoma HeLa cells. Significantly, this work has provided insight for the future in the development of nanoparticle-based therapies.

6.4 References

1. J. S. Beck, J. C. Vartuli, W. J. Roth, M. E. Leonowicz, C. T. Kresge, K. D. Schmitt, C. T. W. Chu, D. H. Olson, E. W. Sheppard, S. B. Mccullen, J. B. Higgins and J. L. Schlenker, *Journal of the American Chemical Society*, 1992, **114**, 10834-10843.
2. C. T. Kresge, M. E. Leonowicz, W. J. Roth, J. C. Vartuli and J. S. Beck, *Nature*, 1992, **359**, 710-712.
3. D. Y. Zhao, J. L. Feng, Q. S. Huo, N. Melosh, G. H. Fredrickson, B. F. Chmelka and G. D. Stucky, *Science*, 1998, **279**, 548-552.
4. S. A. Bagshaw, E. Prouzet and T. J. Pinnavaia, *Science*, 1995, **269**, 1242-1244.
5. S. Inagaki, Y. Fukushima and K. Kuroda, *Journal of the Chemical Society-Chemical Communications*, 1993, 680-682.
6. R. Ryoo, J. M. Kim, C. H. Ko and C. H. Shin, *Journal of Physical Chemistry*, 1996, **100**, 17718-17721.
7. A. T. Dickschat, F. Behrends, M. Bühner, J. Ren, M. Weiß, H. Eckert and A. Studer, *Chemistry – A European Journal*, 2012, **18**, 16689-16697.
8. G. J. D. Soler-illia, C. Sanchez, B. Lebeau and J. Patarin, *Chemical Reviews*, 2002, **102**, 4093-4138.
9. K. K. Unger, D. Kumar, M. Grun, G. Buchel, S. Ludtke, T. Adam, K. Schumacher and S. Renker, *Journal of Chromatography A*, 2000, **892**, 47-55.
10. M. Vallet-Regi, A. Ramila, R. P. del Real and J. Perez-Pariente, *Chemistry of Materials*, 2001, **13**, 308-311.
11. E. Climent, A. Bernardos, R. Martinez-Manez, A. Maquieira, M. D. Marcos, N. Pastor-Navarro, R. Puchades, F. Sancenon, J. Soto and P. Amoros, *Journal of the American Chemical Society*, 2009, **131**, 14075-14080.
12. E. Climent, R. Martinez-Manez, F. Sancenon, M. D. Marcos, J. Soto, A. Maquieira and P. Amoros, *Angewandte Chemie-International Edition*, 2010, **49**, 7281-7283.
13. C. Y. Lai, B. G. Trewyn, D. M. Jeftinija, K. Jeftinija, S. Xu, S. Jeftinija and V. S. Y. Lin, *Journal of the American Chemical Society*, 2003, **125**, 4451-4459.
14. Z. Luo, K. Y. Cai, Y. Hu, L. Zhao, P. Liu, L. Duan and W. H. Yang, *Angewandte Chemie-International Edition*, 2011, **50**, 640-643.
15. V. C. Ozalp and T. Schafer, *Chemistry – A European Journal*, 2011, **17**, 9893-9896.
16. A. Schlossbauer, J. Kecht and T. Bein, *Angewandte Chemie-International Edition*, 2009, **48**, 3092-3095.
17. A. Schlossbauer, S. Warncke, P. M. E. Gramlich, J. Kecht, A. Manetto, T. Carell and T. Bein, *Angewandte Chemie-International Edition*, 2010, **49**, 4734-4737.
18. N. Singh, A. Karambelkar, L. Gu, K. Lin, J. S. Miller, C. S. Chen, M. J. Sailor and S. N. Bhatia, *Journal of the American Chemical Society*, 2011, **133**, 19582-19585.

19. J. L. Vivero-Escoto, I. I. Slowing, C. W. Wu and V. S. Y. Lin, *Journal of the American Chemical Society*, 2009, **131**, 3462-3463.
20. P. DeMuth, M. Hurley, C. W. Wu, S. Galanie, M. R. Zachariah and P. DeShong, *Microporous and Mesoporous Materials*, 2011, **141**, 128-134.
21. C. H. Lee, L. W. Lo, C. Y. Mou and C. S. Yang, *Advanced Functional Materials*, 2008, **18**, 3283-3292.
22. Q. J. He, J. M. Zhang, F. Chen, L. M. Guo, Z. Y. Zhu and J. L. Shi, *Biomaterials*, 2010, **31**, 7785-7796.
23. Q. J. He, J. L. Shi, X. Z. Cui, J. J. Zhao, Y. Chen and J. Zhou, *Journal of Materials Chemistry*, 2009, **19**, 3395-3403.
24. B. Munoz, A. Ramila, J. Perez-Pariente, I. Diaz and M. Vallet-Regi, *Chemistry of Materials*, 2003, **15**, 500-503.
25. S. W. Song, K. Hidajat and S. Kawi, *Langmuir*, 2005, **21**, 9568-9575.
26. P. Horcajada, A. Ramila, J. Perez-Pariente and M. Vallet-Regi, *Microporous and Mesoporous Materials*, 2004, **68**, 105-109.
27. J. Andersson, J. Rosenholm, S. Areva and M. Linden, *Chemistry of Materials*, 2004, **16**, 4160-4167.
28. J. Salonen, L. Laitinen, A. M. Kaukonen, J. Tuura, M. Bjorkqvist, T. Heikkila, K. Vaha-Heikkila, J. Hirvonen and V. P. Lehto, *Journal of Controlled Release*, 2005, **108**, 362-374.
29. J. B. S. Ng, P. Kamali-Zare, H. Brismar and L. Bergstrom, *Langmuir*, 2008, **24**, 11096-11102.
30. N. K. Mal, M. Fujiwara and Y. Tanaka, *Nature*, 2003, **421**, 350-353.
31. D. G. He, X. X. He, K. M. Wang, J. Cao and Y. X. Zhao, *Langmuir*, 2012, **28**, 4003-4008.
32. S. Giri, B. G. Trewyn, M. P. Stellmaker and V. S. Y. Lin, *Angewandte Chemie-International Edition*, 2005, **44**, 5038-5044.
33. S. Angelos, Y. W. Yang, N. M. Khashab, J. F. Stoddart and J. I. Zink, *Journal of the American Chemical Society*, 2009, **131**, 11344-11346.
34. R. Hernandez, H. R. Tseng, J. W. Wong, J. F. Stoddart and J. I. Zink, *Journal of the American Chemical Society*, 2004, **126**, 3370-3371.
35. T. D. Nguyen, H. R. Tseng, P. C. Celestre, A. H. Flood, Y. Liu, J. F. Stoddart and J. I. Zink, *Proceedings of the National Academy of Sciences of the United States of America*, 2005, **102**, 10029-10034.
36. C. Y. Hong, X. Li and C. Y. Pan, *Journal of Materials Chemistry*, 2009, **19**, 5155-5160.
37. Y. Z. You, K. K. Kalebaila, S. L. Brock and D. Oupicky, *Chemistry of Materials*, 2008, **20**, 3354-3359.
38. Y. N. Zhao, B. G. Trewyn, I. I. Slowing and V. S. Y. Lin, *Journal of the American Chemical Society*, 2009, **131**, 8398-8400.
39. F. Alexis, E. M. Pridgen, R. Langer and O. C. Farokhzad, *Handbook of Experimental Pharmacology*, 2010, 55-86.
40. Q. Zhang, F. Liu, K. T. Nguyen, X. Ma, X. J. Wang, B. G. Xing and Y. L. Zhao, *Advanced Functional Materials*, 2012, **22**, 5144-5156.

41. B. Leader, Q. J. Baca and D. E. Golan, *Nature Reviews Drug Discovery*, 2008, **7**, 21-39.
42. P. J. Carter, *Experimental Cell Research*, 2011, **317**, 1261-1269.
43. S. Kobsa and W. M. Saltzman, *Pediatric Research*, 2008, **63**, 513-519.
44. F. Li, A. Srinivasan, Y. Wang, R. C. Armstrong, K. J. Tomaselli and L. C. Fritz, *Journal of Biological Chemistry*, 1997, **272**, 30299-30305.
45. V. Sokolova and M. Epple, *Angewandte Chemie-International Edition*, 2008, **47**, 1382-1395.
46. C. Adessi and C. Soto, *Current Medicinal Chemistry*, 2002, **9**, 963-978.
47. D. A. Smith and H. van de Waterbeemd, *Current Opinion in Chemical Biology*, 1999, **3**, 373-378.
48. N. W. S. Kam and H. J. Dai, *Journal of the American Chemical Society*, 2005, **127**, 6021-6026.
49. S. K. Kim, M. B. Foote and L. Huang, *Biomaterials*, 2012, **33**, 3959-3966.
50. C. H. Lin, S. H. Cheng, W. N. Liao, P. R. Wei, P. J. Sung, C. F. Weng and C. H. Lee, *International Journal of Pharmaceutics*, 2012, **429**, 138-147.
51. H. S. Park, C. Kim, H. J. Lee, J. H. Choi, S. G. Lee, Y. P. Yun, I. C. Kwon, S. J. Lee, S. Y. Jeong and S. C. Lee, *Nanotechnology*, 2010, **21**, 225101-225109.
52. I. I. Slowing, B. G. Trewyn and V. S. Y. Lin, *Journal of the American Chemical Society*, 2007, **129**, 8845-8849.
53. J. Mendez, A. Monteagudo and K. Griebenow, *Bioconjugate Chemistry*, 2012, **23**, 698-704.
54. Y. A. Hannun, *Blood*, 1997, **89**, 1845-1853.
55. F. T. Andon and B. Fadeel, *Accounts of Chemical Research*, 2012.
56. S. Elmore, *Toxicologic Pathology*, 2007, **35**, 495-516.
57. X. J. Jiang and X. D. Wang, *Annual Review of Biochemistry*, 2004, **73**, 87-106.
58. J. W. Anderegg, W. W. Beeman, S. Shulman and P. Kaesberg, *Journal of the American Chemical Society*, 1955, **77**, 2927-2937.
59. U. T. Ruegg and J. Rudinger, *Methods in Enzymology*, 1977, **47**, 111-116.
60. A. Bernardos, E. Aznar, C. Coll, R. Martinez-Manez, J. M. Barat, M. D. Marcos, F. Sancenon, A. Benito and J. Soto, *Journal of Controlled Release*, 2008, **131**, 181-189.
61. H. Y. Lian, Y. H. Liang, Y. Yamauchi and K. C. W. Wu, *Journal of Physical Chemistry C*, 2011, **115**, 6581-6590.
62. A. Koceva-Chyla, M. Jedrzejczak, J. Skierski, K. Kania and Z. Jozwiak, *Apoptosis*, 2005, **10**, 1497-1514.
63. Y. Lee, T. Ishii, H. Cabral, H. J. Kim, J. H. Seo, N. Nishiyama, H. Oshima, K. Osada and K. Kataoka, *Angewandte Chemie-International Edition*, 2009, **48**, 5309-5312.
64. M. P. Barnes and W. C. Shen, *International Journal of Pharmaceutics*, 2009, **369**, 79-84.
65. A. Lawen, *Bioessays*, 2003, **25**, 888-896.
66. G. J. Doherty and H. T. McMahon, *Annual Review of Biochemistry*, 2009, **78**, 857-902.

67. F. Lu, S. H. Wu, Y. Hung and C. Y. Mou, *Small*, 2009, **5**, 1408-1413.
68. C. H. Lee, S. H. Cheng, I. P. Huang, J. S. Souris, C. S. Yang, C. Y. Mou and L. W. Lo, *Angewandte Chemie-International Edition*, 2010, **49**, 8214-8219.
69. D. Baskic, S. Popovic, P. Ristic and N. N. Arsenijevic, *Cell Biology International*, 2006, **30**, 924-932.
70. M. H. Cho, E. J. Lee, M. Son, J. H. Lee, D. Yoo, J. W. Kim, S. W. Park, J. S. Shin and J. Cheon, *Nature Materials*, 2012.
71. Z. Darzynkiewicz, P. Pozarowski, B. W. Lee and G. L. Johnson, *Methods in Molecular Biology*, 2011, **682**, 103-114.
72. E. Ferraro, A. Pulicati, M. T. Cencioni, M. Cozzolino, F. Navoni, S. di Martino, R. Nardacci, M. T. Carri and F. Cecconi, *Molecular Biology of the Cell*, 2008, **19**, 3576-3588.
73. J. Kalia and R. T. Raines, *Current Organic Chemistry*, 2010, **14**, 138-147.
74. B. J. Jordan, R. Hong, B. Gider, J. Hill, T. Emrick and V. M. Rotello, *Soft Matter*, 2006, **2**, 558-560.
75. L. K. Petersen, C. K. Sackett and B. Narasimhan, *Acta Biomaterialia*, 2010, **6**, 3873-3881.
76. A. M. Sauer, A. Schlossbauer, N. Ruthardt, V. Cauda, T. Bein and C. Brauchle, *Nano Letters*, 2010, **10**, 3684-3691.
77. H. A. Huffman, M. Sadeghi, E. Seemuller, W. Baumeister and M. F. Durin, *Biochemistry*, 2003, **42**, 8679-8686.

Chapter 7 Conclusions and Future Work

In this work, the synthesis of responsive theranostic mesoporous silica nanoparticles has been reported. Through fine-tuning the concentration and the reaction duration, it has been possible to control the location of introduced functional group within the mesoporous network, allowing exploitation of the unique network within these silica particles. Clinically used Gd^{3+} molecular MRI contrast agents have been selectively biased either on the external surfaces of the nanoparticles or within the pores. In doing this, one can influence the vital water interactions with the Gd^{3+}-chelate and hence its MR contrast properties. Specifically, the advantageous confined water environment present near the Gd^{3+}-centres internalized within the porous networks of the particles has resulted in an unprecedentedly high contrast (T_1 relaxivity = 39.26 $mM^{-1}s^{-1}$) at clinically relevant field strength. Within this special confined environment, the Gd^{3+}-centres are thought to enjoy fast proton exchange with the bulk solvent and efficient local magnetic field perturbation to the diffusing water. In addition, the beneficial slow tumbling resulting from particle conjugation has also contributed to the overall enhanced imaging contrast. In this way, particles with exceptionally high image contrast at very low Gd^{3+} loading (1.37 wt%) have been prepared.

By virtue of confinement of Gd^{3+} and water, these high contrast MSNs based MRI contrast agents have been further investigated in designing a new class of tunable MRI agents through manipulating water accessibility to the internalised paramagnetic

centres. On conjugating proteins with larger size than the nanoparticles' pores, the facile water access to the Gd^{3+}-centres can be switched off resulting in a transition of contrast from a strong to weak state. Nanoparticles have been successfully biomodified without the disadvantage of contrast loss through the insertion of suitably long PEG chains in between the particle surface and protein. This pegylation technique keeps the steric bulk of protein away from the particle surface so that particle pores remain open and may continue to enjoy the good internal water access necessary for high MR signal contrast. Significantly, under this construct a vectoring protein modified nanoparticle which can simultaneously retain both its targeting capability and high MRI contrast has been prepared. This work has clearly validated the vital importance of efficient communication between internalised Gd^{3+}-centres and water protons and has driven the central concept of a contrast-reversible switch towards the development of nanoparticle-based responsive contrast agents. As a proof of principle, a bulky streptavidin protein has been non-covalently conjugated onto the particle periphery through its interaction with biotin-labelled nanoparticles to gate the porous apertures, resulting in a contrast switch-off. Significantly, the contrast can be switched back on in the presence of a competitive biotinylated BSA. Through this on-off contrast change, one can potentially use MRI as a functional technique to detect a protein and its partner protein.

In addition to this unique MRI switching application, bulky proteins have also been employed in the encapsulation of small model drugs inside MSNs. Significantly, the

undesired premature release of drugs has been shown to be effectively prevented by this capping means. The specific response of the capping proteins to externally reductive stimulation has led to their removal and the subsequent release of the loaded drugs. The model drug released from MSNs in this work has demonstrated a two-step diffusional mechanism where the release began with a faster burst process associated with the removal of drug moieties localized in the pore openings followed by a steady diffusion of more deeply internalised ones. Importantly, the release kinetics can be tuned through controlling the surface charge (achieved through the use of different functional groups). Specifically, the electrostatic interactions between particle surfaces and charged drugs have dictated the effectiveness of triggered release, which is of fundamental importance in the design of any diffusional-based drug delivery vehicle. Nanoparticles with concentrated surface amines possessing positive charges that strongly electrostatically attracted the cationic drugs have been shown to release at a slower rate.

The use of MSNs in therapeutic delivery is not limited in the physical encapsulation of small synthetic drugs. In this work, the delivery of therapeutic proteins through covalent attachment on nanoparticles has been thoroughly investigated. On conjugating these proteins *via* uncleavable linkers on nanoparticles surfaces, their stability and activity can be secured without proteolytic degradation during the transportation to subcellular machinery. Specifically, therapeutic cytochrome *c*, a well-known apoptotic triggering agent which is not readily uptaken by cells in the absence

of a delivery vehicle, has been investigated in inducing programmed cell death (apoptosis). To initiate a cytosolic caspase cascade, an important trigger within the apoptosis pathway, cytochrome *c*-functionalised nanoparticulate vehicles have been introduced to the cytosol of cells, by escape from the default endocytic pathway. Significantly, this has been achieved with a relatively simple consideration of particle surface group pKa (and the resulting nanoparticle pI). Through carefully tuning the surface characteristics of nanoparticles, it has been demonstrated that they undergo cationisation with charge changes exceeding 40 mV during the acidification (maturation) of endocytic vesicles. Such changes in combination with their associated interaction with the negative lipid bilayer of the organelles and the osmotic pressure subsequently generated have led to the particle release into cell cytosols. Cytochrome *c* carried by particles with these surface characteristics has been shown to access the cytosol within 24 h and to efficiently trigger Hela cancer cell apoptotic death.

There are clearly a wide range of practical applications for the functional MSNs described herein. Enhanced contrast with these functional materials will pave the way towards new dual-modal constructs, providing both diagnostics and therapeutics. This will change the face of modern healthcare enabling patient-specific diagnosis and treatment as well as triggered disease specific therapy. Importantly, the targeting therapy based on nanoparticles enables the possibility in lowering the dosage as the vectoring particles can specifically reach the site of interest for triggered payload delivery.

The MSNs synthesised in this work have great potential in a variety of bioapplications. The tracking of stem cells and their associated tissue repair, for example, could be immediately achieved by using our high MRI contrast nanoparticles. For other types of cells such as T-cells in immune systems that are unable to readily internalise silica nanoparticles, the contrast particles developed here could be further tethered with an antibody whose antigen is expressed on cell membranes to specifically tag the cells and to monitor their subsequent immune response by MRI. The MSNs delivery system could also be used in vaccination or gene therapy. Significantly, the ability to escape from destructive endocytic entrapment potentially provides a reliable means to deliver therapeutic nucleic acid to cell nucleus. It is believed that such usage and other relevant arrays of applications could be further achieved with the adaption from the techniques developed in this work.

Appendix

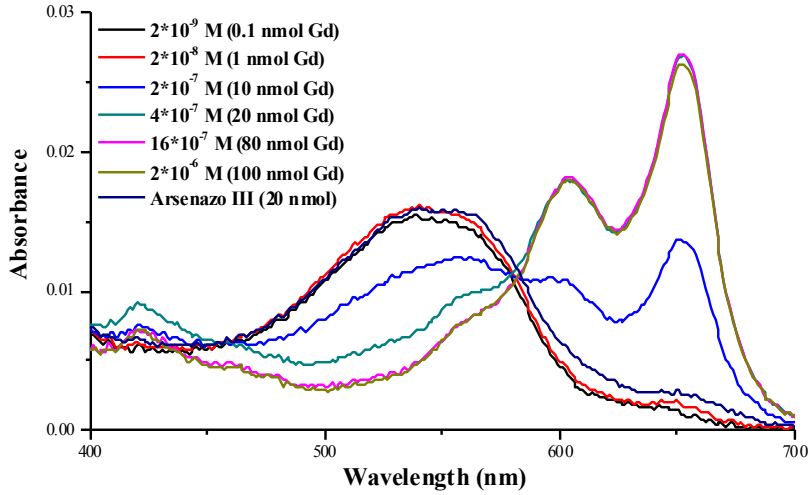


Fig. A1 Absorption spectra of arsenazo III as a function of the concentration of standard Gd^{3+} solution, showing the limit of detection of the arsenazo (III) to be 10 nmol Gd^{3+}.

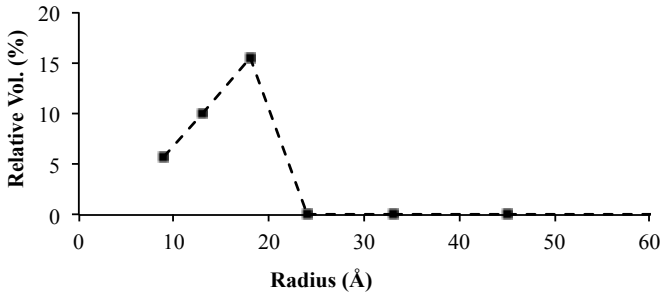


Fig. A2 Pore size distribution graph of volume *vs.* radius of 0.15 mol% NH_2-MSNs determined from nitrogen adsorption/desorption measurement (BET). Mesopores radii: 1.6 ± 0.7 nm.

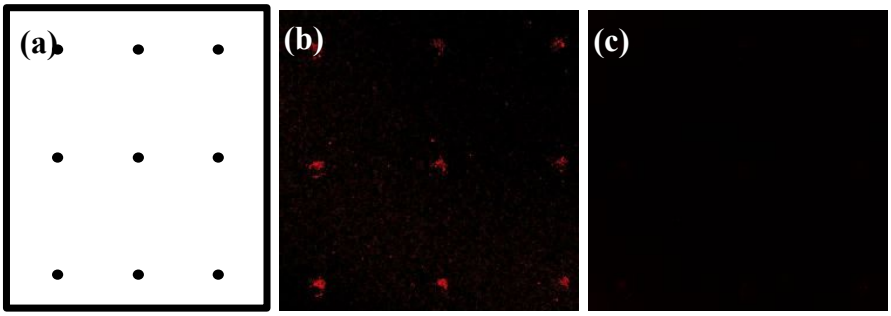


Fig. A3 Microarray spotting of (a) schematic representation of ordered biotinylated BSA arrays; (b) vectored fluorescent STV conjugated Gd^{3+}-dpoed MSNs *via* disulfide linkers (STV-SS-MSNs) prior to bond cleavage, showing binding towards biotinylated BSA spots; and (c) image after reducing agent treatment, showing no fluorescent binding and confirming the removal to fluorescent STV *via* disulfide cleavage.

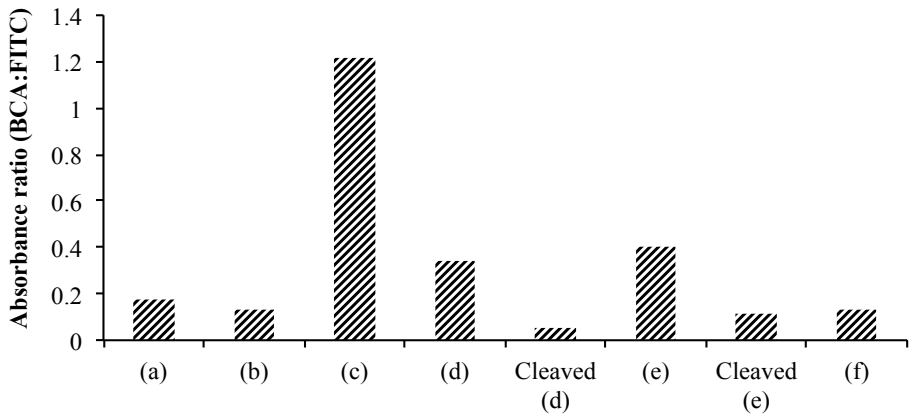


Fig. A4 UV-vis Absorbance ratiometric, the ratio is determined from the absorbance of protein induced bicinchoninic acid-cuprous complexes (BCA assay) with respect to that of FITC on particles, indicating particle type (a), (b) and (f) containing a comparable protein level on particles whereas type (c) bearing a much higher degree of protein coating. The protein levels on type (d) and (e) can not be directly compared with those on other particle types, as the linkages employed can interfere with BCA absorption. The ratio of particle (d) and (e) after bond cleavage were also indicated, showing the successful removal of the proteins. Note that this technique is only designed for qualitative comparison.

Publications and Presentations

Publications

1. W. Y. Huang, G. -L. Davies and J. J. Davis, "Engineering Biomodified Silica Nanoparticles to Induce Programmed Cell Death" Journal of the American Chemical Society, in submission.
2. W. Y. Huang, G. -L. Davies and J. J. Davis (2013), "High Signal Contrast Gating with Biomodified Gd Doped Mesoporous Nanoparticles", Chemical Communications, 49 (1), 60.
3. J. J. Davis, W. Y. Huang and G. -L. Davies (2012), "Location-tuned Relaxivity in Gd-doped Mesoporous Silica Nanoparticles", Journal of Materials Chemistry, 22 (43), 22848.
4. W. Y. Huang and J. J. Davis (2011), "Multimodality and Nanoparticles in Medical Imaging", Dalton Transaction, 40 (23), 6087.

Presentations

1. W. Y. Huang and J. J. Davis, "Biovectoring and T1 Contrast Gating with Mesoporous Silica Nanoparticles" Materials Research Society Meeting 2012 Fall, Boston, USA
2. W. Y. Huang and J. J. Davis, "Biovectoring and T1 Contrast Gating with Mesoporous Silica Nanoparticles" Graduate Symposium 2012, Oxford, UK